Ionization of Diatomic Molecules in Intense Laser Fields

D I S S E R T A T I O N

zur Erlangung des akademischen Grades

d o c t o r r e r u m n a t u r a l i u m
(Dr. rer. nat.)
im Fach Physik

eingereicht an der
Mathematisch-Naturwissenschaftlichen Fakultät
der Humboldt-Universität zu Berlin

von
M. Sc. Abdou Mekky Mousa Hussien

Präsident der der Humboldt-Universität zu Berlin:
Prof. Dr. Dr. Jan-Hendrik Olbertz

Dekan der Mathematisch-Naturwissenschaftlichen Fakultät:
Prof. Dr. Elmar Kulke

Gutachter/innen:
1. Prof. Dr. Alejandro Saenz
2. Prof. Dr. Mikhail Ivanov
3. Prof. Dr. Manfred Lein

Tag der mündlichen Prüfung: 18.09.2015

Abstract

The ionization of some diatomic molecules, H_2, N_2, and O_2, exposed to intense laser fields has been studied by comparing various molecular tunneling–ionization models with each other and with the numerical solution of the time-dependent Schrödinger equation (TDSE). The internuclear-distance dependent ionization yields over a wide range of laser peak intensities are investigated and the validity of the modified atomic and molecular tunneling models is examined. It is found that those models that depend on the quasi-static approximation, where ionization is independent on the oscillation frequency of the applied laser field, are useful for laser-induced ionization processes in only a very small region of the frequency and intensity domain of laser fields, i.e. in the tunneling regime. The models that include a frequency dependent factor are in agreement with the accurate TDSE calculations in both the multi-photon and the tunneling ionization regimes. Furthermore, the influence of the strong internuclear-distance dependence of the ionization yield of H_2 on the vibrational-state distributions in H_2^+ and on the dynamics of the vibrational nuclear wavepacket in H_2^+ is discussed. The deviation from a Franck-Condon-like distribution is clarified. The propagation and revival times of the vibrational nuclear wavepacket of H_2^+ (including the bond-softening effect) are discussed in details.

It is also shown that it is not quite correct, at least for molecules, to consider the circular polarized field as a static field, since a time-varying electric field direction gives rise to a change of the molecular alignment through a cycle of the laser pulse. The alignment-dependent ionization probabilities of H_2 as a function of laser intensity, and the anisotropy in linear and circular polarized fields using molecular tunneling model are investigated. The calculated ratio of the ionization probabilities for laser fields parallel and perpendicular to the molecular axis are in a reasonable agreement with the experimental observations, in contrast to previous statements in literature, especially if the focal volume of the laser field is considered.

The tunneling models are also tested for larger molecules, i.e. N_2 and O_2. A reasonable agreement between the predictions obtained by the tunneling models with the TDSE calculations is found. Moreover, the atomic tunneling models are investigated by choosing the proper values of the quantum numbers l and m that are related to the highest occupied molecular orbital.

Zusammenfassung

In dieser Arbeit wurde die Ionisation einiger zweiatomiger Moleküle (H_2, N_2 und O_2) in intensiven Laserfeldern untersucht. Hierbei wurden verschiedene Modelle zur Beschreibung der Tunnelionisation sowohl untereinander als auch mit der Lösung der zeitabhängigen Schrödingergleichung (TDSE) verglichen. Die kernabstandsabhängige Ionisationswahrscheinlichkeit wurde für verschiedene Intensitäten betrachtet und die Gültigkeit modifizierter atomarer bzw. molekularer Modelle zur Beschreibung der Tunnelionisation analysiert. Es wurde herausgefunden, dass Modelle, die auf der quasistatischen Näherung beruhen (wo die Ionisation unabhängig von der Frequenz des Laserfeldes ist), nur in einem kleinem Frequenz- und Intensitätsbereich hinreichend genaue Ergebnisse liefern, dem Tunnelregime. Modelle mit einem frequenzabhängigen Faktor stimmen hingegen sowohl im Tunnel- als auch im Mehrphotonenregime mit den genaueren TDSE Ergebnissen überein. Weiterhin wurde der Einfluss der starken Kernabstandsabhängigkeit der Ionisationswahrscheinlichkeit von H_2 auf die Besetzungen der H_2^+-Schwingungszustände und die folgende Wellenpaketdynamik im erzeugten H_2^+-Molekül diskutiert. Hierbei wird Abweichung zu den Besetzungen, die man im Rahmen der Franck-Condon Näherung erhält, herausgestellt. Die Propagations- und Revivalzeiten des Kernwellenpakets im H_2^+-Ion (inkl. des Bond-Softening Effekts) werden im Detail diskutiert.

Es wurde außerdem gezeigt, dass es nicht ganz richtig ist, die Tunnelionisation eines zirkular polarisierten Laserfeldes mit der eines statischen Feldes gleichzusetzen, da eine sich mit der Zeit verändernde Feldrichtung zu einer Änderung der Ausrichtung des Moleküls innerhalb einer Periode des Laserfeldes führt. Die ausrichtungsabhängigen Ionisationswahrscheinlichkeiten von H_2 wurden als Funktion der Laserintensität betrachtet und die Anisotropie für linear und zirkular polarisierte Felder mit Hilfe von Modellen zur Beschreibung der molekularen Tunnelionisation untersucht. Das berechnete Verhältnis der Ionisationswahrscheinlichkeiten für parallel und senkrecht zur Molekülachse ausgerichtete Laserfelder sind in hinreichend guter Übereinstimmung mit experimentellen Beobachtungen, im Gegensatz zu Gegenteiligen Behauptungen in der Literatur. Dies gilt insbesondere, wenn die Feldstärkenverteilung im Fokusvolumen des Laserfeldes berücksichtigt wird.

Die Modelle zur Beschreibung der Tunnelionisation wurden auch für die größeren Moleküle N_2 und O_2 getestet. Eine hinreichend gute Übereinstimmung der Vorhersagen aus den Tunnelmodellen mit TDSE Rechnungen wurde beobachtet. Auch die atomaren Tunnelionisationsmodelle wurden hierbei untersucht, wobei die verwendeten Quantenzahlen so gewählt wurden, dass die Orbitalform möglichst gut mit der Form des energetisch höchsten besetzten Molekülorbitals Übereinstimmt.

Contents

1 Introduction

The investigation of the interaction of atoms and molecules with intense laser fields comprises one of the most interesting areas of the current research in atomic and molecular physics. The general motivation for studying molecules in laser fields comes from the possibility of obtaining fundamental understanding of the dynamics of quantum systems on real time scales and of the intermediate processes involved in various physical, chemical, and biological reactions. The recent evolution of laser sources allowed for new frontiers of science which cover observations in broad areas of atomic, molecular, and optical physics (AMOP) to be presented. A confluence of advances in laser science has opened the door to study the laser-matter interaction as the new frontier of the 21^{st} century.

Before the invention of the **laser**, which stands for **L**ight **A**mplification by **S**timulated **E**mission of **R**adiation, the intensity was low and perturbation theory was sufficient to describe light-matter interaction, in which the field is treated as a small perturbation. According to this theory and due to the fact that a weak field drives transitions between atomic or molecular states without much distortion of the material itself, conventional spectroscopy has been used to study the material structure. However, after the invention of the laser and the rapid development of its techniques, it became possible to achieve higher intensities such that it is no longer possible to treat the laser as a small perturbation. Accordingly, nonlinear phenomena associated with ionization of molecules in intense laser fields have encouraged considerable theoretical and experimental interest. Much of the earlier experimental and theoretical studies in this non-perturbative regime of laser–atom interaction in atomic systems has been summarized in [1, 2]. Subsequently, in the atomic case new non-perturbative phenomena have been found like above-threshold ionization (ATI) [1], and tunneling ionization [3–5]. Another important nonlinear process, high-order harmonic generation (HOHG), is currently the most convenient source of attosecond (as) pulses[1] [6]. Similar to atoms, a series of relevant strong-field processes occur in molecular systems including ATI [7–9], double and multiple ionization [10–12], and high-harmonic generation [13]. Apart from atomic photo-ionization,

[1] 1 attosecond = 10^{-18} second.

some characteristic features of molecular ionization have been observed experimentally, such as the orientation dependence of strong–field ionization and suppressed molecular ionization [14, 15]. Moreover, many new concepts in molecules have been theoretically proposed and confirmed experimentally using intense femtosecond laser pulses such as bond-softening (BS) and bond-hardening [16, 17], above-threshold dissociation [18, 19], charge-resonance enhanced ionization [20, 21], Coulomb explosion [22], etc. (for a review see [23] and references therein). The explanations of most of these phenomena are based on tunneling ionization (TI) as the first step of the physical processes. Studying the details of molecular ionization provides an additional insight into these ionization processes, and help in the understanding of those phenomena.

In intense laser fields, one usually distinguishes two regimes for ionization, the *quasi-static* regime and the *multi-photon* regime, where the distinction is based on the Keldysh parameter γ [3], which depends the field strength and the frequency of the laser as well as the ionization energy of the atomic or molecular system[2]. In the present context an intense laser field is characterized by a field strength that is comparable to the Coulomb interaction between the electrons and the nuclei. The typical intensities for this to be the case, depending on the ionization potential of the target system, are $10^{13} - 10^{15}\,\mathrm{W/cm^2}$. In the early days of strong-field physics, the theoretical and experimental studies have been primarily concentrated on atoms.

Within a non-relativistic theory, the accurate ionization yield of atoms or molecules can theoretically be obtained by solving the time-dependent Schrödinger equation (TDSE)[3]. The advantage of the numerical solution is that accurate TDSE calculations can be performed over a wide range of laboratory parameters. While the disadvantage is that the TDSE may often not give a simple physical insight as to why particular types of behavior occur in physical systems. The TDSE is within the non-relativistic description "exact", so it is frequently used to examine the accuracy of the analytical approximations, which give rise to instructive physical interpretations. In spite of theoretical advances in modeling of atoms in laser fields, it is still too difficult to carry out a full *ab initio* calculation of a multi-electron atom, so that the theoretical understanding must rely on some kind of approximation and theoretical modeling. Most treatments are based on the dipole and the single-active-electron (SAE) approximations. In addition to the TDSE calculations for studying the strong-field ionization of atoms or molecules, some simpler analytical models that are quite useful and widely used, were proposed to calculate the ionization rates. The Keldysh–Faisal–Reiss (KFR) theory [3, 24, 25] is used to treat

[2]Please refer to section 2.2.1 for an accurate definition for the Keldysh parameter.

[3]The direct numerical solution of the time-dependent Schrödinger equation for laser-induced processes is referred to as “TDSE”.

the ionization of atoms in a strong laser field, which has been further extended to be applicable for molecules (the so-called the molecular strong-field approximation MO-SFA) [15, 26]. The Ammosov-Delone-Krainov (ADK) theory [27] is another alternative model used to study the tunneling ionization of atoms, which was also generalized to molecular systems [28] and is referred to as the molecular tunneling theory (MO-ADK). Tong and Lin [29] have used the ADK theory in the over-the-barrier ionization (OTBI) regime by modifying the original ADK theory with an empirical correction factor, which will be applied also for the MO-ADK in this thesis. Another tunneling-ionization model proposed by Perelomov, Popov and Terent'ev (PPT) [30–32] was found to fit quite well to the experimental ionization signals in the multi-photon and tunneling ionization regimes. Additionally, the PPT theory will be extended to molecules in analogy to the MO-ADK model, and will be called MO-PPT model. It is important to carefully examine ADK, PPT, MO-ADK, and MO-PPT theory with the more accurate TDSE calculations. This thesis produces a direct comparison of the TDSE results with those obtained within those models for *molecules*. Noteworthy, Zeng-Hua *et al.* [33] compared the ionization probabilities in a short laser pulse of *atoms* that are obtained from the PPT and ADK models with those obtained by the TDSE calculation. It was found that the ionization probabilities obtained from PPT agree well with those from TDSE calculations in both the multi-photon and tunneling ionization regimes, while the ADK model, as expected, fails to give the correct ionization probabilities outside the tunneling regime.

From an experimental point of view, further understanding and investigation of the mechanism behind a specific molecular ionization phenomenon requires an extension of the measurements to other wavelength ranges than 800 nm [34]. One of the experiments performed at a shorter wavelength of 400 nm [35] exhibited a similar behavior for O_2, but a rather different behavior for N_2. The N_2 molecule is found to have a higher ionization probability compared to that of Ar atom for linear polarization, while the difference vanishes for circular polarization. This finding has been explained by a resonant enhancement in N_2, a characteristic feature of a multi-photon ionization (MPI) process. In this work, the laser-wavelength 400 nm will be addressed besides the 800 nm. Moreover, using both linearly and circularly polarized laser fields for ionization of H_2 is discussed. This thesis will report attempts to explore and understand the interaction of the laser fields with homonuclear diatomic molecules like H_2, N_2, and O_2. It provides a detailed study of strong-field ionization of diatomic molecules in the quasi-static regime. The ionization of diatomic molecules within the extended atomic and molecular tunneling models is investigated. One of the main goals of this thesis is to carefully examine the ADK, the frequency-corrected ADK (fc-ADK), PPT, MO-ADK, and MO-PPT approximations by a direct comparison of the ionization probabilities with those of the

accurate TDSE calculations and with few existing experimental data. The dependence of the ionization yields on the laser parameters and on the alignment of the molecules is investigated using those models.

The following questions should be answered in this work: (i) Which of the tunneling formula in this work is suitable to describe the ionization of molecules? And is it valid for diatomic molecules beyond H_2? (ii) Is the quasi-static approximation applicable for realistic laser pulse at all? (iii) Can the tunneling approaches help to understand the influence of vibrational motion on strong laser-field ionization and how does bond softening affect the dynamics of the nuclear vibrational wavepacket? (v) Is it correct to consider a circular polarized laser field as a static field, in the case of molecules? (vi) Does the MO-ADK model fail to predict the intensity-dependent anisotropy of the ionization probabilities for H_2, as has been recently claimed in literature [36–41]? Furthermore, what is the focal-volume effect of the laser pulse on the anisotropy? (vii) Can the simple tunneling approaches correctly predict the R dependence for larger diatomic molecules like N_2 and O_2? How does this affect the vibrational-state distribution in the molecular ion? (viii) Can the MO-ADK and MO-PPT models be used to study the orientation-dependent ionization yield?

This thesis is organized as follows. It is grouped into six chapters. Chapters 2 and 3 cover some of the basic concepts and some of the current theories related to the ionization of atoms and molecules in strong laser fields. The analytical methods that will be used to describe the ionization rates are briefly reviewed in Chapter 2. Chapter 3 describes the TDSE for diatomic molecules in laser fields. Some approaches used for solving the TDSE and obtaining the ionization probability are also included. Chapter 4 discusses the distribution over vibrational states formed in the H_2^+ ion following ionization of the neutral H_2 molecule with linear polarized laser fields (800 and 400 nm). The formation and propagation of the vibrational nuclear wavepacket of H_2^+ is investigated. In addition, the effect of the bond softening on the revival time of the wavepacket is shown. In chapter 5, the alignment-dependent tunneling ionization of H_2 in linear and circular polarized fields is studied within the molecular tunneling models. The difference between the alignment of the molecule in a circular and linear polarized field is demonstrated. Furthermore, the focal volume of the laser pulse and the correction due to barrier-suppressed ionization will also be considered. Chapter 6 discusses the validity of the tunneling ionization models for larger diatomic molecules, i.e. N_2 and O_2. Finally, the summary and conclusion of this work is given in chapter 7, followed by five Appendices and a list of the abbreviations used in this thesis.

2 Tunneling ionization in strong fields

2.1 Basic tunneling theory

The interaction of intense laser pulse with matter leads to electrons tunneling from atoms or molecules to the continuum [42]. Tunneling means that a particle penetrates a potential barrier without having enough energy to overcome it. This is considered a quantum phenomenon that challenges classical intuition. However, quantum-mechanical tunneling processes play an important role in a variety of fields and technologies because of their applications, which include solid-state physics (such as scanning tunneling microscopy (STM) and in various semiconductor devices), nuclear physics, biophysics, as well as atomic and molecular physics. Therefore, the tunneling process is one of the most fundamental concepts of quantum mechanics, since the concept of wave-particle duality and other quantum phenomena, like Heisenberg uncertainty principle, have to be considered to understand tunneling. This chapter describes the basis of the different and often competing ionization processes experienced by atoms and molecules in the presence of a laser field with particular interest on the tunneling process.

2.2 Ionization of atoms

Most interactions of the electromagnetic fields with atoms have been well characterized. When the ionization of an atom by an electromagnetic field is considered, two different basic situations can happen. In the first one an atom absorbs photon with energy greater than the ionization energy of the atom[1]. Hence, the atom is ionized and the electron is liberated. In the second situation, when the ionization potential is much greater than the photon energy, different ionization mechanisms such as **M**ulti-**P**hoton **I**onization (MPI), **T**unneling **I**onization (TI) and **O**ver-**T**he-**B**arrier **I**onization (OTBI), can occur in a non-linear regime. The mentioned ionization processes may occur simultaneously within an atomic system. However, for a given laser intensity and specific frequency

[1] The ionization energy is the energy required to eject the electron from the force field of the nucleus.

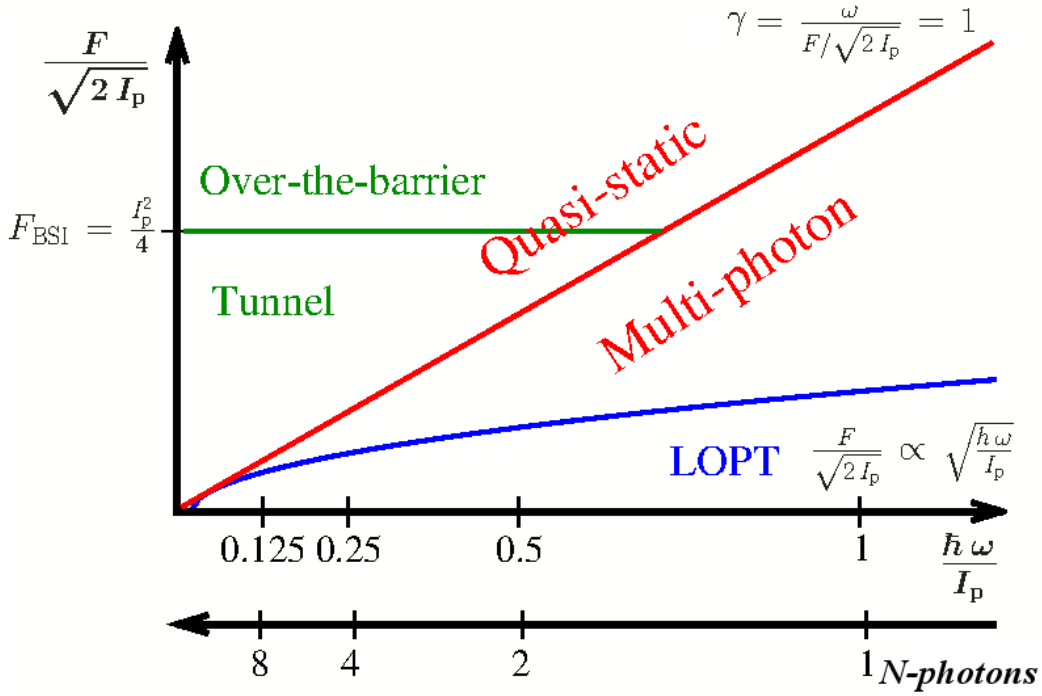

Figure 2.1: A schematic representation of the different ionization regimes motivated by the Keldysh theory. The regimes are characterized by the scaled field strength $F/\sqrt{2\,I_p}$ and the scaled photon energy $\hbar\omega/I_p$ where I_p is the binding energy of the electron. The red line shows $\gamma = 1$, which divides the region into multi-photon and quasi-static regimes. The green line further divides the quasi-static regime into tunnel and over-the-barrier ionization regimes. The blue line separates the lowest-order perturbation theory (LOPT) regime from the multi-photon regime. This figure is taken from Ref. [43].

one of these processes tends to be the dominant process, as will be discussed later. For the first time, Keldysh [3] presented a simple analytical formula for atomic multi-photon ionization beyond usual perturbative theory. He presented a parameter which allows to separate the perturbative multi-photon regime from the nonperturbative quasi-static regime that can be further divided into the tunneling and over-the-barrier regimes. Over-the-barrier and tunnel regimes are well described by the quasi-static approximation if the frequency of the laser is small compared to the inherent time scale of the system exposed to it. The reason for this terminology is that the variation of the laser field is very slow on the time scale of electronic motion that the instantaneous ionization rate is supposed to agree with a static one. Figure 2.1 shows a schematic distribution of the ionization regimes as a function of the electric field amplitude F, and the field frequency ω, both properly scaled with the binding energy I_p of the system. Keldysh theory is

considered the basis for many fruitful concepts in this field, so it will be discussed in the next section.

2.2.1 Keldysh parameter

One of the most important concepts of time-dependent ionization is the distinction between the different ionization processes that was first introduced by Keldysh [3]. In his pioneering work in 1964, Keldysh introduced an adiabatic parameter as the ratio of the laser frequency ω to the tunneling frequency $\omega_{\texttt{tun}}$ of the least bound electron of a system. This adiabaticity parameter is nowadays well known as *Keldysh parameter* γ and it is used as an indicator which ionization mechanism is dominant. The main ionization processes and the oscillating electric-field which tilts the atomic potential are shown in Fig. 2.2. The intrinsic time scale set by the atom-field system can be easily analyzed, as depicted in Fig. 2.2c. In the adiabatic regime, it is helpful to consider the effect of the instantaneous laser field on the atomic Coulomb potential. Thus, the total potential V of an electron confined within an atom by V_{el} and being exposed to an external electric field V_{ex} is given by

$$\begin{aligned} V(\mathbf{r}) &= V_{\text{el}}(\mathbf{r}) - V_{ex}(\mathbf{r}) \\ &= -\frac{Ze}{4\pi\epsilon_0\,|\mathbf{r}|} - \mathbf{r}.e\,\mathbf{F}(t) \quad [\texttt{in SI units}]\,, \end{aligned} \tag{2.1}$$

with the electron charge e, nucleus charge Z and the vacuum permittivity[2] ϵ_0.

Suppose an atomic state with a binding energy of the least bound electron, $-E_b$, in an electric field F of the laser pulse. For a low electric field strength compared with the atomic potential, the various mechanisms of photo-ionization via virtual intermediate states apply, as shown in Fig. 2.2b. If the oscillating field is strong enough and its frequency is low enough (i.e. the field changes slowly in comparison to the electronic time scales, so the electron feels essentially a slow variation), it will be able to distort the potential barrier in a way that an electron gets the possibility to escape from the barrier by tunneling, Fig. 2.2c. It is clear that, as the field strength increases, the barrier becomes smaller and lower until eventually the ground state becomes no longer bound, hence the TI process may change into an OTBI process, Fig. 2.2d, as will be discussed later. Before discussing the different ionization processes in more detail, It is necessary to present the key idea behind point of the popular parameter γ in this field.

[2]The conversion between SI and atomic units (a.u.) is presented in Appindex A.

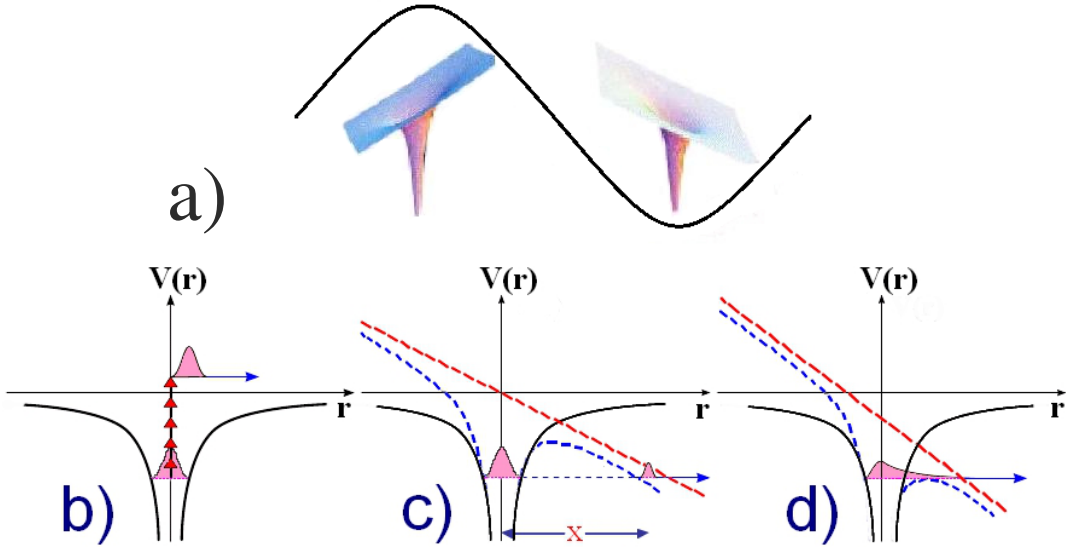

Figure 2.2: Schematic diagram in which the electric field is shown as oscillating field, which tilts the atomic potential (**a**) and the three main ionization mechanisms in the non-linear regime: (**b**) multi-photon ionization, (**c**) tunneling ionization and (**d**) over-the-barrier ionization. The black curves represent the original (field-free) Coulomb potential and the dashed blue curves represent the distorted Coulomb potential by the external field, while the sloped long-dashed line is the laser field potential. The dotted magenta lines show the energy of the least bound electron in the field-free case. The tunneling path is indicated by the red dashed line.

The Keldysh parameter can be derived within the following consideration: According to Fig. 2.2c, the ease or difficulty of tunneling can be expressed as the ratio between the equivalent classical time it takes for the electron to tunnel out the potential barrier, while the potential is bent down, and half of the laser cycle. This dimensionless ratio is called Keldysh parameter γ which it can be defined as

$$\gamma \equiv \frac{\omega}{\omega_{tun}} \equiv \frac{tunneling\,time}{\frac{1}{2}laser\,period} \equiv \frac{\tau_{tun}}{\frac{1}{2}\,\tau_{las}}\,, \tag{2.2}$$

where the tunneling time, t_{tun}, is defined as the time it takes for an accelerated electron to tunnel or cross through the barrier moving in electric field, and τ_{las} $(= 1/2\pi\omega)$ is the period of the laser field oscillation. The classical time of flight of an electron through the potential barrier shown in Fig. 2.2c according to Keldysh theory is expressed as

$$\tau_{tun} = \frac{\text{tunneling} \quad \text{width}}{\text{tunneling} \quad \text{velocity}}\,. \tag{2.3}$$

This ratio is a measure of how fast the barrier oscillates compared to the time it takes for the electron to tunnel ionize. It is assumed that the electron in the classical Coulomb potential well moves back and forth along the width of the barrier with a kinetic energy equal to the binding energy, E_b, before the external field is applied. The average velocity of the outward electron V_{avg} is [44]

$$\langle V_{avg} \rangle \;=\; \left(\frac{2\,E_b}{m_e} \right)^{1/2} , \tag{2.4}$$

where m_e is the electron mass. When the external field is applied[3], the electron will pass with this velocity through the potential barrier, which is classically forbidden region, with the tunneling width

$$x \;=\; \frac{E_b}{|e|\,F} , \tag{2.5}$$

where e is the electron charge. Equations (2.4) and (2.5) can then be combined to determine the tunneling time as given by

$$\tau_{tun} \;=\; \frac{x}{\langle V_{avg} \rangle} \;=\; \frac{\sqrt{E_b\, m_e}}{\sqrt{2}\, e\, F}, \tag{2.6}$$

Tunneling can occur if the mean tunneling time, τ_{tun}, is less than half the period of the laser field (see Eq. (2.2)). Then, the Keldysh adiabaticity parameter can be written as

$$\gamma \;=\; \frac{\omega\,\sqrt{2\,m_e\,E_b}}{|e|\,F} = \sqrt{\frac{|I_p|}{2\,U_p}} , \tag{2.7}$$

where I_p ($\equiv E_b$) is the ionization energy in the Coulomb field and U_p is the ponderomotive energy, which describes the average oscillation energy that is acquired by a free electron in the radiation field of the laser pulse. Subsequently, the definition of the Keldysh parameter is equivalent to the square root of the ratio of the ionization potential and twice the ponderomotive potential of the laser pulse. The ponderomotive energy depends on the square of the wavelength and is linearly dependent on the intensity, this can be written as

$$U_p\,(\mathrm{eV}) = \frac{e^2\,F^2}{4\,m_e\,\omega^2} \;\simeq\; 9.33 \times 10^{-14}\; I\; \left(\mathrm{W}/cm^2\right) \lambda^2\; (\mu m)\;, \tag{2.8}$$

[3]The velocity of the electron as a function of time is given by

$$V(t) \;=\; V_{max} - |F|\,.\,t\,,$$

where $V_{max} \;=\; V_{avg}$. According to the basis of tunneling ionization models [1, 4], the electron is ionized and produced in the continuum with initial zero velocity ($V_{final} \;=\; 0$).

where λ and I are the wavelength and the intensity of the laser field, respectively. Then, γ can be calculated if both the intensity and the laser-wavelength of the laser field as well as the ionization potential are known, since U_p scales as $I\lambda^2$. Noteworthy, the peak intensity and the peak field strength are related by the conversion formula

$$\begin{aligned} F &= \left(\frac{2}{c\,\epsilon_0}\,I\right)^{1/2} && [\texttt{in SI units}] \\ &= \left(\frac{8\,\pi}{c}\,I\right)^{1/2} = \left(\frac{\text{Intensity in W}cm^{-2}}{3.51\,\times 10^{16}}\right)^{1/2} && [\texttt{in atomic units}]\,, \end{aligned} \tag{2.9}$$

where c is the velocity of the light in vacuum.

As discussed earlier, Keldysh parameter allows for a quantification of the different ionization mechanisms more formally as follows. For $\gamma \ll 1$ tunnel ionization should be a good picture. From a practical point of view, it would be convenient to have definite numerical values for γ, not just $\gamma \ll 1$. So, the question arises: how much should be γ smaller than unity? Experimentally, Ilkov *et al.* [45] have found the condition $\gamma < 0.5$ is necessary for the tunneling process to be dominant. This means that the tunneling time is less than 1/4 of the laser field's period (see Eq. (2.2)). This condition seems reasonable because the Coulomb potential of the electron is bent down on one side of the Coulomb potential well during 1/2 of a period. During the most of this half period, the barrier is too large for the electron to escape through. With increasing applied field, one can reach the OTBI regime that occurs starting at a critical value of the field strength, see Sec. 2.2.4. At $\gamma \gg 1$, the multi-photon process is dominant. While in the intermediate region $\gamma \simeq 1$, both the tunneling and multi-photon processes contribute to the ionization, since there is no clear transition between the both processes. The physics of the multi-photon, tunneling, and over-the barrier ionization processes will be discussed in the following three subsections.

2.2.2 Multi-photon ionization (MPI)

For large ionization potentials (compared to the photon energy), high laser frequency, and low intensity ($\sim 10^{13}$ W/cm^2), i.e. $\gamma \gg 1$, the multi-photon process is dominant (Fig. 2.2b). Depending on the quantum system, the photo-ionization process can be parametrized by frequency and intensity of the laser field. The simplest one called "*photoelectric effect*" is single ionization via one-photon absorption which was discovered in 1887 and explained by Einstein in 1905. This phenomenon is one of the non-classical effects which opened the door to establish the quantum theory. It occurs if the photon

energy, $\hbar\omega$, of the incident radiation is higher than the binding energy of the outermost electron in the system. This process is also referred to as a linear photo-ionization, since the ionization rate Γ is proportional to the intensity of the field according to,

$$\Gamma = \sigma\,(\frac{I}{\hbar\omega})\,, \tag{2.10}$$

where σ is the total photo-ionization cross section and the intensity I is sufficiently low. However, if $\hbar\omega$ is lower than the binding energy of the outermost electron, absorption of multiple photons is necessary for ionization, as illustrated in Fig. 2.2b, leading to the so-called *multi-photon ionization* (MPI). Thus, the electron can be transferred to the continuum via multiple photon absorption. It has been assumed that the electron kinetic energy in the continuum states will be given by $N\hbar\omega - E_b$. This is a simple extrapolation of the Einstein picture of the photoelectric effect.

At moderate laser intensity MPI can be accurately described by using **l**owest-**o**rder **p**erturbation **t**heory[4] (LOPT) with respect to the electron-field interaction for early experiments [46, 47]. This picture is valid as long as the strength of the electric field is much smaller than the atomic electric field. This condition allows to treat the external potential as a small perturbation of the Coulomb potential. Then, it is possible to solve the Schrödinger equation using the perturbation theory. The N-photon ionization rate Γ_N, as a function of the generalized N-photon ionization cross-section σ_N and laser intensity is given by

$$\Gamma_N = \sigma_N \left(\frac{I}{\hbar\omega}\right)^N . \tag{2.11}$$

Usually, σ_N decreases rapidly as N increases. Equation (2.11) leads to a linear dependence on a logarithmic scale, where the slope N indicates the minimum number of photons needed for ionization. The N-photon and the ionization cross sections have been accurately measured and found to be in a good agreement with the corresponding ionization cross sections calculated within LOPT, although some complications occurred if MPI happened to go through an intermediate bound state. The latter process, so-called *resonant enhanced multi-photon ionization* (REMPI), causes divergences in LOPT, but adopting the proper formulation within the density-operator formalism these difficulties can be handled.

In fact, at high laser frequencies and low intensities the tunneling time is larger than the laser period (field oscillation) such that the electric field will change its direction while

[4] As the name suggests, LOPT can be only applicable for small perturbations and breaks down at intensities higher than $\sim 5\times 10^{12}$ W/cm^2.

the electron is still confined within the barrier. Therefore, tunnel ionization is completely suppressed and the ionization may happen via the absorption of an integer number of single-photons (small vertical arrows in Fig. 2.2b) within the lifetime of intermediate states (real or virtual). So that, high photon densities will also be necessary, which have become available after the development of intense laser pulses.

2.2.3 Tunneling ionization (TI)

The tunneling-ionization process is dominant at low frequency and high intensity (10^{14} - 10^{15} W/cm^2). In this regime, the laser period is greater than the tunneling time and the field can be treated classically. As mentioned before, the electric field with low frequency may be treated as a quasi-static field. It distorts the Coulomb potential to such an extent that the bound electrons of the system can tunnel out of the potential barrier and thus the system is ionized. Hence, the ionization rate is determined by the width of the barrier, as depicted in Fig. 2.2c. When the laser electric field modifies the atomic potential, the quantum mechanical tunneling becomes more likely. Thus, the electron does not scatter on the system, but it is drawn towards the edge of the system's orbital, from which it can escape by tunneling. Unlike the multi-photon process, which includes the transition between states with different energy, the tunneling is associated with the transition through a barrier, where the initial and final states have the same total energy.

The ionization rate for the $1s$ state of the hydrogen atom in a weak static electric field was derived by Oppenheimer [48]. From a quantum mechanical point of view, the electron can, in this case, leave the system by tunneling through the barrier. Based on the quasi-classical approximation and asymptotically valid for weak fields, Landau and Lifshitz [49] have given a well known and simpler ionization rate formula of the ground state of a hydrogen atom as a function of the field strength[5] F, as

$$\Gamma(F) = \frac{4}{F} \exp\left(-\frac{2}{3\,F}\right) . \tag{2.12}$$

This formula is applicable, as long as the strength of the electric field is clearly smaller than the atomic field. The exponential factor in Eq. (2.12) is the most important one and it is common for most of tunneling ionization rates. It shows that at low field strengths the ionization rate is low and it exponentially increases as the field increases until the

[5] Atomic units ($\hbar = m_e = e = 1$) are used from now throughout this work unless stated otherwise, for more details see appendix A.

over-the-barrier region, where the tunneling equation can not be applied as the electron becomes no longer bound by the barrier.

Perelomov, **P**opov, and **T**erent'ev [30] have extended this result to obtain a general expression for a static and a quasi-static (low-frequency) ionization rate for arbitrary bound states of a hydrogen atom which is the so-called PPT model, which will be discussed in Sec. 2.3.2. It was later generalized using some further approximations to derive an equation for the probability of tunnel ionization of complex atoms or atomic ions, and in arbitrary states by Ammosov, Delone, and Krainov [27], which later known as ADK model. These two models are also extended to molecules that are frequently used nowadays, see Secs. 2.5.1 and 2.5.2.

2.2.4 Over-the-barrier ionization (OTBI)

For some systems and specific laser frequencies, the dominant ionization mechanism may change with increasing the field strength directly from the tunneling regime to the over-the-barrier regime, which is also known as **b**arrier-**s**uppression **i**onization (BSI). As the field strength increases, the barrier becomes more narrow and its height reduces. Starting from the tunneling-ionization picture, it is easy to imagine that increasing the laser intensity to be high enough to deform the atom's electrostatic potential so much that an electron is no longer bound and can pass over the top of the barrier without tunneling (Fig. 2.2d). Hence, the process changes from TI to over the-barrier ionization (OTBI) and subsequently the ionization rate grows smoothly until it reaches to a specific intensity called saturation intensity. The minimum field strength required to be at the top of the barrier is equal to the electron's binding energy. It is designated as the threshold field strength between the two processes (or as critical value for OTBI) and given by

$$F_{\mathrm{C}} = \frac{E_{\mathrm{b}}^2}{4\,Z}\,, \tag{2.13}$$

while the critical value of the intensity threshold is then,

$$I_{\mathrm{C}}(\mathrm{W}/cm^2) = 4 \times 10^9\, \frac{E_{\mathrm{b}}^4\,(\mathtt{eV})}{Z^2}\,. \tag{2.14}$$

At the critical threshold field, F_{C}, the unperturbed atomic energy level lies on the top of the potential barrier. Above this critical field, we enter the barrier-suppression regime and then the ionization rate that depends on the perturbation theory will overestimate the exact ionization rate. This is reflected by an exponential growth in the error of the tunneling ionization rate [29]. In the barrier-suppression regime, where ionization can

occur above the top of the potential barrier, the application of a tunneling theory, e.g., the ADK theory does not work well [50] and leads to a significant error in this regime. Tong and Lin [29] proposed a fit formula to extend the tunneling ionization formula into the barrier-suppression regime to reduce this error in the barrier-suppression region and conserve the simplicity of the tunneling ionization formula. This formula provides an accurate ionization rate for atoms and molecules in intense laser field under the single-active electron (SAE) approximation. The modified formula for $\Gamma^{\mathrm{B}SI}$ in a static field takes the form

$$\Gamma_{st}^{\mathrm{B}SI}(F,\omega) \;=\; \Gamma_{st}(F,\omega)\,\exp\left(-a\,\frac{2\,Z\,F}{\kappa^5}\right)\,, \tag{2.15}$$

where $\kappa = \sqrt{2\,I_p}$, with I_p being the ionization energy. Here, a is an empirical parameter obtained by fitting the formula to the ionization rates calculated from a number of atoms and ions that are obtained by solving the Schrödinger equation using the complex scaling method [51], $a = 6$ for atomic hydrogen [29]. Because of the Stark shift in the ground-state energies of the ion and the neutral atom or molecule in the strong field[6], Saenz [50] introduced a so-called field-dependent vertical ionization potential in atomic ADK formula to agree with *ab initio* results, that is known later as an extended ADK model.

In practice, the ion-yield curves are usually monotonically increasing. At some point, the slope in the log–log plot of ionization yield versus laser peak intensities is changing and asymptotically adjacent to a constant slope of 3/2 above this point [52]. The change in the slope represents the start of the saturation of the single ionization process. In fact, observation and interpretation of the saturation of ionization in the center of the focal volume [53] has not been trivial because a unity probability (i.e. saturation) was originally expected, see also Appendix B.

2.3 Atomic tunneling-ionization models

2.3.1 Tunneling ionization in a quasi-static field and ADK theory

Strong laser fields with low frequency can ionize atoms and molecules efficiently. Tunnel ionization of a hydrogen atom in a static electric field is commonly calculated in parabolic coordinates. Some assumptions are needed to describe tunnel ionization in an

[6]Stark shift is the dynamical shifting of the energy levels in the neutral molecule (here H_2) and its daughter ion (H_2^+) due to an applied electromagnetic field.

electromagnetic field[7] [27]. The first of these assumptions is that the only initial and final states of the electron are significant in tunneling. The intermediate states play no role, in contrast to multi-photon ionization theory, where these states play the main role. To motivate this assumption, one can recognize that a coupling between the ground state and any excited state of an atom or molecule needs some time to develop. From a quantum mechanical point of view, this time is at least one cycle of the field oscillation because the transition (or coupling) probability is obtained by integrating the transition matrix over time of at least one cycle of the laser oscillation. In a time less than one cycle of oscillation, such a coupling could be negligible or meaningless. As pointed out before, the experiments have shown that tunneling ionization can happen when $\gamma < \frac{1}{2}$, i.e. when the tunneling time is smaller than $\frac{1}{4}$ of the field oscillation. Therefore, One does not need to consider the influence of intermediate states [54]. Whereas, the second assumption is a quasi-classical approximation[8], which can be considered in this regime. The results for an alternating field could be easily obtained from those for a static field by substituting F by $F\cos(\omega t)$ and integrating over the period of the field T. Consequently, the ionization rate $\Gamma_{\rm st}$ of an external static electric field from an arbitrary state of a hydrogen atom with binding energy E_b, orbital quantum number l, and its projection m along the direction of the static electric field, is given by the expression [30]

$$\Gamma_{\rm st}(F) \,=\, |C_{n,l}|^2\, f(l,m)\, E_b \left(\frac{2F_0}{F}\right)^{2n-|m|-1} \exp\left(-\frac{2\,F_0}{3\,F}\right), \tag{2.16}$$

where $F_0 \,=\, (2\,E_b)^{3/2}$, and the factor $\left(\frac{2F_0}{F}\right)^{2n}$ is the long-range effect of the Coulomb potential; $C_{n,l}$ and $f(l,\,m)$ contain the information about the initial atomic state. The factor $f(l,\,m)$ is given by

$$f(l,\,m) \,=\, \frac{(2\,l+1)(l+|m|)!}{2^{|m|}|m|!\,(l-|m|)!}\,; \qquad f(0,0) \,=\, 1, \qquad f(1,0) \,=\, f(1,1) \,=\, 3\,, \tag{2.17}$$

while the quantity of the dimensionless constant $C_{n,l}$ is known only for the hydrogen atom [31, 49], and defined by

$$|C_{n,l}|^2 \,=\, \frac{2^{2\,n}}{n(n\,+\,l)!\,(n\,-\,l\,-1)!}\,. \tag{2.18}$$

Ammosov, Delone, and Krainov [27] had extended the scope of the ionization formula of Eq. (2.16) by replacing the principal quantum number of the hydrogen atom n with the effective quantum number $n^* = Z(2E_b)^{-1/2}$, with Z being the charge seen by the

[7] For a static electric field, these assumptions are not needed.

[8] It is also known as WKB theory, in reference to Wentzel, Kramers, and Brillouin, who popularized it.

active electron asymptotically, and the orbital quantum number l by the effective one l^*, where

$$l^* = \begin{cases} 0 & \text{for } l \ll n^* - 1 \ ; \\ n^* - 1 & \text{otherwise} \end{cases} \ . \tag{2.19}$$

To avoid the difficulty of performing the factorial on non-integer numbers, the asymptotic Stirling formula, for $n^* \gg 1$, is applied and one finds[9] [45],

$$|C_{n^*l^*}|^2 = \frac{1}{2\,\pi\,n^*} \left(\frac{4\,e^2}{n^{*^2} \ - \ l^{*^2}} \right)^{n^*} \left(\frac{n^* \ - l^*}{n^* \ + \ l^*} \right)^{l^* + \frac{1}{2}} \ , \tag{2.20}$$

where e ($\simeq 2.71828...$) is the Euler number. If Eq. (2.20) is substituted into Eq. (2.16), the final formula of the ionization rate of larger atoms or ions in the ground state is given by

$$\begin{aligned} \Gamma_{\rm st}(F) \ = \ & \frac{F}{8\,\pi\,Z}\, f(l,\,m) \left(\frac{4\,e^2}{(n^{*^2} \ - \ l^{*^2})} \right)^{n^*} \left(\frac{n^* \ - \ l^*}{n^* \ + \ l^*} \right)^{l^* + 1/2} \\ & \times \left(\frac{2\,Z^3}{n^{*^3}\,F} \right)^{2n^* - |m|} \exp\left(-\frac{2\,Z^3}{3\,n^{*^3}\,F} \right) . \end{aligned} \tag{2.21}$$

This modified formula can be applied to more complex electronic structures (atomic or ionic systems) and also to an arbitrary orbital momentum. Usually $\dfrac{2\,Z^3}{n^{*^3}\,F} \gg 1$, hence the ionization rate is the largest for the case $|m| = 0$, while the other terms with values of $m = \pm 1,\ \pm 2,\ ...$ show negligibly ionization rates. In other words, according to Eqs. (2.16) and (2.21), atoms prepared in a state with $m \neq 0$ will ionize much more slowly than atoms with $m = 0$. Therefore, an approximation for Eq. (2.21), which is often used for $m = 0$, is given by (considering $l^* = n^* - 1$)

$$\Gamma_{\rm st}^{m=0}(F) = \frac{e}{2\,\pi} \frac{Z^2(2l+1)}{n^{*^3}\sqrt{(2n^* - 1)}} \left(\frac{4\,e\,Z^3}{(2n^* - 1)n^{*^3}F} \right)^{2n^* - 1} \exp\left(-\frac{2Z^3}{3n^{*^3}F} \right) . \tag{2.22}$$

Consequently, the relation between the ionization rates in the two cases ($l = 0$ and $l = 1$) can be directly extracted from Eq. (2.22) as

$$\Gamma_{st,\,l=1}^{m=0}(F) \ = \ 3\ \Gamma_{st,\,l=0}^{m=0}(F)\,. \tag{2.23}$$

It is important to remind that Eq. (2.21) is valid for a static field. The dependence of the ionization rate on the oscillating field was treated in [27, 30] as follows. The situation is

[9] In the original paper [27], there are a number of misprints that have been corrected in Ref. [45].

considered in which the external electric field is oscillating as

$$\mathbf{F}(t) \;=\; F\,\left[\cos\left(\omega t\right)e_x \;+\; \varepsilon\,\sin\left(\omega t\right)e_y\right]\;, \tag{2.24}$$

and an electron is located in a Coulomb potential. The parameter ε describes the polarization of the field, $\varepsilon = 0$ (± 1) for a linearly (circularly) polarized field, otherwise it is an elliptically polarized field.

Let us consider the case of a linearly polarized field ($\varepsilon = 0$), and assume the adiabatic approximation is valid, i.e. the tunneling time of the electron is much smaller than the optical period corresponding to the tunneling regime. Whereas the atom adiabatically follows the changes in the external field, one can obtain the instantaneous ionization rate by inserting the formula of linear polarized pulse instead of the static one directly in Eq. (2.21). As a result with typical frequencies which correspond to wavelengths in the infrared region, the ionization rate will be an average of the instantaneous ionization rate, $\Gamma(t)$, over the period of the external field. Subsequently, the ionization rate in a linear polarized field Γ_{lin} is given by Bisgaard and Madsen [55] as

$$\Gamma_{lin}(F) \;=\frac{1}{\pi}\int_{-\pi/2}^{\pi/2}\Gamma(t)\,d(\omega t)\,, \tag{2.25}$$

where $\Gamma(t)$ is the instantaneous rate. The dependence of the exponential part on the field strength shows clearly that the dominant contribution to the rate is for $\cos(\omega t) \to 1$ (i.e. $\omega t \sim 0$). Because the exponential is much more rapidly changing than any other power, the time dependence of the pre-exponential factor can approximately be neglected. If the Taylor expansion of $1/\cos(\omega t)$ at $\omega t \sim 0$ is used, the time-dependent rate is approximated as

$$\Gamma(t) \;\approx\; \Gamma_{st}\exp\left(-\frac{F_0}{3\,F}\left(\omega t\right)^2\right)\;, \tag{2.26}$$

From Eqs. (2.25) and (2.26), the relation between the ionization rate in a linear polarized and a static field is given by

$$\begin{aligned}\Gamma_{lin}(F) \;\approx&\Gamma_{st}\,\frac{1}{\pi}\int_{-\pi/2}^{\pi/2}\exp\left(-\frac{F_0}{3\,F}\left(\omega t\right)^2\right)\,d(\omega t)\\ \approx&\left(\frac{3\,F}{\pi\,F_0}\right)^{1/2}\Gamma_{st}\,.\end{aligned} \tag{2.27}$$

Where the integration limits have been extended to infinity assuming $F_0/F \gg 1$. This means that in the adiabatic case, the ionization rate of an atom occurs mainly at the times when the field reaches its maximum values. Because of $F \ll F_0$ the rates for the

linear polarized field are always lower than the rates for a static field. It is necessary to emphasize that F is the peak value of the electric-field component of the laser field.

In a circularly polarized field, the magnitude of the electric field is a constant (time-independent). Accordingly, it has often been erroneously assumed that the ionization rate in a circular polarized field is similar to that of the static field, i.e. $\Gamma_{\texttt{cir}} = \Gamma_{st}$. This adiabatic picture, which ignores the electric field direction during the tunneling event is, if at all, applicable to atoms, while it may not be a good approximation for molecules. This point will be discussed in more detail in chapter 5.

For a slightly elliptical polarized field, with $\varepsilon \ll 1$, the ionization rate, $\Gamma_{\texttt{ell}}$, is calculated from

$$\Gamma_{\texttt{ell}}(F) \simeq \left(\frac{3\,F}{\pi\,F_0\,(1-\varepsilon^2)}\right)^{1/2} \Gamma_{\rm st}(F)\,, \tag{2.28}$$

assuming that $F_0/F \gg (1-\varepsilon^2)$. Noteworthy, Eq. (2.27) is often known in the literatures as ADK rate, although Perelomove, Popov, and Terent'ev derived it much earlier [30]. Even more importantly, they went beyond this level of approximation and proposed an analytical theory, named PPT theory, valid for a large range of γ values. This theory will be discussed in the next subsection and in chapter 4.

2.3.2 PPT theory

Ilkov and co-workers [45] concluded that whenever one wants to compare experimental data with the ADK theory, one must make sure that the tunnel-ionization conditions, $F < E_b^2/4Z$ and $\gamma < 0.5$, are satisfied. Otherwise, the results could even in the best case only be considered as a qualitative guide and needs to be scaled. In contrast, the PPT theory goes beyond the purely static model and can fit most of the experimental data very well. The reason for the success of the PPT model comes seemingly from the inclusion of the frequency dependent factor in addition to Coulomb field effect on the outgoing electron during ionization.

Perelomov *et al.* [30] studied the interaction of atomic systems with laser light and introduced a possible general formula (PPT model). It was derived for a short-range potential and then corrected to take the long range Coulomb interaction into account. The PPT theory derives the ionization of an atomic bound state under the action of an alternating, (linear, circular and elliptically polarized) electric field. Some of the important results of their paper will be highlighted in the following.

1. **The case of a linear polarized field**

According to PPT theory, the tunneling ionization rate within a linear polarized field for a hydrogen-like atom, after correcting a number of misprints in Refs. [30, 45, 56, 57], is given by[10],

$$\Gamma_{lin}^{PPT}(F,\omega) = |C_{n^*l^*}|^2\, f(l,\,m)\, E_b \sqrt{\frac{6}{\pi}} \left(\frac{2F_0}{F\sqrt{1+\gamma^2}}\right)^{2n^*-|m|-3/2} \\ \text{x } A_m(\omega,\gamma)\, \exp\left(-\frac{2\,F_0}{3\,F}\, g(\gamma)\right), \tag{2.29}$$

with

$$A_m(\omega,\gamma) = \frac{4}{\sqrt{3\,\pi}}\, \frac{1}{|m|!}\, \frac{\gamma^2}{1+\gamma^2} \sum_{\tilde{n}>\nu}^{\infty} \left[e^{-\alpha(\gamma).(\tilde{n}-\nu)} W_m(\sqrt{\beta(\gamma).(\tilde{n}-\nu)})\right]; \tag{2.30}$$

$$W_m(x) = \frac{x^{2|m|+1}}{2} \int_0^1 \frac{e^{-x^2\,t}\, t^{|m|}}{\sqrt{1-t}} dt\,,$$

$$\alpha(\gamma) = 2\left[\sinh^{-1}(\gamma) - \frac{\gamma}{\sqrt{1+\gamma^2}}\right], \qquad \beta(\gamma) = \frac{2\,\gamma}{\sqrt{1+\gamma^2}}\,,$$

$$g(\gamma) = \frac{3}{2\gamma}\left\{\left(1 + \frac{1}{2\gamma^2}\right)\sinh^{-1}(\gamma) - \frac{\sqrt{1+\gamma^2}}{2\gamma}\right\} \\ = \begin{cases} 1 - \frac{1}{10}\,\gamma^2 + \frac{9}{280}\,\gamma^4 & \text{for } \gamma \ll 1\,, \\ \frac{3}{2\gamma}\,(\ln 2\gamma - \frac{1}{2}) & \text{for } \gamma \gg 1\,, \end{cases} \tag{2.31}$$

$$\nu = \frac{E_b}{\omega}\left(1 + \frac{1}{2\,\gamma^2}\right), \qquad \texttt{and} \qquad \tilde{n} = \langle \frac{E_b}{\omega} + 1\rangle + S\,.$$

Where S=0,1,2,... and the symbols $\langle\,\rangle$ indicate the integer part of the number inside, which refers to the minimum number of photons required to ionize the system. As before, ω is the energy of one photon and F is the peak value of the external electric field. The quantities $f(l,\,m)$ and $|C_{n^*l^*}|^2$ are defined by equations (2.20) and (2.17). All the other symbols have the same meaning as before.

[10] Note that the term $\left(\frac{2F_0}{F\sqrt{1+\gamma^2}}\right)^{2n^*}$ was missed in the expression for Γ_{lin}^{PPT} given in Eq. (54) of Ref. [30], while in Ref. [45] a factor 2 was missed in Eq. (8). Also the factor $(\frac{1}{\sqrt{1+\gamma^2}})^{2n^*}$ was missed in both Eq. (10) of Ref. [56] and Eq. (A2) in Ref. [57].

The physical meaning of Eq. (2.29) is understood as follows. As pointed out earlier by Keldysh [3], the probability of ionization is the sum of the probabilities of multi-photon processes, each of which corresponds to the absorption of an integer number ($\tilde{n} \geqslant \nu$) of quanta. The main factor in Eq. (2.29) is the exponential, which increases rapidly for $\gamma \ll 1$. To see how the coefficient of the exponential varies with the frequency, the following two cases will be considered:

a) At low frequencies ($\gamma \to 0$), there is a large number of contributing terms to the sum in Eq. (2.30), and $A_m(\omega, \gamma)$ goes to 1. Hence, Eq. (2.29) approaches the corresponding standard formula of the adiabatic approximation (Eq. (2.27)), while the multi-photon nature vanishes.

b) At high frequencies ($\gamma \gg 1$), one can adopt the approximation

$$\frac{F}{2\,F_0}\,\sqrt{1\,+\,\gamma^2} \approx \frac{\omega}{4\,E_b} \approx \frac{\omega}{4\,\omega_0}\,, \tag{2.32}$$

where $\omega_0 \equiv E_b$ is the binding energy of the electron and the function $A_m(\omega, \gamma)$ reduces to the first term of the series. The coefficient of the exponential in this frequency range is a rapidly varying function, with singularities at the thresholds for absorption of $\tilde{n}$ photon, which implies that the multi-photon process dominates in this regime.

In fact, despite the importance and higher accuracy of the PPT formula, most of the experimentalists and even theorists neglected it and prefer the simpler ADK formula instead. This neglect may come from the complexity of the calculation of both the $A_m(\omega, \gamma)$ factor and the $g(\gamma)$ function. However, the latter one is not complicated to such an extent that it should be neglected. Furthermore, it plays an important role in the ionization-rate formula for two reasons; first it is present in the exponential term and second it shows the influence of the wavelength and subsequently the frequency of the applied field, which is missed in the simpler ADK formula. In this thesis, an approximation for PPT model is given as [58]

$$\Gamma_{lin}^{fc-ADK}(F,\omega) = |C_{n^*l^*}|^2 f(l,m) E_b \sqrt{\frac{6}{\pi}} \left(\frac{2F_0}{F\sqrt{1+\gamma^2}}\right)^{2n^*-|m|-\frac{3}{2}} \exp\left(-\frac{2F_0}{3F} g(\gamma)\right) \tag{2.33}$$

by keeping $g(\gamma)$ and neglecting the $A_m(\omega, \gamma)$ factor in Eq. (2.29), the so-called **f**requency **c**orrected ADK (fc-ADK) model, will be examined in chapter 4. All the symbols have the same meaning like before. For $\gamma \to 0$, PPT theory and fc-ADK converge to the standard ADK rate, since the ADK model is a simplified version

of PPT.

2. The case of a circular polarized field

When a circular polarized field is applied to an atom, we note that the difference from the linear case is that the threshold for ionization (the minimum number of quanta) is $\nu = \frac{E_b}{\omega}\,(1+\frac{1}{\gamma^2})$. This is due to the fact that the mean kinetic energy of the electron in the field of the circularly polarized field is twice its mean energy in the field of the linear polarized field. Therefore, the total ionization rate formula for an s level in a circularly polarized field will be[11]

$$\Gamma_{cir}^{\mathrm{P}PT}(F,\omega) = |C_{n^*l^*}|^2\, E_b\, f(l,\,m)\, \left(\frac{2\,F_0}{F}\right)^{2n^*-|m|-1} h(\gamma)\, \exp\left(-\frac{2\,F_0}{3\,F}\, g_c(\gamma)\right), \tag{2.34}$$

where

$$g_c(\gamma) \,=\, \frac{3\,t_0}{\gamma^2\,(1\,-\,t_0^2)}\, \left[(1\,+\,\gamma^2)\,\left(1\,+\,\frac{t_0^2}{\gamma^2}\right)\right]^{1/2}, \tag{2.35}$$

$$h(\gamma) \,=\, (1\,-\,t_0)\, \left[\frac{(1\,+\,\gamma^2)\,(1\,-\,t_0^2)}{(1\,+\,t_0^2/\gamma^2)\,(1\,+\,t_0^2\,+\,2\,t_0^2/\gamma^2)}\right]^{1/2}, \tag{2.36}$$

and

$$t_0(\gamma) \,=\, \begin{cases} \frac{1}{3}\,\gamma^2\,(1\,-\,\frac{28}{45}\,\gamma^2\,+\,...) & \text{for } \gamma \ll 1; \\ 1\,-\,1/\ln\gamma\,+\,... & \text{for } \gamma \gg 1\,. \end{cases} \tag{2.37}$$

In the limit $\gamma \to 0$,

$$\lim_{\gamma\to 0} g_c(\gamma) \,\simeq\, (1\,-\,\gamma^2/15), \quad \texttt{and} \quad \lim_{\gamma\to 0} h(\gamma) \,\simeq\, 1\,,$$

and $\Gamma_{\mathrm{cir}}(F,\omega)$ goes over into $\Gamma_{\mathrm{st}}(F)$, as it should. For $\gamma \gg 1$ one can get

$$g_c(\gamma) \,\approx\, (3\,\gamma/2)\ln\gamma\,,$$

which leads to a rapid increase of the ionization probability.

A direct comparison between Eqs. (2.31) and (2.36) demonstrates that the argument of the exponential in the formula for $\Gamma(F,\omega)$ has different frequency dependencies for linear and circular polarized fields, i.e. the exponential is not a universal

[11] This equation is written after correcting some of misprints that are found in Eq. (68) of Ref. [30].

function of γ [30].

So far, only the case where $\omega \ll \omega_{tun}$ (tunneling region) has been discussed. In that case, the adiabatic approximation was applied and the effect of the atomic Coulomb potential is neglected in the Keldysh theory. However, for high intensity and $\omega \gg \omega_{tun}$, the adiabatic approximation becomes invalid and cannot be applied. To find the ionization rate one has to solve the time-dependent Schrödinger equation.

2.4 Diatomic molecules in a strong laser field

Strong-field laser-matter interactions can take place in molecules as well as in atoms. The interaction of high intensity laser pulses with many simple molecules has been widely studied, see, e.g., [59, 60]. The first investigations on simple atomic systems led to the discovery of interesting processes like high-order harmonic generation (HOHG) [61–64], above-threshold ionization (ATI) [65–69] or stabilization against ionization [70–73]. HOHG is the creation of very high, odd harmonics of the laser field through coherent excitation and de-excitation of highly energetic continuum states. Thus, the HOHG effect is a coherent emission of photons with shorter wavelengths than the incident photons. This is the non-linear response of the atom to the intense laser field by emitting photons with integer multiples of the incident laser frequency. The second effect, ATI, occurs when electrons absorb a larger number of photons than the minimum number required to reach above the ionization threshold. The third effect is the stabilization of an atom against ionization at sufficiently high intensities and/or high photon frequencies.

In diatomic molecules, the nuclear potential is simply the sum of the potentials from each nucleus plus the interaction potential between the nuclei. While this sounds simple in theory, in fact it is hardly a simple extension of atoms, for more details the reader is referred to, e.g., the textbook by Haken and Wolf [74]. Similar to the ionization process in atoms, the interaction of a high-intensity laser field with a molecule manipulates the system's eigenstates. The study of the ionization process for molecules becomes significantly more complex, even in the simplest case of the H_2^+ ion. Although MPI and ATI features are readily observable in molecules, as for atoms, the extra degrees of freedom of molecules that are absent in atoms, arising from vibration and rotation of the constituent atoms about the center of mass and along the internuclear axis, leads to a number of new and interesting high-field phenomena not seen in the interactions with atomic systems. For example, nuclear motion can be affected by the field which causes

molecules to change their rotational and vibrational quantum numbers and redistribute the energy between different modes. Molecules can also fragment or dissociate in the field, leading to a more complex final state. Because of the duration of the ultra-short pulses being of the order or shorter than the characteristic time scales of the nuclear dynamics (vibration $\simeq 10\,\mathrm{fs}$, rotation $\simeq 1\,\mathrm{ps}$) within which the control can be realized, the observation of the molecular dynamics can primarily be achieved.

Furthermore, in a molecule the internuclear separation and the relative angle between the polarization of the applied field and the molecular axis are important parameters. The molecular symmetry axis provides a clear reference for interactions with an electric field, since the axis can be oriented from parallel to perpendicular with regards to the applied field (see Sec. 2.4.2). If the field is oriented perpendicular to the molecular axis, the interaction is approximately comparable to the atomic case for simple molecules [75]. However, if there is a significant field component along the molecular axis, the electron can tunnel out of both Coulomb wells [20].

Several new effects due to the molecular character were also proposed and confirmed experimentally using intense femtosecond laser pulses. This includes bond softening and hardening, above-threshold dissociation, charge resonance enhanced ionization, Coulomb explosion, etc. Most of those phenomena are based on tunneling ionization as the first step of the processes. I will not go into the details of all these phenomena, but some of the phenomena that have been already discovered are discussed briefly in the next sections.

2.4.1 Symmetry and configurations of the electronic states

Unlike atoms, molecules lack spherical symmetry. The breaking of the symmetry affects the electronic states. Although the electronic angular momentum l is not conserved in diatomic molecules, the potential is symmetric around the internuclear axis. The component of the angular momentum, λ, along this axis remains conserved and can be used to classify the electronic states of a diatomic molecule. The orbital wavefunctions associated with $\lambda = 0, 1, 2, 3, ...$ are named σ, π, δ, $\varphi, ...$ in analogy to $s, p, d, f, ...$ in atoms for $l = 0, 1, 2, 3$, etc. In homonuclear diatomic molecules (e.g., H_2, N_2, and O_2) one property is particular. The energy of a state should not vary for a simultaneous change of all electronic coordinates under the reflection on a plane bisecting the internuclear axis. So, double reflection should again return to the original function. Therefore, there should be two kinds of states in the diatomic homonuclear molecules: those that are invariant to the transformation and those that change their sign. The former are called *even* states

(German: *gerade*) and the latter are named *odd* (German: *ungerade*). Thus, the even and odd states are denoted by g and u, respectively. This leads to the designation of the single electronic orbitals in diatomic molecules as follows: the quantum number n, followed by the Roman letter corresponding to the quantum number l, followed by the Greek letter describing the quantum number λ. In addition, for homonuclear diatomic molecules *even* (g) or *odd* (u) parity has to be specified. Therefore, the electronic orbitals are written as $n\,l\,\lambda\,{}_{g(u)}$. For example, the two lowest lying electronic states of the hydrogen molecular ion H_2^+ using these notations are called $1s\sigma_g$ and $2p\sigma_u$.

For multi-electron configurations, it is appropriate to classify the states according to the total angular momentum Λ along the internuclear axis. According to this classification, the spatial wavefunctions with $\Lambda = 0, 1, 2, 3, ...$ are labeled $\Sigma, \Pi, \Delta, \Phi, ...$ states (similar to the atomic case). All the states with $\Lambda > 0$ are doubly degenerate, while Σ states are non-degenerate. The molecular state has also to be characterized by the total spin S of the electrons. Because of the different possible orientations of the spin vector, a state with the total spin S has $(2S + 1)$-fold degeneracy. The number $(2S + 1)$ is called the *multiplicity* of the state and designated by a superscript placed before the Greek letter describing Λ. It takes the values 1 for singlet multiplicity and 3 for triplet multiplicity. One should also distinguish the inversion symmetry that is named as g or u, as well as the spatial symmetry with respect to a reflection through the internuclear axis by $(^+)$ and $(^-)$. For example, the ground state of H_2 is labeled as $^1\Sigma_g^+$ and the one of O_2 as $^3\Sigma_g^-$. From a multi-photon point of view, these electronic states of diatomic molecules can contribute to multi-photon resonances. Special attention is paid to the **h**ighest **o**ccupied **m**olecular **o**rbital (HOMO), which allows for a quick determination whether a particular diatomic molecule is covalently bonded. The HOMO is the orbital that could act as an electron donor, since it is the outermost orbital containing electrons (with highest energy). The tunneling rate depends on the electric field as well as on the internuclear distance. Furthermore, it is well known that there is a critical internuclear distance, R_c, for which tunneling ionization is maximized for a given electric field [20, 21, 76].

The vibrational states[12] are labeled with ν and the separation of these energy levels are typically on the order of 10's of meV. The effect of vibrational motion on the internuclear positions has an effect on the ionization rates only at distances smaller than the equilibrium distance [77]. The rotational states, labeled with J, are very closely spaced in energy (meV).

[12]States that differ in units of vibrational energy of the nuclei.

2.4.2 Alignment versus rotation

It has been observed that when molecules are exposed to electromagnetic fields, they tend to align themselves. In ionization studies of molecules, alignment plays an important role [78]. Those molecules that are aligned parallel to the electric field of the laser, are more easily ionized than those that are not [79–82]. Alignment of molecules in electric fields has been studied extensively [83]. It has been discovered that the alignment of molecules is feasible. Stapelfeldt and Seideman [78] presented a review on the progress which was achieved in this field until 2003. To understand the physical background and the corresponding theories concerning alignment, the reader is advised to read [84]. From a simple quasi-static picture, it is clear that fields aligned along the internuclear axis distort the potential more than fields aligned perpendicularly [16]. Usually, alignment is quantified using the $\cos^2(\theta)$ parameter, where θ is the angle between the electric field vector and the molecular axis. This type of alignment, along a specific axis, is possible only with linearly polarized laser fields, while the polarization vector of circularly polarized light varies very quickly [82]. However, with circularly polarized light, molecules can be aligned within a plane.

If a molecule is exposed to an electric field, any anisotropy in the polarizability of the various axes of the molecule will produce alignment effects. The more polarizable an axis is the larger the alignment with the field. This is the case in homonuclear diatomic such as hydrogen, where the asymmetry is relatively small. If a laser pulse duration is equal to (or longer than) the natural rotational period of the molecule in question, the alignment exists only when the laser is on and it is called adiabatic alignment. However, when the laser pulse duration is shorter than the molecular rotational period, the alignment is more transient in nature, and can be thought of as the molecule suffering a push or kick towards alignment [85]. The dynamic alignment creates a coherent rotational wavepacket. After the laser is off, the evolution of the wavepacket results in transient alignment. This dynamic alignment has the advantage of the coherence of the laser pulse and is therefore often referred to as field-free alignment[13]. However, in a thermal sample of a diatomic gas the molecules will be randomly aligned, as there is no preferred axis.

2.4.3 Dissociation and Coulomb explosion

It is not necessary that the excited states of diatomic molecules are unbound. If enough energy is given, neutral dissociation can be happen. Even bound states of the molecule

[13]The field-free alignment provides the aligned molecules without the presence of an external electric field.

may be coupled to states that dissociate if a bound state has enough coupling with a dissociating state. This process is known as *pre-dissociation* and it usually occurs at some longer time scale. It is of course influenced by the presence of a laser field that leads to bond softening [16], which will be discussed below.

Both processes, dissociation and Coulomb explosion, may also occur in excited molecular ions, leading to dissociation that results in one or more charged atomic ions. If a many-electrons molecule is already highly ionized and the removal of electrons is continued, the nuclear repulsion will finally cause a rapid Coulomb explosion, resulting in multiply charged ions [79, 86, 87]. Studies of multiply-charged molecular dissociation of molecules by measuring the kinetic energies of the dissociation products have been undertaken for decades [75, 88–91]. Spatially resolved detection of fragments contains information about the structure and dynamics of the parent molecule [92]. Molecules can also be Coulomb exploded through the interaction with intense laser pulses. Coulomb explosion happens when the molecule or molecular ion is rapidly ionized, leading to an energetic break up of the molecule due to the mutual Coulomb repulsion between the positively charged constituent ions. In this thesis, the study mainly focuses on the single-ionization processes.

2.4.4 Bond softening and bond hardening

When studying the laser-molecule interaction, it is important to consider the effect of the laser on the molecular energy levels. Because of the time dependence of the molecule-laser interaction, energy is not conserved in the molecular system by itself. In case of the molecule-laser system as a whole, however, quasi-stationary states may exist that depend strongly on the intensity of the laser pulse. These "dressed states" can result in significant changes of the molecular potential energy curves, particularly near field-free curve crossings. Zavriyev *et al.* [18] observed evidence for the field-dressed molecular potentials when studying of the dissociation of H_2^+. They considered the situation in which two potential-energy curves corresponding to electronic states of opposite parity are coupled by an odd number of photons at some internuclear distance R_0. In this case, the strong single or multi-photon coupling between the electronic levels creates an avoided crossing of the levels as a function of internuclear distance, centered around R_0. The width of this gap (illustrated in Fig. 2.3) depends on the strength of the coupling between the electronic levels and it increases with intensity. Interestingly, bound vibrational states of the lower curve can become dissociative (i.e. unstable) as the gap widens, leading to a process that is known as "*bond softening (BS)*". Although

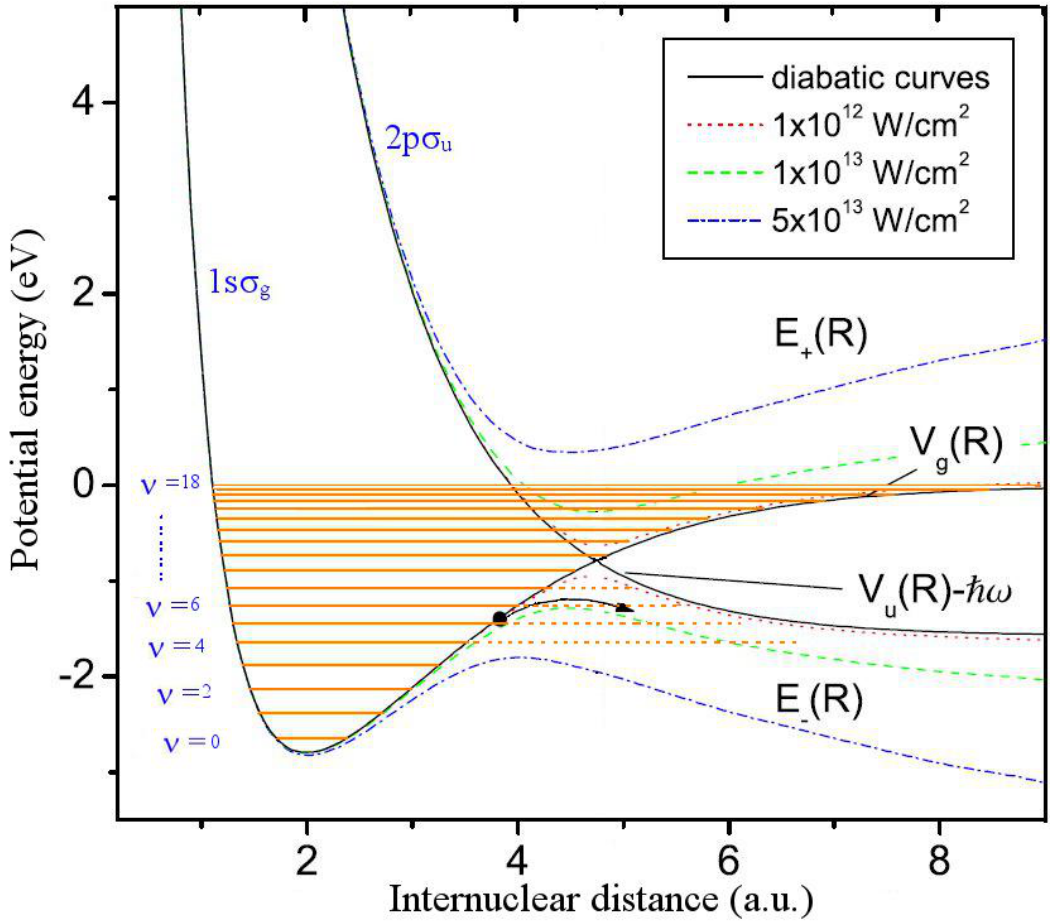

Figure 2.3: Bond softening mechanism for the H_2^+ ion. Field-dressed diabatic and adiabatic potential curves of $1s\sigma_g$ and $2p\sigma_u$ for three different low intensities. The degeneracy of two potential curves is lifted by the intense laser field. Trapped vibrational states become clearly unbound (such as $\nu > 6$) when increasing the intensity and the gap of the avoided crossing increases (adopted from [93]).

this was first studied and observed with the smallest diatomic ions (like H_2^+ and D_2^+), there are some predictions aimed to apply this phenomenon to neutral diatomic [94]. Noteworthy, Hiskes predicted BS for diatomic molecular ions like H_2^+ and concluded that this effect does not happen for neutral, covalently bound diatomic molecules such as H_2 [95]. However, Saenz [50, 94, 96] showed, in contrast to the latter prediction of Hiskes, that the neutral H_2 also shows the effect of bond softening. In view of possible control applications this is very important, since it implies that a substantial deformation of potential curves is possible, even if there is no degeneracy of the two field-free potential curves that is lifted by the field, as was the case for H_2^+ . A small amount of dissociation

may occur even if the vibrational state is below the bottom of the one-photon crossing gab because of tunneling.

On the other side, it is possible for bound vibrational states to be created above avoided crossing gaps, as the field-altered energy curves can form local potential wells at internuclear distances noticeably larger than the ground state separation. This process is called molecular stabilization, light-induced vibrational trapping, or "*bond hardening*". It was predicted in the early nineties [97] and was also experimentally observed [17, 98, 99]. The bond-hardening mechanism occurs when part of the vibrational wavepacket of the system gets trapped in an induced potential well at the peak of the laser pulse.

2.5 Molecular tunneling-ionization theory

As mentioned in Secs. 2.3, a simple tunneling-ionization model that was suggested by Perelomov *et al.* [30] and simplified by Ammosov *et al.* [27] has often been used to explain atomic tunneling ionization. Some studies are shown that many aspects of strong-field ionization of molecules are similar to those in atoms. However, further investigations on diatomic molecules demonstrated that there is a strong "*suppressed ionization*"[14] for the cases of D_2 (I_p = 15.467 eV) and O_2 (I_p = 12.060 eV) in comparison to their companion noble gas atoms Ar (I_p = 15.76 eV) and Xe (I_p =12.13 eV), respectively. It has been found that the ionization yield of D_2 (O_2) molecules is much smaller than that for Ar (Xe) atoms despite the almost identical ionization potentials. On the other hand, the ionization rate of N_2 (I_p = 15.58 eV) and F_2 (I_p = 15.697 eV) is comparable to their companion Ar (I_p = 15.76 eV) atom [100–104]. Suppressed ionization is experimentally reported for most simple diatomic molecules to organic compounds [100, 105, 106]. Accordingly, ADK formula cannot be used for all molecules, and it should be extended to the molecular ADK theory [28] (often referred to as MO-ADK), which will be presented in the next subsection.

2.5.1 Molecular ADK model (MO-ADK)

Tong *et al.* [28] introduced a molecular ADK model (MO-ADK), which is based on the assumptions of the ADK model for tunneling ionization atoms. It was modified to account for the difference in the electronic wavefunctions of atoms and molecules. They considered the modification of the radial wavefunctions of the valence electron in the

[14] Suppressed ionization describes the effect that a molecule with the same ionization potential as the one of some so-called companion atom is harder to ionize in an intense laser field.

asymptotic region. With respect to *suppressed ionization*, their predicted MO-ADK ratios are in good agreement with the measured ratios of the ionization signals for pairs with suppression (D_2:Ar, O_2:Xe) and pairs without suppression (N_2:Ar, CO:Kr). The results are also in agreement with the measured ionization signals of NO, S_2, and SO, but there are no convenient atoms for comparison. Unfortunately, this model predicted suppression for F_2:Ar, which is in disagreement with experiment; leaving this as a puzzling exception or maybe the MO-ADK model is not valid for the fully filled anti-bonding orbitals. Tong *et al.* [28, 107] derived the molecular tunneling model (MO-ADK) as follows.

In the case of atoms, the tunneling model was derived for an electronic state that is initially well defined by a single spherical harmonic. The asymptotic wavefunction in spherical coordinates of the valence electron with angular momentum quantum numbers l and m at a large distance r, where tunneling happens, can be written as

$$\Psi^m(\mathbf{r}) \;=\; \sum_l F_{lm}(r)\, Y_{lm}(\hat{\mathbf{r}})\,, \tag{2.38}$$

with

$$F_{lm}(r \to \infty) \;=\; C_{lm}\, r^{(Z_c/k)\,-\,1}\, e^{-\kappa\, r}\,, \tag{2.39}$$

where Z_c is the effective Coulomb charge, $\kappa = \sqrt{2\, I_p}$ since I_p is the ionization energy for a given valence orbital, and $Y_{lm}(\hat{r})$ is the usual spherical harmonic. The electronic wavefunction of molecules has naturally a multicenter character. Accordingly, to employ the analytical expressions for the ionization rates for molecules, one has to expand the electronic wavefunction in the asymptotic region (at large internuclear-distances) in terms of a superposition of spherical harmonics in a one-center form. So, Eq. (2.38) can be rewritten as

$$\Psi^m(\mathbf{r}) \;=\; \sum_l C_{lm}\, F_l(r)\, Y_{lm}(\hat{\mathbf{r}})\,, \tag{2.40}$$

where m is the projection of the angular momentum on the molecular axis (m = 0, 1,... for the σ_g, π,... orbitals). The coefficients, C_{lm}, which are also called fit parameters in view of Eq. (2.39), are normalized in such a way that the radial wavefunction of the molecules in the asymptotic region can be expressed as

$$F_l(r) \;=\; r^{(Z_c/k)\,-\,1}\, e^{-\kappa\, r}\,. \tag{2.41}$$

These coefficients depend on both the internuclear separation and the electronic state. They can be calculated in a number of different ways, e.g., the multiple scattering

method [28], the Hartree-Fock method [39, 108, 109], and the density-functional-theory (DFT) [110].

If the molecular axis is assumed to be aligned along the external field direction, the valence electron will be ionized along the field direction at $\theta \simeq 0$. The leading term of the spherical harmonic along this direction is

$$Y_{lm}(\hat{\mathbf{r}}) \simeq Q(l,m)\,\frac{\sin^{|m|}(\theta)}{2^{|m|}\,|m|!}\,\frac{e^{im\varphi}}{\sqrt{2\pi}}\,, \tag{2.42}$$

with

$$Q(l,m) = (-1)^m \sqrt{\frac{(2\,l\,+\,1)(l\,+\,|m|)!}{2\,(l\,-\,|m|)!}}\,. \tag{2.43}$$

By substituting Eqs.(2.39) and (2.42) in Eq.(2.40), the wavefunction in the tunneling region can be rewritten as

$$\begin{aligned}\Psi^m(r,\theta,\varphi) &\simeq \sum_l C_{lm}\,Q(l,m)\,r^{(Z_c/\kappa)-1}\,e^{-\kappa\,r}\,\frac{\sin^{|m|}(\theta)}{2^{|m|}\,|m|!}\,\frac{e^{im\varphi}}{\sqrt{2\pi}} \\ &\simeq B(m)\,r^{(Z_c/\kappa)-1}\,e^{-\kappa\,r}\,\frac{\sin^{|m|}(\theta)}{2^{|m|}\,|m|!}\,\frac{e^{im\varphi}}{\sqrt{2\pi}}\end{aligned} \tag{2.44}$$

with

$$B(m) = \sum_{l\geq m} C_{lm}\,Q(l,m)\,. \tag{2.45}$$

The final expression for the ionization rate for a diatomic molecule with its axis aligned with the static field strength F is given by

$$W_{\rm st}^{MO-ADK}(F,\theta=0) = \frac{B^2(m)}{2^{|m|}\,|m|!}\;\frac{1}{\kappa^{\frac{2\,Z_c}{\kappa}-1}}\left(\frac{2\,\kappa^3}{F}\right)^{\frac{2\,Z_c}{\kappa}-|m|-1}\exp\left(-\frac{2\,\kappa^3}{3\,F}\right)\,. \tag{2.46}$$

The factor $B^2(m)$ contains all information about the electron density in the tunneling region along the direction of the electric field. In the MO-ADK model, Eq. (2.45) reduces to the traditional ADK model for atoms, if l is taken to be the orbital angular momentum quantum number of the valence electron. For diatomic molecules, the summation over l is a consequence of expanding the two-center electronic wavefunction of a valence orbital in terms of single-center atomic orbitals. The valence electron for N_2 is a σ_g orbital such that $m = 0$ in Eq. (2.46), while for O_2 is a π_g orbital such that $m = 1$. For molecules that have the outermost electrons in the σ orbital, the electron density is large along the molecular axis and thus, the ionization rate will be large if the molecular axis is

aligned along the laser polarization direction. For electrons in π orbitals, the electron density along the molecular axis vanishes and subsequently the tunneling ionization rates approach zero if the molecular axis is aligned in the direction of the laser polarization. This is the most transparent consequence of the tunneling-ionization theory for molecules in laser fields. N_2 and O_2 molecules will be discussed in more details in chapter 6.

In contrast, if the molecular axis is not aligned along the field direction, but at an arbitrary angle θ, then the $B(m)$ in Eq.(2.45) can be obtained through a rotation, and are reformulated as [28, 107]

$$B(m') = \sum_{l \geq m} C_{lm}\, Q(l, m')\, D^{l}_{m',\, m}(0, \theta, 0)\,, \tag{2.47}$$

where θ is the Euler angle between the molecular axis and the field direction. The $D^{l}_{m',m}$ function reflects the rotation matrix of the electronic wave function from the direction of the molecular axis to the laser polarization direction with Euler angles $(0, \theta, 0)$. In this case, it will be the middle term of Wigner's angular function [111], which can be rewritten as

$$\begin{aligned} D^{l}_{m',\, m}(\theta) = \sum_{j} (-1)^{j} \, & \frac{\sqrt{(l+m)!\,(l-m)!\,(l+m')!\,(l-m')!}}{(l-m'-j)!\,(l+m-j)!\,j!\,(j+m'-m)!} \\ & \times \left(\cos\frac{\theta}{2}\right)^{2l+m-m'-2j} \left(\sin\frac{\theta}{2}\right)^{2j+m'-m}\,, \end{aligned} \tag{2.48}$$

The summation $\sum_j$ extends over all integers of j for which the arguments of the factorials are positive or zero. In the case of the HOMO orbital in H_2 (m=m′= 0), $D^{l}_{0,0}(\theta) = P_l(\cos\theta)$, since P_l is the Legendre polynomial, Eq.(2.47) can be rewritten as

$$B(m'=0) = \sum_{l \geq 0} \sqrt{\frac{(2\,l\,+\,1)}{2}}\, C_{l0}\, P_l(\cos\,\theta)\,. \tag{2.49}$$

Finally, the molecular ionization rate in a static field is

$$W^{MO-ADK}_{st}(F, \theta) = \sum_{m'} \frac{B^2(m')}{2^{|m'|}\,|m'|!}\; \frac{1}{\kappa^{\frac{2\,Z_c}{\kappa}-1}} \left(\frac{2\,\kappa^3}{F}\right)^{\frac{2\,Z_c}{\kappa}-|m'|-1} \exp\left(-\frac{2\,\kappa^3}{3\,F}\right)\,. \tag{2.50}$$

However, the ionization rate in a low-frequency linear polarized laser field, as in the case

of atoms, is given by

$$W_{lin}(F,\theta) \simeq \left(\frac{3\,F_{max}}{\pi\,\kappa^3}\right)^{1/2} W_{\rm st}(F_{\rm max},\theta)\,, \tag{2.51}$$

where F_{max} is the peak field strength within the half cycle. The factor $\left(\frac{3\,F_{max}}{\pi\,\kappa^3}\right)^{1/2}$ is a result of averaging the rate over one cycle the field, see Eq. (2.27). The values of the C_{lm} coefficients needed to perform MO-ADK calculations for H_2, N_2, O_2, and other diatomic molecules have been provided in different literatures, e.g., [28, 39, 108–110], see chapters 5 and 6.

2.5.2 Molecular PPT (MO-PPT)

Extending the validity regime of the MO-ADK model to a large range of Keldysh parameters, one can go back to the original work of Perelomov *et al.* [30] (PPT theory), which has been discussed in Sec. 2.3.2. The frequency- and the wavelength-dependent of the laser field should be included. In the PPT model, the MO-ADK tunneling ionization rate for molecules in a low-frequency strong field can be expressed as [112]

$$\begin{aligned} W_{\rm st}^{MO-PPT}(F,\theta) =& A_m(\omega,\gamma)\sum_{m'}\frac{B^2(m')}{2^{|m'|}|m'|!}\frac{1}{\kappa^{\frac{2Z_c}{\kappa}-1}}\left(\frac{2\,\kappa^3}{F\sqrt{1+\gamma^2}}\right)^{\frac{2Z_c}{\kappa}-|m'|-1} \\ &\times \exp\left(-\frac{2\,\kappa^3}{3\,F}\,g(\gamma)\right)\,, \end{aligned} \tag{2.52}$$

where the factors $A_m(\omega,\gamma)$ and $g(\gamma)$ are given by Eqs. (2.30) and (2.31) for a linear polarized field and in Eqs. (2.36) and (2.35) for a circular polarized field, respectively. It is worth noting that the PPT model was originally derived for a short-range potential including the effect of the long-range Coulomb interaction through the first-order correction in the quasi-classical action. This model is tested in this thesis, i.e. the so-called molecular PPT model (hereafter referred to as MO-PPT). It is expected that it is helpful and may be valid for a wider range of intensities compared to the MO-ADK model. Furthermore, the ionization rates of molecules obtained from MO-PPT model depend on the frequency (wavelength) of the laser field.

Although MO-ADK and MO-PPT models require to first calculate the values of the C_{lm} coefficients to obtain analytically the ionization rates, it is still much simpler than the full solution of the TDSE that will be discussed in the next chapter.

2.6 Summary

This chapter contains an introduction to the main models that will be discussed in this thesis and thus provide the foundations for the most of this work. A brief discussion of strong-field ionization processes in atoms and molecules has been given, with the major works highlighted. The Keldysh parameter that is used to distinguish between the multi-photon and the tunneling regimes (according to its value $\gamma \gg 1$ or $\gamma \ll 1$) has been introduced. However, there is no clear transition between the tunneling and the multi-photon regimes at $\gamma \simeq 1$, both may contribute in this intermediate region. An increase of the electric field amplitude takes us into the tunneling regime reaching the over-the barrier regime. The tunneling ionization model that was suggested by Perelomov *et al.* (PPT) and simplified by Ammosov *et al.* (ADK) has been discussed and the correct formulas for them have been given. These models are based on the concept of the tunneling of an electron through the suppressed potential barrier of the combined atomic field and the external electric field. On the other hand, further effects and interesting phenomena in molecules have been discussed briefly. Furthermore, a review of the molecular tunneling model (MO-ADK), which includes the structure of the molecular wavefunction in the tunneling region, has been given. Additionally, an extension of the MO-ADK to be valid through a wide range of laser intensities and larger molecules than H_2 is presented by inserting the frequency-dependent factors (as in the PPT theory). This extended model is referred to in this thesis as the MO-PPT model. This thesis will focus on the tunneling process. Therefore, it is recommend to keep Secs. 2.3.1, 2.3.2, 2.5 and 2.5.2 in mind.

In the next chapter, the numerical method used to solve the TDSE, using the single active electron (SAE) approximation, will be briefly presented. It can be used to calculate the ionization rate and yield for molecules.

3 Time-dependent quantum processes in laser fields

3.1 Introduction

The numerical solution of the time-dependent Schrödinger equation (TDSE) for an atom or molecule in an intense laser field is the ultimate theoretical tool available for studying strong-field phenomena in the non-relativistic regime. The reason for this is that the intra-atomic force becomes comparable to the strong field which ionizes the system. The presence of two almost equally strong, competing pieces in the Hamiltonian leads to a number of unexpected effects. It also requires a non-perturbative approach for its accurate description. The solution of the TDSE not only allows us to treat the interactions on an equal basis, without making some assumptions about the relative importance of the forces, but it has also the flexibility to treat a wide range of physical systems and laser parameters. This means that the researchers can address a broad range of experimental data [113].

The "three-step" model [4, 115, 116] is a simple model, which predicts the effect of an intense laser field on an atom. Figure 3.1 schematically shows the semi-classical three-step model. This model uses a simple classical picture of the emitted electron to describe the dynamics in the strong laser field. In much of what follows, it is assumed that there is effectively a single electron in the system, which strongly interacts with the laser. This electron is initially in a spatially localized bound state when it is exposed to a sufficient strength laser field leading to some significant ionization, such as the tunnel ionization under the barrier created by the oscillating electric field of the laser. This is the first step, which is called tunneling in Fig. 3.1. The second step is propagation or acceleration, where the classical electron is pushed away from the ion and then turned around by the field and accelerated back to the parent ion. In other words, as the magnitude of the laser field rises and falls periodically, part of the bound-state wavefunction evolves into a continuum wavepacket, initially with very little energy. This wavepacket can continue to interact with the remaining ion or gain energy from the laser field. A

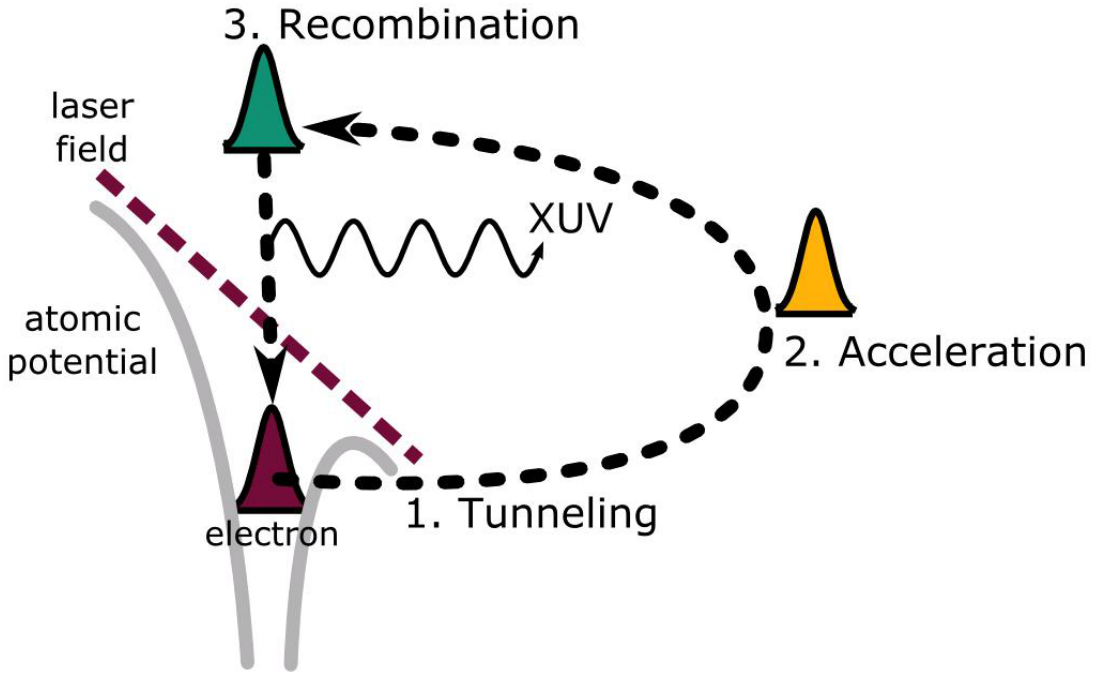

Figure 3.1: Schematic of the three step model (taken from [114]) showing:
1. The tunneling ionization step. 2. The acceleration step. 3. The recombination step.

part of each wavepacket will move away from the ion core and never return. Another part will be driven back toward the ion core, returning after about one optical cycle in the third step, which is named re-collision step. In this step, in which the electron collides with the parent ion, several things can happen: elastic scattering, leading to diffraction (i.e. changing direction) or inelastic scattering that may cause non-sequential double ionization as the free electron may have acquired enough energy to kick out another electron. The wavepacket can also coherently overlap with the remaining bound-state amplitude and recombine, causing a time-dependent dipole moment and stimulated photon emission, i.e. high-order harmonic generation (HOHG). The simple "three-step" model of strong field processes, though an oversimplification, is remarkably successful.

If there is a stationary system and one decides to apply an external time-dependent potential on it, it can be expected that the system is responding to the external potential and it is quantum mechanically described by the TDSE (within non-relativistic theory). In this chapter some of the theoretical concepts and numerical methods available for solving the strong-field TDSE using the spectral method will be reviewed briefly. The discussion will not be comprehensive and focuses instead on introducing the main

concepts that motivate the most widely used numerical methods. A brief introduction to these methods will be given. Some of the numerical tools, which are available for extracting information from the time-dependent wavefunction for a comparison with experimental and other theoretical data will be illustrated. First, the Hamiltonian that describes a molecule coupled to an external electric field in the different gauges will be introduced. A general description follows for the TDSE within vibronic and rotational motions. Some approaches that have been applied numerically to simplify and solve the complexity of the full TDSE which describes the molecule will be clarified too.

3.2 Molecular Hamiltonian and coupling to the laser field

3.2.1 Molecular Hamilton operator

The total non-relativistic time-dependent Hamiltonian $\hat{\mathrm{H}}(t)$ describing electrons of any diatomic molecular system exposed to a laser pulse can be written as the sum of the time-independent Hamiltonian $\hat{\mathrm{H}}_{\mathrm{m}ol}$, describing the electronic motion of the unperturbed molecular system (without laser), and the coupling with the external electric field $\hat{\mathrm{H}}_{\mathrm{i}nt}(t)$ (the so called the time-dependent laser-electron interaction) as

$$\hat{\mathrm{H}}(\vec{r},\vec{R},t) \;=\; \hat{\mathrm{H}}_{\mathrm{m}ol}(\vec{r},\vec{R}) \;+\; \hat{\mathrm{H}}_{\mathrm{i}nt}(t)\,, \tag{3.1}$$

where the time-independent field-free Hamiltonian operator of a molecule is given by

$$\hat{\mathrm{H}}_{\mathrm{m}ol}(\vec{r},\vec{R}) \;=\; \hat{\mathrm{T}}_N(\vec{R}) \;+\; \hat{\mathrm{H}}_{\mathrm{e}l}(\vec{r},\vec{R})\,, \tag{3.2}$$

where $\hat{\mathrm{H}}_{el}$ is the electronic Hamiltonian, which depends parametrically on R and contains all the potential-energy terms (including the nucleus-nucleus repulsion), i.e.

$$\hat{\mathrm{H}}_{el}(\vec{r},\vec{R}) \;=\; \hat{\mathrm{T}}_e(\vec{r}) \;+\; \hat{\mathrm{V}}_{ee}(\vec{r}) \;+\; \hat{\mathrm{V}}_{eN}(\vec{r},\vec{R}) \;+\; \hat{\mathrm{V}}_{NN}(\vec{R})\,. \tag{3.3}$$

The kinetic energy operators for the electrons and nuclei are

$$\hat{\mathrm{T}}_e \;=\; -\sum_{i=1}^{n} \frac{1}{2}\,\hat{\mathrm{p}}_i^2, \qquad \texttt{and} \qquad \hat{\mathrm{T}}_N \;=\; -\sum_{j=1}^{N} \frac{1}{2\,M_j}\,\hat{\mathrm{p}}_j^2\,, \tag{3.4}$$

respectively, where $\hat{\mathrm{p}}_i$ ($\hat{\mathrm{p}}_j$) are the momentum operators of the electrons (nuclei) and M_j is the mass of the nucleus j. The electron-electron ($\hat{\mathrm{V}}_{ee}$) and the nucleus-nucleus ($\hat{\mathrm{V}}_{NN}$)

repulsion operators are given by

$$\hat{\mathrm{V}}_{ee}(\vec{r}) \;=\; \sum_{j>i}^{n} \frac{1}{|\vec{r}_i \;-\; \vec{r}_j|} \qquad \texttt{and} \qquad \hat{\mathrm{V}}_{NN}(\vec{R}) \;=\; \sum_{j>i}^{N} \frac{Z_i\, Z_j}{|\vec{R}_i \;-\; \vec{R}_j|}\,. \tag{3.5}$$

The electron-nucleus attraction operator $\hat{\mathrm{V}}_{eN}$ is given as

$$\hat{\mathrm{V}}_{eN}(\vec{r},\vec{R}) \;=\; \sum_{i=1}^{n}\sum_{j=1}^{N} \frac{Z_j}{|\vec{r}_i \;-\; \vec{R}_j|} \tag{3.6}$$

with the atomic number Z_j of the nucleus j. The vector $\vec{r}$ indicates all the electronic coordinates and $\vec{R}$ indicates all the nuclear coordinates.

For a linearly polarized laser field with the polarization vector $\vec{\varepsilon}$, the interaction operator $\hat{\mathrm{H}}_{int}(t)$ describing the interaction of the molecule with the time-dependent laser electric field $E(t)$ is given in the dipole approximation, in length gauge (LG), by

$$\hat{\mathrm{H}}_{int} \;=\; -\,E(t)\,\vec{\varepsilon}\,.\,\hat{\mathrm{M}}\,, \tag{3.7}$$

where $\hat{\mathrm{M}}$ is the electric dipole operator and in the diatomic molecules it may be resolved into two parts where one depends on the electrons and the other depends on the nuclei,

$$\hat{\mathrm{M}} \;=\; \sum_{j=1}^{N} \vec{R}_j \;+\; \sum_{i=1}^{n} \vec{r}_i \;=\; \hat{\mathrm{M}}_N \;+\; \hat{\mathrm{M}}_e\,. \tag{3.8}$$

In the dipole approximation adopted here, the interaction term may also be expressed in the velocity gauge (VG) form. In the velocity gauge $\hat{\mathrm{H}}_{int}(t)$ is given by

$$\hat{\mathrm{H}}_{int} \;=\; -\,\vec{A}(t)\,\vec{\varepsilon}\,.\,\hat{\mathrm{p}}\,, \tag{3.9}$$

where $\vec{A(t)}$ is the vector potential and $\hat{\mathrm{p}}$ is the total momentum operator of the electrons and nuclei.

3.2.2 Choice of gauge

Using either of the two mentioned different gauges, one can solve the TDSE to obtain the time-dependent wavefunction. The wavefunctions obtained with either gauge differ only by a phase factor. All physical observables obtained with the two wavefunctions are the same, if an exact treatment is performed and subsequently the wavefunctions are exact.

In practice, using a finite representation for the wavefunction may lead to differences, if the results are not sufficiently converged. In turn, the convergence behavior is gauge dependent, since the finite basis has to represent the two different phase factors in the two gauges.

Furthermore, an approximate treatment often leads to gauge-dependent predictions for physical observables. For instance, the use of a truncated series expansion may result in a gauge dependence for the prediction of physical observables. This is valid both for theories based on the S-matrix expansion (like different versions of SFA) and numerical methods for solving the TDSE in which the Hilbert space [1] is restricted in some way. Moreover, the physical interpretations of processes that occurred in a strong field may differ rather drastically in the different gauges. For example, there is no tunneling picture in the velocity gauge. This leads us, in the current work, to prefer the length gauge as a natural choice for the gauge in studying the tunneling processes[2].

In general, the choice of the electromagnetic gauge has a large influence on the numerical effort involved in strong-field calculations through both the number of spherical harmonics and the time steps that are required for convergence [117]. Usually, the velocity gauge shows faster convergence properties than the length gauge [109, 118, 119].

3.3 Time-dependent Schrödinger equation (TDSE)

It will be assumed in the following that there is no interaction between vibrational and rotational motions, so that the rotational wavefunctions can be factored out. Also, the dipole approximation will be used for the description of the laser-molecule interaction. Because of the number of particles involved, the problem is very complicated and a set of reasonable simplifications will be required to approach it. The most important approximation usually adopted in the molecular description is the Born-Oppenheimer approximation[3] (BOA), which decouples the nuclear and electronic wavefunctions. One starts by calculating the electronic eigenstates of the system as a function of the nuclear coordinates. Then, the nuclei are assumed to move on those calculated electronic potentials and one solves the Schrödinger equation for nuclear motion.

[1] Hilbert space is defined as an infinite dimensional space or a complete inner product space or vector space.

[2] The length gauge will be used throughout this work unless stated otherwise.

[3] The Born-Oppenheimer approximation is based on the fact that electrons are much lighter and much more mobile than nuclei. Accordingly, one can freeze the nuclear motion while solving the Schrödinger equation for the electrons.

In order to describe the molecular behavior in a strong laser field, one has to be at least able to describe the molecule when the field is off (i.e. $\hat{\mathrm{H}}_{int}(t) = 0$). In this case the behavior of the molecule is given by the solution of the electronic Schrödinger equation,

$$\hat{\mathrm{H}}_{\mathrm{el}}\, \varphi^{(n,\Lambda)}(\vec{r}; R) = U_{\mathrm{el}}^{(n,\Lambda)}(R)\, \varphi^{(n,\Lambda)}(\vec{r}; R)\,, \tag{3.10}$$

for fixed nuclear positions. The index Λ represents the total angular momentum number (Σ, Π, Δ, ...) and the symmetry *gerade* or *ungerade*, in the case of Σ symmetry also $(+)$ and $(-)$. The index n is just an index of a state with the particular symmetry Λ (see Sec. 2.4.1). It is assumed that $\varphi^{(n,\Lambda)}(\vec{r}; R)$ are the electronic eigenfunctions; functions of the coordinates of the nuclei, R_j, as well as of the electrons, r_i, and $U_{\mathrm{el}}^{(n,\Lambda)}(R)$ are the electronic eigenvalues.

For each electronic state there is a number of vibrational states. The nuclear vibrational eigenfunctions $\chi_{\nu,J}^{(n,\Lambda)}(\vec{R})$ satisfy the time-independent Schrödinger equation,

$$[\hat{\mathrm{T}}_N + U_{el}^{(n,\Lambda)}(\vec{R})]\, \chi_{\nu,J}^{(n,\Lambda)}(\vec{R}) = E_{\nu,J,M_J}^{(n,\Lambda)}\, \chi_{\nu,J}^{(n,\Lambda)}(\vec{R})\,. \tag{3.11}$$

Here, $\hat{\mathrm{T}}_N$ is the kinetic nuclear operator ($\simeq \frac{1}{2\mu}\nabla^2$, where μ denotes the reduced mass). $U_{el}^{(n,\Lambda)}(\vec{R})$ is the Born-Oppenheimer potential-energy curve of the electronic state of the molecule (resulting from solving Eq. (3.10)) and $E_{\nu,J,M_J}^{(n,\Lambda)}$ is the total energy of the molecule. The nuclear eigenfunctions may be written as

$$\phi_{\nu,J,M_J}^{(n,\Lambda)}(\vec{R}, \Omega) = \chi_{\nu,J}^{(n,\Lambda)}(\vec{R})\, Y_J^{m_J}(\Omega)\,, \tag{3.12}$$

where the spherical harmonics $Y_J^{m_J}(\Omega)$ are the rotational wavefunctions, while ν and $\{J, M_J\}$ are the vibrational and rotational quantum numbers, respectively.

The TDSE is solved by expanding the time-dependent wavefunction in terms of field-free (time-independent) states. The total wavefunction $\Psi(\vec{r}, \vec{R}, t)$ is expanded in the basis of a complete wavefunction of the molecule, which results from multiplying the electronic wavefunctions $\varphi^{(n,\Lambda)}(\vec{r}; R)$ that diagonalize the electronic Hamiltonian $\hat{\mathrm{H}}_{el}$, by the nuclear wavefunction $\chi_{\nu,J}^{(n,\Lambda)}(\vec{R})$, which diagonalize the molecular Hamiltonian $\hat{\mathrm{H}}_{mol}$, i.e.[4]

$$\Psi(\vec{r}, \vec{R}, t) = \sum_{n,\Lambda,\nu,J,M_J} C_{\nu,J,M_J}^{(n,\Lambda)}(t)\, \varphi^{(n,\Lambda)}(\vec{r}; R)\, \phi_{\nu,J,M_J}^{(n,\Lambda)}(\vec{R}, \Omega)\,. \tag{3.13}$$

This equation comprises a superposition of electronic (n, Λ) and nuclear ν, J, M_J wavefunctions (it is a complete molecule's wavefunction) to generate a wavepacket. The

[4]This equation is considered a complete molecule's wavepacket.

TDSE for $\Psi(\vec{r},\vec{R},t)$ with the total Hamiltonian, Eq. (3.1), leads to

$$i\frac{\partial}{\partial t}\Psi(\vec{r},\vec{R},t) = [\{\hat{\mathrm{T}}_N \,+\, U_{el}^{(n,\Lambda)}(\vec{R})\} \,+\, \hat{\mathrm{H}}_{int}(t)]\,\Psi(\vec{r},\vec{R},t)\,. \tag{3.14}$$

If the expansion for $\Psi(\vec{r},\vec{R},t)$, Eq. (3.13), is inserted into this equation using BOA and the approximation

$$\{\hat{\mathrm{T}}_N \,+\, U_{el}^{(n,\Lambda)}(\vec{R})\}\,\Psi(\vec{r},\vec{R},t) = E_{\nu,J,M_J}^{(n,\Lambda)}\,\Psi(\vec{r},\vec{R},t)\,, \tag{3.15}$$

one obtains the equation

$$\begin{aligned} i\frac{\partial}{\partial t}\sum_{n,\Lambda,\nu,J,M_J} C_{\nu,J,M_J}^{(n,\Lambda)}(t)\,\varphi^{(n,\Lambda)}(\vec{r};R)\,\phi_{\nu,J,M_J}^{(n,\Lambda)}(\vec{R},\Omega) \;=\; \\ \sum_{n,\Lambda,\nu,J,M_J} C_{\nu,J,M_J}^{(n,\Lambda)}(t)\,\varphi^{(n,\Lambda)}(\vec{r};R)\,\phi_{\nu,J,M_J}^{(n,\Lambda)}(\vec{R},\Omega)\,[E_{\nu,J,M_J}^{(n,\Lambda)} \,+\, \hat{\mathrm{H}}_{int}(t)]\,. \end{aligned} \tag{3.16}$$

Multiplying by $\varphi^{(n,\Lambda_i)}(\vec{r};R)$ on the left and integrating over the electronic coordinates using the orthonormality condition $\langle\varphi^{(n,\Lambda_i)}(\vec{r};R)|\varphi^{(n,\Lambda)}(\vec{r};R)\rangle = \delta_{\Lambda_i,\Lambda}$, one obtains

$$\begin{aligned} i\frac{\partial}{\partial t}[\sum_{n,\nu,J,M_J} C_{\nu,J,M_J}^{(n,\Lambda_i)}(t)\,\phi_{\nu,J,M_J}^{(n,\Lambda_i)}(\vec{R},\Omega)] = \sum_{n,\nu,J,M_J}[E_{\nu,J,M_J}^{(n,\Lambda_i)}\,C_{\nu,J,M_J}^{(n,\Lambda_i)}(t)\,\phi_{\nu,J,M_J}^{(n,\Lambda_i)}(\vec{R},\Omega)] \\ -\; E(t)\sum_{n,\Lambda,\nu,J,M_J} C_{\nu,J,M_J}^{(n,\Lambda)}(t)\,\langle\varphi^{(n,\Lambda_i)}(\vec{r};R)|\hat{\mathrm{M}}|\varphi^{(n,\Lambda)}(\vec{r};R)\,\phi_{\nu,J,M_J}^{(n,\Lambda)}(\vec{R},\Omega)\rangle\,. \end{aligned} \tag{3.17}$$

Also, multiplying Eq. (3.17) by $\phi_{\tilde{\nu},J,M_J}^{(n,\Lambda_i)}(\vec{R},\Omega)$ from the left, and integration over the nuclear coordinates using the orthonormality condition

$$\langle\phi_{\tilde{\nu},J,M_J}^{(n,\Lambda_i)}(\vec{R},\Omega)|\phi_{\nu,J,M_J}^{(n,\Lambda_i)}(\vec{R},\Omega)\rangle \;=\; \delta_{\nu,\tilde{\nu}}^{(n,\Lambda_i)}\,, \tag{3.18}$$

(for each specific value of $n,\Lambda_i,\tilde{\nu},J,M_J$) gives

$$\begin{aligned} i\frac{\partial}{\partial t}\,C_{\tilde{\nu},J,M_J}^{(n,\Lambda_i)}(t) \;=& E_{\tilde{\nu},J,M_J}^{(n,\Lambda_i)}\,C_{\tilde{\nu},J,M_J}^{(n,\Lambda_i)}(t) \;-\; E(t)\sum_{n,\Lambda,\nu,J,M_J} C_{\nu,J,M_J}^{(n,\Lambda)}(t) \\ & \underbrace{\langle\phi_{\tilde{\nu},J,M_J}^{(n,\Lambda_i)}(\vec{R},\Omega)\varphi^{(n,\Lambda_i)}(\vec{r};R)|\hat{\mathrm{M}}|\varphi^{(n,\Lambda)}(\vec{r};R)\phi_{\nu,J,M_J}^{(n,\Lambda)}(\vec{R},\Omega)\rangle}_{D_{\nu,\tilde{\nu},J,M_J}^{(n,\Lambda),(n,\Lambda_i)}} \end{aligned} \tag{3.19}$$

where the brackets indicate integration over electronic coordinates. Now, we will calcu-

late the last term in Eq. (3.19), which will be denoted $D^{(n,\Lambda),(n,\Lambda_i)}_{\nu,\tilde{\nu},J,M_J}$, as

$$\begin{aligned} D^{(n,\Lambda),(n,\Lambda_i)}_{\nu,\tilde{\nu},J,M_J} &= \langle \phi^{(n,\Lambda_i)}_{\tilde{\nu},J,M_J}(\vec{R},\Omega)\varphi^{(n,\Lambda_i)}(\vec{r};R)|(\hat{\mathrm{M}}_N+\hat{\mathrm{M}}_e)|\varphi^{(n,\Lambda)}(\vec{r};R)\phi^{(n,\Lambda)}_{\nu,J,M_J}(\vec{R},\Omega)\rangle \\ &= \underbrace{\int \phi^{(n,\Lambda_i)}_{\tilde{\nu},J,M_J}(\vec{R},\Omega)\varphi^{(n,\Lambda_i)}(\vec{r};R)\,\hat{\mathrm{M}}_N\,\varphi^{(n,\Lambda)}(\vec{r};R)\phi^{(n,\Lambda)}_{\nu,J,M_J}(\vec{R},\Omega)dR\,dr}_{I} \\ &\quad + \underbrace{\int \phi^{(n,\Lambda_i)}_{\tilde{\nu},J,M_J}(\vec{R},\Omega)\varphi^{(n,\Lambda_i)}(\vec{r};R)\,\hat{\mathrm{M}}_e\,\varphi^{(n,\Lambda)}(\vec{r};R)\phi^{(n,\Lambda)}_{\nu,J,M_J}(\vec{R},\Omega)drdR}_{II}\,. \end{aligned} \tag{3.20}$$

Since $\hat{\mathrm{M}}_N$ is independent on the electronic coordinates, the first term, I, can be rearranged as

$$\begin{aligned} I &= \int \phi^{(n,\Lambda_i)}_{\tilde{\nu},J,M_J}(\vec{R},\Omega)\,\hat{\mathrm{M}}_N\,\phi^{(n,\Lambda)}_{\nu,J,M_J}(\vec{R},\Omega)dR\,\underbrace{\int \varphi^{(n,\Lambda_i)}(\vec{r};R)\varphi^{(n,\Lambda)}(\vec{r};R)dr}_{\delta_{\Lambda_i,\Lambda}} \\ &= \delta_{\Lambda_i,\Lambda}\int \phi^{(n,\Lambda_i)}_{\tilde{\nu},J,M_J}(\vec{R},\Omega)\,\hat{\mathrm{M}}_N\,\phi^{(n,\Lambda)}_{\nu,J,M_J}(\vec{R},\Omega)dR\,, \end{aligned} \tag{3.21}$$

because the electronic eigenfunctions belonging to different electronic states are orthogonal to one another. The second term, II, in Eq. (3.20) can be re-written as

$$\begin{aligned} II &= \int \phi^{(n,\Lambda_i)}_{\tilde{\nu},J,M_J}(\vec{R},\Omega)\,\phi^{(n,\Lambda)}_{\nu,J,M_J}(\vec{R},\Omega)dR\,\underbrace{\int \hat{\mathrm{M}}_e\,\varphi^{(n,\Lambda_i)}(\vec{r};R)\varphi^{(n,\Lambda)}(\vec{r};R)dr}_{d^n_{\Lambda_i\Lambda}(R)} \\ &= \int d^n_{\Lambda_i\Lambda}(R)\,\phi^{(n,\Lambda_i)}_{\tilde{\nu},J,M_J}(\vec{R},\Omega)\,\phi^{(n,\Lambda)}_{\nu,J,M_J}(\vec{R},\Omega)dR\,, \end{aligned} \tag{3.22}$$

where $d^n_{\Lambda_i\Lambda}$ describes the electronic transition dipole moment between the states igenfunctions $\varphi^{(n,\Lambda_i)}(\vec{r};R)$ and $\varphi^{(n,\Lambda)}(\vec{r};R)$ which depends on the internuclear distance R.

Returning to Eq. (3.20), it can be re-written as

$$\begin{aligned} D^{(n,\Lambda),(n,\Lambda_i)}_{\nu,\tilde{\nu},J,M_J} = \delta_{\Lambda_i,\Lambda}&\int \phi^{(n,\Lambda_i)}_{\tilde{\nu},J,M_J}(\vec{R},\Omega)\,\hat{\mathrm{M}}_N\,\phi^{(n,\Lambda)}_{\nu,J,M_J}(\vec{R},\Omega)dR \\ &+ \int d^n_{\Lambda_i\Lambda}(R)\,\phi^{(n,\Lambda_i)}_{\tilde{\nu},J,M_J}(\vec{R},\Omega)\,\phi^{(n,\Lambda)}_{\nu,J,M_J}(\vec{R},\Omega)dR\,, \end{aligned} \tag{3.23}$$

since due to the $\delta_{\Lambda_i,\Lambda}$ function the first term would be non-zero only for equal values of Λ_i and Λ, but then the integral vanishes due to selection rules. The transition dipole

moment $D^{(n,\Lambda),(n,\Lambda_i)}_{\nu,\tilde{\nu},J,M_J}$ is given finally by

$$D^{(n,\Lambda),(n,\Lambda_i)}_{\nu,\tilde{\nu},J,M_J} = \int d^n_{\Lambda_i\Lambda}\, \phi^{(n,\Lambda_i)}_{\tilde{\nu},J,M_J}(\vec{R},\Omega)\, \phi^{(n,\Lambda)}_{\nu,J,M_J}(\vec{R},\Omega) dR\,. \tag{3.24}$$

Now, Eq. (3.19) can be re-written in the form:

$$i\frac{\partial}{\partial t} C^{(n,\Lambda_i)}_{\tilde{\nu},J,M_J}(t) = E^{(n,\Lambda_i)}_{\tilde{\nu},J,M_J}\, C^{(n,\Lambda_i)}_{\tilde{\nu},J,M_J}(t) - E(t) \sum_{n,\Lambda,\nu,J,M_J} D^{(n,\Lambda),(n,\Lambda_i)}_{\nu,\tilde{\nu},J,M_J}\, C^{(n,\Lambda)}_{\nu,J,M_J}(t)\,. \tag{3.25}$$

The coefficients $C^{(n,\Lambda_i)}_{\tilde{\nu},J,M_J}(t)$ are complex variables, so one can transform the complex equation, Eq. (3.25), to a real equation by separating the coefficients $C^{(n,\Lambda_i)}_{\tilde{\nu},J,M_J}(t)$ into the real and imaginary components. For simplicity, the notations $\tilde{\nu}, J, M_J, (n,\Lambda_i)$ will be dropped temporarily and re-put again at the end of the formulation. Hence, if we put $C = C^{\mathrm{R}e} + i\, C^{\mathrm{I}m}$, Eq. (3.25) becomes

$$i\frac{\partial}{\partial t}[C^{\mathrm{R}e} + i\, C^{\mathrm{I}m}] = E^{(n,\Lambda_i)}_{\tilde{\nu},J,M_J}[C^{\mathrm{R}e} + i\, C^{\mathrm{I}m}] - E(t) \sum_{n,\Lambda,\nu,J,M_J} D^{(n,\Lambda),(n,\Lambda_i)}_{\nu,\tilde{\nu},J,M_J}\, [C^{\mathrm{R}e} + i\, C^{\mathrm{I}m}]\,. \tag{3.26}$$

Separating out the real and imaginary parts, one obtains

$$\frac{\partial}{\partial t} C^{\mathrm{I}m}_{\tilde{\nu},J,M_J}(t) = -\, E^{(n,\Lambda_i)}_{\tilde{\nu},J,M_J}\, C^{\mathrm{R}e}_{\tilde{\nu},J,M_J}(t) + E(t) \sum_{n,\Lambda,\nu,J,M_J} D^{(n,\Lambda),(n,\Lambda_i)}_{\nu,\tilde{\nu},J,M_J}\, C^{\mathrm{R}e}_{\nu,J,M_J}(t)\,, \tag{3.27}$$

$$\frac{\partial}{\partial t} C^{\mathrm{R}e}_{\tilde{\nu},J,M_J}(t) = E^{(n,\Lambda_i)}_{\tilde{\nu},J,M_J}\, C^{\mathrm{I}m}_{\tilde{\nu},J,M_J}(t) - E(t) \sum_{n,\Lambda,\nu,J,M_J} D^{(n,\Lambda),(n,\Lambda_i)}_{\nu,\tilde{\nu},J,M_J}\, C^{\mathrm{I}m}_{\nu,J,M_J}(t)\,. \tag{3.28}$$

The last two equations have real variables and can be solved numerically by using a solver for coupled first-order differential equations. There are many free and commercial solvers available for such a problem.

At this point, if the transition dipole moments $D^{(n,\Lambda),(n,\Lambda_i)}_{\nu,\tilde{\nu},J,M_J}$ are calculated from Eq. (3.24) and the parameters of electromagnetic field are known, the TDSE can be solved numerically obtaining the values of the coefficients $C^{(n,\Lambda_i)}_{\tilde{\nu},J,M_J}(t)$ as a function of time. Hence, the wavefunction $\Psi(\vec{r},\vec{R},t)$, Eq. (3.13), can be calculated and propagated. It can be used to analyze strong-field processes. Hence, system properties can be derived from the wavefunctions.

The previous relations are useful when one wants to study all the electronic states, which are coupled by a laser field, and the probability of populating states, but it is not an

easy task. Only the vibrational motion and one electronic state will be considered in this work. Furthermore, the rotational motion during the interaction with the laser field will be neglected, as is any non-adiabatic effect. Accordingly, within the TDSE method the time-dependent vibrational wavefunction $\Psi(R,t)$ is expanded with time-dependent coefficients in the basis of vibrational eigenstates of the molecules, χ_ν, i.e. as

$$\Psi(R,t) = \sum_{\nu}^{\infty} C_\nu(t)\,\chi_\nu(R) \tag{3.29}$$

where the coefficients $C_\nu(t)$ represent the contribution of each vibrational state ν to the total vibrational wavefunction (wavepacket) and its squares represent the populations of the vibrational states ν (see chapter 4). Substituting Eq. (3.29) into the TDSE yields a system of ordinary differential equations whose explicit form depends on the gauge adopted for describing the molecule in the field. The system of ordinary differential equations is then solved numerically employing the NAG routine D02CJF based on a variable-order, variable-step Adams method.

The original work of the solution of the field-free two-electron Schrödinger equation for diatomic molecules was implemented by Vanne and Saenz [120]. The method calculates accurately the various electronic states of H_2, including the doubly excited states. Building on this work, Awasthi *et al.* [119] developed a method to efficiently solve the electronic TDSE for H_2 in the basis of field-free H_2 states. They introduced the first solution of the TDSE for H_2 in full dimensionality using the spectral method. For further details about this method see Appendix C. This method will be used in the current work to obtain ionization yields of H_2 (chapters 4 and 5). Petretti *et al.* [121] developed a method[5] to cope with larger molecules such as the linear molecules N_2, O_2, and CO_2, and the non-linear molecules H_2O, and SO_2, where the latter has recently been studied by Limor *et al.* [123]. They used in their method some simplifications such as the Born-Oppenheimer approximation, the non-relativistic approximation, the dipole approximation, and the single-active electron approximation that are commonly used in many other approaches. They computed the electronic structure of the molecule using the density functional theory and explicitly accounting for the molecular symmetry. The spectral *ansatz* is also used to solve the TDSE. This method is also applied in chapter 6 of this work for obtaining the ionization yields for different alignments and intensities for both N_2 and O_2 molecules.

The TDSE for diatomic molecules with effectively two electrons can be solved in three steps. The first one solves the field-free one-electron Schrödinger equation for the di-

[5] A more detailed study of this method is presented in the PhD thesis of S. Petretti (2013) [122].

atomic molecular one-electron ion in a full dimensionality. The second step is a configuration interaction (CI) calculation using the one-electron orbitals. The CI calculation gives the two-electron wavefunctions for the molecule. In the third step, a time-propagation is performed in the basis of field-free states that are obtained from the CI calculation. This method is referred to as CI-TDSE. The CI can be implemented using Gaussian basis functions, which are widely used in quantum-chemistry packages. These codes provide many options, but are not usually symmetry adapted for diatomic molecules and thus vast resources. However, these methods have the advantage of efficiently treating many electrons.

Elliptic (prolate-spheroidal) coordinates are used in the codes adopted here for the H_2 molecule. The use of prolate-spheroidal coordinates automatically accounts for the electron-nucleus Coulombic cusp condition and dramatically reduces the amount of basis functions needed for convergence. The Gaussian-based multipurpose codes have to use a large basis in order to implement the Coulombic cusp condition.

3.4 Theoretical approaches

In fact, the TDSE that describes molecules in intense laser fields is too demanding for a numerical solution due to the presence of non-local exchange terms and also an exploding Hilbert space. Even putting aside time-dependence, the problem of finding the ground-state exponentially increases with the number of variables, since there is an increase in the number of electron configurations in searching for the ground-state wavefunction. Accordingly, solving the many-body Schrödinger equation is a very difficult task. So far, to the knowledge of the author, full solutions of the TDSE equation describing molecules in strong laser fields are only achieved for one- or two-electron molecules. Therefore, a set of acceptable approximations has to be used to simplify the TDSE and to solve it numerically. Some approaches, like the single-active electron (SAE), density functional theory (DFT), and time-dependent density functional theory (TDDFT), will be discussed briefly in the following.

3.4.1 Single-active electron in strong laser field (SAE)

The strong-field ionization process for an atom or a molecule can be described assuming one active electron experiencing an effective potential formed by the nucleus and other electrons. This model is known as the single-active-electron (SAE) approximation [124].

It is assumed in the SAE approximation that only a single electron occupying the highest molecular orbital strongly interacts with the laser field, while all other electrons remain unaffected (frozen in their field-free orbitals).

Expressing the many-electron wavefunction in form of a single Slater determinant built by orthonormal one-electron wavefunctions χ_ν that are eigenfunctions of $\hat{\mathrm{H}}_{\mathrm{m}ol}$, freezing all except one electron, using orthonormality, as well as Slater-Condon rules, leads finally to an effective one-electron Hamiltonian,

$$\hat{\mathrm{h}}(t) \;=\; \hat{\mathrm{h}}_{\mathrm{m}ol} \;+\; \hat{\mathrm{d}}_{\mathrm{i}nt}(t) \quad . \tag{3.30}$$

The dipole interaction term $\hat{\mathrm{d}}_{\mathrm{i}nt}(t)$ is equivalent to $\hat{\mathrm{H}}_{\mathrm{i}nt}(t)$ in Equation (3.1), but with the single-electron momentum operator $\hat{\mathrm{p}}$ instead of the total momentum operator $\hat{\mathrm{P}}$ in the VG (Eq. (3.9)) and operator $\hat{\mathrm{r}}$ instead of total operator $\hat{\mathrm{M}}$ in the LG (Eq. (3.7)). The operator $\hat{\mathrm{h}}_{\mathrm{m}ol}$ describes the motion of the active electron in the potential formed by the nuclei and the remaining frozen electrons, as mentioned previously.

The most obvious shortcoming of the SAE is the neglect of the simultaneous interaction of more than one electron with the laser field. Additionally, it also ignores the possibility of interaction of the active electron with other electrons in the system and a process that can lead to non-sequential multiple ionization. The great advantage of the SAE is not only the reduction in complexity that it provides as one-electron approximation, but also the fact that it is a linear equation automatically allowing for the kind of superposition (bound + continuum) solutions characterizing strong-field processes. The SAE calculations can also be done exactly to within the numerical error. This means that they can be used as a benchmark in determining the extent of one-electron versus multi-electron effects in an experiment.

The potentials that are used to model intra-atomic forces in SAE calculations may be divided into two types; model potentials and pseudo-potentials. Model potentials are applied because of their simplicity, which allows for fast computation in one dimension and also for a compliant treatment of electron–electron interactions in multiple dimensions. Additionally, they can be used to examine the effect of certain features of the atomic system, for instance, by removing excited states from the calculation. Pseudo-potentials are constructed to facilitate detailed comparison to the experiment and striving for an accurate representation of the active electron wavefunction as possible, for more detail see [113].

3.4.2 Density functional theory (DFT) and time-dependent DFT

There are many sophisticated methods for solving the many-body Schrödinger equation based on the expansion of the wavefunction in Slater determinants. The simplest one is the Hartree–Fock (HF) method, which is the most basic *ab initio* molecular orbital approach. However, the problem with this method is the huge computational effort making it nearly impossible to apply them efficiently to very complex systems. Density functional theory (DFT) is an alternative approach to the HF-based methods. It considers the electron density as the basic variable, instead of the wavefunction. For the numerical solution DFT transforms the many-body Schrödinger wave equation into a far more tractable one-electron equation. In DFT, the properties of a many-electron system can be determined using functionals, i.e. functions of another function, which in this case is the position-dependent electron density, which explains the name. Computational costs of this theory are relatively low compared with traditional methods, such as HF theory. DFT was initiated with the fundamental work of Hohenberg and Kohn in 1964 [125], however it is considered the most widely used method for electronic structure calculations after the introduction of Kohn and Sham orbitals proposed by Kohn and Sham 1965[6] [126]. For more details of a general exposition of DFT, the reader is referred to the text book of Parr and Yang [127].

In the Kohn-Sham approach [126], the difficult interacting many-body system obeying the Hamiltonian equation can be replaced with a different auxiliary system, which can be solved more easily. Kohn and Sham assumed that the ground-state density of the original interacting system is equal to that of some non-interacting system. This assumption leads to independent-particle equations for the non-interacting system that can be considered exactly soluble (by numerical calculations) with all the difficult many-body terms inserted into an exchange-correlation functional of the density. Subsequently, the main idea of DFT is the description of an interacting system of fermions via its density, but not through its many-body wavefunction. This leads to a reformulation of the basic variable of the Schrödinger equations from being the exact ground-state electronic wavefunction $\psi_0(\mathbf{r}_1, \mathbf{r}_2, \mathbf{r}_3, ..., \mathbf{r}_n)$, including all exchange and correlation effects, to that of the ground-state single-electron density $\rho(\mathbf{r})$,

$$\rho(\mathbf{r}) \;=\; \int\int ... \int |\psi_0(\mathbf{r}, \mathbf{r}_2, \mathbf{r}_3, ..., \mathbf{r}_N)|^2 d\mathbf{r}_2 d\mathbf{r}_3 ... d\mathbf{r}_N \,. \tag{3.31}$$

This effectively reduces the 3N degrees of freedom to just 3 for an N electron system, the spatial coordinates x, y, and z. DFT provides an appealing alternative, being much more

[6] It took quite some time after 1965 for DFT to really before that popular.

flexible, since it provides a way to systematically determine the many-body problem, with $\hat{V}_{ee}$, onto a single-particle problem without $\hat{V}_{ee}$.

Practical applications of DFT are based on approximations for the so-called exchange-correlation potential. The latter describes the effects of the Pauli principle and the Coulomb potential beyond the pure electrostatic interaction between electrons in an average sense. Possessing the exact exchange-correlation potential means that one can solve the many-body problem exactly, which is complicated in large molecules.

Density functional theory is only valid for the ground-state properties. For an accurate treatment of atomic and molecular dynamics, such as collisions or multi-photon ionization processes, a more accurate description of both the ionization potential and the excited-state properties are required. Accordingly, time-dependent processes require an extension.

Runge and Gross [128], twenty years after DFT was introduced, have extended the concept of stationary DFT to the time-dependent domain (TDDFT). The TDDFT method, which can be applied to calculate the excited states, is based on the fact that the frequency-dependent linear response of a finite system with respect to a time-dependent perturbation has discrete poles at the exact, correlated excitation energies of the unperturbed system. For any interacting many-particle quantum system subject to a given time-dependent potential all physical observables are only determined by the information of the time-dependent density and the state of the system at any instant of time [129]. This unique relationship allows for the derivation of a computational scheme in which the effect of the particle-particle interaction is represented by a density-dependent single-particle potential. Therefore, the time evolution of an interacting system can be investigated by solving a time-dependent auxiliary single-particle problem. The success of the TDDFT is due to the Kohn-Sham system, where the density of the interacting many-electron system is obtained as the density of an auxiliary system of non-interacting fermions, living in a one-body potential [130]. In the last several years, there is considerable effort and success in the extension of the (weak-field) TDDFT and the use of linear-response theory for the study of excitation energies [131, 132].

3.5 Ionization probability

According to Eq. (3.29), the total ionization yield is defined as the sum of occupations of all eigenstates at the end of the pulse,

$$P_{ion} = \sum_{\nu} |C_{\nu}(\infty)|^2 = \sum_{\nu} |C_{\nu}(T_f)|^2 , \tag{3.32}$$

since the pulse is only non-zero between 0 and T_f, where T_f is the time at the end of the laser pulse (the pulse duration). In multi-electron molecules, e.g. N_2, the ionization reveals not only information about the HOMO, but also about the HOMO-1[7] [133]. The importance of the HOMO-1 is obvious for perpendicular alignment of the molecular axis with respect to the laser direction, which favors the induced dipole moment of the HOMO-1 over that of the HOMO, due to the molecular orbital structure. The total ionization yield is given by the sum of individual ionization yields of all occupied orbitals [121].

3.6 Summary

In this chapter, some of the theoretical concepts which are necessary for understanding the numerical results presented in this thesis are clarified. The three-step model and the Hamiltonian describing a molecule coupled to an external electromagnetic field have been discussed. A full description of the TDSE for diatomic molecules in a laser field has been also presented. Then, some approximations that are used to simplify and solve the TDSE, such as single-active electron (SAE), density functional theory (DFT), and time-dependent density functional theory (TDDFT) have been briefly described.

To assist the understanding of the numerically obtained TDSE solution, simple models providing additional qualitative physical pictures are essential. The applicability of these simple models can be verified by comparing their predictions with the TDSE solution. However, TDSE yields exact results that can be used as a guide for simple analytical models like those which have been introduced in the previous chapter. Of course, the TDSE solution may also help to improve existing models or develop new one. However, the numerical solution of the TDSE, sometimes, may lead to a loss of physical insight and qualitative physical pictures.

[7] HOMO-1 is the molecular orbital that is energetically below the HOMO.

4 Generating vibrational wavepackets in H_2^+ by exposing H_2 to intense laser fields

4.1 Introduction

Interactions of the hydrogen molecule, H_2, and its ion, H_2^+, with intense laser pulses have been favorite targets for many years for both experimentalists and theorists. Understanding the behavior of molecular hydrogen is an important step toward larger and more complex molecules. The simplest molecule existing in nature is H_2^+, which consists of two protons bound by a single electron. If it is put into a sufficiently strong electromagnetic field, an amazing wealth of physical phenomena has been observed, resulting from the nontrivial time-dependent interaction of nuclear wavepacket motion and strong-field electron dynamics [21, 134–137]. Despite being the simplest neutral molecule, H_2 is nevertheless rather challenging due to its light nuclei and correspondingly fast motion. Although a strong electromagnetic field mainly affects the electrons, their motion is very efficiently coupled to the rotational (by the anisotropic polarizability) and the vibrational (by the R-dependent dipole moment and ionization rate) nuclear degrees of freedom. Accordingly, even a non-resonant laser pulse causes vibrational and rotational excitation of the molecule. Moreover, excitations are produced within a range of vibrational and rotational states with definite relative phases, originating in coherent vibrational and rotational wavepackets. Classically, those wavepackets can be viewed as very fast axial and angular motions of the molecule. For instance, the 10 fs are evident from the vibrational period, but the rotational period is much longer than 20 fs. Therefore, with pulses of 20 fs and longer H_2 may undergo a wide range of motions during the pulse, hiding any possible effects differential with respect to internuclear-distance or molecular alignment. Laser pulses shorter than 10 fs are needed not only to efficiently generate fast vibrational and rotational wavepackets but also to detect and measure their properties in a time-resolved way.

During the last two decades, femtosecond laser spectroscopy has become a standard tool for time-resolved studies of molecular processes. One of the nonlinear spectroscopic

experiments is a pump-probe set-up, which has opened up the opportunity to study molecular dynamics at very short time scales (in real time) [138, 139], especially after the tremendous advances in the technology of lasers and ultra-short pulses. Usually, in pump-probe spectroscopy the pulse coming from an ultrafast laser is split into two pulses. The first one is used as a pump pulse exciting the molecule and inducing some time evolution in the molecule. The changes induced in the molecule are probed by the second pulse (probe pulse), which is suitably delayed with respect to the pump pulse. By changing the time delay between the two pulses, one can get a spectrum of the photo-ionization. It was demonstrated that using a few-cycle 800 nm laser pulse can effectively "freeze" vibrational motion in H_2 [140]. A series of pump-probe experiments followed this experiment and have traced the time evolution of nuclear wavepackets generated by the ionization of neutral hydrogen on the ground (σ_g) and the first excited (σ_u) potential energy surfaces of H_2^+ [141, 142], and even in the ground state of the neutral molecule itself [143]. Those experiments focus on the nuclear vibrational motion. In this chapter, the wavepacket created by the pump pulse will be studied.

As was discussed earlier in chapter 2, exposing molecules to strong laser fields leads to a distortion of their potential-energy curves according to the field strength. A number of the bound states becomes unbound (bond softening, BS). In the current chapter, the effect of the BS on the dissociation threshold energy, the evolution of the wavepacket, and on the revival time, will be discussed. This chapter is organized as follows. The theoretical calculations of the generated vibrational wavepacket will be explained in Sec. 4.2. A detailed explanation for the ionization probability and its dependence on the internuclear distance as well as on the laser parameters will be shown in Sec. 4.3. Afterwords, the validity of the tunneling models (ADK, fc-ADK, and PPT) compared to the accurate TDSE calculations will be examined. Additionally, the population of the dissociative states under an external electric field and the evolution of the initial nuclear wavepacket molecular ion on the $1s\sigma_g$ level are described for two different cases: (i) ignoring the distortion of the $1s\sigma_g$ potential curve (i.e. excluding BS, Sec. 4.4), and (ii) considering the distortion in the potential energy curve (i.e. including BS, Sec. 4.5). The propagation of the initial nuclear wavepacket and its revival time in an external laser field with different intensities are presented in Sec. 4.6. A summary for this chapter is given in Sec. 4.7.

4.2 Generation of vibrational wavepackets in H_2^+

A wavepacket is a coherent superposition of several quantum states created, e.g., by a short laser pulse. Two conditions have to be fulfilled by the pump laser pulse for efficiently obtaining a coherent vibrational wavepacket in H_2^+: The intensity needs to be sufficiently large to singly ionize the parent H_2 molecule and small enough to avoid instant Coulomb explosion following double ionization. Furthermore, the pulse length should be short enough for its spectral band width to be of the order of (or larger than) the frequency difference of neighboring vibrational states. The last condition is necessary for exciting the molecule coherently and to couple several energy states due to the large spectral width of the short laser pulse. Figure 4.1 shows schematically a diatomic molecule exposed to a short laser pulse to be excited. The possible energy values of the system in the upper graph are represented by the horizontal lines labeled by E_ν. Examples of wave functions $|\chi_\nu(R)\rangle$ corresponding to $\nu = 0$ - 5 are plotted, with the zero of the wavefunction amplitude axis set equal in each case to the corresponding energy value. The sign of the wavefunction alternates from positive to negative with a spatial period determined by the kinetic energy, which is zero at the walls of the well and has its maximum value at the center. If the pulse duration (upper graph) is shorter than the classical vibrational period of the molecule, which is typically on the order of femtosecond, its bandwidth is then broad enough to cover multiple vibrational eigenstates. Those eigenstates are superposed and interfere with each other resulting in constructive or destructive interferences as a function of time and space creating a spatially localized wavepacket (lower graph), see Eq. (4.1). As a consequence of the initial ionization of H_2, a correlated electron wavepacket and a vibrational wavepacket are created at t_0. The vibrational wavepacket $\Psi(\vec{R},t)$ is a coherent superposition of the wavefunctions for the vibrational eigenstates[1] of H_2^+, $\chi_\nu^{H_2^+}$. Due to the heavy mass of the nuclei, the vibrational motion is supposed to be frozen during the laser pulse (i.e., vertical transition will be assumed). The time evolution of the vibrational wavepacket is thus described by [145]

$$\Psi(\vec{R},t) \;=\; \sum_{\nu=0}^{N} a_\nu \, e^{-iE_\nu t} \, \chi_\nu^{H_2^+}(R), \tag{4.1}$$

[1] In general, χ_ν can be electronic, vibrational or rotational eigenstates of the molecule. Here, in this thesis, the vibrational eigenstates will be only treated explicitly.

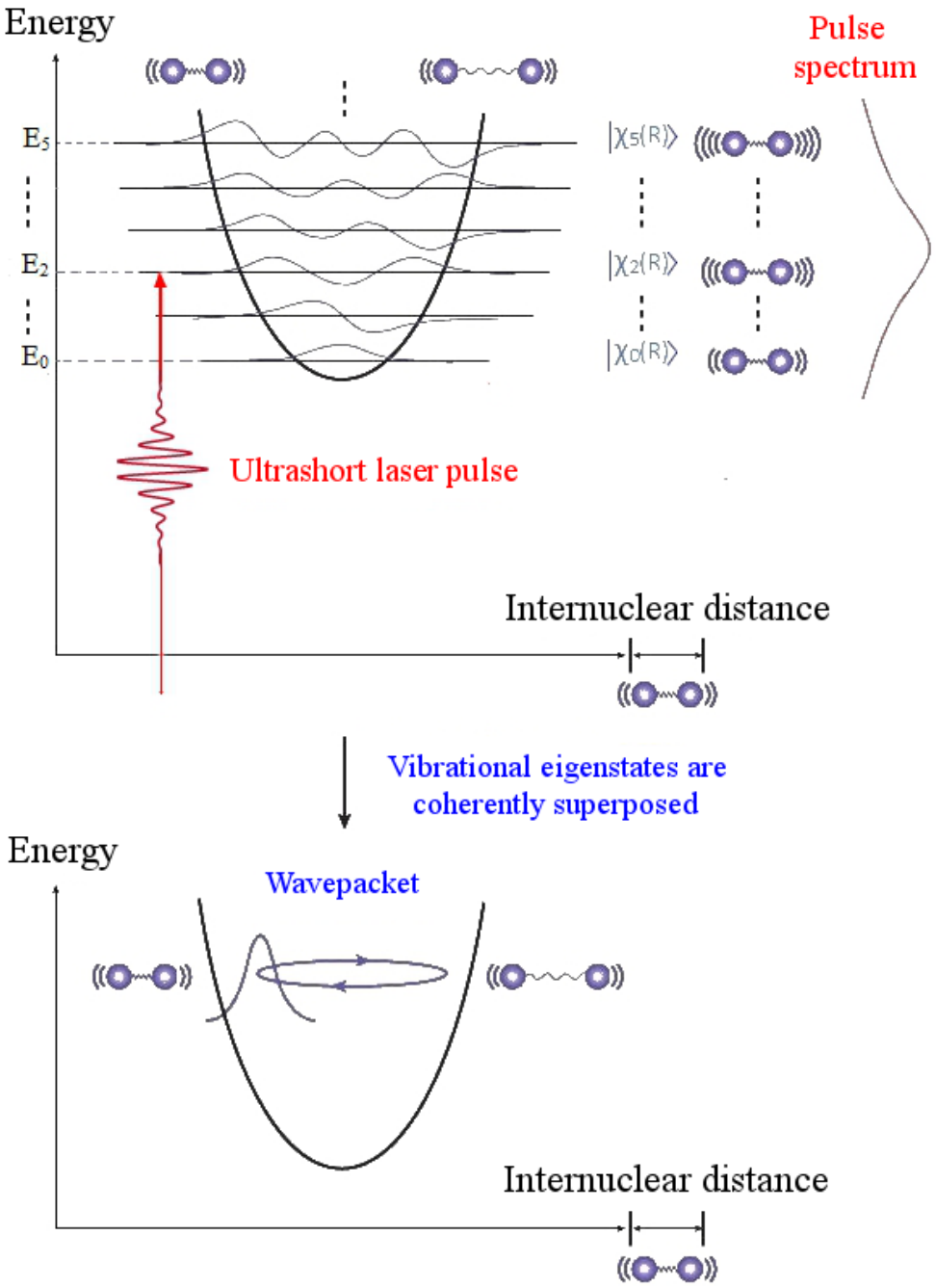

Figure 4.1: Schematic shows the generation of a vibrational wavepacket in a diatomic molecule, approximated by harmonic oscillator potential, with an ultrashort laser pulse (see text). This figure is adopted from Ref. [144]. The upper part shows the stationary wavefunctions and an ultrashort laser pulse (before interaction). The lower part shows the vibrational eigenstates after a coherent superposition created a spatially localized wavepacket (after interaction).

with the excitation coefficients [146, 147]

$$a_\nu \;=\; \langle\, \chi_\nu^{\mathrm{H}_2^+}(R) \,|\, [Y(R)]^{1/2} \,|\, \chi_{\tilde{\nu}=0}^{\mathrm{H}_2}(R) \,\rangle\,, \tag{4.2}$$

where $\chi_{\tilde{\nu}=0}^{\mathrm{H}_2}(R)$ is the stationary ground vibrational wavefunction of H_2 and E_ν is the eigenenergy of the eigenstate ν of H_2^+. While, $|a_\nu|^2\,(\equiv P_\nu)$ can be understood as the weight or the probability of the stationary vibrational state χ_ν in Ψ, i.e. the relative contributions of the wavefunctions $\chi_\nu^{\mathrm{H}_2^+}$ to the superposition. According to Eq. (4.2), this probability depends on the overlap between the ground state wavefunction of H_2 and the wavefunctions of the vibrational states of the molecular ion H_2^+ as well as the internuclear-distance-dependent probability of the ionization process, which is also called the ionization yield, $Y(R)$. $Y(R)$ have a constant values, here it is assumed 1, if the Franck-Condon (FC) approximation adopting[2], otherwise, it has to be calculated as discussed in the next section. The superposition of the eigenstates, Eq. (4.1), is called a wavepacket.

The squared absolute value of the vibrational wavepacket, $|\Psi(\vec{R},t)|^2$, is called the probability density distribution of the wavepacket. At a given time, t, the probability density of the wavepacket can be obtained by squaring Eq. (4.1) and using the next relation

$$\mathtt{e}^{-iE_\nu t} \;=\; \mathtt{cos}(E_\nu t) \;-\; i\,\mathtt{sin}(E_\nu t)\,. \tag{4.3}$$

It can be rewritten (after rearrangement) as

$$|\Psi(\vec{R},t)|^2 \;=\; \sum_{\nu=0}^{N} p_{\nu\nu}(t)\;|\chi_\nu(R)|^2 \;+\; 2\,\Re_e\left\{\sum_{\nu\neq\mu}^{N} p_{\nu\mu}(t)\;\chi_\nu(R)\,\chi_\mu(R)\right\} \tag{4.4}$$

with the time-dependent density-matrix elements

$$p_{\nu\mu}(t) \;=\; a_\nu a_\mu^*\;\exp\left(-iE_{\nu\mu}t\right)$$

where

$$E_{\nu\mu} \;=\; E_\nu - E_\mu\,.$$

The first sum in Eq. (4.4) is a temporally invariant sum of standing waves. It contains only the time-independent diagonal elements of the density matrix. The coherence, expressed by the off-diagonal elements in the real part of the second term, contains

[2]The ionization probability in FC approached is the square of the overlap integral between the vibrational wavefunctions of the ground and the excited electronic states and thus does not depend on the laser parameters nor internuclear distances.

all the time dependence of the wavepacket. At $t = 0$, the exponential term is unity for all terms in the sum. However, as the time evolves, this expression is dictated by the interference terms between the energy differences between the vibrational states ($E_{\nu\mu}$, since the phase factors do not cancel). So, the expected outcome of a position measurement changes with time and then, the system is in motion. In this chapter, the probability density of the IWP generated on the electronic potential surface of H_2^+ by a superposition of 180 vibrational states, weighted by the square root of the population of each state, will be presented.

Because the periods $2\,\pi/E_\nu$ of a temporal oscillation of the wavefunction of the eigenstates depend on the energy of the vibrational state ν, the interference at a specific R becomes alternately constructive and destructive. This alternation makes the wavepacket moving back and forth along the internuclear axis with a period of the classical vibrational motion of the molecule. The wavepacket of H_2^+ is supposed to be formed on the inner wall of the $1s\sigma_g$ of the molecular ion after ionization from the neutral H_2 ground state. Then, the wavepacket (in contrast to its components) evolves on the electronic potential curve proceeding back and forth across the potential well with their respective time periods, as referred before. Subsequently, the wavepacket may undergo rearrangement and dissociate depending on both the deposited energy and the nature of the ionic surface. Therefore, the wavepacket suffers or passes periods of dephasing and revivals as will be shown in Sec. 4.6.

4.3 Ion-yield calculation

The ionization rate in a pulsed-laser field depends on the shape of the field strength (laser's temporal and spatial profiles), molecular alignment, and most importantly on the ionization potential. Because of the fast ionization process compared to the vibrational period, the binding energy is taken as the vertical binding energy, which is a function of the internuclear distance. For comparing theoretical calculations with experimental ionization signals, all these factors have to be included. To calculate the R-dependent ionization *yield*, $Y(R, I)$, for a specific laser pulse, it can be obtained from the R-dependent ionization *rate* Γ according to [29]

$$Y(R, I) \;=\; 1 \;-\; exp\{-\int_{pulse} dt\, \Gamma_\xi\, [I_p(R), \mathbf{F}(t)]\}\,, \tag{4.5}$$

where the integration is performed over the whole pulse duration. The electric field strength $\mathbf{F}(t)$ varies during the pulse length and is given for a linear polarized field as

$$\mathbf{F}(t) \;=\; F\; f(t)\cos(\omega t \,+\, \varphi) \tag{4.6}$$

with the amplitude F, laser frequency ω, and envelope function $f(t)$, which is considered as $\cos^2$-shaped in this thesis. φ is the carrier-envelope phase and it describes the distance of the electric field maxima with respect to the maximum of the envelope[3]. The relation between the electric field strength F and the laser intensity I is given by Eq. (2.9). The R-dependent ionization rates Γ_ξ (ξ=ADK, fc-ADK or PPT) are calculated within the ADK, fc-ADK, or PPT models by using Eqs. (2.27), (2.33), or (2.29), respectively, taking into account the laser intensity variation during the laser period. The tunneling ionization yields are obtained according to Eq. (4.5) by substituting the rates Γ_ξ with $\Gamma_{ADK}, \Gamma_{\mathrm{fc}-ADK}$, and Γ_{PPT}. The results for H_2 will be compared with those obtained within the full molecular two-electron calculations, which are denoted as TDSE yields.

4.3.1 Variation of the ionization yield with the internuclear distance

In order to achieve a complete picture of processes that occur when H_2 molecules are exposed to laser fields, the nuclear motion has to be considered. When talking about the nuclear motion, experimentalists for a long time assumed that the distribution over vibrational states formed in the molecular ion following ionization of the neutral molecule obeys the Franck-Condon (FC) distribution[4]. It was argued that the nuclear motion is practically frozen during the electronic tunneling region. Therefore, an FC approximation was supposed to be appropriate in the tunneling regime ($\gamma \ll 1$). Interestingly, Saenz [146] predicted a non-Franck-Condon distribution and suggested that the use of the Franck-Condon principle is often inaccurate because the rapid increase of the tunneling ionization rate with the internuclear distance R. Later, based on the *ab initio* calculation of the electric-field induced distortions of the potential curves and ionization rates Urbain *et al.* [147] developed a time-averaged quasi-static model that allowed to predict the vibrational distribution of H_2^+ produced by strong-laser-field ionization of H_2 molecules. They experimentally confirmed that the predicted distribution differs substantially from the FC distribution. This observation was explained on the basis of the strong dependence of the ionization rate on the internuclear distance.

[3] In this thesis, $\varphi = 0$ will be considered.

[4] Due to the simplicity, until recently some experimentalists, e.g. [148, 149], assumed the FC transition (although it is not quite correct) to model the pump pulse to initiate the H_2^+ vibrations (see also [147] and reference therein).

In order to consider the influence of vibrational motion on the strong-field ionization rate within the quasi-static approximation (QSA), the assumption of a fast ionization process, compared with the motion of the nuclei, can be used to evaluate an R-dependent ionization rate and then to solve the Schrödinger equation describing vibrational motion [77]. For sufficiently small rates, this reduces effectively to the convolution of the R-dependent ionization rate with the vibrational ground-state wavefunction. Saenz [77] showed that the total ionization rate is influenced by vibrational motion. He obtained the ionization rates within the extended ADK model (for simplicity) after replacing the atomic ionization potential $\mathrm{I}_p(\equiv E_b)$ in the rate formula with the R-dependent vertical difference binding energy $\mathrm{I}_p(R)$ that is defined as the energy gap between the Born-Oppenheimer potential curves of the neutral diatomic molecule and its daughter molecular ion in their respective ground electronic states. For example, in the case of H_2, the pronounced variation of $\mathrm{I}_p(R)$ with R leads to a dramatic R variation of the ADK ionization rate. In a subsequent work, it was demonstrated that the R variation of the predicted static ionization rate for H_2 by a simple ADK model agrees very well with that obtained by a full static-field *ab initio* calculation [50, 94], if the intensities belong to the tunnel regime for which ADK was derived.

Despite the fact that the predicted influence of the R dependence on the total ionization rate of H_2 requires very accurate measurements for its experimental confirmation, more pronounced effects are expected for differential rates like the vibrational-state distribution (VSD) of the H_2^+ ions resulting from exposing H_2 to femtosecond laser pulses. The VSD of the formed ions is important for modeling all subsequent processes like Coulomb explosion. Even if the laser pulse could be sufficiently short and intense to remove enough electrons from the molecule for immediate Coulomb explosion, the R-dependent ionization rate would lead to a correspondingly distorted the initial vibrational wavefunction of the formed ion. Therfore, understanding the R dependence of the strong-field ionization rate is very important.

In this section, the R dependence of the ionization processes will be investigated using the ADK, fc-ADK, and PPT models as well as a full solution of the three-dimensional TDSE. The investigation will mainly focus on laser parameters found in Refs. [58, 150]. In order to demonstrate the difference in the R-dependent behavior in the multi-photon regime, where QSA is not expected to be valid, the results for a wavelength shorter than 800 nm (namely for 400 nm) will be also presented.

The dependence of the ionization rates, and subsequently ionization yields, on the internuclear distance R is obtained within the R range in which the vibrational ground-state wavefunction is non-vanishing (Franck-Condon window). The rotational motion will be

neglected, while the following two cases of alignment are considered. In the first one the molecular axis is parallel to the electric field of a linearly polarized laser beam (parallel orientation $\|$), while in the second case it is perpendicular to the electric field (perpendicular orientation $\perp$). The TDSE describing molecular hydrogen within the fixed-nuclear approximation is solved for 30 different values of R (between $1.0\,a_0$ and $2.5\,a_0$) [58, 150]. This was repeated for five different values of the peak intensity: $2.0{\times}10^{13}$, $5.0{\times}10^{13}$, $8.0{\times}10^{13}$, $1.0{\times}10^{14}$, and $1.3{\times}10^{14}\,\mathrm{W/cm^2}$. A summary of the method, which is used to solve the TDSE describing molecular hydrogen exposed to the laser field for parallel and perpendicular orientations, is presented in Appendix C and discussed in more detail in [119, 150, 151].

The different tunneling ionization yields and the TDSE yields ($\|$ and $\perp$) for H_2 are plotted in Fig. 4.2 on a semi-logarithmic scale as a function of R for various laser pulses. The laser-pulse parameters are 20 cycles (FWHM), $\cos^2$-shaped envelope, a central wavelength of 800 nm (left panel) and 400 nm (right panel). Various peak intensities: $2.0{\times}10^{13}$ (top panel), $8.0{\times}10^{13}$ (middle panel), and $1.3{\times}10^{14}\,\mathrm{W/cm^2}$ (bottom panel) are used. Increasing ionization yields for increasing R can be easily observed, furthermore the appearance of some resonance structures that depend on the peak intensity of the laser pulse and on the wavelength. However, the R-dependent ionization yield and the structures decrease for increasing peak intensity, not only for 800 but also for 400 nm. The observed structures are due to classical multi-photon phenomena (channel closing and/or REMPI) [150]. Since multi-photon ionization takes place at lower intensities, the structures in this regime are not surprising. On the other hand, at high intensities the barrier-suppression ionization takes place.

As can be seen from Fig. 4.2, a surprisingly good agreement between the simple analytical formula (fc-ADK) and the TDSE ionization yields as well as PPT yields is found. It nicely reproduces an exponential dependence for both R and a wide range of I. This agreement is also found to be quantitatively good, which is not the case for the simple ADK model. In the latter, a scaling factor is required for the comparison with the TDSE yields (see graphs). These properties make fc-ADK superior to ADK models, which conserves the simplicity of the ADK model compared with the PPT model.

For the lowest peak intensity, $2.0{\times}10^{13}\,\mathrm{W/cm^2}$, the ADK yields underestimate the TDSE results in a drastic fashion, namely by about a factor of 3×10^3 for the 800 nm and 10^6 for the 400 nm wavelengths. However, scaling the ADK yields by those two factors shows that the R-dependent ionization yields predicted by the ADK model qualitatively agree with the TDSE result for $R > 1.75\,a_0$. The PPT yields show some structures as the TDSE yields that are missed in both the ADK and fc-ADK yields. Clearly, the resonant

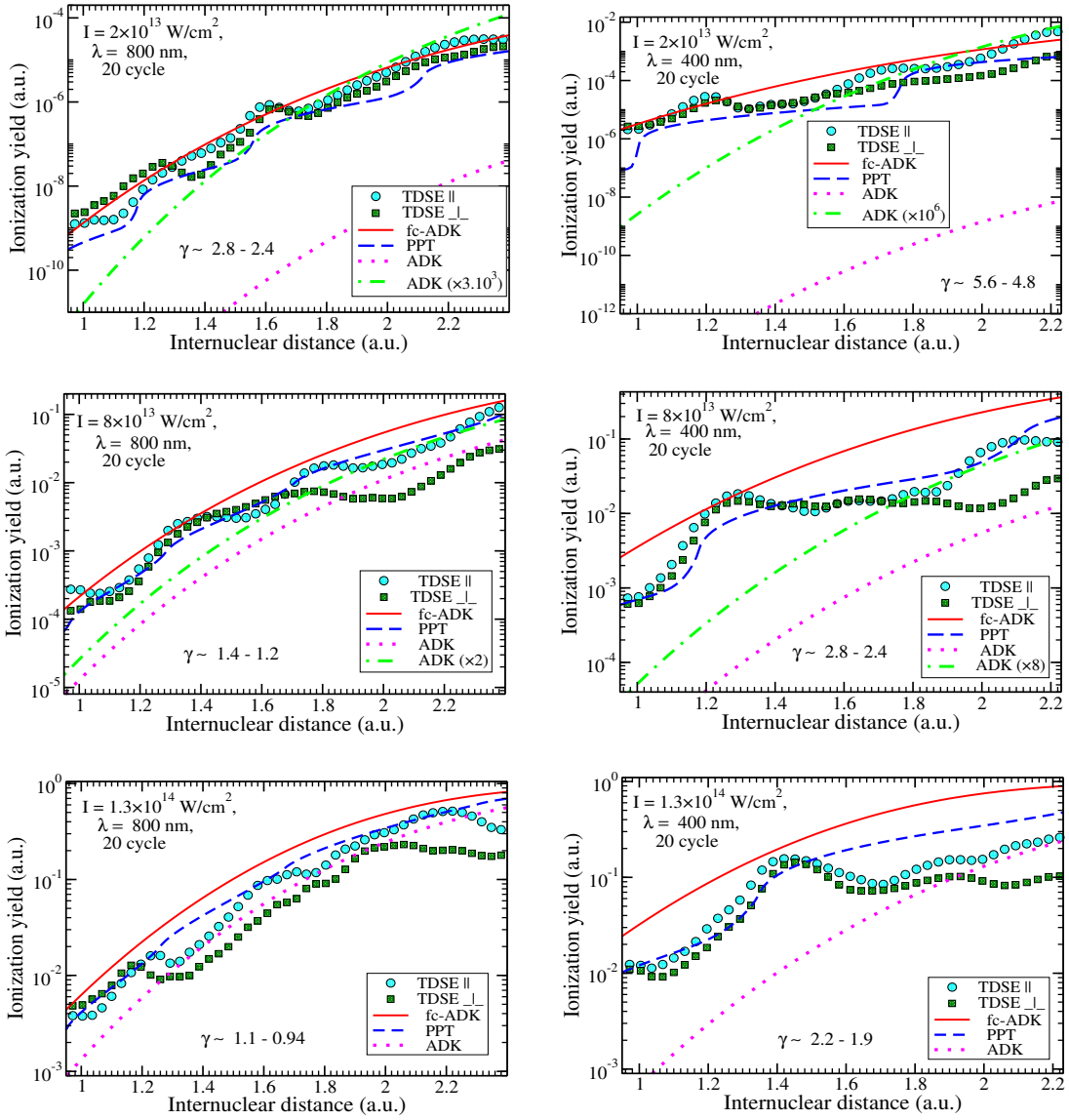

Figure 4.2: Ionization yields for a parallel and a perpendicular aligned H_2 molecule (circles and squares) as a function of the internuclear distance in a 20 cycles $\cos^2$-shaped, 800 nm (left panel) and 400 nm (right panel) laser pulse with different peak intensities. The TDSE yields are compared with those predicted by extended atomic models, fc-ADK (solid lines), PPT (dashed lines), ADK (dotted lines), and the scaled ADK yields (chain). The parameters of the laser pulse and the range of Keldysh parameters are given inside each graph. Every circle or squared point corresponds to a full solution of the TDSE [150] (a semi-logarithmic scale is plotted).

structures in the TDSE and PPT yields remain absent in ADK or fc-ADK yields even after scaling. The structures in the TDSE and the PPT yields can be attributed to multi-photon channel closings. Generally, the ponderomotive energy increases with an increase of the intensity. This determines the number of photons needed for ionization. Whenever the number of photons needed for ionization changes with the intensity, a channel closing (or opening) is expected to occur. The multi-photon channel closings appears also in the PPT model. The structures in the PPT yields could be expected due to the occurrence of the factor $A_m(\omega, \gamma)$ (Eq. (2.29)), which can be calculated according to Eq. (2.30). The first term in this equation depends on the value of $\tilde{n}$ which relies on ν ($\tilde{n} \geqslant \nu$). Both $\tilde{n}$ and ν depend on the internuclear distance R because they are functions of the binding energy (or ionization potential). However, the binding energy decreases for increasing R and thus the value of ν will also decrease. Accordingly, the summation will be started at an earlier value of $\tilde{n}$. This means that a number of terms will suddenly add to the summation in A_m for increasing R. According to the value of $\tilde{n}$, which depends on the binding energy, a new channel is expected to close at a multi-photon ionization threshold, i.e. when the number of photons required for ionization changes. To summarize, because of the minimum number of photons needed for ionization, $\tilde{n}$, decreases as a step function with increasing R, an increase in the A_m function is expected. This behavior is clearly displayed in the PPT yields, while it is completely absent in the ADK yields, which is a pure static-field model, and also in the the fc-ADK yields. Interestingly, it can be noted that the ionization yields from PPT and even the fc-ADK models as well as TDSE calculations depend on the laser wavelength. However, the ADK model fails to give the wavelength dependence of the ionization yields, as expected from Eq. (2.33). For fc-ADK and PPT models, the wavelength dependence of the ionization yield can be attributed to the function $g(\gamma)$ and $(\sqrt{1+\nu^2})^{3/2+|m|-2\,n^*}$ in Eq. (2.33) in addition to functions $A_m(\omega, \gamma)$ in Eq. (2.29), respectively.

Increasing the peak intensity and keeping the other laser parameters constant leads to a clearly improved quantitative agreement between the TDSE yields and those obtained within the ADK model. For instance, at peak intensity $8{\times}10^{13}\,\mathrm{W/cm^2}$, the required scaling factor to obtain a reasonable quantitative overall agreement decreases to 2 for 800 nm and 8 for 400 nm. At a higher peak intensity, e.g. $1.3{\times}10^{14}\,\mathrm{W/cm^2}$, there is no need for a scaling factor (see Fig. 4.2). Therfore, it can be said that the ADK model fails in most cases to predict the ionization yield *quantitatively*, but especially the R dependence is well *qualitatively* described for intensities greater than $8{\times}10^{13}\,\mathrm{W/cm^2}$. Since for the highest peak intensity a good quantitative agreement is obtained with the TDSE yields without the need of scaling of the tunneling ionization yields, especially for 800 nm. This improvement is due to the fact that the TDSE results show less structures

for increasing intensity. Since the ADK model predicts a smooth variation of the yield with R, the absence of structures in the TDSE yields is necessary for agreement of the two approaches. However, the standard ADK is not well suitable for a very intense field (see Eq. (2.13)), where the molecular barrier is significantly suppressed and tunneling formulas tend to overestimate the total ionization yield, so a new scaling factor is needed.

In the extended tunneling models and the TDSE method, the R-dependent ionization yields are predicted to vary by orders of magnitude within the FC window. Thus, the TDSE calculations favor the original prediction of the distribution of H_2^+ vibrational states after strong-field ionization of H_2, based on the strong dependence of the ionization yield on the internuclear distance [147]. Accordingly, the wavepacket created at $t = 0$ on the potential curve of H_2^+, which will be called the initial wavepacket (IWP), is affected by the ionization yields, as will be illustrated later. The discussions of the VSD and the IWP are presented in the next two sections. As said before, the first discussion neglects the distortion of the electronic ground-state potential energy, while it is considered in the second part that will be discussed in Sec. 4.4 and Sec 4.5, respectively.

4.4 Vibrational-state distributions and initial wavepacket

The probabilities of the electronic transitions, H_2 to H_2^+, under the influence of two different values of the laser wavelengths, 800 nm (1.55 eV) and 400 nm (3.1 eV), are shown in this section. As shown below, this study focuses mainly on the TDSE (for both cases $\parallel$ and $\perp$), PPT, fc-ADK, and ADK models. Furthermore, a comparison with the FC approximation has been performed.

4.4.1 Radiation with 800 nm wavelength

The vibrational-state distribution (VSD) of the eigenstates of H_2^+, calculated from Eq. (4.2), for a central laser wavelength of 800 nm, pulse length of 20 cycles, and for different intensities: 5.0×10^{13}, 8.0×10^{13}, and 1.3×10^{14} W/cm^2, are presented in Fig. 4.3. In this figure, the amplitudes of the normalized VSD as a function of the vibrational states ν are plotted. The results of the TDSE ($\parallel$ and $\perp$), fc-ADK, PPT, and ADK models are compared. The standard Franck-Condon distribution, assuming vertical transition with R-independent ionization, is also shown for comparison. The experimental data presented by Urbain *et al.* [147] (green bars) are shown for intensity 5×10^{13} W/cm^2 for comparison with the predicted distributions. At first glance, the observed and predicted

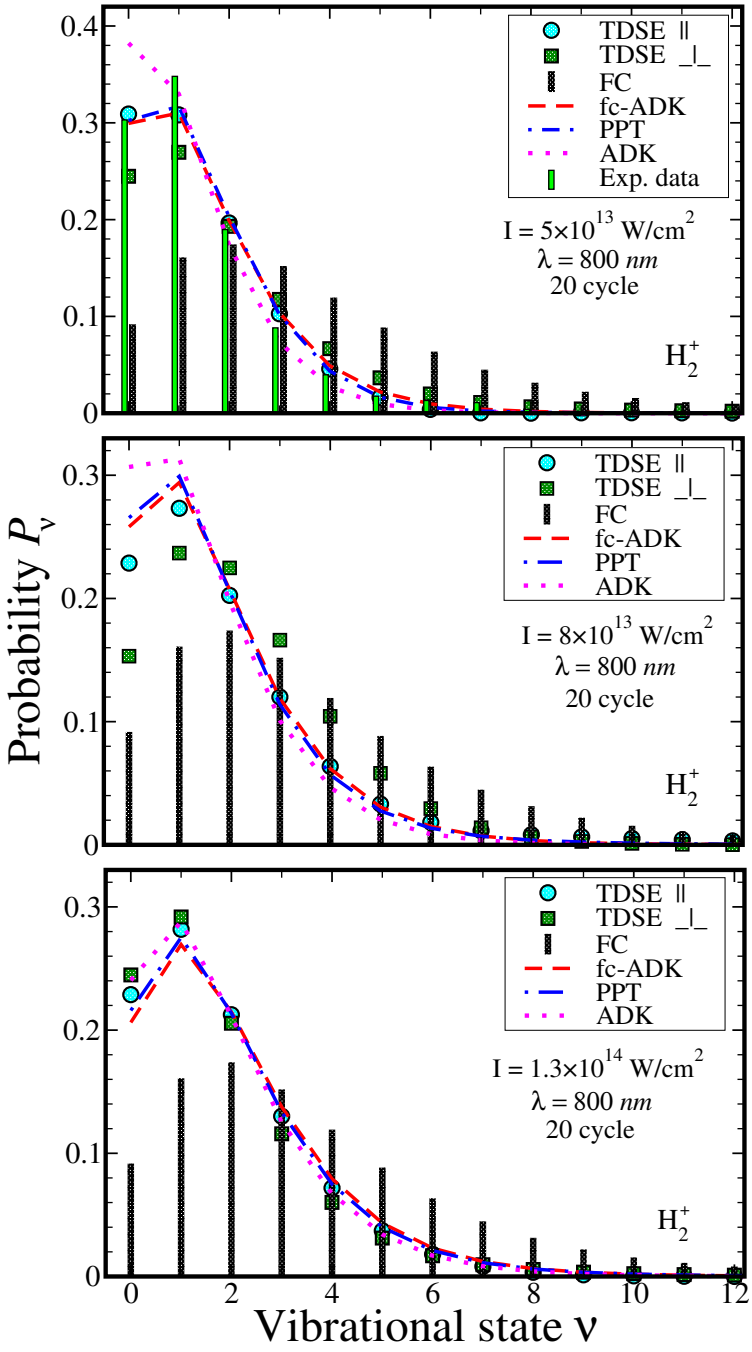

Figure 4.3: The relative vibrational-state distribution of H_2^+ after ionization in an intense laser field (800 nm) predicted according to TDSE, parallel (cyan circle) and perpendicular (green square). These predictions are compared with the predictions of the fc-ADK (red dashed lines), PPT (blue dot-dashed lines), and the standard ADK (magenta dot lines) models. The Franck-Condon distribution is indicated with black bars, for comparison. The green bars in the top panel indicate the experimental observations [147] at peak intensity 4.8×10^{13} W/cm^2 and pulse duration 45 fs. The population of the vibrational states are normalized, i.e. $\sum_\nu a_\nu^2 = 1$. The laser-pulse parameters are given inside each panel.

vibrational distributions deviate significantly from the FC distribution. For intensity 5.0×10^{13} W/cm^2, there is an excellent agreement with a maximum of the distribution at the lowest two vibrational states (0, 1) between the observed and the ones predicted with the R-dependent tunneling models, especially in the cases of TDSE ($\|$) and for both fc-ADK and PPT models, although the Keldysh parameter is greater than 1.5. In practice, there is no dissociation at the lowest intensity. Therefore, the predicted and observed vibrational distributions shown in Fig. 4.3 are similar. This means that the dominant contributions to the IWP come from the two lowest states. This agrees with the experimental results in [147, 152]. At higher intensity, e.g. 8.0×10^{13} W/cm^2, a reasonable quantitative agreement between the TDSE ($\|$) results and those obtained by tunneling models, especially fc-ADK and PPT models, is found. Obviously, all distributions are shifted to something between vertical ionization FC (peaking at $\nu = 2$) and tunneling ionization models, peaking at $\nu = 0$ or 1, (Fig. 4.3). It is worth to note that at high intensities (e.g. 1.3×10^{14} W/cm^2), the ionization yields and subsequently the relative distributions of the populations of the vibrational states are independent on the orientations of the laser field (see the results of the TDSE in the cases $\|$ and $\perp$). This can be understood easily because at high intensity, the molecule can be completely ionized by tunneling (since $\gamma < 1$) and over-the-barrier processes. Clearly, the largest discrepancy between FC and the populations predicted by R-dependent ionization models occurs at low intensity agreeing with what was found experimentally in [147, 153].

Figure 4.4 shows the probability density of the IWP as a function of R corresponding to the above VSDs. In order to clarify the influence of the dissociative states[5] on the IWP, the density of the *full IWP*[6] including the dissociative states and the *bound IWP* excluding them are shown in the left and right panels, respectively. As exhibited in this figure, the *full IWP*s obtained by both the fc-ADK and ADK models vary more smoothly than that obtained with the TDSE and even the PPT models, although their populations in the vibrational bound states does not possess significant differences, especially in the fc-ADK distributions. There are resonance structures clearly visible in the TDSE and slightly visible in the PPT distributions, particularly at low intensity, and they decrease with increasing intensity [150, 154]. These structures can be attributed to the multiphoton process that is a dominant at low intensities. At 5.0×10^{13} W/cm^2 the *full IWP* obtained with TDSE ($\|$) yields is more localized than those of the TDSE ($\perp$). One

[5]The states which lie above the dissociation threshold (continuum states).

[6]Henceforth, *full IWP* will be used referring to the complete initial wave packet that includes both the bound and the dissociative states, while the *bound IWP* is the part of the IWP that only includes the bound states.

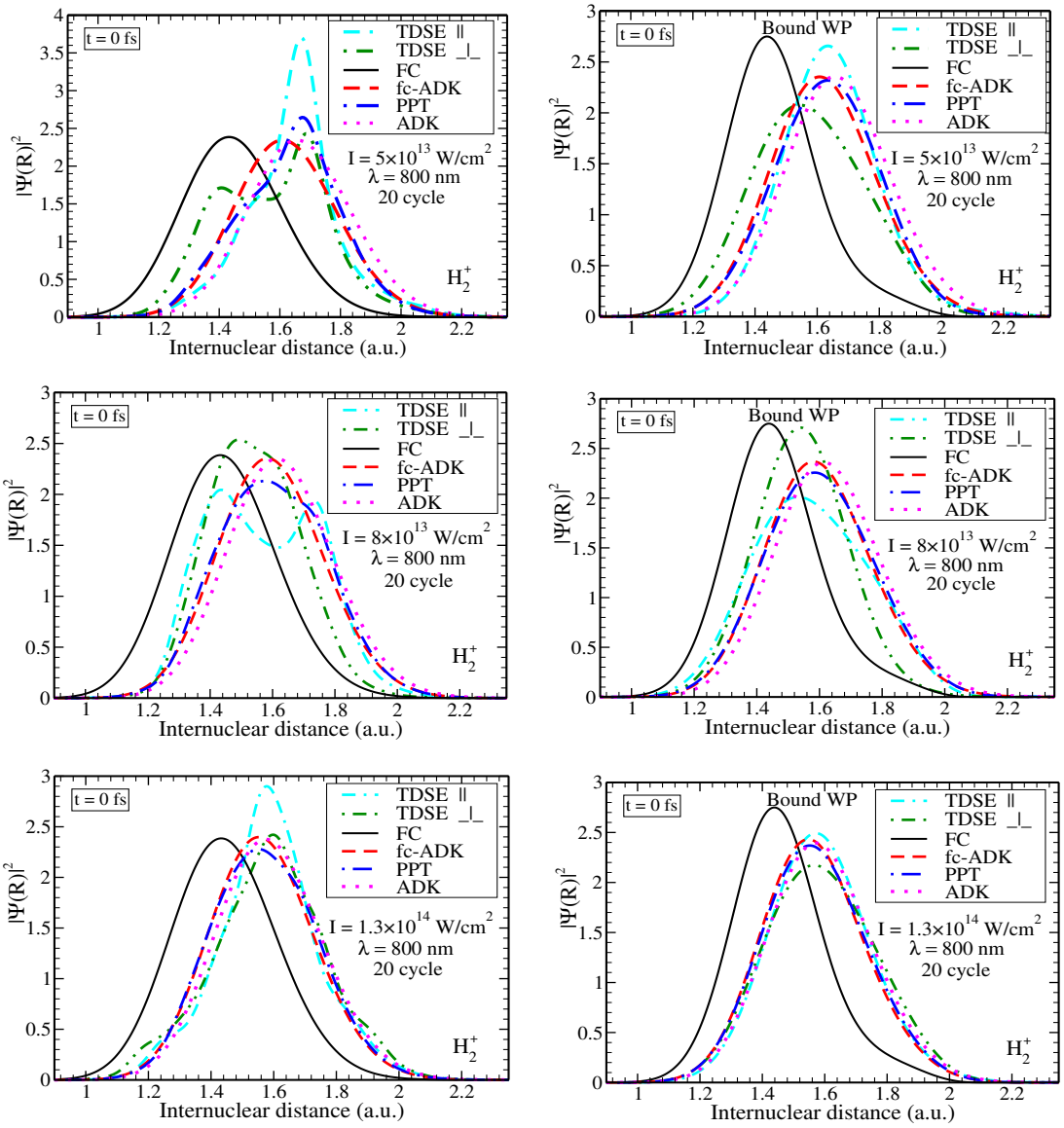

Figure 4.4: The probability density of initial wavepackets including (left panels) and excluding (right panels) the dissociative states are shown. These densities are according to the a_ν coefficients computed within TDSE, parallel (cyan lines) and perpendicular (green lines), fc-ADK (red dashed lines), PPT (blue dot-dashed lines), and the standard ADK (magenta-dot lines) models, that are shown in Fig. 4.3. The Franck-Condon IWP density is indicated with a black solid line, for comparison. The parameters of the laser pulses are given inside each graph.

hump (a maximum probability at $1.67\,a_0$) is observed when the field is parallel to the internuclear distance, whereas for the perpendicular alignment two humps are observed

(at 1.4 and 1.68 a_0). At 8.0×10^{13} W/cm^2, the *full IWP* for perpendicular alignment appears smoother than the parallel one, since there is one maximum (at 1.49 a_0) in the former, while it has two maxima (at 1.43 and 1.73 a_0) in the latter. These structures disappear at high intensity, e.g. 1.3×10^{14} W/cm^2. On the other side, one can note that there are small shifts between the maxima of the IWP obtained with each of the fc-ADK, PPT, and the ADK models. This shift decreases with increasing the intensity, since the tunneling ionization becomes dominant. Comparing to the bound IWP, one can conclude that the additional peaks observed in the *full IWP* of the TDSE or even the PPT model are attributed to the contributions of the dissociative states. However, the *bound IWP* approaches the Franck-Condon IWP for increasing the intensity. At high intensities and for long wavelengths (low frequency), the limit $g(\gamma) \Rightarrow 1$ is approached. Hence, the fc-ADK and the PPT models approach the standard ADK in the tunneling regime, see Eqs. (2.29) and (2.33), while the effects of the two functions, $g(\gamma)$ and $A_m(\gamma)$, become substantial at low intensities, i.e. in the multi-photon regime. In the case of the FC distributions, both the *full IWP* and the *bound IWP* are similar and possess one maximum value close to the equilibrium distance of H_2 (at 1.44 a_0). Noteworthy, in the tunneling models (ADK and fc-ADK) the effect of the dissociative states are almost negligible. Therefore the resonance structures is most prominent in the TDSE yields.

Certainly, the structures in the *full IWP* are related to those found in the ionization yields, see the left panel of Fig. 4.2 for the intensities 8.0×10^{13} and 1.3×10^{13} W/cm^2, and Fig. 4.5 for 5.0×10^{13} W/cm^2. This relation comes from the fact that the probability density of the IWP depends on the total population of the states, which can be defined as the ionization yields multiplied by the probability density of the ground vibrational state of neutral H_2 molecule according to[7]

$$P_{tot} = \sum_{\nu} |a_\nu|^2 = \int Y(R) \left[\chi^{H_2}_{\nu=0}(R)\right]^2 dR\,. \tag{4.7}$$

This equation indicates that the IWP depends directly not only on the initial vibrational wavefunctions of H_2 but also on the ionization yields.

In order to illustrate the contributions of the dissociative part to the *full* IWP, the absolute probability of the contributions of both the bound states (18 states) and the

[7] This equation is directly obtained by calculating the total population of the states, P_{tot} as:

$$P_{tot} = \sum_{\nu} |a_\nu|^2 = \sum_{\nu=0}^{N} \left| \langle\, \chi^{H_2^+}_{\nu}(R) \,|\, Y^{\frac{1}{2}}(R) \,|\, \chi^{H_2}_{\nu=0}(R) \,\rangle \right|^2$$

which can be rearranged, taking the orthonormality of the basis into account, as follows:

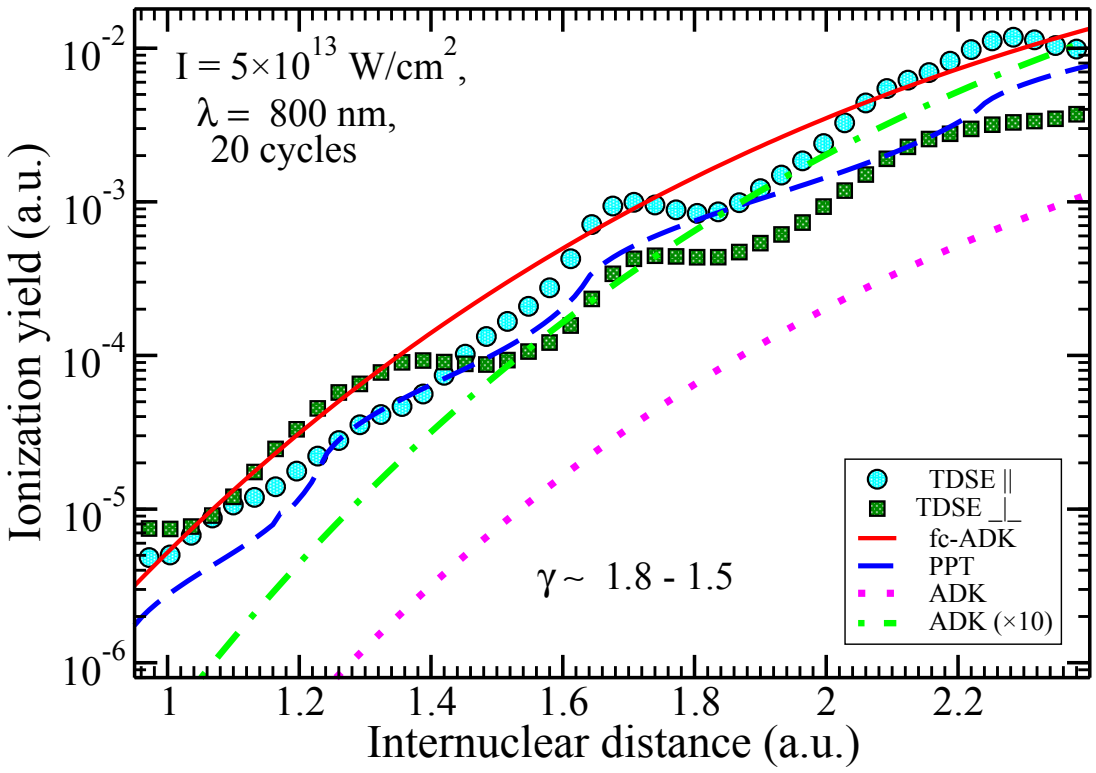

Figure 4.5: As the left panels of Fig. 4.2, but for laser intensity 5.0×10^{13} W/cm^2.

dissociation states (here represented numerically by 162 discretized continuum states) to the wavepacket at intensities 5.0×10^{13} and 8.0×10^{13} W/cm^2 are plotted in Fig. 4.6. To allow for a direct comparison, the continuum states of H_2^+ are renormalized to δ_{ij}. This figure displays the contributions of a number of dissociative states that are populated by the multi-photon processes, in both cases of the TDSE ($\parallel$ and $\perp$), and even the PPT model. These contributions decrease for increasing intensity, since the probability

$$
\begin{aligned}
P_{tot} &= \sum_\nu \langle \chi_\nu^{H_2^+}(R)\,|\,Y^{\frac{1}{2}}(R)\,|\,\chi_{\nu=0}^{H_2}(R)\rangle\,\langle \chi_{\nu=0}^{H_2}(R)\,|\,Y^{\frac{1}{2}}(R)\,|\,\chi_\nu^{H_2^+}(R)\rangle\,,\\
&= \sum_\nu \langle \chi_{\nu=0}^{H_2}(R)\,|\,Y^{\frac{1}{2}}(R)\,|\,\chi_\nu^{H_2^+}(R)\rangle\,\langle \chi_\nu^{H_2^+}(R)\,|\,Y^{\frac{1}{2}}(R)\,|\,\chi_{\nu=0}^{H_2}(R)\rangle\,,\\
&= \langle \chi_{\nu=0}^{H_2}(R)\,|\,Y^{\frac{1}{2}}(R)\,|\,\underbrace{\sum_\nu |\chi_\nu^{H_2^+}(R)\rangle\,\langle \chi_\nu^{H_2^+(R)}|}_{=1}\,Y^{\frac{1}{2}}(R)\,|\,\chi_{\nu=0}^{H_2}(R)\rangle\,,\\
&= \langle \chi_{\nu=0}^{H_2}(R)\,|\,Y(R)\,|\,\chi_{\nu=0}^{H_2}(R)\rangle\,,\\
&= \int Y(R)\,|\,\chi_{\nu=0}^{H_2}(R)|^2 dR\,.
\end{aligned}
$$

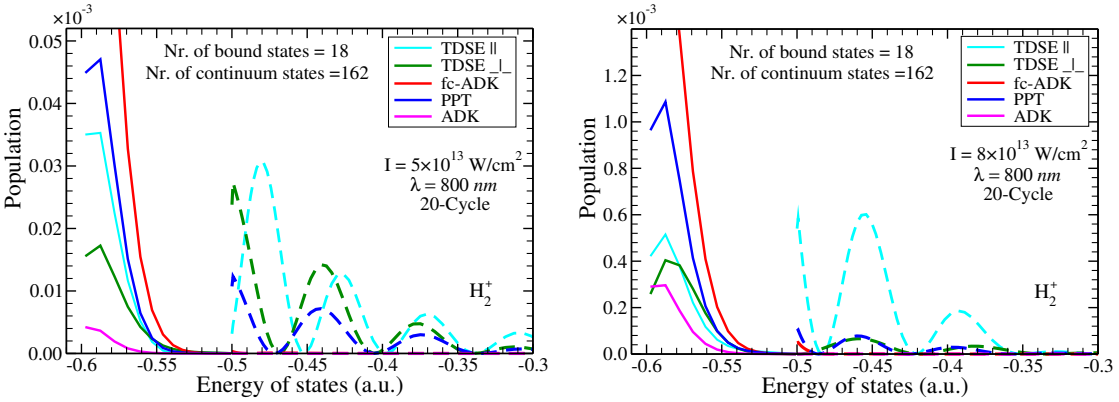

Figure 4.6: Bound and dissociation spectrum for H_2^+ for 800 nm laser field, according to the TDSE ($\parallel$ and $\perp$), fc-ADK, PPT, and the ADK models. The solid (dashed) lines indicate the spectrum of the bound (dissociative) states. The effect of the laser field on the potential energy is neglected (i.e. the BS is ignored). The laser parameters are specified inside each panel.

of the MPI decreases. Whereas the minimum number of photons essential for reaching the electronic continuum and a particular vibrational state ν in the ion increases with intensity [155]. The contributions of a number of dissociative states to the *full IWP* in the PPT model indicates, as discussed before, the importance of the factor $A_m(\gamma)$ in the PPT model, which depends on the number of photons needed to ionize the molecule. This emphasizes the increased range of validity of the PPT model compared to both the fc-ADK and the ADK models. Therefore, it is not appropriate to associate the validity of the PPT model with the only domination of tunneling process in a strong laser-field. Clearly, there are negligible or no contributions of the dissociative states to the *full IWP* in the fc-ADK and the ADK models as well as in the FC approximation. The fc-ADK and ADK models predict a smooth variation of the yields with R and subsequently a smooth variation in the *full IWP* (see Figs. 4.2 and 4.6) is expected.

4.4.2 Radiation with 400 nm wavelength

Now, the results for the shorter wavelength of 400 nm will be discussed. Furthermore, this section investigates both the influence of the pulse duration and the laser peak intensity.

First, the influence of varying the laser pulse duration on the VSDs and the probability density of the IWP at comparatively low intensity, e.g. 5.0×10^{13} W/cm^2, is studied. Similar to the case of 800 nm in the previous section, the VSDs for different pulse dura-

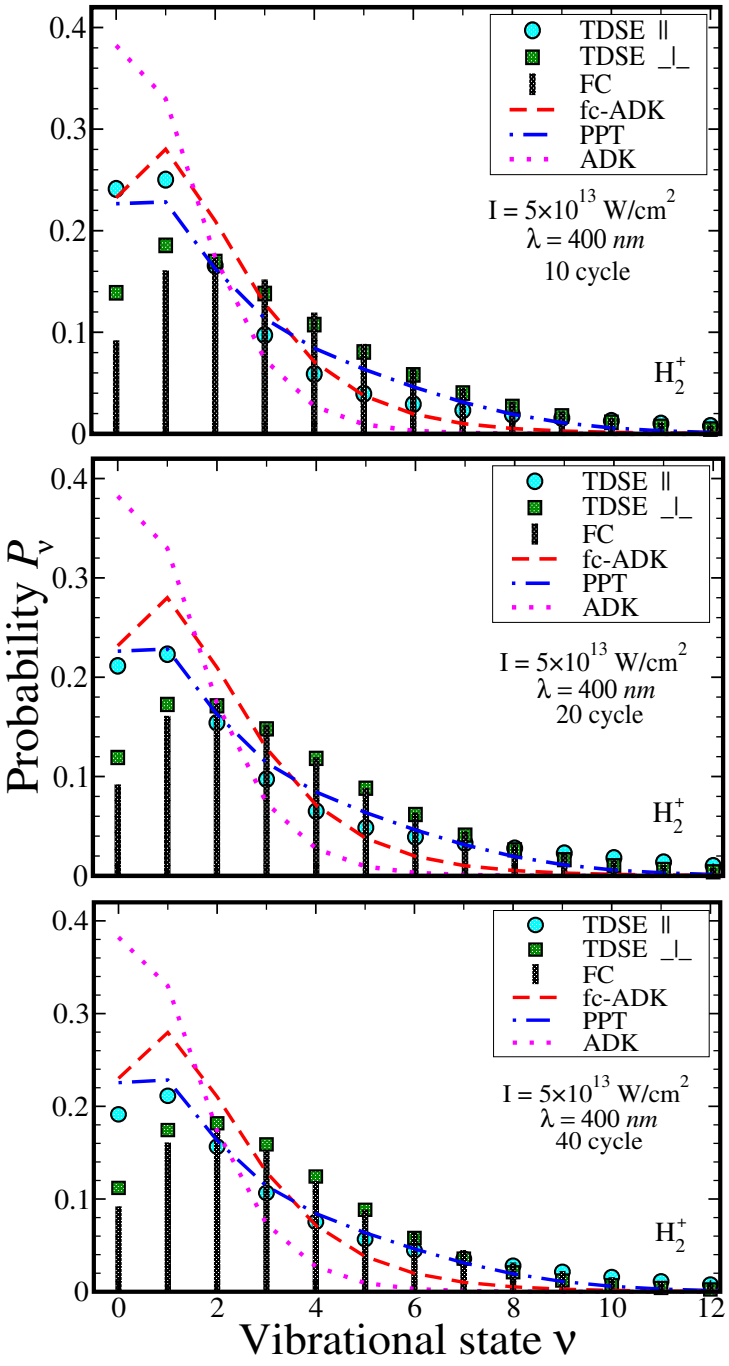

Figure 4.7: The vibrational distribution of H_2^+, after ionization in an intense laser field, that are predicted according to TDSE, parallel (cyan circle) and perpendicular (green square). These predictions are compared with the predictions of the fc-ADK (red dashed lines), PPT (blue dot-dashed lines), and the standard ADK (magenta dot lines) models. In all panels the laser wavelength is 400 nm and the laser intensity is 5.0×10^{13} W/cm^2. The pulse durations are 10 (top), 20 (middle), and 40 cycles (bottom). The Franck-Condon distribution is given for comparison (black bars).

tions: 10, 20, and 40 cycles, are shown in Fig. 4.7. For comparison, FC distributions are also shown. This figure confirms again that the PPT model can reproduce the TDSE calculations better than both the fc-ADK and the ADK models. The multi-photon ionization process is expected to be the dominant process (since, $\gamma \geqslant 3$), where γ is independent on the pulse duration. It can also be observed that a number of higher vibrational bound states are populated in a higher frequency radiation (400 nm) more than the case of lower frequency radiation (800 nm). Since in the high-frequency regime Furthermore, there is a partial agreement between the VSDs obtained from solving the TDSE (in the $\perp$ case) and the FC distributions for a long pulse. Otherwise, a discrepancy between the FC distribution and those predicted by both the extended tunneling models that take R-dependent ionization rates into account and the TDSE distributions can be observed.

Figure 4.8 shows the probability density of the *full IWP* (left panel) and *bound IWP* (right panel) corresponding to the previous VSDs for pulse durations 10, 20, and 40 cycles. From this figure it can be seen that despite the fact that the predicted TDSE VSDs depend slightly on the pulse duration, more than one hump is observed in the *full IWP* for increasing duration of the laser pulse. These resonant structures disappear almost completely in the *bound* IWP. It can be concluded that increasing the laser bandwidth (reducing the pulse duration) leads to spectra which show less details compared to the relatively long 40 cycles pulse. The densities of the *full IWP* curves for the 10 cycles pulse are almost smooth, except the one of the TDSE ($\|$) that shows a slight distortion for values of $R > 1.44\,a_0$. The appearance of the structures in the long pulses can be explained by closing and opening N-photons ionization channels, where the humps become sharper when increasing the pulse length. Interestingly, a smaller slope at large R (steep gradient in the curve) is observed for the IWP in the perpendicular orientation as compared to the parallel orientation. This indicates that at low laser intensity the decays in the IWP for H_2 at large R values are much faster for a perpendicular orientations compared to the parallel one.

The same strategies used to indicate the origin of structures in the *full IWP* in the case of 800 nm (previous section) have been applied in the case of 400 nm. In Fig. 4.9, the ionization yields as a function of R (left panel) as well as the absolute values of the contributions of both the bound and the dissociative states to the IWP (right panels) are plotted. The latter shows clearly the effect of the dissociative states, especially for long pulses in the TDSE and in the PPT model. This may be understood as follows: at low intensities, more molecules can be ionized in the long pulses than in the short ones. These structures reflect the behavior of the ionization yields, as discussed before

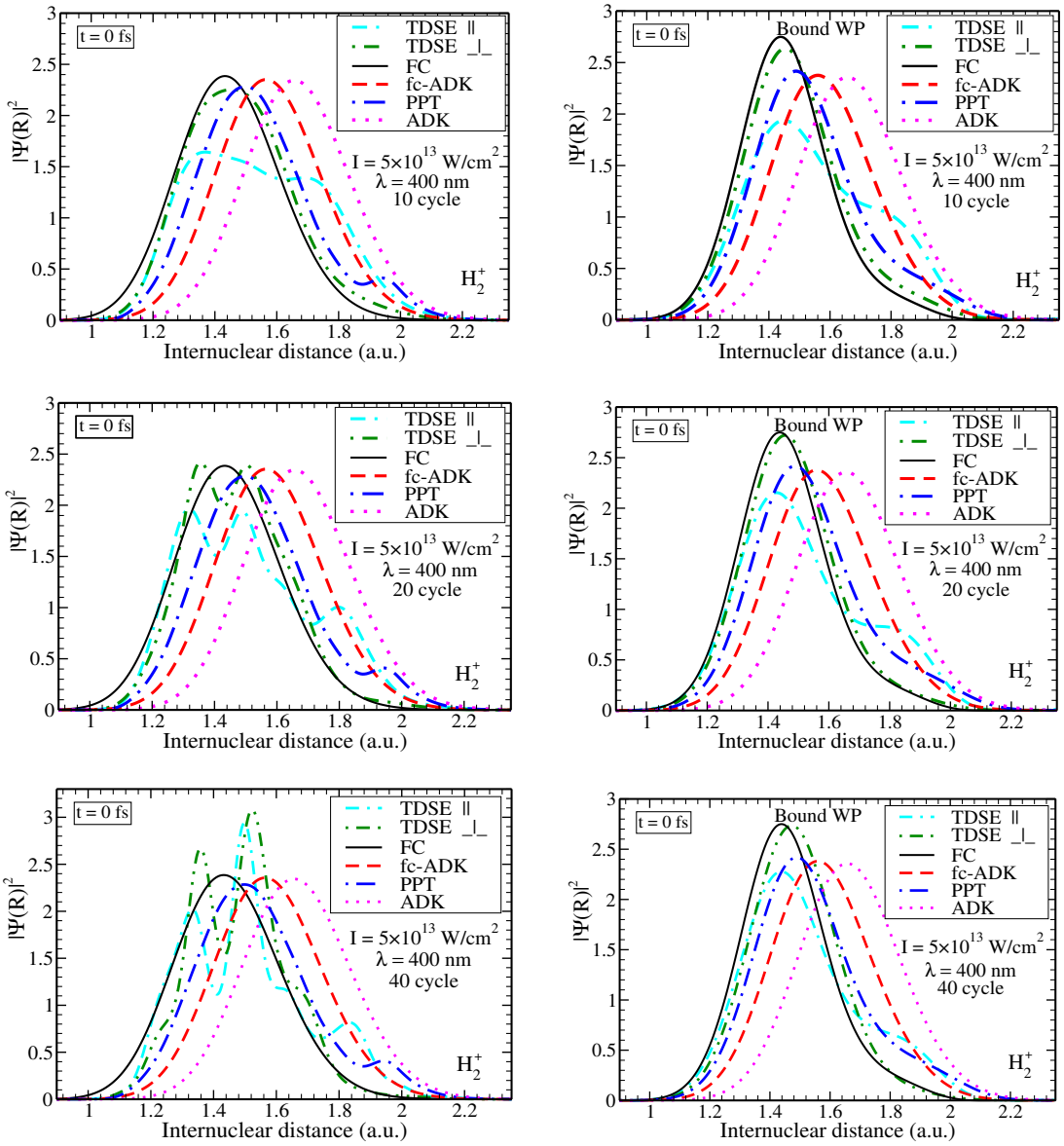

Figure 4.8: As in figure 4.4, but for wavelength 400 nm, intensity 5.0×10^{13} W/cm^2, and pulse lengths 10 (top), 20 (middle), and 40 (bottom) cycles. The effect of the dissociative part on the probability density of the IWP becomes more pronounced for long pulse durations.

[see Eqs. (4.2) and (4.7)].

The second goal of this section is the study of the influence of the laser peak intensity on the VSD and the IWP. To study this question and to avoid the pedestal effect [156], which can be noticed in short pulses, a long pulse duration (40 cycles) is considered with different peak intensities: 8.0×10^{13}, 1.0×10^{14}, and 1.3×10^{14} W/cm^2. Figure 4.10

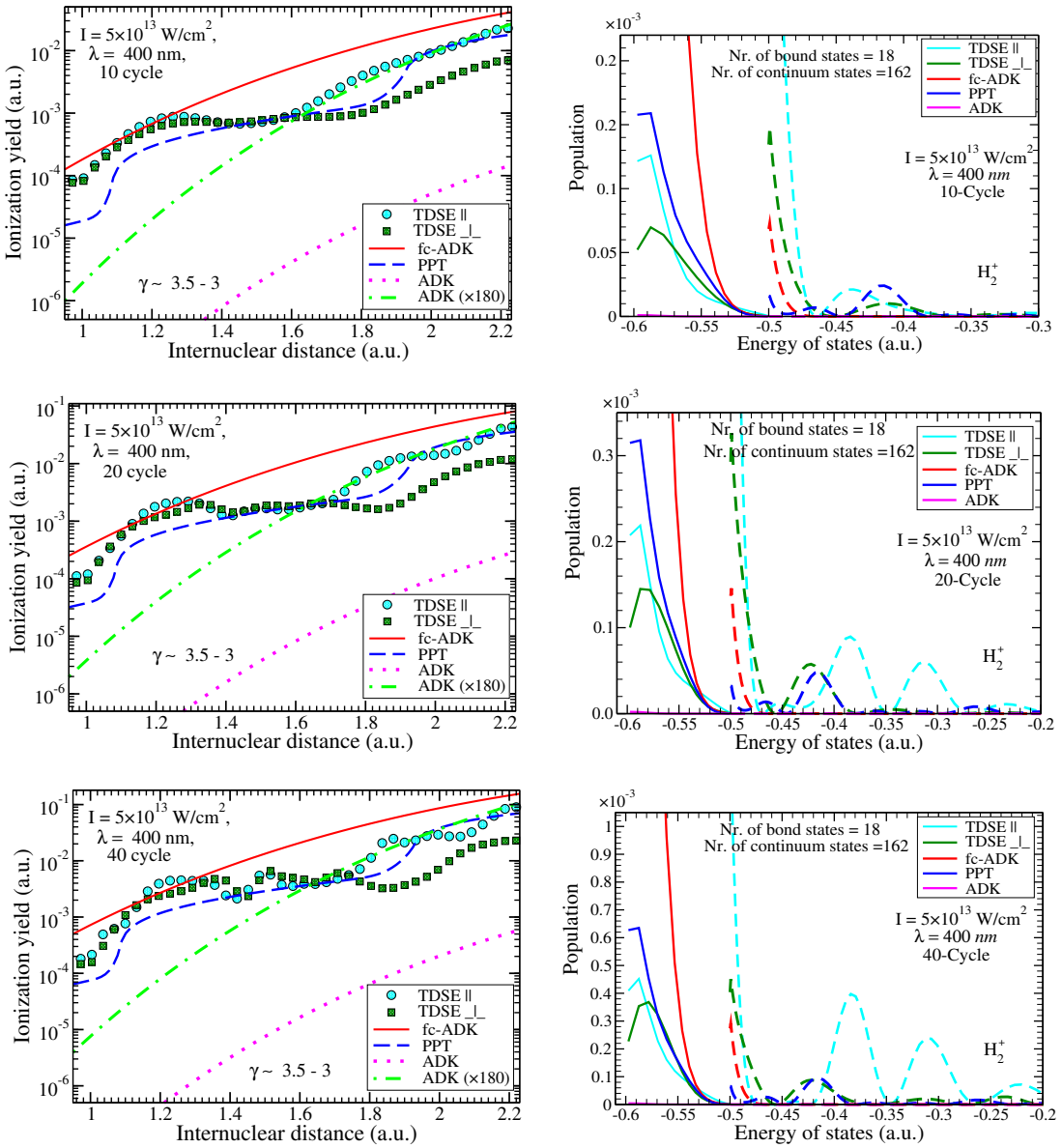

Figure 4.9: Ionization yields as a function of internuclear distance (left panels) and energy spectrum: bound and dissociative states, (right panels) as in Figs. 4.2 and 4.6, respectively, but for intensity 5.0×10^{13} W/cm^2 and the pulse widths of 10, 20, and 40 cycles.

displays the outcome providing the important comparison of the results of both the TDSE and tunneling models with the FC distribution. As in the case of 800 nm, there is a significant difference between the predicted VSDs obtained within the TDSE (||), fc-ADK, PPT, and the ADK models and the VSDs obtained with the FC approximation. A reasonable agreement between the vibrational distributions obtained with the TDSE

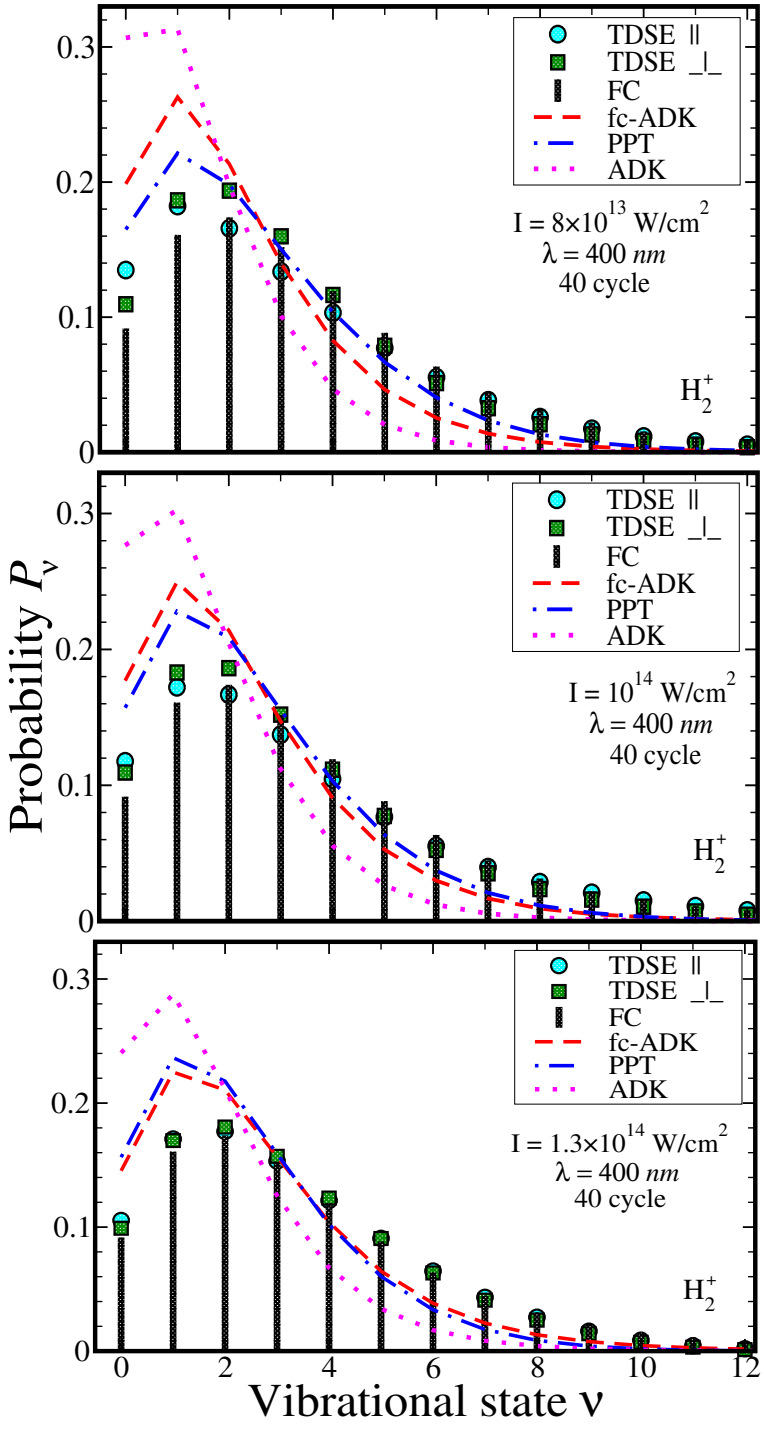

Figure 4.10: As figure 4.7, but for a pulse length of 40 cycles and peaks intensities: 8×10^{13} (top), 10^{14} (middle), and 1.3×10^{14} W/cm^2 (bottom).

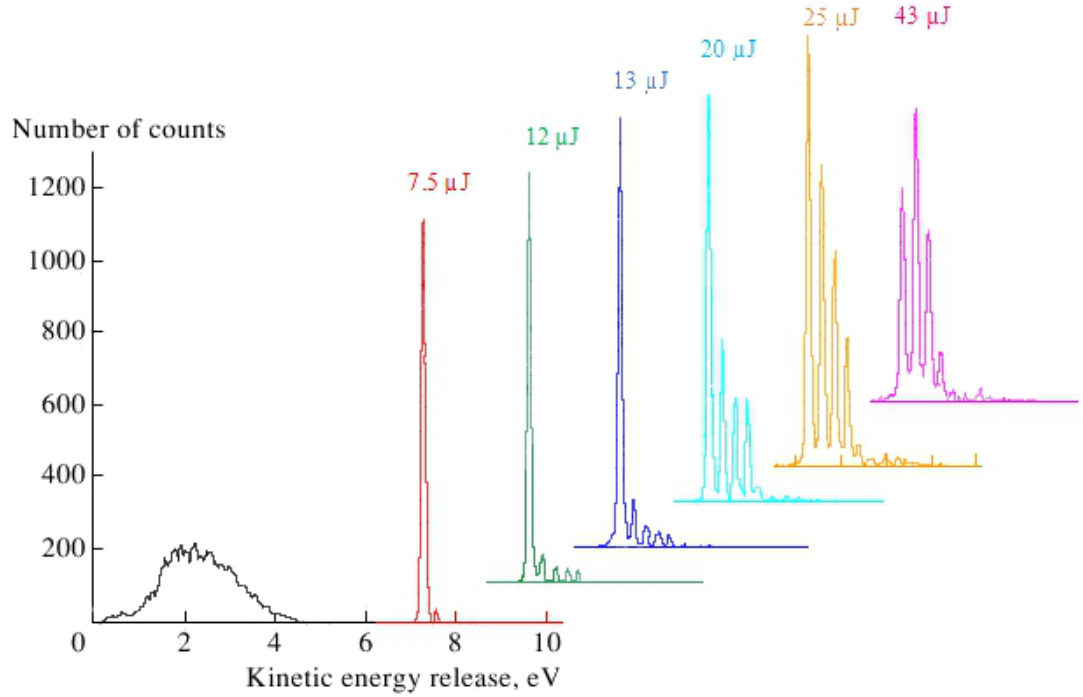

Figure 4.11: Kinetic energy release spectra as a function of the laser pulse energy (different colors in the figure) for the case in which H_2 is ionized by a femtosecond laser pulse at 400 nm with a linear polarization. This figure is adopted from Ref. [152].

($\perp$) for $5.0{\times}10^{13}$ W/cm^2 and the FC distributions is observed in Fig. 4.7, while a good agreement at higher intensities, e.g. for $1.3{\times}10^{14}$ W/cm^2, is exhibited in Fig. 4.10. On the other hand, in the case of the TDSE ($\parallel$), the peak maximum is shifted to $\nu = 1$, where it becomes similar to the FC distribution when increasing the intensity above 10^{14} W/cm^2. Hence, a good agreement with the FC distribution can be observed (Figs. 4.7 and 4.10). In principle, at high intensities and high frequencies, the ionization probability increases and the dependence on R becomes smaller. Consequently, one can expect that the VSD is going to be more and more Franck-Condon like. These results agree qualitatively with the experimental results by Fabre *et al* [152], see Fig 4.11 (taken from Ref. [152]). It is clear that at low intensities (low energies of the pulse in Fig 4.11)[8], practically only the first vibrational state ($\nu = 0$) is populated, while at high intensities

[8]The relation between the laser pulse energy E_{lp} (energy per pulse) and its intensity I is given by

$$I(\mathtt{W/cm^2}) = \frac{E_{lp}(\mathtt{Joules})}{A(\mathtt{cm^2}) \times \tau(\mathtt{sec.})}, \tag{4.8}$$

where A ($=\pi \times (\mathtt{beam\ radius})^2$) is the area of laser spot and τ is the pulse duration.

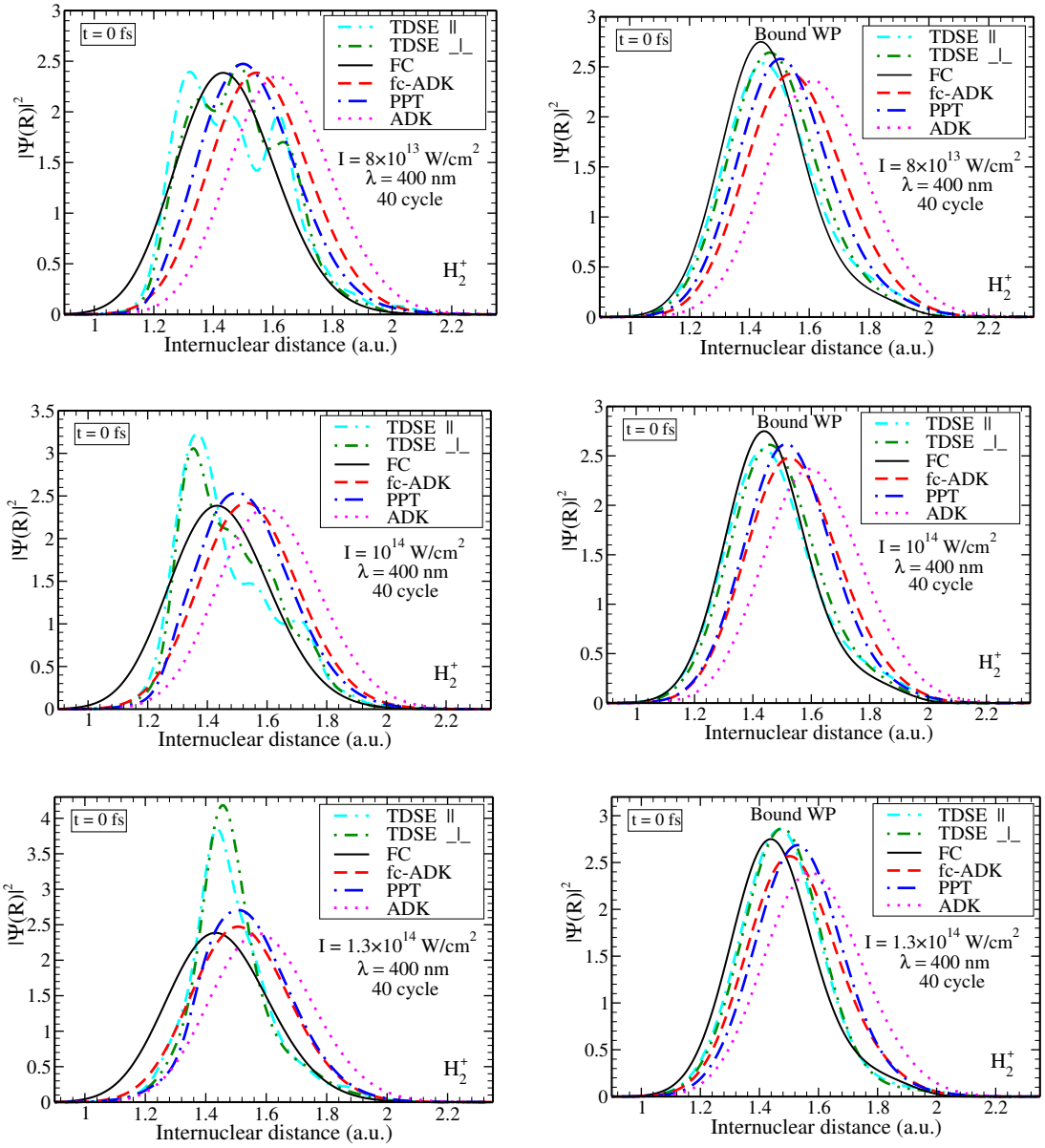

Figure 4.12: As figure 4.8, but for pulse length 40 cycles and peaks intensities: 8×10^{13} (top panels), 10^{14} (middle panels), and 1.3×10^{14} W/cm^2 (bottom panels).

(large pulse energies) one can expect that the results are going to be similar to the FC distribution.

To show the effect of the peak intensity on the IWP at shorter wavelength (400 nm), the *full IWP* (left panels) and the *bound IWP* (right panels) are plotted in Fig. 4.12. This figure shows some structures (or distortions) in the *full IWP* at comparatively

low intensities, 8×10^{13} and 10^{14} W/cm^2, (see also Fig. 4.8 for 5×10^{13} W/cm^2). These distortions in the *full IWP* disappear and the *full IWP* is more smoothly at higher intensities, e.g. at 1.3×10^{14} W/cm^2. This smoothing can also be observed in the *bound IWP* for all intensities. There is also a small shift between the *bound IWP* computed within the FC approximation and those computed within the R-dependent ionization models. In addition, one can note that the VSDs and IWPs predicted by both fc-ADK and ADK models are independent on the pulse length and approach the FC distributions at high intensity. As discussed previously, the structures appearing in the *full IWP* can be attributed to the dissociative states, in addition to the ionization yields. To confirm this result, Fig. 4.13 shows the R dependence ionization yields curves (left panels), and the population of the vibrational states, bound (solid lines) and dissociative (dashed lines) in the right panels.

Until now, the distortion of the potential curves caused by the external laser field was neglected, i.e. the effect of the bond softening was ignored. Therfore, the value of the dissociation energy in the previous energy spectrum curves was always equal to 0.5 a.u. as the energy of the field free case. In the next section, bond softening is considered and the threshold ionization energy which depends on the intensity of the external laser field, will be determined. Furthermore, the propagation of the wavepacket on the $1s\sigma_g$ potential surface of H_2^+ will be discussed.

4.5 Population of dissociative states including bond softening

The interaction of molecules with strong laser fields can alternatively be represented by the Floquet (or dressed-state) formalism [157]. In the simplest description, H_2^+ is reduced to the two lowest lying electronic states, where one is bound ($1s\sigma_g$) and the other is repulsive ($2p\sigma_u$). For a parallel alignment, the laser field induces a strong coupling between those two lowest lying potential energy surfaces. Interaction of the molecule with the strong-laser field shifts the energy of the upper repulsive potential curve down by the photon energy (Fig 2.3). By increasing the laser intensity the formerly bound vibrational states in the electronic ground states become unbound as the gap of the avoided crossing increases. In addition, the molecule exhibits dynamic alignment with the field polarization. Therfore, for a sufficiently strong field[9], the higher lying bound states can cross the barrier and dissociate via *bond softening* (BS) [16].

[9] In strong fields the adiabatic picture can be used as long as the time-scale of the molecular vibration is greater than the pulse duration [23].

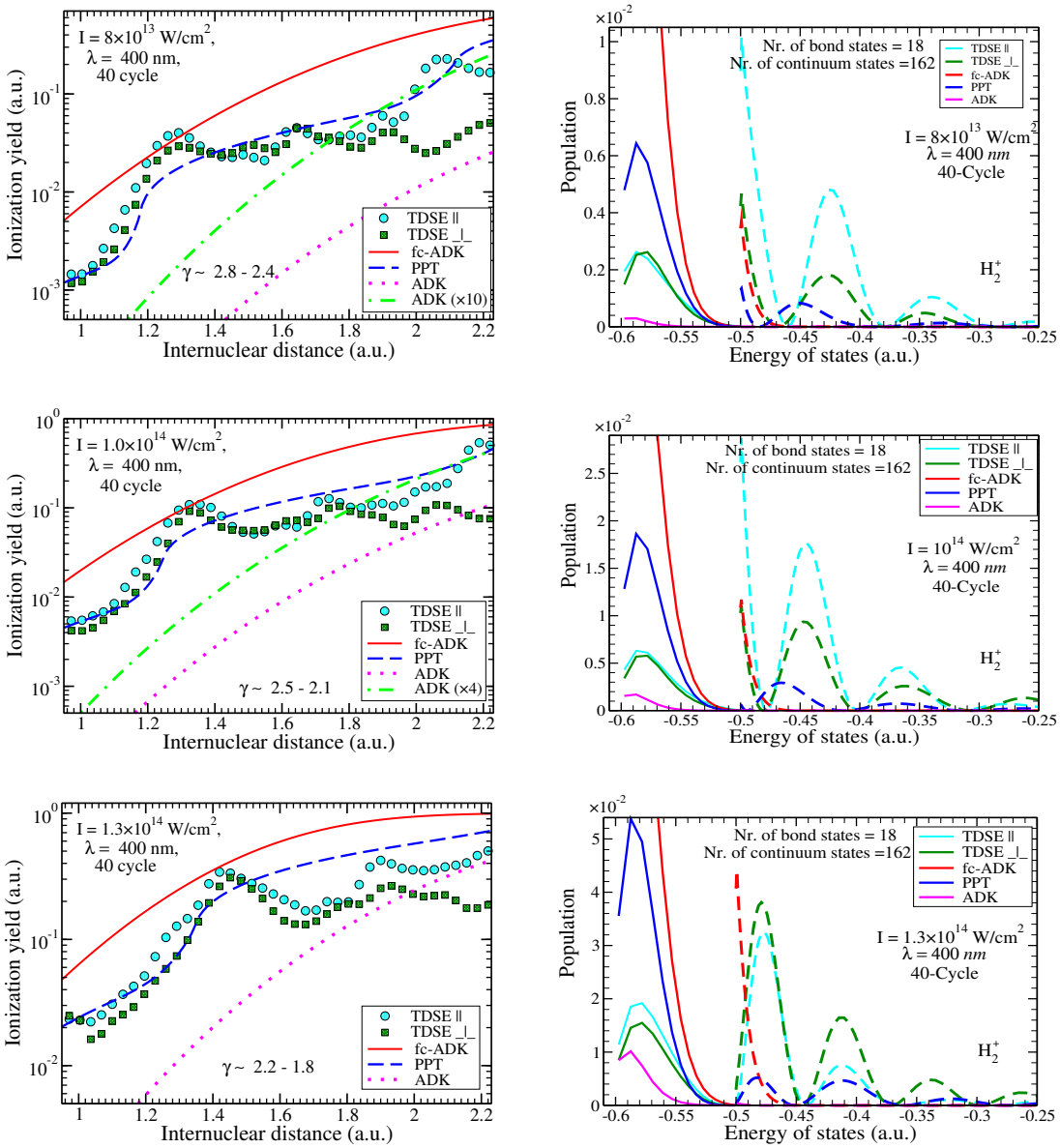

Figure 4.13: As the right panels of Fig. 4.9, but for a pulse width of 40 cycles and different peak intensities: 8×10^{13} (top), 10^{14} (middle), and 1.3×10^{14} W/cm^2 (bottom).

In a simplified description of the time dynamics of BS, the time averaged laser-field strength, $F_{av}= 2F_0/\pi$, is used to calculate the potential curve and then the vibrational states [147]. The distortion of the ground state $1s\sigma_g$ potential curve can be quantified

according to [158–160].

$$V(R) \;=\; \frac{V_{2p\sigma_u}(R) \;+\; V_{1s\sigma_g}(R)}{2} \;+\; \sqrt{\frac{\Delta V(R)^2}{4} \;+\; \{-d(R)\,.\,\mathrm{F_{av}}\}^2}\,. \qquad (4.9)$$

Here $V(R)$ is the distorted $1s\sigma_g$ potential curve (adiabatic curve), $V_{2p\sigma_u}$ and $V_{1s\sigma_g}$ are the field-free potential surfaces of either σ_u or σ_g, respectively. $\Delta V(R)$ is the energy difference $(V_{2p\sigma_u}(R) \;-\; V_{1s\sigma_g}(R))$, while $d(R)$ is the electronic transition dipole matrix element between the σ_g and σ_u states in length form.

Figure 4.14 displays the field-free potential curve for the ground state of H_2^+ together with the in-field curves for the electric fields corresponding to previous laser peak intensities, i.e. $5.0{\times}10^{13}$, $8.0{\times}10^{13}$, $1.0{\times}10^{14}$, and $1.3{\times}10^{14}$ W/cm^2. Furthermore, the field-free potential-energy curve of the ground state of H_2 is shown. The effect of the laser field on the potential curves is significant, where the distortion of the potential curves increases with increasing the laser intensity. As a result of the distortion of the ground-state potential curve the high-lying vibrational bound states become unbound (dissociative) or can tunnel through the distorted potential curve (predissociation). Accordingly, the $1s\sigma_g$ curve will support less bound states in the presence of the field than of the case without fields. The energy values of the bound states are shifted to lower energies. The Stark shifts of the bound states and the threshold of the continuum are only shown for the averaged of the laser field.

The dissociation threshold depends on the distortion of the potential curve and the eigenvalue spectrum of the vibrational states. The new dissociation thresholds of H_2^+ under external fields are obtained as follows. First, the radial (J = 0) Schrödinger equation is solved for obtaining the complete spectrum of molecular vibrational wavefunctions and the corresponding eigenvalues (see Appendix D). The equation is solved by expanding the nuclear wavefunctions in terms of B-spline basis functions [77]. In this way the Schrödinger equation is transformed into a matrix eigenvalue problem. A B-spline basis (200 B-splines of order eight, expanded on a linear knot sequence spanning $R = 0 - 12.5\,\mathrm{a_0}$) is found to give converged results[10]. The reduced mass, the dissociation energy, and the potential-energy curve are required as input. In order to determine the exact value of the dissociation energy of $1s\sigma_g$ of H_2^+ in an external field, the dissociation energy is supposed to be $-\infty$ at infinite values of R, so it is set to be $-\infty$ as an input value into the *nucfix* program. By running the program, the eigenvalues and the wave-

[10]The results are obtained by running the nuclear motion with B-splines using fixed boundary conditions program (*nucfix*) and rovibrational-transition (*rovib-trans*) programs (after modifications) that were original implemented by A. Saenz.

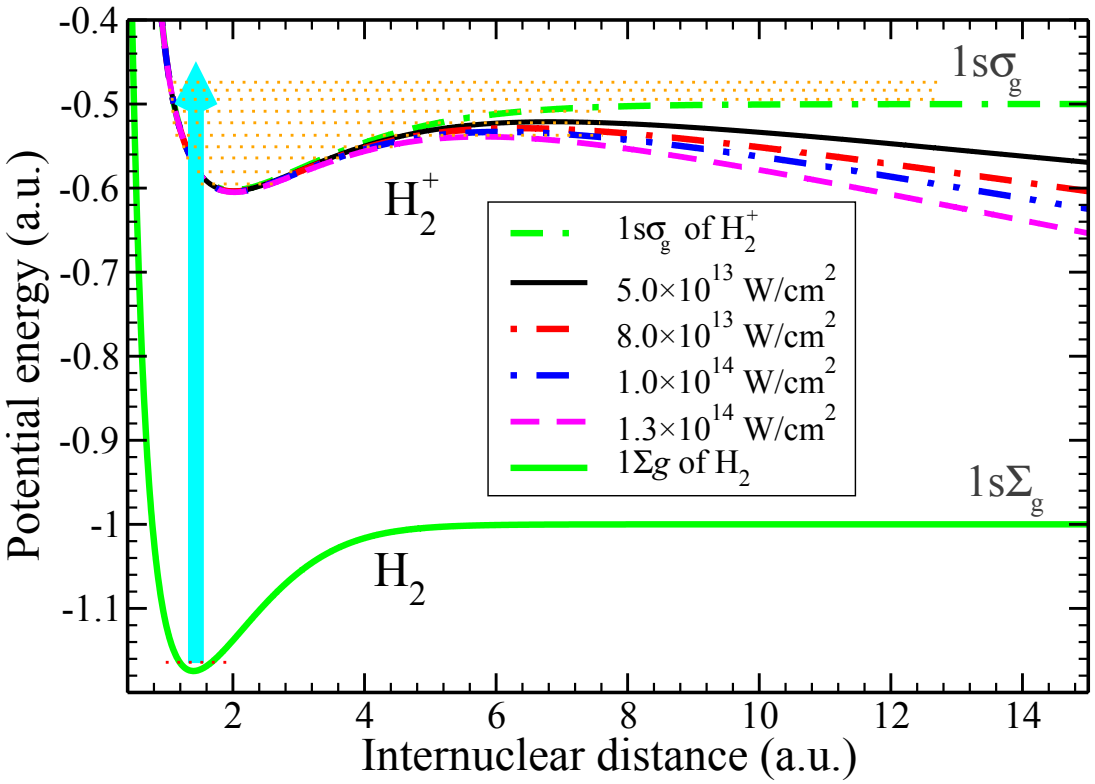

Figure 4.14: Field-dressed adiabatic potential curves for the $1s\sigma_g$ state of H_2^+ for different intensities. The adiabatic potential curve of the ground state of H_2 ($1s\Sigma_g$) is also presented. The horizontal dotted lines refer to the vibrational states, while the vertical thick line indicates the electronic transition from the first vibrational state of H_2 to the vibrational states (bound and dissociative) of H_2^+ .

functions of the vibrational states of H_2^+ are obtained. Furthermore, the normalized wavefunction of the ground vibrational states of H_2 is obtained (by running the program with the electronic ground-state potential curve of H_2). The transition probability is obtained in the Franck-Condon approximation.

Figure 4.15 shows the transition probabilities (populations) of the vibrational states of H_2^+ after suppressing the potential energy by three different laser peak intensities: 5.0×10^{13}, 8.0×10^{13}, and 1.3×10^{14} W/cm^2 for 800 nm. It is clear that the widths of the low-lying states are very narrow and sharp. This means that the nuclear wavepacket remains within the potential curve, since the width of the barrier is very large and prevents the wavepacket to escape. Then, these states remain practically bound. Going to the higher-lying states (towards the threshold energy), the dissociation peaks become wider. Therfore, these states are practically unstable with respect to predissociation (broad

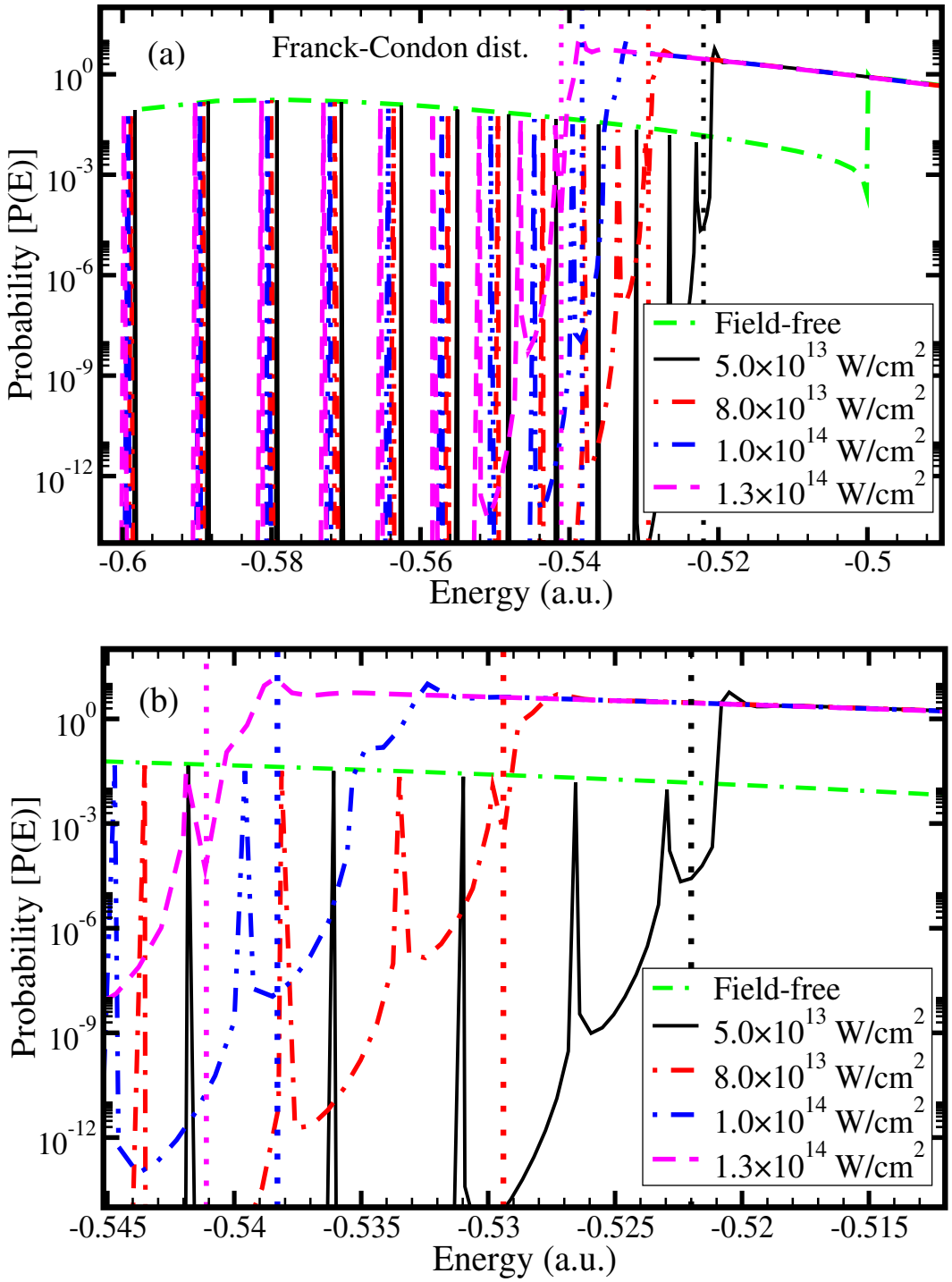

Figure 4.15: The transition probability for H_2^+ vibrational states (bound and continuum) after exposure to intense laser fields 800 nm according to the Franck-Condon principle and considering bond softening. The dissociation thresholds for each peak intensity are indicated by the vertical dotted lines. The bottom panel is an enlargement of the region (from $-.545$ to $-.512$ a.u.) of the top panels.

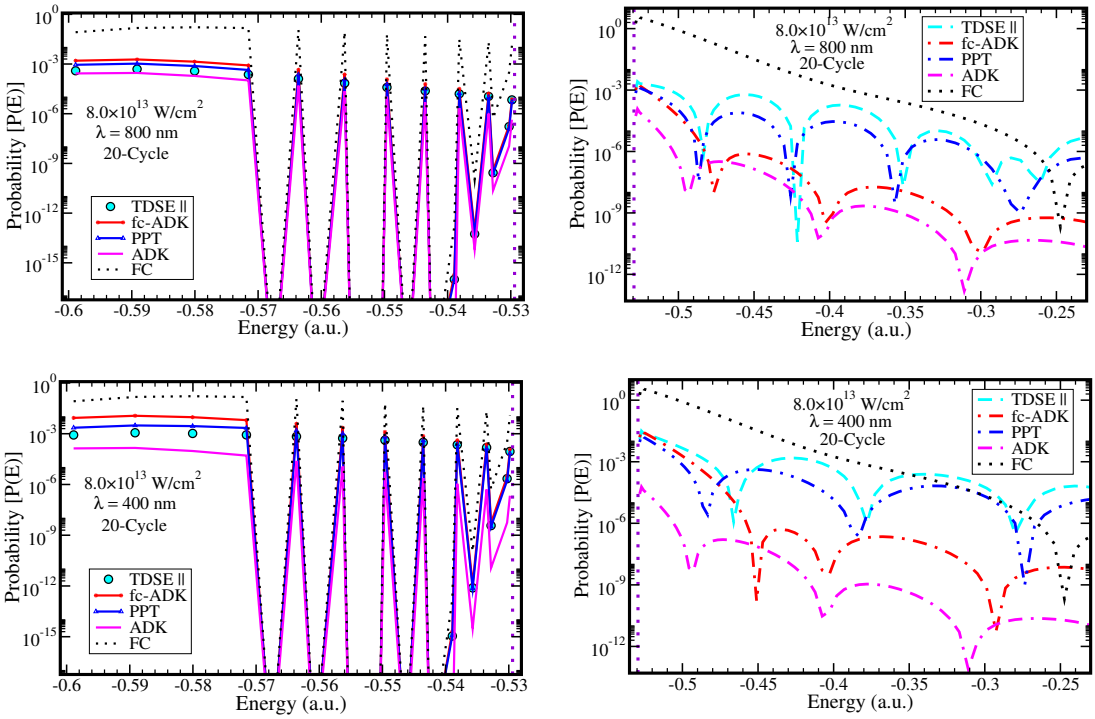

Figure 4.16: The populations of the bound states (left) and dissociative states (right) for H_2^+, driven by laser pulse 8.0×10^{13} W/cm^2, 800 nm (top), and 400 nm (bottom). Results are shown for the TDSE (||), fc-ADK, PPT, and the standard ADK models, including bond softening. The vertical dotted line refers to the dissociation threshold (-0.529 a.u.). The FC distribution is also exhibited.

line-width) or even over-the-barrier dissociation. Hence, the wavepacket can escape to the continuum or dissociative states via tunneling. At this point, the dissociation energy (threshold energy) can be accurately determined. The dissociation thresholds are illustrated in Fig. 4.15b, which is an enlargement of Fig. 4.15a, by the vertical dotted lines for each peak intensity. Subsequently, the new dissociation thresholds are -0.522, -0.529, and -0.541 a.u., for 5.0×10^{13}, 8.0×10^{13}, and 1.3×10^{14} W/cm^2, respectively. The values of the dissociation energies corresponding to different laser intensities are listed in Table 4.1.

Clearly, it is an interesting question how the previous Stark shift (laser-field dressing or bond softening) affects the VSDs and the IWPs. To answer this question, the above calculations are repeated, but after considering the field-dressed diabatic potential energy curves of H_2^+ for different intensities. Figure 4.16 displays the transition probability to the vibrational states of H_2^+ including both bound and dissociative states following ionization driven by the laser intensity 8.0×10^{13} W/cm^2, with wavelengths 800 (top

panels) and 400 nm (bottom panels), and pulse length of 20 cycles. In the case of 800 nm, it is observed that starting from the 4^{th} vibrational state, the populations of the bound states alternate (i.e. one is populated and the next one is not). Furthermore, the highest lying bound states are shifted into the continuum (or unbound). Moreover, the structures in the dissociative states obtained with the R-dependent tunneling models and TDSE start earlier than those obtained within the FC approximation. Because our calculations are converged, the behavior of the spectrum in the dissociation region reflects the effect of the coupling term in Eq. (4.2) (the ionization yield) on the overlap between the wavefunction of the ground state of H_2 and the wavefunctions of the higher dissociative states (repulsive states) of H_2^+. The overlap has a maximum if the maximum value of the wavefunctions of the dissociative states lies approximately above the maximum value of the wavefunction of the ground state (so-called reflection approximation[11] [161]). The slight displacements in the phase of the dissociative states lead to the perodic structure shown in Fig. 4.16. The earlier start of the structures in the dissociative states (left panel) in the case of R-dependent ionization models (e.g., TDSE, fc-ADK, PPT, and ADK) than in the case of FC approximation indicates the effect of the strong R-dependent ionization yield. This latter effect leads to the shift of the IWPs of these models from the IWP of the FC approximation (which was observed in Fig. 4.4). For the case of 400 nm, the same features as for 800 nm can be observed (low panel of Fig. 4.16), except that the widths of the structures in the dissociative part for TDSE calculations are increased because of a change of the ionization yields due to MPI and REMPI phenomena, since the photon energy (~ 0.114 a.u.) is, in this case, larger than in the 800 nm (~ 0.057 a.u.) case. Including bond softening does not affect the shape of the IWP, because the IWP is independent on the final state, but depends only on both the initial state and the ionization yields, Eq. (4.7). Of course, small changes in the ionization potential due to the BS mechanism lead to small variations in the ionization yields, which are, however, found to be negligible. While, BS has an essential effect on the dynamics of the wavepacket and affects the revival time of the nuclear wavepacket as shown in the next section.

4.6 Time evolution of the nuclear wavepackets

Due to the movement of the wavepacket back and forth across the potential surface of the ion, the wavepacket exposes to scatter through R (dephase) and then regain its

[11] In the reflection approximation cancellation of the oscillatory part leads effectively to a δ function for the overlap at the classical turning point.

locality (revive). The dispersion occurring in the wavepacket is referred to as a collapse of the wavepacket, while the recovery is referred to as the revival of the wavepacket. This behavior is well known as quantum revival. However, the dephasing caused by the anharmonicity of the molecular potential curve [162] (the nonequal spacing of the vibrational eigenstates) and the subsequent revival is expected to continue until an external field causes the system to loose coherence (breakdown).

In principle, the coherence and subsequently the revival times of the wavepacket depend on the phase differences between the different eigenstate components of the wavepacket, $E_{\nu\mu}$ in Eq. (4.4), which are called the beat frequencies. Because of the distortion in the potential curve of H_2^+ by an external field via the BS phenomena, the dissociation threshold and the eigenvalues of the eigenstates have values different from the field-free case, as discussed before. Therefore, a change in the revival time of the wavepacket could be expected. To clarify this point, the propagation of the wavepacket in both cases, i.e. in the field-free situation (ignoring the BS) and in the presence of an external field is shown in this section.

The results of a simulation of the vibrational wavepacket dynamics in H_2^+ are plotted in Fig. 4.17, assuming the FC transition induced by the pump pulse from the ground state of H_2. This figure shows how the probability density of the full wavepacket evolves in times between 0 and 650 fs in the internuclear-distance regime between 1 and 5 a_0. At each time, the wavepacket probability sums to unity over the full R range. The wavepacket is initially localized between the equilibrium distances of the ground state of H_2 ($\sim 1.43\,a_0$) and that of the H_2^+ ($\sim 2.0\,a_0$). Because the FC transitions are restricted to this narrow range of low values of R, a dominant population of the lower vibrational states is expected. The wavepacket moves on the bound $1s\sigma_g$ potential curve towards its outer or inner classical turning point. Hence, the wavepacket appears in the density colour map as a broad band between $R = 1.5$ and $R = 4.0\,a_0$, corresponding to the inner and outer turning points, respectively. Oscillations of the wavepacket dynamics across the potential well back and forth with collapse and revival are well observable. For example, in the field-free case (top panel), the first full revival occurs at $\simeq 283$ fs, whereas the second happens at $\simeq 566$ fs. Noteworthy, this revival time is larger than the experimentally observed value, 275 fs (using 5×10^{14} W/cm^2 and 13 fs duration pulse). The discrepancy between the characteristic revival time of the experimental data and the results of a simple numerical simulation was also observed by Rudenko *et al.* [163]. The most likely reasons for this discrepancy originate from the simplifications used in the theoretical (FC) model, which does not account for the R dependence of the H_2^+ ionization probability and furthermore neglects the influence of the rotational motion.

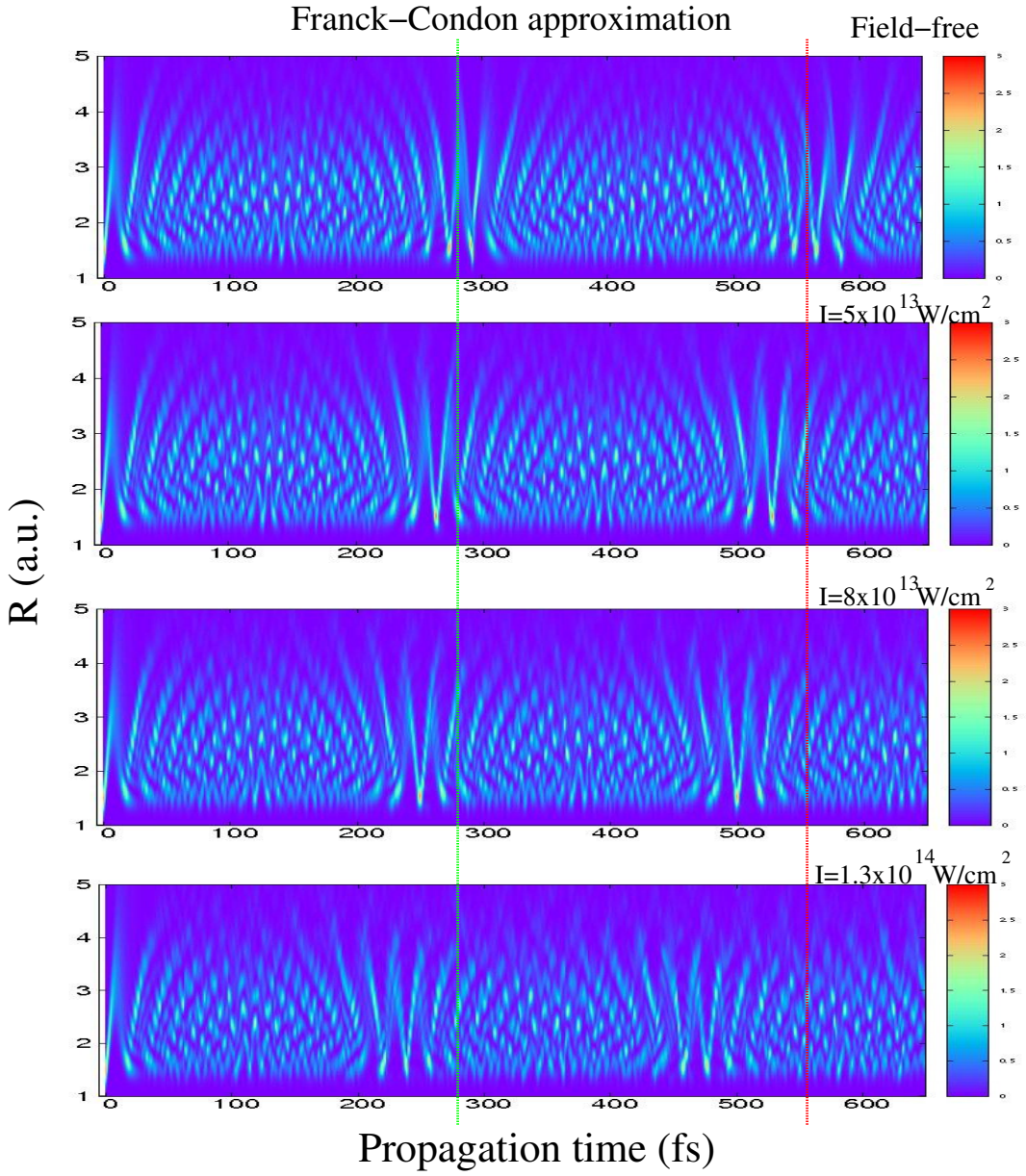

Figure 4.17: The probability distribution $|\Psi(\vec{R},t)|^2$ of the full vibrational wavepacket as a function of internuclear distance, R, and propagation time t. The vibrational-state distributions are obtained by adopting the Franck-Condon approximation. The bond-softening effects caused by different peaks intensities (shown above each panel), are taken into account. Dephasing and revival of the wavepacket can be observed in the plots. The colour scale runs from blue (low probability) to red (high probability). The vertical dotted green (red) line refers to the first (second) revival time for the field-free case (top panel), i.e. 283 fs (566 fs), see Table 4.1.

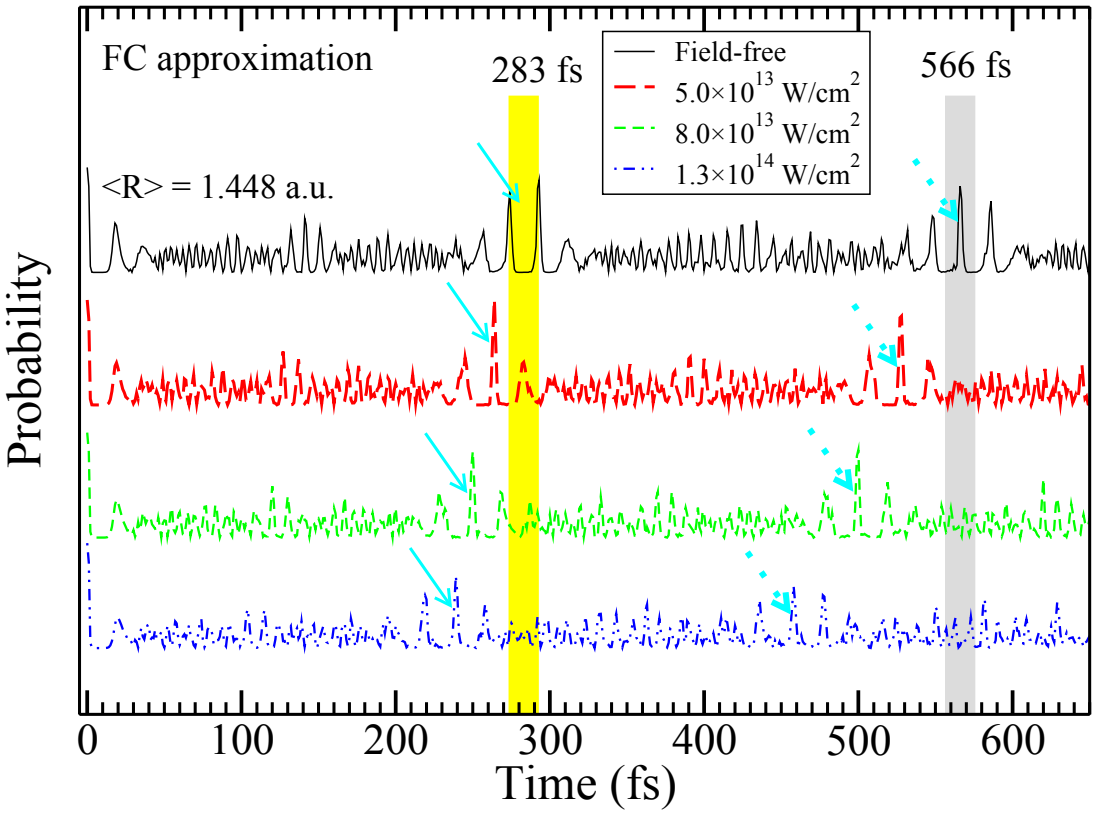

Figure 4.18: Wavepacket evolution over the range 0 to 650 fs demonstrating the revivals and fractional revivals times, for different intensities and with the mean value of $\langle R \rangle$. These curves are a cut at 1.448 a.u. through the colour density map in Fig. 4.17. The shaded area indicates the first and the second revival times of the field-free curve. The solid (dotted) arrows refer to the first (second) revival times of each curve (see Table 4.1).

At the revival time, all the vibrational states contained in the superposition to create the wavepacket are in phase with each other. Around this time, the wavepacket revives without any phase shift, if the wavepacket probability matches well its initial profile (at t = 0 fs). As the wavepacket evolves, the localized position disappears and then the localization is partially regained at intermediate times, called fractional revivals [164]. A fractional revival time is also observed, which is almost around half of the main revival time. At a fractional revival time, the first recurrence of the wavepacket to its original shape takes place. Moreover, there is a π-phase difference between the odd and even eigenstates contributing to the wavepacket [165]. The wavepacket probability near the first and second fractional revival times can be seen in the colour density plots, e.g. in the field-free case around $\sim$ 140 and $\sim$ 425 fs, respectively (see also Fig. 4.18). On the other hand, if BS is considered, it can be clearly observed that the revival

Table 4.1: The dissociation thresholds and the first as well as the second values for the fractional and full revival time of the wavepacket in the $1s\sigma_g$ potential of H_2^+ created by different laser intensities of the pump pulses. The times labeled by bold characters refer to the FC wavepacket in the field-free case.

Intensity ($\times 10^{13}$ W/cm^2)	Diss. Threshold (a.u.)	Fract. Revival First/Second (fs)	Revival Time First/Second (fs)
00.0	-0.500	**141/424** 140/421	**283/566** 275/550
05.0	-0.522	132/395	264/528
08.0	-0.529	125/375	250/500
13.0	-0.541	114/360	239/478

time decreases with increasing intensity. For example, the revival time decreases from $\simeq 283$ fs (field-free, top panel) to $\simeq 239$ fs (bottom panel) when increasing the intensity up to 1.3×10^{14} W/cm^2. The effect of BS on the revival times of the wavepacket and its propagation is illustrated in Fig. 4.18, which shows cuts through the density map in Fig. 4.17 at the mean expectation value ($R = 1.448\, a_0$). This figure shows the probability of the wavepacket at the expectation values $\langle R\rangle$ of the wavepacket $\Psi(R)$, which are calculated from

$$\langle R\rangle \;=\; \frac{\langle\Psi(R)|R|\Psi(R)\rangle}{\langle\Psi(R)|\Psi(R)\rangle}\,, \tag{4.10}$$

as a function of time. The top curve illustrates the evolution of the wavepacket in the field-free case, while the other curves are for different intensities where the BS is included. The corresponding dissociation thresholds in the field-free or in-field, the first and the second values of the fractional and the full revival times of the nuclear vibrational wavepacket in the $1s\sigma_g$ level of the H_2^+ are given. These values, corresponding to different intensities of the pump laser pulses, are listed in Table 4.1.

To study experimentally the propagation of the wavepacket on the $1s\sigma_g$ potential of the molecular ion, experimentalists have to choose the pulse length to be (at least) longer than the travel time of the wavepacket reaching the outer barrier of the $1s\sigma_g$ potential (half period time $\simeq 8.5$ fs). In this theoretical work, the pulse length is considered as 20 cycles for 800 nm and 40 cycles for 400 nm (FWHM = 14.43 fs). In this way, it should be tested if the wavelength and the R-dependent ionization yields have an effect on the revival time, as expected before, or not. To do this, the same methodology used in the case of assuming FC transition is followed, but using the TDSE ($\|$) and PPT models, in the next two sections, in the cases of 800 nm and 400 nm.

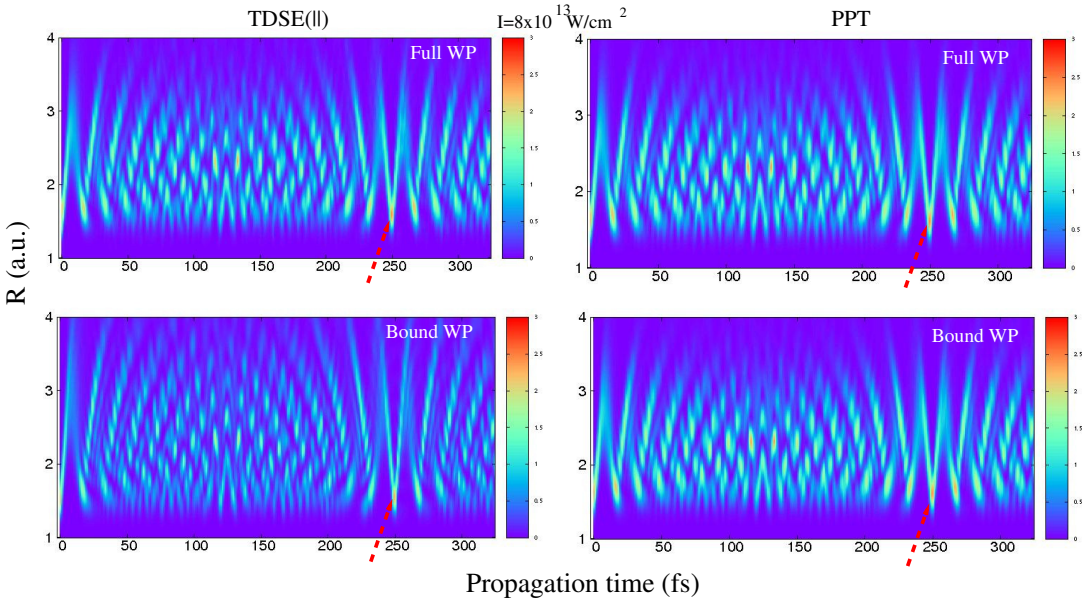

Figure 4.19: The probability density, $|\Psi(\vec{R},t)|^2$, of the vibrational nuclear wavepacket as a function of the internuclear distance R and the evolution time t generated by ionizing a neutral H_2 by a pump pulse with 800 nm, 20 cycles, and 8.0×10^{13} W/cm^2 intensity using TDSE $\|$ (PPT) results, left (right) panels. Dephasing and revival of the wavepacket can be observed in the plots. The colour scale runs from blue (low probability) to red (high probability). The top panels of the figure show the evolution of the full wavepacket, while the bottom panels show the propagation of the bound wavepacket.

4.6.1 The case of 800 nm wavelength

The excitation coefficients, a_ν, obtained within TDSE $\|$, PPT, fc-ADK, and ADK models from Eq. (4.2) are considered to generate the wavepacket. The effect of the number of states, which contribute in creating the wavepacket are also studied (i.e. the *full* and the *bound* wavepackets). Qualitatively, the results obtained with all these approximations do agree with each other and with what was discussed above. Therefore, the colour density plot for the *full* and the *bound* wavepackets constructed within the TDSE and the PPT models for 8.0×10^{13} W/cm^2 are only shown. The probability density of the wavepacket is shown at the expectation value $\langle R\rangle$ versus time for the field-free case or the in-field case corresponding to intensities 5.0×10^{13}, 8.0×10^{13}, and 1.3×10^{14} W/cm^2.

Figure 4.19 shows the *full* (top panels) and the *bound* (bottom panels) wavepacket as a function of both the internuclear distance from $1\,a_0$ to $4\,a_0$ and the evolution time between 0 and 325 fs for both the TDSE (left panels) and the PPT model (right panels). A similar tendency can be seen like in the case of the R-independent ionization yield

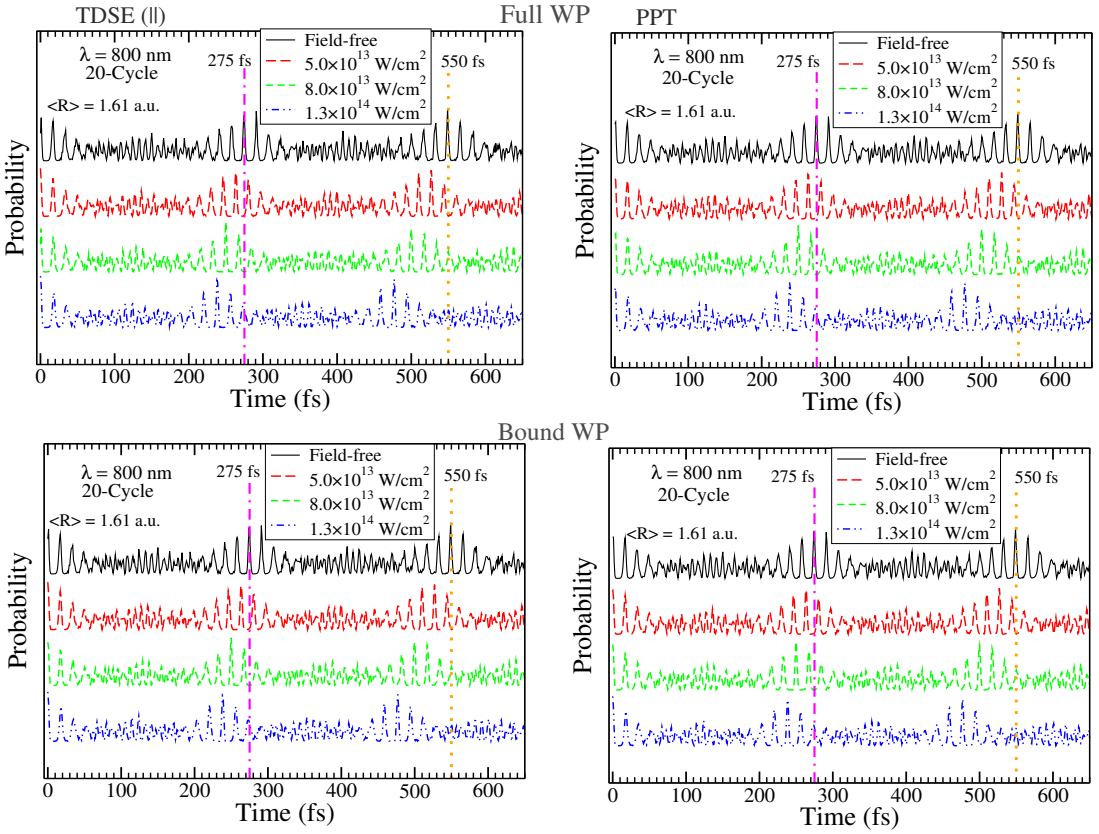

Figure 4.20: Each panel as in Fig. 4.18, but for the *full* and *bound* wavepacket top (bottom) panels within TDSE ∥ (left panels) and the PPT model (right panels) for 800 nm. The expectation values of $\langle R \rangle$ in the case of the TDSE are displayed on each curve with the laser parameters of the pump pulse.

(vertical FC transition), since the phenomena of dephasing and revival of the wavepacket are visible in the *full* and the *bound* wavepacket as well. However, the full revival occurs around $\simeq 250$ fs, while the fractional revival happens around $\simeq 124$ and 128 fs.

The wavepacket evolution between 0 to 650 fs at the expectation value $\langle R \rangle = 1.61\, a_0$ is illustrated in Fig. 4.20 for both the field-free and the in-field cases for different laser intensities. All curves, and subsequently the revival times, are comparable to that obtained within FC assumption (Fig. 4.18), except the field-free case (i.e. if the BS is ignored). However, in the field-free case, the revival time reduces to 250 fs instead of 286 fs. Furthermore, the wavepacket re-appears identical as the initial wavepacket without any shifts after the revival time. This difference may be attributed to the fact that the main contributions to the wavepacket come from the lowest two bound states in the R-dependent models, see also the VSDs in Fig. 4.3. This means that the wavepacket

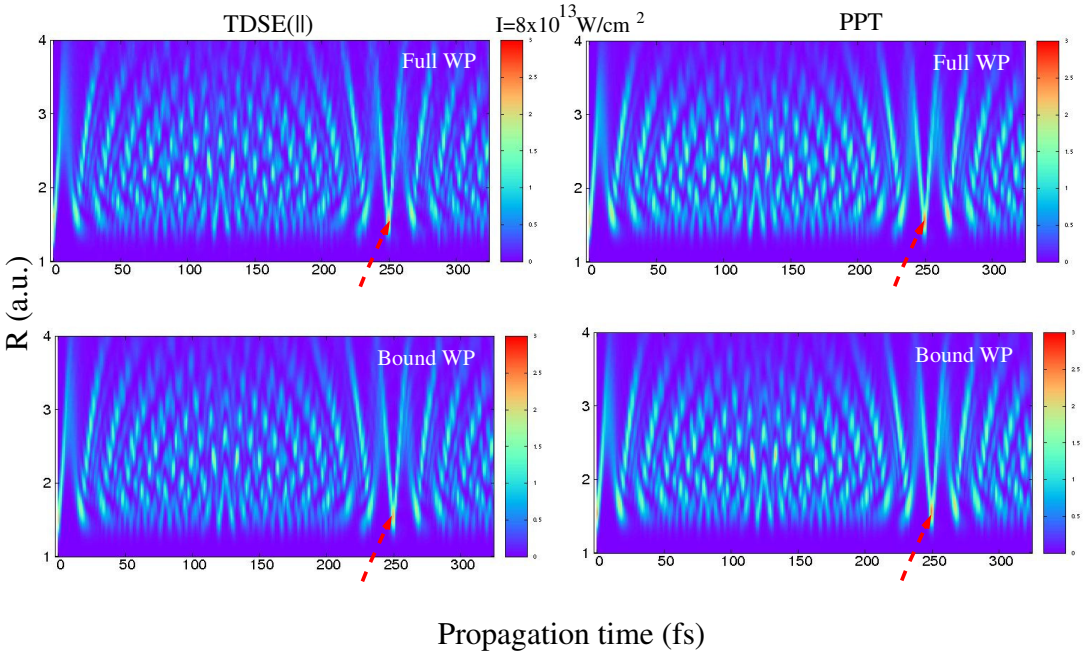

Figure 4.21: As Fig. 4.19, but for 400 nm wavelength and 40 cycles pulse length.

is more localized and the revival time decreases compared to the case of adopting FC approximation. In the FC approach, the first 6 bound-states contribute dominantly to the wavepacket and accordingly there are more different phases than the cases of the R-dependent models. Subsequently, the revival time will be greater than in the former case. Furthermore, the wavepacket in this case is not completely identical to the initial wavepacket after the revival time. The two values of the revival and fractional times in the field-free case according to the FC approximation (labeled by bold characters) and R dependent models are shown in Table 4.1. From this table experimentalists can conclude the importance of considering the R-dependent ionization rates not Franck-Condon principle in their experiments.

4.6.2 The case of 400 nm wavelength

The evolution of the wavepacket created with 400 nm wavelength and 40 cycles pulse length is shown by the same way as the results for 800 nm. There is no essential difference in the theoretical results from the ones found in the 800 nm case or in the field-free case. Some of the results are displayed in Figs. 4.21 and 4.22, as the case of 800 nm. It can be seen that the regions of dephasing and revival appear in the way as in the previous cases. Moreover, the full and the fractional revival times are comparable to

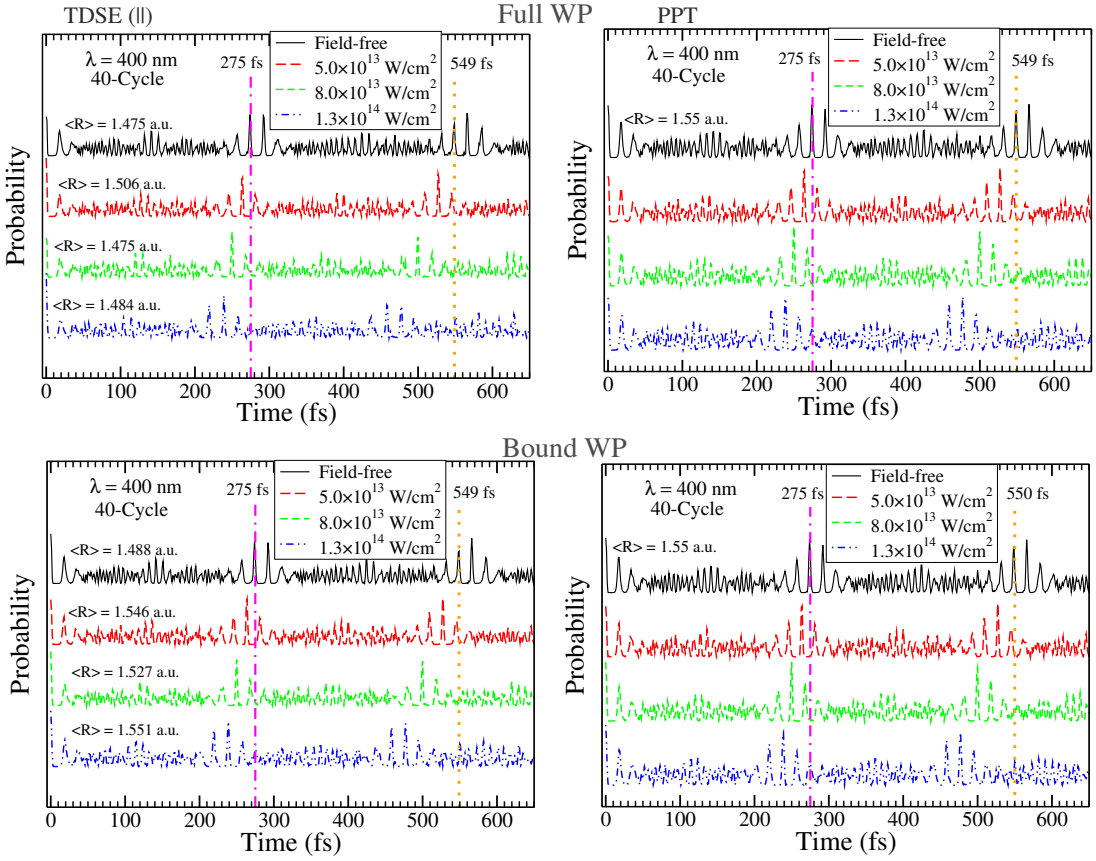

Figure 4.22: As Fig. 4.20, but for wavelength 400 nm, and a pulse length of 40 cycles.

those observed at 800 nm (see Fig. 4.22). For example, the revival time appears at 250 fs for the intensity 8.0×10^{13} W/cm^2 in the TDSE $\|$ and PPT results for both the *full* and the *bound* wavepacket. Clearly, the revival time of the wavepacket depends only on the distortion of the potential surface caused by the laser-field, while it does not depend on the ionization yield nor the laser-wavelength. Furthermore, the revival time of the wavepacket in the case of an assumed FC transitions (283 fs) is slightly greater than that of adopting R-dependent models (275 fs), which comparable to the experimental value. Additionally, there is a small shift between the localized FC wavepacket at the first and the second revival times, which is absent in the case of R-dependent models.

Finally, it can be concluded that both the full and the fractional revival times of the vibrational nuclear wavepacket decrease for increase peak intensity of the external laser field. These values depend on neither wavelength of the laser nor the approximation used in the transition. The reason is that the bond-softening mechanism is only caused by the laser peak intensity, which is the main reason for changing the revival time. This result

agrees with the fact that the wavepacket revival time depends on the phases between the eigenstates content in the superposition, as mentioned previously. Unlike the differences in the revival times, all the evolutions of the wavepacket have a very similar behavior.

4.7 Summary

In this chapter, the extended Ammosov-Delone-Krainov (ADK) model, the Perelomov-Popov-Terent'ev (PPT) model and the frequency corrected ADK (fc-ADK) model are examined by comparing with the numerical solution of the full molecular two-electron time-dependent Schrödinger equation (TDSE) and with few existing experimental data. A theoretical calculations for the vibrational-state distributions (VSDs) and the generated vibrational nuclear wavepacket in the $1s\sigma_g$ state of H_2^+ are presented. The calculations are performed for two wavelengths (800 nm and 400 nm) in a linear polarized field for different intensities and pulse lengths. It is found that the PPT model and even fc-ADK model with inclusion of R-dependent ionization yield, explain the observed vibrational distributions of H_2^+ molecule produced by strong-field ionization of H_2 molecules. The theoretical and experimental distributions of the vibrational states are comparable and both differ from those predicted by Franck-Condon approximation by being shifted towards smaller vibrational quantum numbers, if the concept of an R-dependent ionization rates is used. The comparison showed a satisfactory agreement not only for 800 nm, but also for 400 nm, especially in the parallel orientation case. Furthermore, in the case of the second harmonic of the Ti-sapphire laser (400 nm), more signatures of multi-photon ionization processes are observed. The effects of the pulse length and the laser intensity are investigated. As expected, the TDSE calculations showed that the spectra in a long pulse have more details compared to the short pulse, especially at low intensity. However, at high intensity the molecule is almost ionized and the ionization process is slightly dependent on the pulse length. The effect of the bond-softening phenomenon on the evolution of the vibrational wavepacket and on the revival times are also discussed. The two well-known effects of wavepackets, dephasing and revival, have been shown. Noteworthy, the revival time obtained when adopting the FC principle ($\simeq 283$ fs) is larger than the experimentally observed value ($\simeq 275$ fs) due to the limitations of this model. On the other hand, a good agreement between the predicted revival time of the vibrational wavepacket, if adopting R-dependent ionization models, with the experimental revival time is obtained It is also found a decrease in the revival time with increasing laser intensity. This decrease can be attributed to the bending down of the potential surface caused by the laser-field. The identical form and

occurrence time of the revivals are determined by the anharmonicity of the potential and the distribution of the vibrational state population.

5 Alignment-dependent tunneling ionization of H_2 in linear and circular polarized fields

5.1 Introduction

The lack of spherical symmetry in molecules leads to an alignment-dependent ionization probability. This alignment dependence was found to depend on the laser intensity presented in strong-field phenomena. Tunneling ionization of molecules in strong laser fields is the first step in many interesting strong-field phenomena such as emission of high-energy above-threshold ionization electrons, high-order harmonic generation (HOHG) and non-sequential double ionization (SDI). A basic understanding of these processes can be gained by studying the angular dependence of molecular ionization rates.

In fact, the angular-dependent ionization probability $P(\theta)$ of a linear molecule fixed in space depends on the angle θ between the molecular axis and the direction of the electric field component of the laser. Most of the experimental and theoretical works within strong-field physics have dealt with linearly polarized (LP) laser fields. However, in recent years there has been growing interest in the study of the ionization of atoms and molecules by circular polarized (CP) fields [36, 37, 166, 167]. In a CP field the laser prevents the outermost electron, which is emitted from the molecule by tunneling-ionization, from returning to the molecule, unlike the LP field, where recollision of the freed electron with its parent ion occurs. Furthermore, the polarization plane is two-dimensional, which allows for a more transparent interrogation of the angular orbital structure. Accordingly, a strong CP probe pulse rather than a LP has been recently preferred for probing angular orbital structure through photo-electron angular distributions [168, 169].

The ionization probability $P(\theta)$ of N_2 and O_2 was first determined experimentally by Alnaser *et al.* [169] from SDI processes, where the alignment of the molecule is deter-

mined by Coulomb explosion of the molecular ions or mostly by the character of the molecule's HOMO. In addition, the $P(\theta)$ can be determined by partially ionized aligned molecules with a weaker pump pulse [14, 168] as well as by measuring the angular distribution of electrons removed by a CP laser. The latter measurements were performed by Staudte *et al.* [36], where the angular tunneling ionization probability of H_2 molecules, and the anisotropy were measured. They found that the anisotropy of H_2 varies as a function of laser intensity. They also reported that the measured ratio is larger than that predicted by the MO-ADK model which does not depend on the laser intensity nor on the wavelength. The latter conclusion will be discussed and investigated later in Sec. 5.4. The alignment of the molecular axis in both above methods is determined by Coulomb explosion if the molecular ion is ionized by an intense CP laser. In the experimental measurements, $P(\theta)$ is not determined directly for a fixed angle, but some approximations are usually used in order to determine the alignment-dependent ionization probability [110].

On the other hand, $P(\theta)$ can be theoretically obtained from a direct numerical solution of the TDSE within the SAE model [121] or using TDDFT [170] for multi-electron molecular systems. However, exact *ab initio* calculations are only possible for the simplest molecules like H_2^+ and H_2. Even for the simplest molecule H_2^+, solutions of the TDSE are found by different groups still exhibits relatively large differences [110]. Furthermore, the calculations for molecules like H_2 are not trivial, with a difficult accuracy estimation, and rather time consuming. Besides the numerical methods, the alignment-dependent tunneling-ionization rates and ionization probabilities for molecules can also be calculated with simple models, such as the molecular strong-field approximation (SFA) [15, 26, 108], and the molecular tunneling-ionization theory [28, 171]. However, the main physical pictures of the ionization process are different in these two models. The MO-ADK theory treats the ionization of molecules as a tunneling process which is basically identical to that of atoms. Hence, the ionization is mainly determined by the asymptotic behavior of the bound state wavefunction at large distance. However, in the SFA theory the ionization rate is calculated by the S-matrix theory which treats the external laser field in a nonperturbative way. The MO-ADK model has been widely used because of its further predicts simple alignment dependence of the ionization rates such as H_2, N_2, and O_2[1]. Throughout this chapter the molecular tunneling models are used for calculating the ionization probability.

In this chapter, first an introduction to molecules in a CP field is given. Then, the dependence of the ionization probability on the angular alignment of H_2 in a LP and in

[1]This point will be discussed in chapter 6.

a CP field within the MO-ADK model is shown. The dependence of the ionization yield on the laser peak intensity within the MO-PPT, MO-ADK models and the numerical solution of the TDSE is presented. Furthermore, the variation of the ratio $\Re$ ($=P_{\parallel}/P_{\perp}$) of the ionization probabilities with the laser peak intensity and pulse duration is discussed within the tunneling MO-ADK model in linear and in circular polarized fields. Here, $P_{\parallel}$ and $P_{\perp}$ stands for the ionization probability when the laser field is parallel and perpendicular to the molecular axis, respectively. The effect of the focal-volume for the laser pulse and the barrier-suppression correction on the ratio $\Re$ are also demonstrated.

5.2 Molecules in a circular polarized field

Tunneling of the electron from atoms and molecules in a low-frequency laser field is often described as an adiabatic process. This means that the dynamical distortion of the tunneling barrier does not affect the electron dynamics during tunneling. In a CP field the adiabatic picture assumes that the electron escapes along the instantaneous direction of the electric field, ignoring its rotation during the tunneling event. This assumption may be a good approximation in the case of atoms with initial states $m = 0$, but it does not seem to be appropriate for molecules and even for atoms with initial states $m \neq 0$ [172]. The reason for this possible failure is attributed to the propagation geometry of the CP field, which discussed in the following.

Two issues have to be considered in a CP field. First, although the absolute value of the electric field intensity is time independent, the projection of the electron angular momentum onto the direction of the light wave propagation is conserved rather than the one onto the electric field direction which varies with time. Therefore, it is not quite correct to consider the probability of tunneling in the presence of a circularly polarized field to be the same as the one of a static field [173]. The idea is that the electric field of a circular polarized laser field is defined by a viewer positioned around the molecular axis looking in the direction, as depicted in Fig. 5.1. The top sketch illustrates the right-handed[2] clockwise circularly polarized light. The helix composes a right-handed screw, since it is traced out by the electric field vector of the laser. It indicates that along the direction of the propagation, the electric field has a constant magnitude, while its direction steadily changes in a rotary type manner. This is a consequence of the fact that the vector of the electric field is always perpendicular to the direction of the

[2] Right hand rule is a physics principle applied to electric current passing through a straight wire resulting in a magnetic field. The thumb points in the direction of the conventional current (from positive to negative), and the fingers in the direction of the magnetic field.

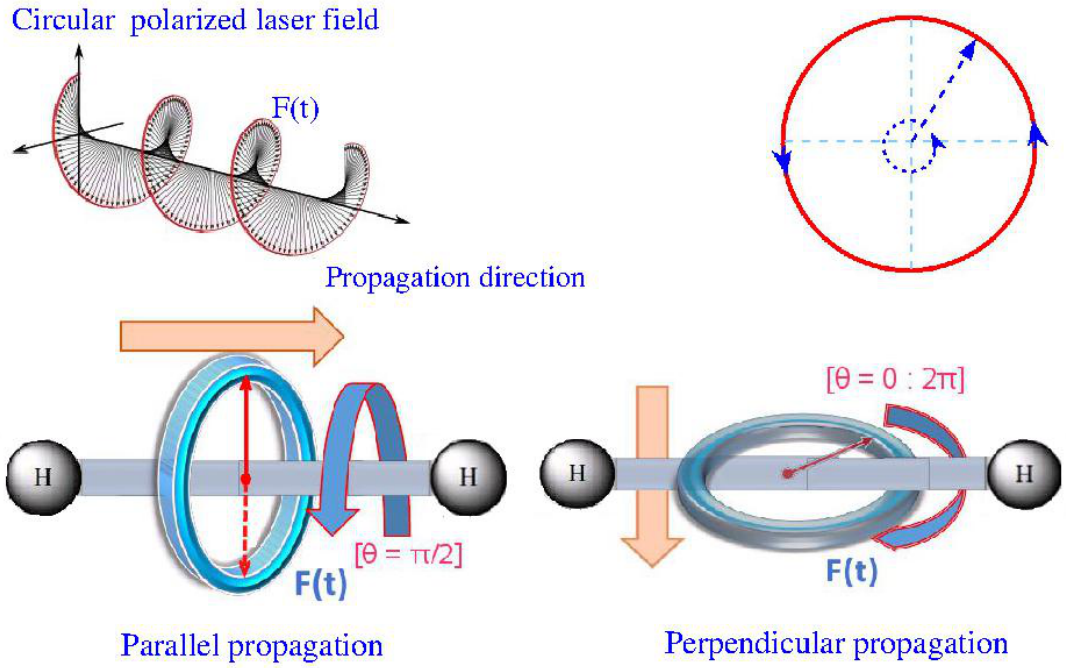

Figure 5.1: The upper part shows the right-handed, clockwise circularly polarized electromagnetic wave displayed without the use of components. The lower part shows an H_2 molecule in a circularly polarized field, if the laser pulse propagates parallel (left) or perpendicular (right) to the molecular axis.

laser pulse propagation. For example, if the direction of the laser pulse propagation is parallel to the molecular axis (right side in the bottom sketch), the electric field will be perpendicular to the direction of the laser propagation as well as to the molecular axis all the time. In contrast, if the propagation is perpendicular to the molecular axis (left side in the bottom sketch), the electric field will be always perpendicular to the laser propagation, while its direction relative to the molecular axis depends on time. In this case, the electric field is covering all the directions around the molecular axis $\{0 \rightarrow 2\pi\}$. Thus, the average value of the ionization rate over all directions should be taken into account. Accordingly, the tunneling ionization rate in a circular polarized field should be reformulated as

$$W_{\rm cir}(F^c) = \begin{cases} W_{\rm st}(F^c, \theta = \pi/2) & \text{for parallel propagation}\,, \\ \frac{1}{2\pi}\int_0^{2\pi} W_{\rm st}(F^c, \theta)\, d\theta\,, & \text{for perpendicular propagation}\,, \end{cases} \tag{5.1}$$

where F^c is the electric field of a CP laser field. Accordingly, it is expected that the ratio of parallel to perpendicular ionization probabilities in a CP field will be smaller than that

in the case of a LP field, as will be shown in Sec. 5.4. Although the importance of this issue, especially when the propagation of the CP field is considered to be perpendicular to the molecular axis, it seems to have been completely ignored by the researchers.

The *second issue*, which has to be considered in a CP field is that for a given intensity I the electric field-strength F^c is smaller by a square root of 2 than the LP electric field F. This is due to the fact that the value of the vector potential for a LP field is the square root of two times bigger than that of the CP one. This point is usually considered by researchers when they compared the ionization results in a LP field with those obtained in a CP field.

5.3 Angular and field-dependent ionization probability

The ionization rate for a molecule aligned at an angle θ relative to the laser polarization axis can be analytically calculated by the MO-ADK model, as was described in chapter 2. In the MO-ADK model, the ionization rate depends on the electric field of the laser pulse and on the ionization potential of the molecule. Furthermore, it depends on some structural parameters defined by the electronic density of the HOMO in the asymptotic region (see Sec. 2.5.1). The total ionization probability $P(I,\theta)$ in a laser field for an alignment angle θ and the peak intensity is given by

$$P(I,\theta) = 1 - \exp\left\{-\int_{pulse} W_\xi[\mathbf{F}(t),\theta]dt\right\}, \tag{5.2}$$

where $\mathbf{F} = (\frac{8\pi}{c}I)^{1/2}$ is the electric-field strength, and the W_ξ is the computed ionization rate for molecules in the case of using a static field (ξ= st), a linear polarized field (ξ= lin), or a circular polarized field (ξ= cir). The ionization rates W_ξ for all three cases are calculated from Eqs. (2.50), (2.51), and (5.1), respectively. Because of the strong dependence of the tunneling-ionization rate on the ionization potential, the ionization of the HOMO is usually calculated. However, it was theoretically claimed [121, 174, 175] and experimentally confirmed [133, 175] that in some larger molecules the ionization of the HOMO-1 (even HOMO-5, depending on the geometry of the molecule and its orbital energy spacings) can show a significant contribution. In this thesis, the discussion will be restricted to ionization from the HOMO and the rates are multiplied by the number of active electrons, corresponding to the number of the identical electrons occupying the HOMO (HOMO occupancy, 2 electron for the molecules under study in this thesis).

For small ionization rates, the approximation

$$\tilde{P}(I,\theta) = \int_{pulse} W_{\xi}[\mathbf{F}(t),\theta]\, dt\,, \tag{5.3}$$

can be safely used to calculate the ionization probability, where $\tilde{P}(I,\theta)$ is an approximation to $P(I,\theta)$. This approximation becomes equivalent to Eq. (5.2) for small values of the ionization rate, but differs significantly at large values. The difference is due to the saturation effect which is completely ignored in Eq. (5.3), as will be discussed later.

5.3.1 Angular-dependent ionization probability

The ionization probability depends on the orientation of the molecular axis relative to the direction of the electric field (so called angle-dependent ionization probability). Figure 5.2 displays the normalized angle-dependent ionization probabilities of H_2 at 2.3×10^{14} W/cm^2 in CP (left panel) and at 1.15×10^{14} W/cm^2 in LP fields (right panel). To simplify the comparison, all the probabilities are normalized to 1.0 at the maximum. However, for a given laser intensity, as mentioned before, the electric field of the CP field is smaller than that of a LP field by a factor of $\sqrt{2}$. The MO-ADK ionization probabilities are calculated for a 40 fs pulse (FWHM). For comparison purposes, four versions of asymptotic coefficients C_{lm} are used for the MO-ADK model. The original ones, which was calculated by Tong *et al.* [28] using the multiple-scattering method (MSM), the values given by both Awasthi *et al.* [109] and Chu [39] that are based on the Hartree-Fock method (HF), and the coefficients presented by Zhau *et al.* [110] using density-functional-theory (DFT) in their computations of C_{lm} values. Those asymptotic coefficients are tabulated in Table 5.1 for the HOMO of H_2 (in the present case of linear molecules, σ orbitals, the values for $m = 0$ are only required). Noteworthy, using the C_{lm} coefficients presented in [108], listed also below, gave results agreeing very well with those obtained when using the C_{lm} values that are given in [109] (since, the HF method was used for extracting C_{lm} values). Therefore, the results obtained with the former coefficients are not shown in Fig. 5.2.

The MO-ADK predictions are compared to the normalized experimental ionization probabilities taken from Ref. [110] in which they have been extracted from the experimental data of Staudte *et al.* [36]. These experimental data were measured by applying a CP laser field with peak intensity 2.3×10^{14} W/cm^2 and 40 fs (FWHM). It should be reminded that in the MO-ADK rate, the experimental vertical ionization energy is preferred to use in the tunneling ionization model, since the tunneling-ionization rate

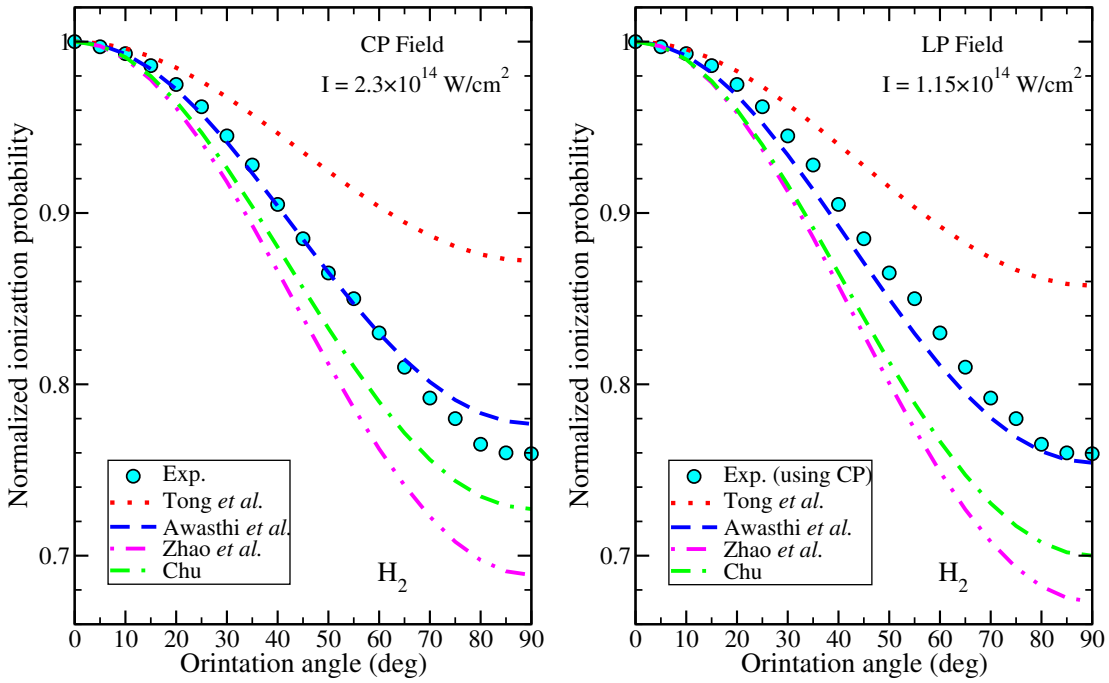

Figure 5.2: Normalized alignment dependence of the ionization probability of H_2 in circularly (left) and linearly (right) polarized fields. The prediction of the MO-ADK model for a laser pulse (800 nm, 40 fs FWHM) using different sets of C_{lm} values, given by Tong *et al.* [28] (blue dotted), Awasthi *et al.* [109] (red dashed), Zhau *et al.* [110] (magenta dot-dot-dash) as well as Chu [39] (green dash-dash-dot), is compared to the experimental data [36] (blue circles, 40 fs, 800 nm, circular polarization). The intensities of the laser pulses are given in the graph.

depends exponentially on the ionization potential. The ionization potential used here for H_2 is 15.47 eV (= 0.5685 a.u.) at the equilibrium distance $R = 1.4\,a_0$. Although the shapes of the curves agree qualitatively well, using the C_{lm} coefficients extracted by Tong *et al.* [28] (using MSM), significantly underestimate the ionization probability for both circular and linear polarizations. However, the results obtained with the C_{lm} coefficients extracted within either the HF or the DFT approaches agree much better with the experimental data than that extracted within MSM. Depending on the laser's polarization direction relative to the molecular axis, the ratio between the maximum and the minimum values of the ionization probability (i.e. anisotropy) as a function of the peak intensity will be shown later in more details.

Table 5.1: Asymptotic coefficients C_{lm} for the spherical harmonic l and m for H_2 taken from Refs. [28, 39, 108–110]. They are extracted within different electronic structure models; density-functional theory (DFT), Hartree-Fock (HF), and multiple-scattering (MSM) approaches.

Method	C_{00}	C_{20}	C_{40}	Ref.
Multiple-Scattering Method	2.510	0.060	0.0000	[28]
Hartree-Fock	2.440	0.140	0.0000	[108]
	2.435	0.107	0.0010	[109]
	2.443	0.136	0.0024	[39]
Density-Functional Theory	1.780	0.110	0.0000	[110]

5.3.2 Field-dependent ionization probability

In the previous chapter, it is found that the ionization probabilities for H_2 obtained from the PPT model agree quite well with those obtained from the TDSE calculations in a wider range, in both MPI and TI regimes, while the ADK model fails to give the correct ionization probability in the MPI regime and its results are reliable only in the TI regime. In this section, the validity of the molecular tunneling models, MO-ADK and MO-PPT models, within a wider range of laser intensities will also be carefully examined, by comparing the ionization probabilities with those of the accurate CI-TDSE calculations. Noteworthy, Awasthi *et al.* [109] showed that how MO-ADK fails quantitatively and even qualitatively in the description of the overall intensity-dependence of the ionization probability for H_2 with the popular Ti:Sapphire laser wavelength of 800 nm. This failure was also found earlier in the ADK model by Awasthi and Saenz [154]. The failure of the ADK model is solved in chapter 4 by adopting the PPT model. The PPT model can be able to quantitatively correctly reproducing the TDSE calculation of the ionization probability for H_2, not only with the long laser wavelength (800 nm), but also for the shorter one (400 nm). In this section, the molecular ionization behavior in laser fields outside the range of validity of MO-ADK (i.e. $\gamma \gg 1$), can be modeled by the MO-PPT model (see Sec. 2.5.2), as the following.

Figure 5.3 displays the ionization-probability as a function of the laser-peak intensity with 800 nm wavelength and 12 cycles duration. The ionization probabilities obtained within MO-ADK (dotted lines) and MO-PPT (dashed lines) are compared with those obtained from the full two-electrons TDSE calculations[3] (circles). The molecule lies parallel to the laser polarization direction ($\theta = 0$), and the values of the C_{lm} coefficients taken from Refs. [109, 110] are used.

[3]The numerical results are taken from Ref. [109].

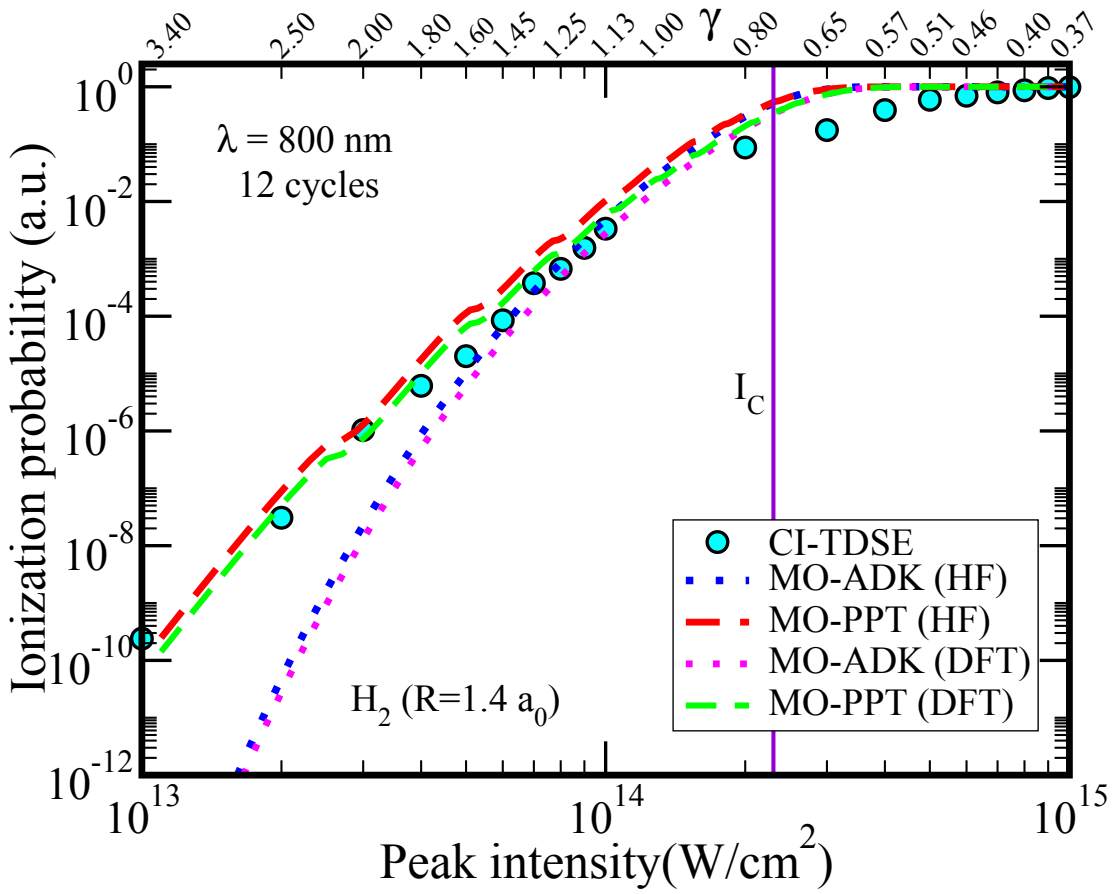

Figure 5.3: Ionization probability of H_2 (12-cycle, 800 nm, parallel alignment) obtained from the MO-ADK (HF) (blue dotted), MO-ADK(DFT) (magenta dotted), MO-PPT(HF) (red dashes), and MO-PPT(DFT) (green dashes) models as well as the exact values obtained from solving the full two-electron TDSE using a configuration interaction (CI) CI-TDSE method [119]. The molecular parameters C_{lm} are taken from Ref. [109] (HF) and Ref. [110] (DFT). The corresponding Keldysh parameter values are given on the upper scale. The vertical line corresponds to the critical value of the intensity threshold I_C for over the-barrier ionization (OTBI).

As explained in chapter 2, the strong-field ionization can be qualitatively classified by the Keldysh parameter. The ionization probability varies according to the competition between MPI and TI. In order to easily distinguish between the MPI ($\gamma \gg 1$) and TI ($\gamma \ll 1$) regions, the corresponding values of Keldysh parameter are also labeled on the upper scale of Fig. 5.3. In the multi-photon region ($\gamma > 1$), the MO-ADK model using C_{lm} [109, 110] underestimates the full TDSE ionization probability. This agrees with the previous results of Awasthi *et al.* [109], which mentioned above. Furthermore, the slope of the MO-ADK curve at low intensities is too large and crosses, accidentally,

the TDSE curve at a peak intensity of about 9×10^{13} W/cm^2 corresponding to γ value close to 1. In other words, the MO-ADK prediction of the ionization probability is too small at low intensities and reaches saturation, i.e. complete single ionization, at higher intensities, but earlier than the TDSE calculations. This failure of the tunneling MO-ADK model is not surprising in the MPI region. However, the MO-PPT model matches the full TDSE calculations well and cures the failure in the original tunneling MO-ADK model. Therefore, one can say that MO-PPT model is capable to correctly predict the dependence of the ionization probability for almost all laser-intensities (i.e. in both of MPI and TI regimes), as illustrated in Fig. 5.3. The only deviations are near the critical value of the intensity threshold I_C ($= 2.3\times10^{14}$ W/cm^2, see Eq. (2.14)) for OTBI region. This deviation is totally expected as a number of theories breaks down in this region. In the TI region, $\gamma < 1$, the results of the MO-ADK model agree partially with those obtained by the MO-PPT model, since MO-PPT transforms to MO-ADK in the adiabatic limit, $\gamma \ll 1$. For intensities above I_C one reaches the classical OTBI regime, i.e. the electron can escape over the field-suppressed potential barrier. In OTBI regime MO-ADK and MO-PPT models are known to overestimate the ionization rates [109]. However, at the critical intensity I_C, γ has dropped to a value~ 0.72 (Fig. 5.3). Accidentally quantitative agreement between the MO-ADK prediction and the full TDSE calculations is found for γ close to or even slightly larger than one. For intensities MO-ADK predicts the intensity dependence of the ionization probability in a quantitatively correct way between 8×10^{13} and 2×10^{14} W/cm^2. Unexpectedly, for γ less than one, where MO-ADK and MO-PPT should be more appropriate, the agreement with the TDSE results is, however, not good. The reason is due to OTBI or so-called barrier-suppression ionization (BSI), see Sec. 2.2.4 and Sec. 5.5. Noteworthy, the value of the saturation intensity depends slightly on the C_{lm} values used in the MO-ADK and MO-PPT models, since for HF ($\simeq 4.0 \times 10^{14}$ W/cm^2) is lower than for the DFT parameters ($\simeq 4.7 \times 10^{14}$ W/cm^2). Of course, there is an agreement between MO-ADK and MO-PPT with TDSE at higher intensities than I_C. However, in this case the ionization probability approaches one and thus it is a trivial case.

To summarize, the MO-PPT model succeeds to predict qualitatively and even quantitatively the overall intensity dependence of the ionization probability for H_2 up to the BSI regime, unlike the tunneling MO-ADK model which it is not able at low intensities ($\gamma \gg 1$) to predict the correct field-dependence of the ionization probability. In the next section, the intensity dependence of the anisotropy for the ionization probabilities $P_\parallel/P_\perp$ of H_2 within the MO-ADK model [28] is investigated and compared with the experimental data [36, 37]. Since, the MO-ADK and MO-PPT predictions are comparable in the range of the intensities that are used in those experiments.

5.4 Intensity-dependent anisotropy $P_{\parallel}/P_{\perp}$ for H_2

The ratio of the ionization probability for H_2 molecule aligned parallel or perpendicular relative to the polarization axis was measured experimentally [36, 37] and considered also theoretically [39, 40]. Staudte *et al.* [36] carried out experiments on H_2 in 800 nm CP laser pulses of about 40 fs duration for different intensities: 2.0×10^{14}, 2.32×10^{14}, 4.0×10^{14}, and 4.5×10^{14} W/cm^2. They found that the value of the experimental anisotropy decreases from 1.3 to 1.18 with increasing intensity. Furthermore, they suggested a simple theoretical model based on the length-gauge molecular strong-field approximation (MO-SFA) to explain the decrease in the anisotropy. Although this model significantly overestimates the experimental anisotropy values, it was reproducing the decrease with increasing peak intensity. A similar measurement for longer wavelength (1850 nm) and 50 fs pulse duration was carried out by Magrakvelidze *et al.* [37] at one intensity (2.0×10^{14} W/cm^2). This measurement showed that the ionization for parallel alignment was 1.15 times higher than that for perpendicular alignment. Interestingly, this ratio has been reported to be 3.0 in another experiment [38] using LP field with laser parameters 740 nm, 5 fs, and 1.2×10^{14} W/cm^2, while the theoretical model in the same paper gives a ratio of 2.1. Zhao *et al.* [110] commented on this difference by pointing out that the ratio is taken as the maximum to the minimum ionization probabilities and this is sensitive to the angular average. Then, the comparisons of the rates over the whole angular range would be preferable. As is argued below, the difference between the results of the two experiments [37, 38] is most likely due to using different polarization pulses, LP and CP field, as well as different pulse length, as will be seen later.

In a recent work by Jin *et al.* [40], the ionization probability $P(\theta, I)$ for the H_2 molecule is presented by solving the TDSE in a linear polarized laser field adopting a model potential. They calculated the ratio $\Re$ and compared their results with the experimental data [36]. They have accidentally found a good agreement with the experimental data for a long pulse ($\sim$40 fs) and 800 nm, after dividing the experimental peak intensity by a factor 2, since a CP field was used in the experiment. They compared also the experimental and the numerical values of the ratio $\Re$ with the tunneling MO-ADK prediction [28] and claimed a defect of the MO-ADK model. They found that the ratio of the ionization probability for parallel to perpendicular alignment predicted by the MO-ADK model is a constant ($\approx$ 1.17) and it is independent on the laser parameters. Noteworthy, this value gradually approaches the experimental values only for high intensities. Interestingly, although this result of the tunneling MO-ADK model is not correct, as will be shown below, it has been found and reported by other researchers, e.g. for H_2 [36–39]

and for H_2^+ [41]. The possibility of the previous -*wrong*- prediction for the MO-ADK model can be come from the direct division of the ionization rates, Eq. (2.50), for parallel to perpendicular alignment. In this case the ratio gives a constant value, which independent on the laser parameters. This result can also be obtained if the ionization probability is calculated from Eq. (5.3), as an approximation, which is not acceptable at high intensities, the ratio $\Re$ will also be a constant, since the saturation effect is ignored.

The following sections invalidate the previous prediction for tunneling MO-ADK, in the range of the laser intensities used in the experiments, and confirm that the MO-ADK tunneling model is able to correctly predict the intensity-dependent anisotropy of the ionization yields. Moreover, the ratio between the ionization yields for parallel to perpendicular alignment depends on the laser parameters at high intensity in both linear and circular polarized fields, as will be shown later. The ratio $\Re$ for LP and CP fields is calculated within MO-ADK and compared with the experimental data [36, 37]. Of course, a comparison of the absolute value of the ion yields between LP and CP laser pulses is not quite correct, so the comparison is restricted on the qualitative shape (general behavior) of the anisotropy.

5.4.1 In linear polarized fields (LP)

As mentioned before, the approximation given in Eq. (5.3) is not quite correct to represent the ionization probability or the ratio $\Re$ at high ionization rates (i.e. high intensities). Figure 5.4 shows the approximate ionization probabilities $\tilde{P}_{\|}$ and $\tilde{P}_{\perp}$ obtained from Eq. (5.3) as well as the ionization probabilities $P_{\|}$ and $P_{\perp}$ for H_2 obtained by Eq. (5.2) as a function of the laser intensity for two different pulse lengths (20 fs and 40 fs). The direction of the electric field is aligned along or perpendicular to molecular axis. The C_{lm} coefficients [110] (reported in Table 5.1) are used in the MO-ADK model. It is obvious that $\tilde{P}_{\|}$ and $\tilde{P}_{\perp}$ increase with increasing intensity and pulse duration. The probabilities $P_{\|}$ ($P_{\perp}$) are in agreement with $\tilde{P}_{\|}$ ($\tilde{P}_{\perp}$) at low intensities as it is expected, since the ionization probability is still small. For increasing intensity, $P_{\|}$ ($P_{\perp}$) approaches unity due to the saturation effect which occurs and becomes essential at high intensities. This means that the ratio $\Re$ of the ionization probabilities between parallel and perpendicular alignments will not be a constant at all intensities, but it should decrease with increasing intensity. It is approaching one at high intensities.

Figure 5.5 displays the ratio $\Re$ of H_2, exposed to an 800 nm laser pulse, predicted by MO-ADK as a function of laser peak intensity for different pulse lengths. The left panel shows the ratio $\Re$ before including the focal-volume effect (FVE) of the laser pulse, while

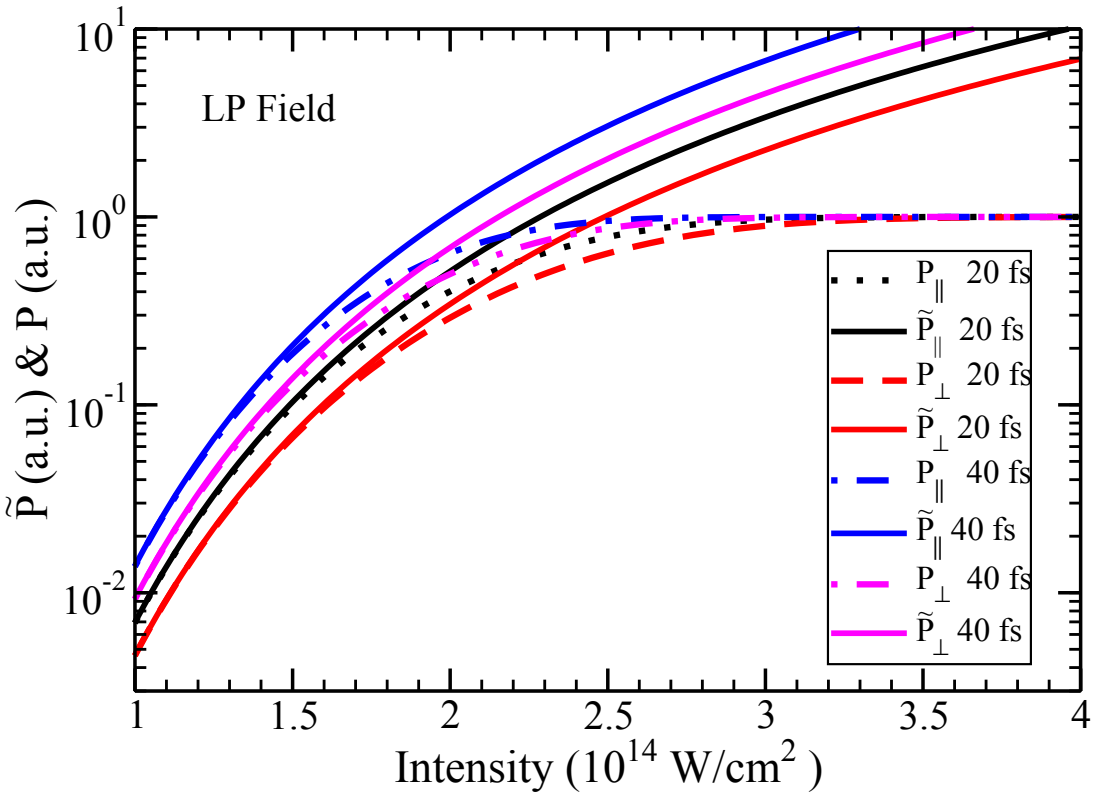

Figure 5.4: The MO-ADK ionization probability $\tilde{P}_{\|}$ ($\tilde{P}_{\perp}$) computed from Eq. (5.3) (solid lines) and $P_{\|}$ ($P_{\perp}$) computed from Eq. (5.2) (dashed lines) of H_2 versus laser intensity for 800 nm and two different pulse durations (20 and 40 fs FWHM), if the H_2 molecule is aligned along or perpendicular to the electric laser-field direction (see the text for details). The C_{lm} coefficients in [110] are used in the MO-ADK model.

the right panel after including the FVE. The FVE is taken into account, for a specific alignment angle θ, according to the relation [176]

$$P^{FVE}(I_0) \propto \int_0^{I_0} P(I) \left[\frac{I_0}{3\,I^2} \sqrt{\frac{I_0}{I} - 1} \left(\frac{2\,I}{I_0} + 1 \right) \right] dI\,, \tag{5.4}$$

where I_0 is the laser peak intensity. For a comparison with the experimental data, the FVE should be taken into account, especially in the saturation region. More details about the FVE are given in Appendix B. The ratio $\Re$ predicted by MO-ADK in a LP field is compared to the experimentally measured ratio of the ionization probabilities for a CP field with (800 nm, 40 fs) [36] and (1850 nm, 50 fs) [37]. Therfore, the laser intensity of the experimental data is scaled down by factor 2. Dividing the ratio obtained within the MO-ADK model by a factor 1.16 gave a good agreement with the experimental data,

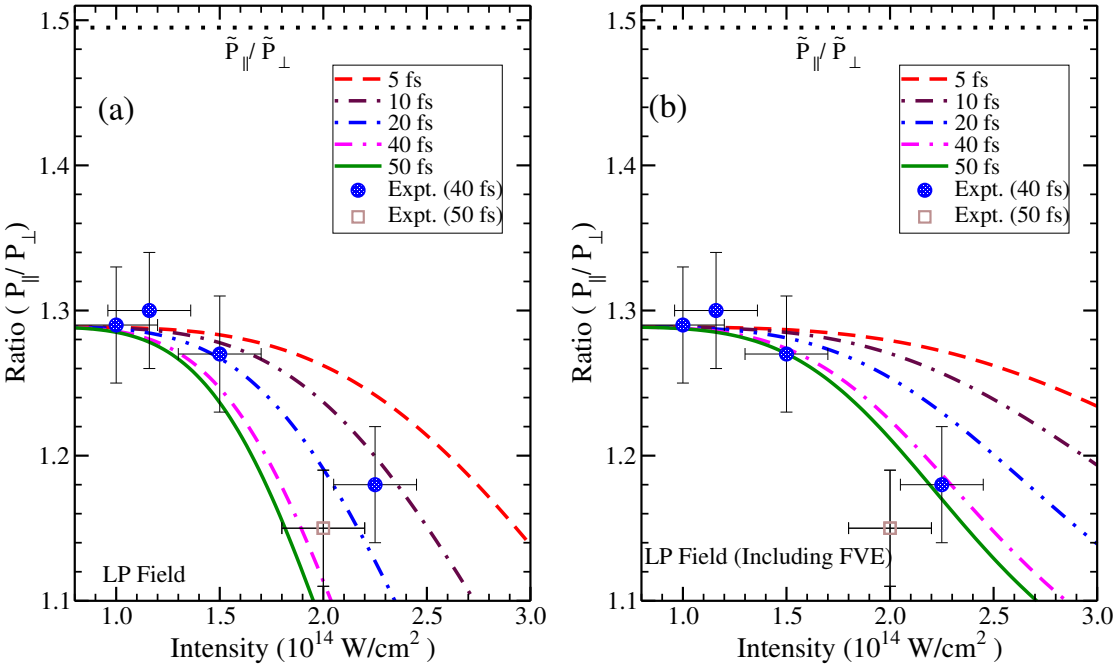

Figure 5.5: Comparison of the ratio of the parallel to perpendicular ionization yields ($P_\parallel/P_\perp$) for H_2 obtained experimentally (800 nm, 40 fs, solid blue circles [36] or 1850 nm, 50 fs, hollow square [37]) and the prediction of the MO-ADK model - after scaling down by a factor 1.16 - with different pulse lengths (5 to 50 fs, 800 nm, linear polarization).
(a) Without focal-volume effect (FVE). **(b)** Including focal-volume effect (FVE). The C_{lm} values are taken from Ref. [110]. The laser intensity of the experimental data was reduced by a factor 2 to compare the data with the linear polarized predictions (see text). The horizontal dotted lines show the MO-ADK prediction for the ratio $\tilde{P}_\parallel/\tilde{P}_\perp$ without scaling.

since the ratio decreases for increasing the laser intensity. It was found that the ratio does slightly depend on the laser pulse length at low intensities, while at higher intensities it decreases as the pulse duration increases. This can be understood from the fact that the ionization probability at low intensity is very small and proportional to the pulse duration. However, at high intensity and for long pulses the molecule becomes almost completely ionized at any alignment angle and the ratio goes down to close to unity. Noteworthy, these results are also in agreement with the numerical TDSE calculations that are presented by Jin *et al.*[4] [40]. The horizontal dotted line in Fig. 5.5 indicates the value of the ratio $\tilde{P}_\parallel/\tilde{P}_\perp$ ($\simeq$1.49) predicted by MO-ADK without scaling. This constant value of $\tilde{P}_\parallel/\tilde{P}_\perp$ agrees with the previous inaccurate predictions, as in [36, 40], which

[4]In Ref. [40], the alignment-dependent ionization of H_2 was studied by extending the two-dimensional TDSE [177] to a three-dimensional one. They studied the system in prolate spheroidal coordinates, which can properly describe a two-center problem. The TDSE is solved within a model potential.

Table 5.2: Values of the ratio $\tilde{P}_{\parallel}/\tilde{P}_{\perp}$ between parallel and perpendicular alignments of H_2 predicted by MO-ADK for linear as well as circular polarized fields using different structure parameters C_{lm}. The methods used for extracting the values of C_{lm} and the references are specified in the Table.

Method	$(\tilde{P}_{\parallel}/\tilde{P}_{\perp})^{Lin}$	$(\tilde{P}_{\parallel}/\tilde{P}_{\perp})^{Cir}$[a]	Reference
Multiple-Scattering	1.17	1.08	[28]
Hartree-Fock (HF)	1.45	1.22	[108]
	1.34	1.16	[109]
	1.44	1.21	[39]
Density Function(DFT)	1.49	1.24	[110]

[a] The experimental value $\simeq 1.29$ [36].

are stated that MO-ADK predicts, *erroneously*, the intensity-independent anisotropy of the ionization probabilities, as mentioned earlier. The value of the ratio $\tilde{P}_{\parallel}/\tilde{P}_{\perp}$ depends on the polarization of the laser (i.e. LP or CP) and on the C_{lm} molecular parameters. Table 5.2 shows the values of the ratio $\tilde{P}_{\parallel}/\tilde{P}_{\perp}$ computed from the approximate formula in LP and CP fields using different sets of C_{lm} values given in Table 5.1. Obviously, the value of $\tilde{P}_{\parallel}/\tilde{P}_{\perp}$, which in fact is equal to the ratio between the ionization rates in parallel and perpendicular orientations, is independent on the laser intensity and the pulse duration. Furthermore, the value of $\tilde{P}_{\parallel}/\tilde{P}_{\perp}$ in LP fields is greater than that in the CP fields (see Table 5.2).

Figure 5.6 is thus comparable to Fig. 5.5, but using two different sets of the C_{lm} coefficients that are given in [28] (top panels) and in [109] (bottom panels). The ratios $\Re$ predicted by MO-ADK are scaled up by a factor 1.104 in the top panels and scaled down by a factor 1.035 in the bottom panels. The results in this figure agree qualitatively with those in Fig. 5.5, but are quantitatively different. In other words, the ratio $\Re$ decreases as the laser intensity increases. Interestingly, the constant value of the ratio $\tilde{P}_{\parallel}/\tilde{P}_{\perp} = 1.17$ using the C_{lm} values given by Tong *et al.* [28] is equivalent to what has been reported in [36, 37, 39, 40]. As said before, this value is equivalent to the ratio between the ionization *rates*. According to Figs. 5.5 and 5.6, one set of the C_{lm} parameters from those listed in Table 5.1, specifically that was given by Zhao *et al.* [110], will be used in the MO-ADK model, as shown below.

Vanne and Saenz [178] have also compared the full *ab initio* TDSE results of the ratio $P_{\parallel}/P_{\perp}$, computed with 10-cycle $\cos^2$-shaped linear-polarized laser pulse, with the experimental data [36]. They found that the ratio is a non-monotonic function of the laser peak intensity, even if focal-volume averaging is performed. They showed also that the

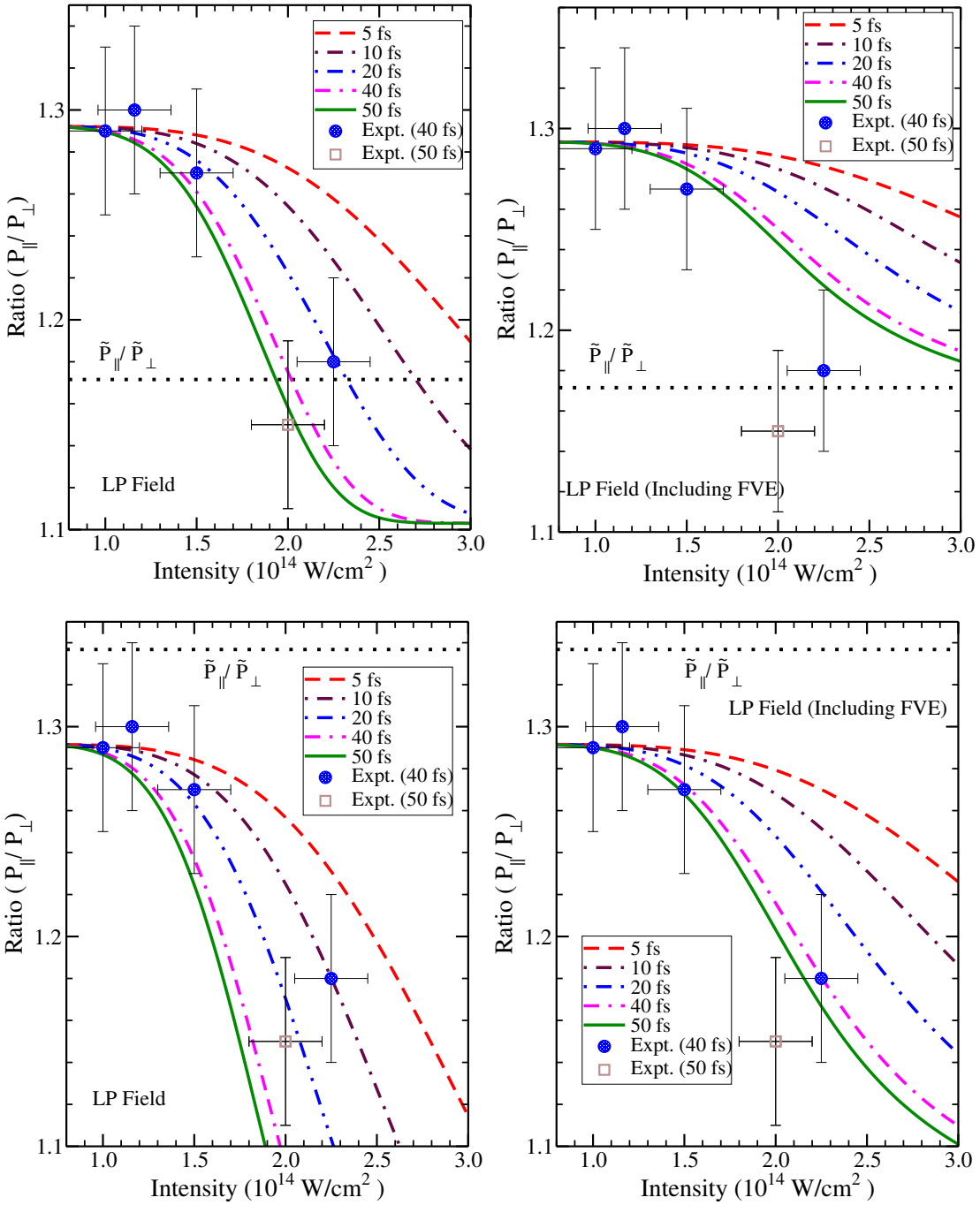

Figure 5.6: As Fig. 5.5, but using different sets of the C_{lm} coefficients, which are given by Tong *et al.* [28] (top panels) and Awasthi *et al.* [109] (bottom panels). The MO-ADK predictions are scaled up by a factor 1.104 (top panels) and down by a factor 1.035 (bottom panels).

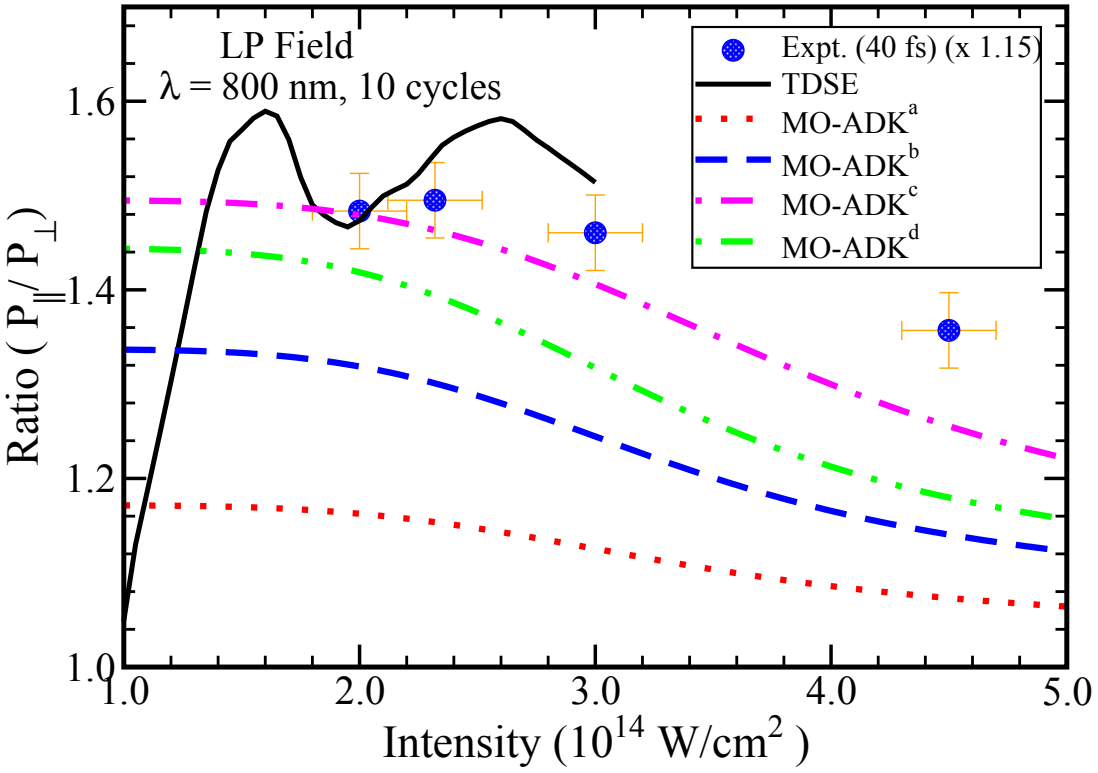

Figure 5.7: The MO-ADK ratio $P_{\|}/P_{\perp}$ for H_2 molecules (at internuclear distance $R = 1.4\,a_0$) in an 800 nm linear polarized, 10-cycle $\cos^2$-shaped laser pulse using different sets of C_{lm} values published in Ref. [28] (MO-ADK^a, dotted red), [109] (MO-ADK^b, dashed blue), [110] (MO-ADK^c, dotted-dashed magenta), and [39] (MO-ADK^d, double dotted-dashed green), including the focal-volume averaging. These results are compared with the TDSE results [178] (solid black line) including focal-volume averaging. The experimental data [36], however for circular polarization, are also shown after scaling them down by a factor 1.16, (blue circles, 800 nm, 40 fs).

ratio is in reasonable agreement with the first three data points of the experiment after scaling the TDSE results down by a factor 1.18. Interestingly, although they studied the ratio in a LP field, they have considered the intensity as in the experiment, where a CP field has been applied. This unexpected agreement between the LP and CP fields results with the same intensities is due to that the pulse length used in the experiment (≈ 80 fs) is three times the pulse length used in the theoretical work (≈ 26 fs) [178]. This difference in the pulse duration partly compensates the effect of the difference of the intensity between LP and CP fields, which had to be considered. Generally, the TDSE results [178] can be considered as a proper reference for LP fields. Thus, these results are compared to the MO-ADK predictions in Fig. 5.7, including the focal-volume aver-

aging. The MO-ADK probability is obtained by using the different sets of C_{lm} values given in Table 5.1. It is clear that the MO-ADK results and the saturation intensity depend on the structure parameters C_{lm}. Clearly, using C_{lm} values for H_2 given by Zhao *et al.* [110] gives the best results, since it agrees with the numerical TDSE results as well as with the experimental data. Therefore, these values of C_{lm} will be used in the remaining of the MO-ADK calculations in this chapter, as said before. Noteworthy, the determination of the alignment dependence from the experimental data requires to take an angular average, which was not included in the previous theoretical calculations. If it is incorporated in the theoretical calculations, it should be reduced the values of the theoretical ratio $\Re$.

The importance of the above comparison comes from two facts. First, it is a good to test the validity of the MO-ADK model because of a direct comparison with the TDSE results. Furthermore, this comparison allows for determination of the optimal C_{lm} parameters, since all calculations are carried out under the same physical circumstances, such as a LP laser pulse is used in both of them with the same laser pulse and the same ionization potential (0.59036788 a.u.). Moreover, the FVE is included in the both of calculations. Second, the TDSE results showed that the ratio $P_{\parallel}/P_{\perp}$ is not a constant but it decreases to unity for increasing intensity, as it is found at high intensity for the MO-ADK model.

5.4.2 In circular polarized fields (CP)

In the case of CP fields, there is not a significant difference between the results than that was found in a LP case. Figure 5.8 is comparable to Fig. 5.4, but for a CP field. In fact, the behavior of $\tilde{P}_{\parallel}$ and $\tilde{P}_{\perp}$ is not different from that are shown already for the LP field, since $\tilde{P}_{\parallel}$ and $\tilde{P}_{\perp}$ increase for increasing intensity or pulse length. On the other hand, $P_{\parallel}$ and $P_{\perp}$ increase with intensity and approach unity at high intensities. A decrease in the values of the ratio $\tilde{P}_{\parallel}/\tilde{P}_{\perp}$ from 1.49, within a LP field, to the value 1.235, in a CP field, is observed (see Table 5.2). This decrease can be understood by taking into account the geometry aspects discussed in Sec. 5.2. If the laser pulse propagates parallel to the molecular axis, the direction of the electric field is always perpendicular to the molecular axis ($\theta = \pi/2$) and it is independent of the polarization of the pulse. Therefore, the ionization rates and subsequently the ionization yields should be completely calculated along this direction ($\theta = \pi/2$). However, if the propagation is perpendicular to the molecular axis, the electric field direction of the LP field will be parallel to the molecular axis ($\theta = 0$). Unlike the CP field, where all the directions of the electric field around the

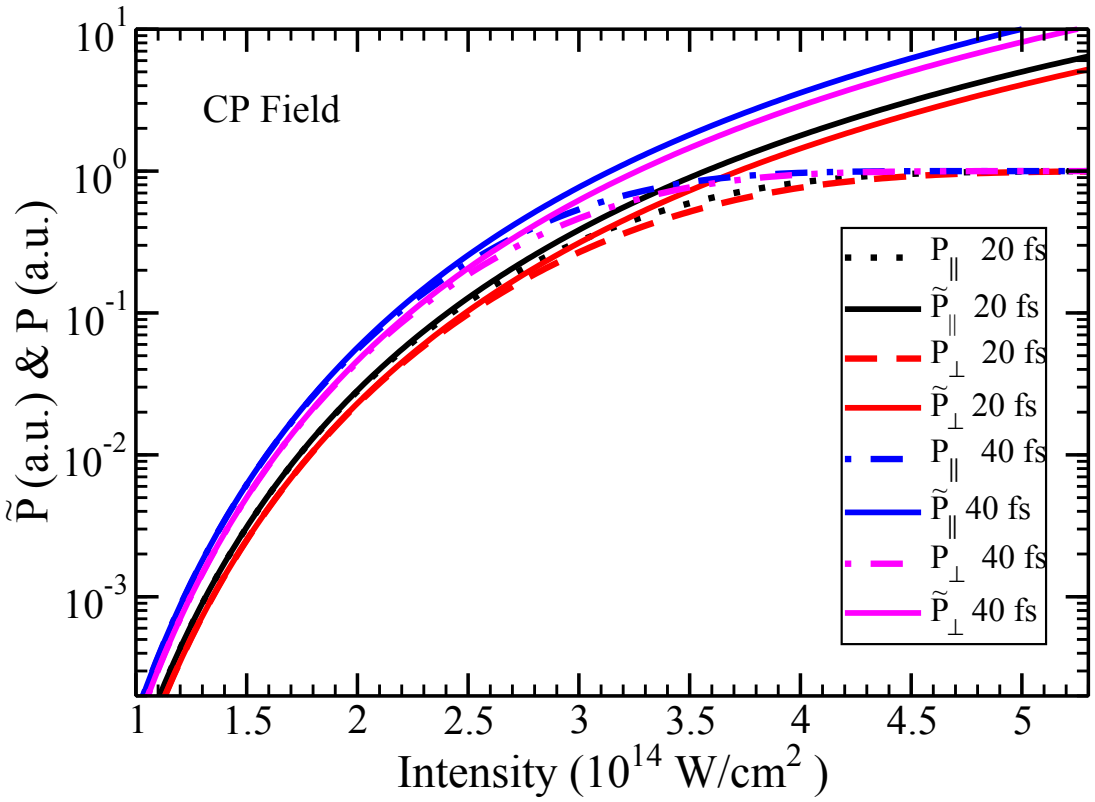

Figure 5.8: As Fig. 5.4, but for a circular polarized field.

molecular axis will be possible in this case (i.e. $\theta = 0$ to 2π, see Fig. 5.1). Accordingly, the rate in the last case is not determined solely by the pure parallel components, but it is an average over 2π, including also the perpendicular orientation. Therfore, it is expected to be smaller than the case of a pure parallel component. Subsequently, the ratio $\tilde{P}_{\|}/\tilde{P}_{\perp}$ in a CP field will be smaller than that in the LP field. In the latter, it has always a pure parallel component to the molecular axis.

Dependence the ratio $\Re$ in CP fields on both intensity and pulse duration is shown in Fig. 5.9. This figure is similar to the case of a LP field shown in Fig. 5.5, except the laser intensity of the experimental data are plotted without scaling and the MO-ADK predicted ratio $\Re$ is scaled up by factor 1.05. The horizontal dotted-line is the value of the ratio $\tilde{P}_{\|}/\tilde{P}_{\perp}$ predicted by MO-ADK ($\simeq 1.235$). According to Fig. 5.9, the dependence of the ratio $\Re$ on the laser parameters is similar to what was found in the case of the LP fields. It decreases with increasing laser intensity, where the decrease pattern depends on the laser pulse duration (see Figs. 5.5 and 5.9). Obviously, including the FVE (right panel) improves the agreement between the ratio predicted by MO-ADK model with

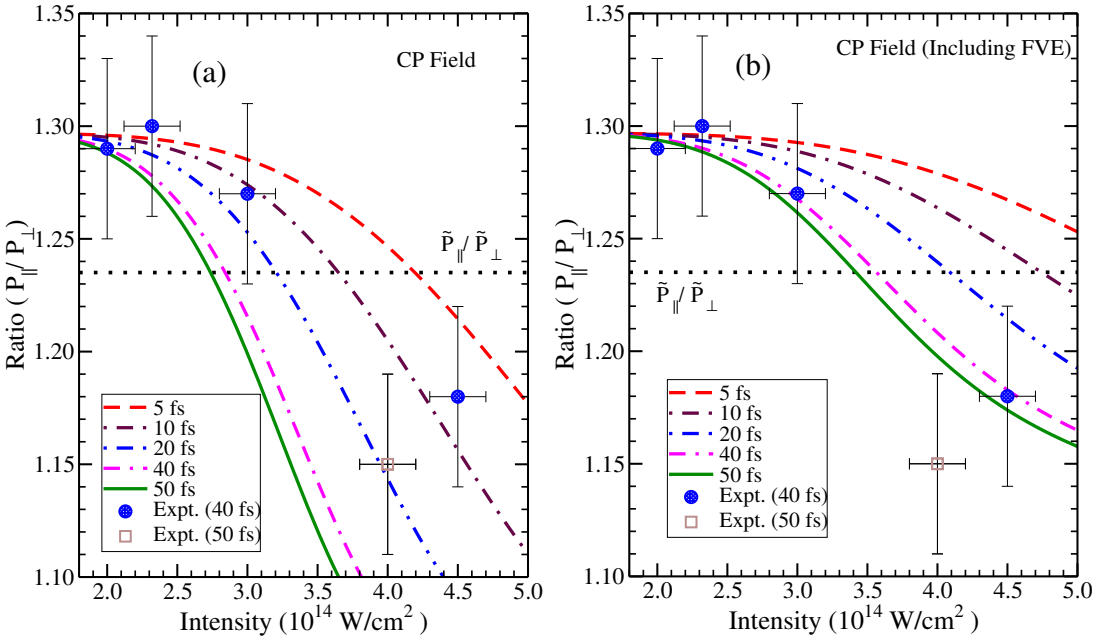

Figure 5.9: As Fig. 5.5, but for a circular polarized field and the MO-ADK ratios $\Re$ are scaled by factor 1.05.

that obtained experimentally at 40 fs.

It is worthwhile to remind that the comparison to the experiment usually requires to take the averages over molecular parameters (rotational and vibrational degrees of freedom corresponding to orientation and nuclear geometry, respectively) as well as over the laser parameters like the spatio-temporal pulse profile. Furthermore, the intense laser pulse parameters like pulse shape and peak intensity are often known only with limited accuracy. In view of the exponential dependence of the ionization probability on the laser intensity, an experimental uncertainty of about 20 % with respect to the peak intensity[5], which is rather common in strong-field experiments, leads to difficult quantitative comparisons [109]. Therefore, these averaging and uncertainties can strongly influence conclusions on the comparison between theory and experiment. Furthermore, experiments usually do not obtain absolute ionization yields, so only the qualitative comparisons are possible, as said before.

[5]In the ionization of atoms or molecules by multi-cycles fast laser fields, the target interacts with several half-cycles, many of them have an intensity significantly lower than the peak intensity of the laser pulse.

5.5 Barrier-suppressed ionization (BSI)

As remarked previously, the ionization occurs at high intensities above the top of the potential barrier in the so-called barrier-suppression regime. In this regime, the ADK and MO-ADK theories do not work well [50]. For this reason, Tong and Lin [29] proposed a simple empirical formula to extend the atomic tunneling-ionization model into the barrier-suppression regime, which provides accurate ionization rates for atoms and molecules in strong laser fields within the SAE approximation. Saturation effect should be considered at high intensities to explain the experimental data given in Refs. [36, 37]. Therefore, a modified tunneling theory which takes the simple exponential factor [29] into account is considered to model the ionization process. Then, the modified tunneling theory (corrected ADK formula) becomes

$$W^{BSI}(F,\theta) \;=\; W_{st}(F,\theta)\,\exp\left(-\alpha\,\frac{2\,F}{k^5}\right)\,, \tag{5.5}$$

where α is an empirical fitting parameter, as shown in Eq. (2.15), which is reported to be equal to 6 for the hydrogen atom [29]. Furthermore, as discussed earlier, Saenz [50] adopted a physical description to calculate the tunneling rates in the barrier-suppression regime and proposed that for a stronger field a so-called field-dependent vertical ionization potential should be inserted into the atomic ADK formula (which known later by the extended ADK model) to agree with *ab initio* results. He referred to his suggestion which includes barrier-suppression ionization as a modified ADK (MADK) model. In this thesis, this Stark shift is substituted by extending the fit formula [Eq. (5.5)] to reproduce the accurate *ab initio* ionization rates presented in [50], using the ionization potential value ($I_P \;=\; 0.60437874\,$a.u.) at the equilibrium geometry. The adjustable numerical factor α is required for fitting ionization rates with those obtained based on the *ab initio* calculations. The ionization rates obtained with both of MO-ADK and ADK models fit the *ab initio* results when introducing the numerical factor α. A factor $\alpha \simeq 1.868$ is found to adjust the tunneling rates obtained by MO-ADK model with the *ab initio* results, while $\alpha \simeq 3.031$ is required to fit the results obtained by the ADK model with the same *ab initio* results. Figure 5.10 shows the ionization rates for H_2 as a function of the field strength obtained by MO-ADK (solid red), ADK (solid black), and using the BSI formula with the two values of α, in MO-ADK (dotted blue curve) as well as in ADK (magenta dashed) models. Additionally, the ionization rates obtained by inserting the field-dependent vertical ionization potential, as was suggested in Ref. [50], into the original ADK model, which called MADK, (solid green) are also shown. The accurate *ab initio* results [50] (solid circles) in the fixed-nuclei approximation are shown

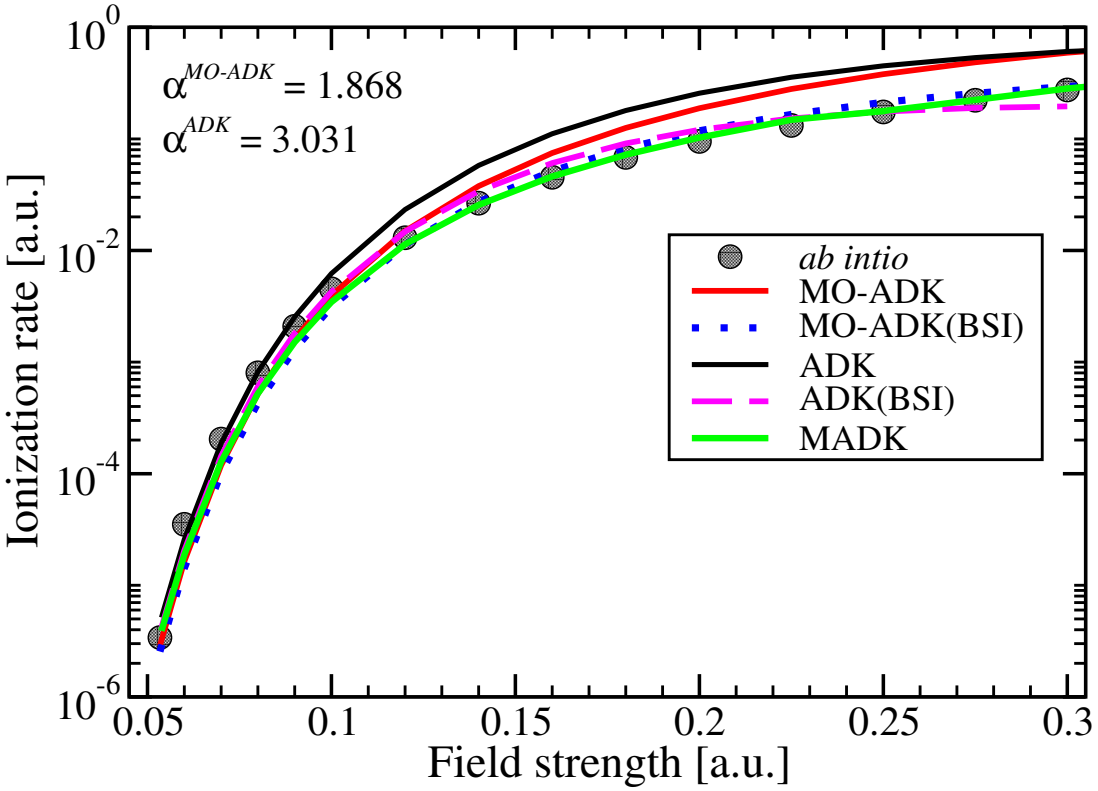

Figure 5.10: Ionization rates of H_2 in a static electric field calculated by different models: MO-ADK (solid red), MO-ADK(BSI) (dotted blue), ADK (solid black), ADK(BSI) (magenta dashed), using the vertical ionization potential at the equilibrium distance $R = 1.4\,a_0$, and MADK using a field-dependent vertical ionization potential (solid green). The *ab initio* ionization rates in the fixed-nuclei approximation (solid circles) [50] are also shown.

for comparison. Clearly, ADK and MO-ADK significantly overestimate the ratio for lower intensities reaching the ratio 1 at the saturation intensity. In other words, the MO-ADK and ADK predictions for the ionization rates agree well with the numerical *ab initio* calculations up to the field strength $\simeq 0.12$ a.u. and $\simeq 0.10$ a.u., respectively, i.e. in the tunneling regime. Above this field strength, one can see that the ionization rates predicted by both the tunneling MO-ADK and ADK models are larger than that obtained by the *ab initio* calculations. On the other hand, a nice agreement between *ab initio* results and those obtained using a modified MO-ADK in the BSI regime (using Eq. (5.5), with $\alpha = 1.868$) is found over all values of the electric field, see the blue dotted line (MO-ADK(BSI)) in Fig. 5.10. A good agreement is also obtained with the ADK results if the BSI formula is used with $\alpha = 3.031$ (magenta dashed curve). A rather good agreement with the *ab initio* rate is observed in the whole investigated range of the

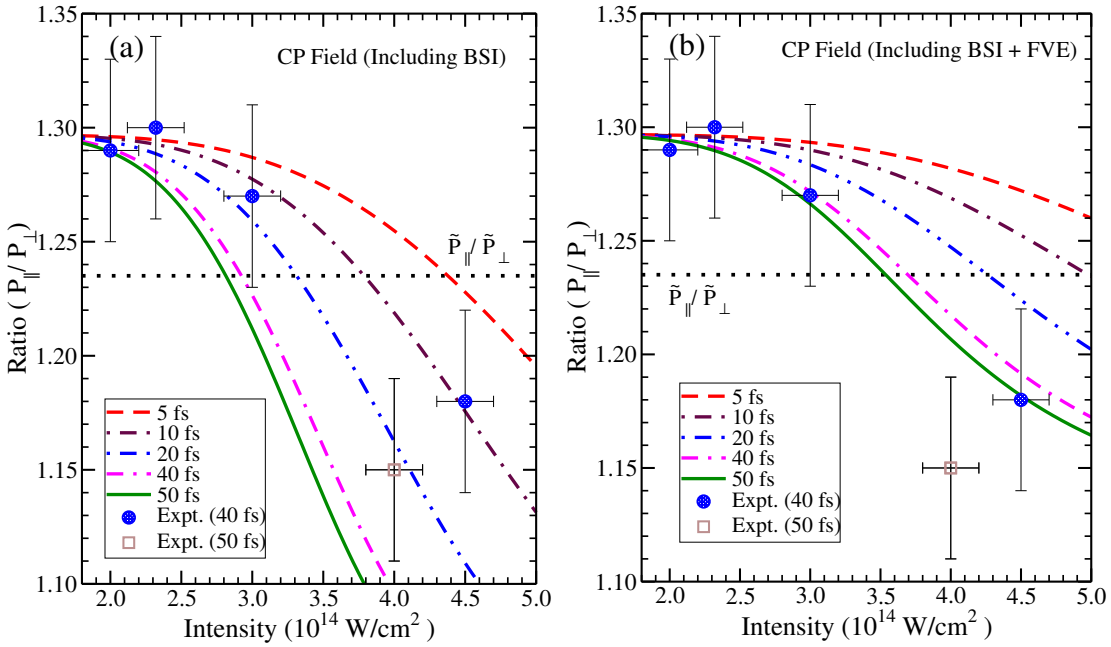

Figure 5.11: As Fig. 5.9, but including the exponential factor that considers the barrier-suppressed-ionization (BSI) effect.

field strength values for MADK, especially in the barrier-suppression regime (solid green curve). This result was interpreted in terms of Stark suppression of the ionization [50]. Whereas, around the equilibrium distance of H_2, its potential curve is more strongly lowered than that of its ion (H_2^+). Accordingly, the effective ionization potential increases with increasing the field strength. Increasing of the ionization potential implies a decrease of the ionization rate and thereby the ionization probability. This is observed in the strong-field barrier-suppression regime. Consequently, it can say that saturation factor plays an important role at high intensities, since the ratio $\Re$ at high intensities and long pulses approaching 1 will be expected. An estimate for this ratio with MO-ADK including the saturation effect (BSI) with our fitting parameter $\alpha = 1.868$ is also shown (blue dotted).

Considering the exponential factor in the barrier-suppression-region leads to an increase of the value of the saturation intensity. Consequently, a decrease of the absolute values of the ratio $\Re$ at high electric field strengths is expected. Figure 5.11 shows the ratio $\Re$ predicted by MO-ADK in the BSI regime for different pulse durations versus the peak intensity. This figure is similar to Fig. 5.9, but includes the BSI effect. Clearly, a modified tunneling model improves slightly the MO-ADK results, especially at high intensity, since the barrier suppression plays an important role in the ionization process.

This improvement in the MO-ADK results indicates the effect of the barrier-suppression correction at high intensities [using Eq. (5.5)]. Including the FVE into the calculations (right panel) leads to a good agreement with the experimental data. Thus, the focal-volume of the laser pulse plays the major rule in the ionization rates at high intensities.

5.6 Summary

In this chapter, the alignment-dependence ionization of H_2 molecules related to molecular axis in linear and circular polarized fields has been theoretically investigated. It was shown that the circular polarized field differs from both static and linear polarized ones. This different is because the projection of the electron angular momentum is not conserved along the electric field direction and depends on time. The validity of the molecular tunneling models, MO-ADK and MO-PPT models, within a wider range of laser intensities was examined, by comparing the ionization probabilities with those of the accurate TDSE calculations. In contrast to the MO-ADK model, the MO-PPT model is able to quantitatively correctly reproduce almost the complete intensity-dependence ionization probability (below barrier-suppression regime) as well as the exact TDSE calculations. This success of the MO-PPT model motivates us to examine it with molecules which have more electrons than H_2, like N_2 and O_2, in the next chapter.

The ratio ($\Re = P_{\parallel}/P_{\perp}$) of the angular ionization probabilities of H_2 between parallel and perpendicular molecular orientations in linear and circular polarized fields using molecular tunneling theory was also studied. It was found that the ratio $\Re$ for an H_2 molecule in a strong field decreases generally with increasing laser intensity, where the pattern of decrease depends on the duration of the laser pulse. The effect of the focal-volume for laser pulse on the anisotropy is investigated. It was observed that including this effect into the calculations is very important and improves the MO-ADK results, especially at high intensities. The MO-ADK model is able to reproduce very well the intensity-dependent anisotropy and predicts an even higher degree of experiment data, especially if the focal-volume effect is included. Interestingly, our results invalidate the main result of Jin *et al.* [40], and corresponding statements in other works, e.g. [36, 37, 39], where it was claimed -*erroneously*- that MO-ADK theory failed completely to predict the intensity-dependent anisotropy of H_2 strong-field ionization and gave a constant value for the ratio. Noteworthy, the constant value predicted by MO-ADK model is the ratio between the ionization *rates* (not *yields*) of H_2 between parallel and perpendicular molecular orientations, which independent on the laser parameters. The absolute value of the ratio $\Re$ depends on the polarization of the laser field, i.e. linear or circular polarized.

This result is important in future works, if a comparison with experimental data obtained in a circular polarized laser field is required. Moreover, based on accurate *ab initio* ionization rates calculations for H_2 in the fixed-nuclei approximation, an adjustable parameter ($\alpha \simeq 1.868$) for the MO-ADK tunneling model into the barrier-suppression regime is presented. A further improvement in the MO-ADK predictions was found, if this correction in addition to the focal volume effect are considered. Hence, a reasonable comparison with the experimental data is obtained.

6 Applying molecular tunneling theory to larger diatomic molecules

6.1 Introduction

In the last few decades the interaction of atoms and molecules with intense laser pulses has attracted widespread interest. This highly nonperturbative interaction results in a number of nonlinear processes such as high-harmonic generation, laser-induced electron diffraction (LIED), above-threshold ionization, and double ionization. The common process in all of those cases is single-electron ionization that gives rise (either directly or indirectly) to the other processes. Although the atomic ionization has been extensively investigated theoretically and experimentally, the study of molecular ionization is still far from complete. As said earlier in Sec. 2.5, the experimental data [100–104] indicated that in intense laser fields ionization signals of diatomic molecules and noble gas atoms with comparable ionization potentials behaved similarly. This was assumed to be understandable in terms of the tunneling ionization process in which the probability of ionization depends primarily on the ionization energy of the system. However, further investigations of diatomic molecules showed that the ionization is strongly suppressed for the cases of D_2 and O_2 in comparison to their companion atoms (Ar and Xe, respectively). On the other hand, the ionization rate for N_2 and F_2 is comparable to their companion Ar atom. Several attempts have been done to interpret why some diatomic molecules are harder to ionize than their companion atoms, particularly for the case of O_2. Muth-Bohm *et al.* [15] proposed that the ionization suppression in O_2 with respect to Xe and its absence in N_2 relative to Ar is due to a destructive or constructive interference of the electrons emitted from the two centers, depending on the molecular HOMO symmetry. Thus, for O_2 in which the HOMO has an antibonding character (ground-state configuration: $1\sigma_g^2 1\sigma_u^2 2\sigma_g^2 2\sigma_u^2 3\sigma_g^2 1\pi_u^4 2\pi_g^2$), single ionization should show suppression. While for N_2, in which the HOMO has a bonding character (ground-state configuration: $1\sigma_g^2 1\sigma_u^2 2\sigma_g^2 2\sigma_u^2 1\pi_u^4 3\sigma_g^2$), single ionization should not be suppressed. This interference model failed to explain the suppression of D_2. Moreover,

it predicts suppression for F_2 according to the given symmetry argument, since F_2 has ionization potential similar to N_2 and Ar ($\sim 15.69\,\mathrm{eV}$), but it has valence electrons with the same symmetry as O_2 (ground-state configuration of F_2: $1\sigma_g^2 1\sigma_u^2 2\sigma_g^2 2\sigma_u^2 3\sigma_g^2 1\pi_u^4 1\pi_g^4$). According to the interference model [15], the ionization of F_2 should also be suppressed with respect to either N_2 or Ar. However, this prediction disagrees with the experimental observations [103, 104] that showed that the ionization of F_2 is not suppressed with respect to that of N_2. Saenz [146] studied the influence of vibrational motion and field-induced changes in the bond lengths on the ionization rates of molecules like H_2, N_2, and O_2. He also predicted reduced ionization rates relative to companion atoms of the same ionization potential for H_2 and O_2 and no suppression for N_2, but the model could not quantitatively account for the observed suppression. In another study for Dundas and Rost [179], suppression of single ionization has been found in O_2 and its absence in both F_2 and N_2, in accordance with the experimental results at $\lambda = 800\,\mathrm{nm}$. They also concluded that the suppressed ionization of O_2 with respect to its companion noble-gas atom (xenon) does not arise from the multiplicity of the ground state of O_2. They explained the deviations from the above predictions [15] within their framework a time-dependent density functional approach to be based on the symmetry of the HOMO and they reported that the multi-electron molecular correlation leads to the dominant ionization of an orbit with a symmetry different from that of the HOMO. This is the reason of the failure of the prediction based on the symmetry of the HOMO [15].

Noteworthy, Full numerical approaches are very demanding computationally and sometimes they are difficult to interpret. However, these numerical studies provide an important basis for testing approximate analytical theories. It was a breakthrough when fully correlated calculations for H_2 became available [151, 154]. Extensions to larger systems rely on the TDDFT [128] or the SAE approximation [121, 180]. A general understanding of atomic ionization models have also been extended to match molecular systems [28, 181].

As mentioned in chapter 2, the most important ingredients in the ADK theory are the ionization potential (I_p) and the angular momentum of the valence electron (l). The angular momentum is not a good quantum number in the general molecular case. Thus, the molecular symmetry has to be taken into account in the molecular tunneling theory (MO-ADK). Nevertheless, the atomic ADK was applied to some diatomic molecules, such as N_2 and O_2, even using the values of the structure parameters l and m for the Ar and Xe atoms, ($l = 1$, $m = 0$) [54]. Some authors have considered $l = 0$, $m = 0$ [183], regardless the structure of the HOMO. However, a consistent *ansatz* to extend the atomic ADK model to diatomic molecules needs to consider which values of l and m should be

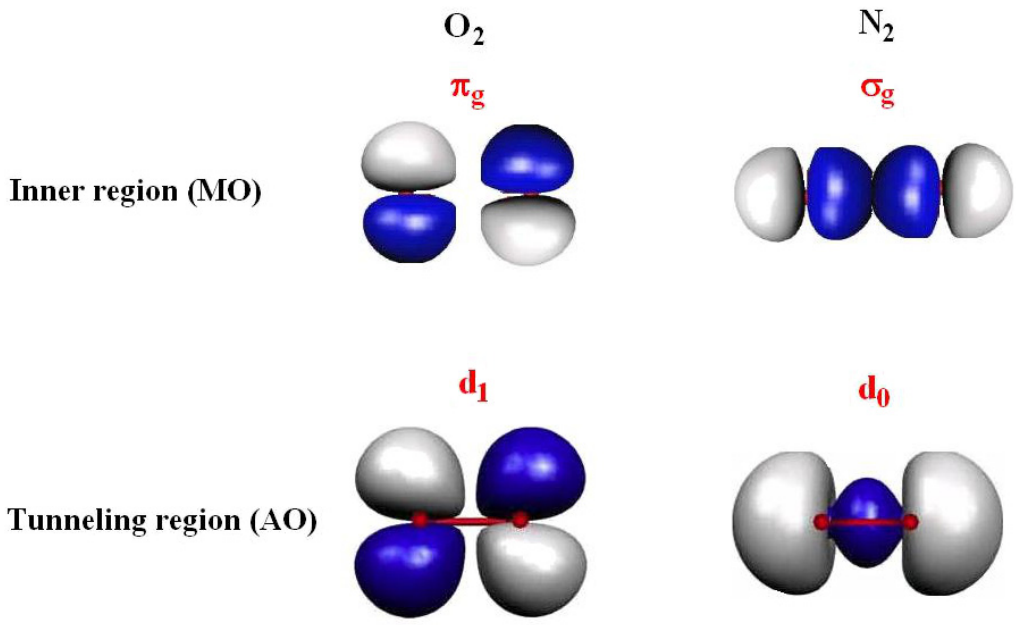

Figure 6.1: Two-centered molecular orbitals of the valence electrons of O_2 (π_g) and N_2 (σ_g) in addition to the one-centered d-type atomic orbitals that are most similarly shaped. Only the asymptotic region of the electronic wavefunction is of interest. Lighter gray colour represents positive values of the wavefunction and darker blue colour negative values (adopted from [182]).

used. This question has been discussed and answered by Shan *et al.* [182] as follows. The wavefunction of the electron in the tunneling (asymptotic) region is the key point in the MO-ADK model. In the asymptotic region, the molecular orbital can be expressed as a superposition of the atomic orbitals at the two centers. To apply the ADK model on the diatomic molecules, one needs to extract the dominant atomic orbital or partial waves centered at the charge center of the molecule. Figure 6.1 shows the approximate two-centered molecular orbitals and their closest atomic-orbital counterparts centered at the midpoint of the internuclear axis. The different colour shadings indicate opposite signs of the orbital. The O_2 valence orbital (π_g) in the asymptotic region is constructed mainly by the two $2p_1$ orbitals located at the two nuclei. In terms of atomic orbitals centered at the midpoint of the molecules it is best approximated by the d_1 orbital, i.e. $l = 2$, $m = 1$. However, $l = 2$ and $m = 0$ are considered for the N_2 valence orbital (σ_g), as shown in Fig. 6.1. The above parameters are for molecules aligned along the direction

of the laser field [182].

In this chapter, exposing nitrogen and oxygen molecules to strong laser fields is studied. Ionization probabilities obtained numerically by solving the single-active electron approximation based time-dependent Schrödinger equation (SAE-TDSE) [109, 122] are compared with those obtained from semi-analytical models like ADK, PPT (after choosing values for l and m corresponding to the probed HOMO), MO-ADK, and MO-PPT models. The dependence of the ionization probability on the internuclear distance, which affects on the population distributions in vibrational states of the molecular ions, is presented. Furthermore, the ionization yield as a function of the laser peak intensity and also of the angle between molecular axis and laser field direction is investigated.

The vibrational wavefunctions of the molecule and the molecular ion are obtained by solving the nuclear motion in the adiabatic BO potential curves by expanding the nuclear wavefunctions in B-splines for the radial part times spherical harmonics describing the angular part [77] (see appendix D). The radial Schrödinger equation is solved in a spherical box whose boundary is defined by R_{max}. The box leads to a discretization of the vibrational states. A B-spline basis 300 B-splines of order eight, expanded on a linear knot sequence spanning $R = 0 - 10\,\mathrm{a_0}$ has been shown to give converged results in N_2, O_2, and their ions. The influence of the laser field on the electronic-vibronic states is neglected, since the states of present interest, the ground and the lowest excited states of N_2 (O_2) and N_2^+ (O_2^+), are more stable[1].

6.2 Variation of internuclear distance

As it is discussed in Sec. 2.5.1, the MO-ADK theory gives analytically the ionization of molecules as did the ADK model in the atomic case. It depends on the structure parameters C_{lm} which are related to the electronic density of the HOMO in the asymptotic region. These parameters depend on the l and m quantum numbers and they can be determined by fitting the asymptotic molecular wavefunctions at large distances, taking into account the dependence on the internuclear distance and the electronic state. In reality, it is difficult to obtain accurate values for C_{lm} at sufficiently large internuclear distances for diatomic molecules. Recently, Zhang *et al.* [41] reported C_{lm} values sets at different internuclear distances for the $1\sigma_g$ state of H_2^+. However, for N_2 and O_2 molecules, to our knowledge, the C_{lm} values are only available at the equilibrium dis-

[1] They have bond order, which is a measure to the stability of the molecules, greater than one (triple (double) bond for N_2 (O_2) and 2.5 for N_2^+ as well as O_2^+).

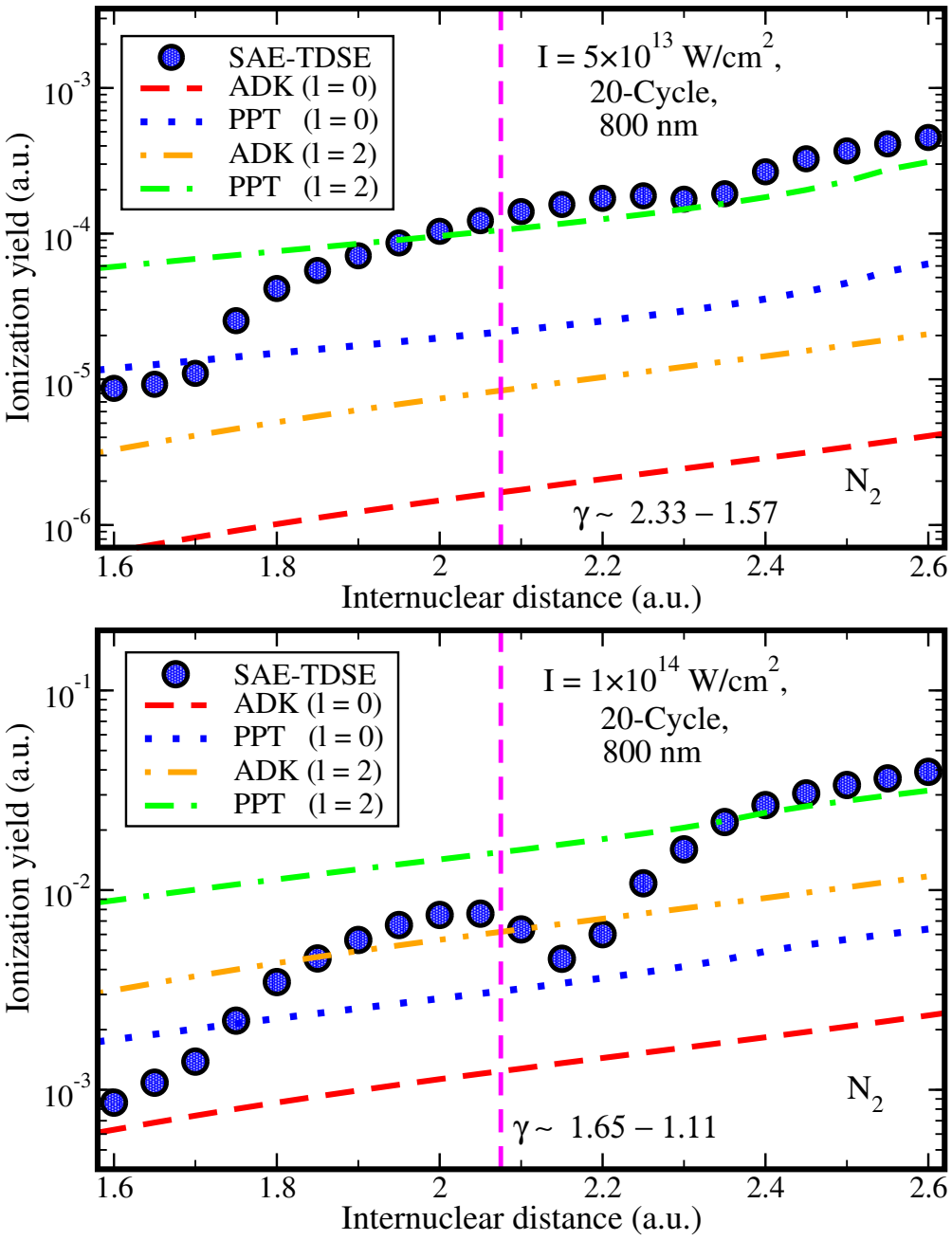

Figure 6.2: SAE-TDSE results of the ionization probability for parallel-aligned N_2 molecule (circles) as a function of the internuclear distance for two different peak intensities. Each circle corresponds to the numerical solution of the TDSE within the SAE approximation. They are compared with those obtained from the extended ADK and PPT models with R-dependent ionization potential using $l = 0$ (red dashed and blue dotted lines) and $l = 2$ (orange dot-dot-dash and green dash-dash-dot lines). The vertical dashed line shows the equilibrium distance ($2.075\,a_0$) of N_2. The parameters of the laser pulse and the range of Keldysh parameter are given in each graph.

tances. In this section, the dependence of the ionization probability of N_2 and O_2 on the internuclear distance are investigated, using the extended ADK and PPT models, after choosing proper values of l and m corresponding to the structure of the HOMO (see Fig 6.1). These results are compared with those numerical results obtained by SAE-TDSE method [109], which was extended for larger molecules in [122], more details can be found in chapter 3, and appendix C.

Figure 6.2 illustrates the ionization probabilities, for a parallel orientation of N_2 molecular axis with respect to the polarization vector and 20-cycle $\cos^2$-shaped (FWHM of about 10 fs) laser pulses, as a function of internuclear distance, using three different methods, i.e. the TDSE, the ADK model, and the PPT model. The laser wavelength 800 nm with two different intensities: $5{\times}10^{13}$ (top panel), and $1{\times}10^{14}$ W/cm^2 (bottom panel), are used. The TDSE results are obtained by using the time propagation-single active electron (TP-SAE) approximation code of our group[2]. For the ADK and PPT models, the values $m = 0$ and $l = \{0, 2\}$ are used to see the effect of the l parameter. In the top panel, corresponding to the MPI region ($\gamma > 1$), it can be noted that the PPT curves with $l = 2$ are most consistent with the SAE-TDSE calculations, especially for $R > 1.9\,a_0$. On the other hand, the simple ADK model underestimates the TDSE results by orders of magnitudes. At the higher peak intensity, e.g. 10^{14} W/cm^2 (bottom panel), the Keldysh parameter decreases with increasing internuclear distance approaching ~ 1 at large distance, where the ionization potential decreases. Then, the ADK model (with $l = 2$) works well in the tunneling region and agrees, specifically at $R > 1.85\,a_0$, with the TDSE results. While the results of the PPT model with the same value of l overestimate the TDSE results at distances smaller than $2.3\,a_0$, but agrees with the results at larger values. Noteworthy, the ionization probability of N_2 at internuclear distances smaller than $1.75\,a_0$ is very small and increases for increasing the laser intensity. This small ionization probability due to the high ionization energy at small internuclear distances, since the potential curves of N_2 ($X^1\Sigma_g$) and N_2^+ ($X^2\Sigma_g^+$) states are very similar around the equilibrium internuclear distances. Furthermore, the ionization probabilities obtained within SAE-TDSE shows a REMPI resonance, where its position depends on the laser intensity.

Figure 6.3 displays the dependence of the ionization yield on the alignment of the molecules relative to the laser field as well as the internuclear distance. This figure shows the ionization probability obtained by solving the SAE-TDSE as a function of the internuclear distance for N_2 at three different alignment angles ($\theta = 0°, 45°$ and $90°$) and their average, neglecting the focal volume effect. The laser parameters are

[2]More details about this code are presented in the PhD thesis of S. Petretti (2013) [122].

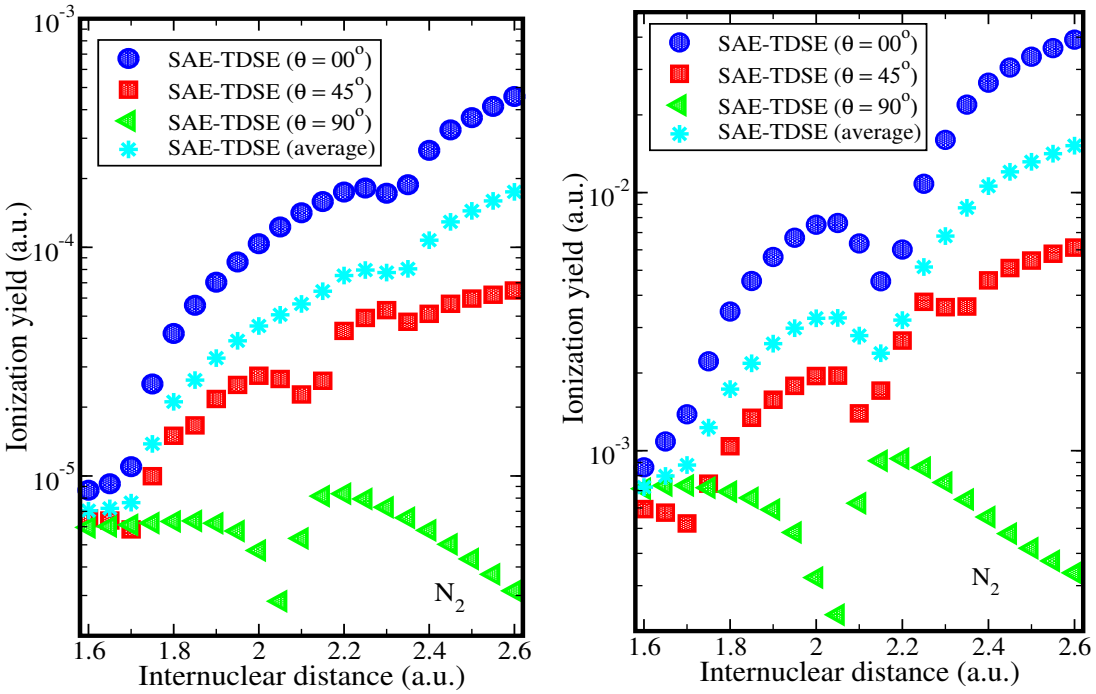

Figure 6.3: Ionization yield obtained numerically by solving TDSE as a function of internuclear distance for N_2 at three different alignments and its average. Two different laser peak intensities, 5×10^{13} W/cm^2 (left panel) and 1×10^{14} W/cm^2 (right panel), with the same pulse length (20-cycle) and wavelength (800 nm) are used,

800 nm wavelength and 20-cycle pulse length with peak intensities 5×10^{13} (left panel) and 1×10^{14} W/cm^2 (right panel). Looking at the curves, one can observe that the structures depend on the alignment, where the angle-dependent ionization minimum is clearly visible. Moreover, for the case of $\theta = 0°$, the structures depend on the laser peak intensity, similar to what was observed in H_2 in chapter 4.

The distribution of the charge density around the nucleus constituted the molecule may be responsible for the dependence of the ionization on the internuclear distance besides the ionization potential as follows. Lein *et al.* [184] discussed that the electron density of the HOMO is crucial and it is not necessarily connected to R. They gave a derivation based on the very high localization of electron wavefunctions at the position of the nuclei. Their discussion has been considered one of the first publications on the two-point scattering model[3]. However, in a real molecule the charge density can be pushed away from nuclear positions if the orbitals are antisymmetric. The HOMO orbital for nitrogen

[3]The two-center models was earlier always attributed to the nuclear positions (electron-density maximum). Lein *et al.* noted that the maxima of the electron density needs not to agree with the one of the nuclear.

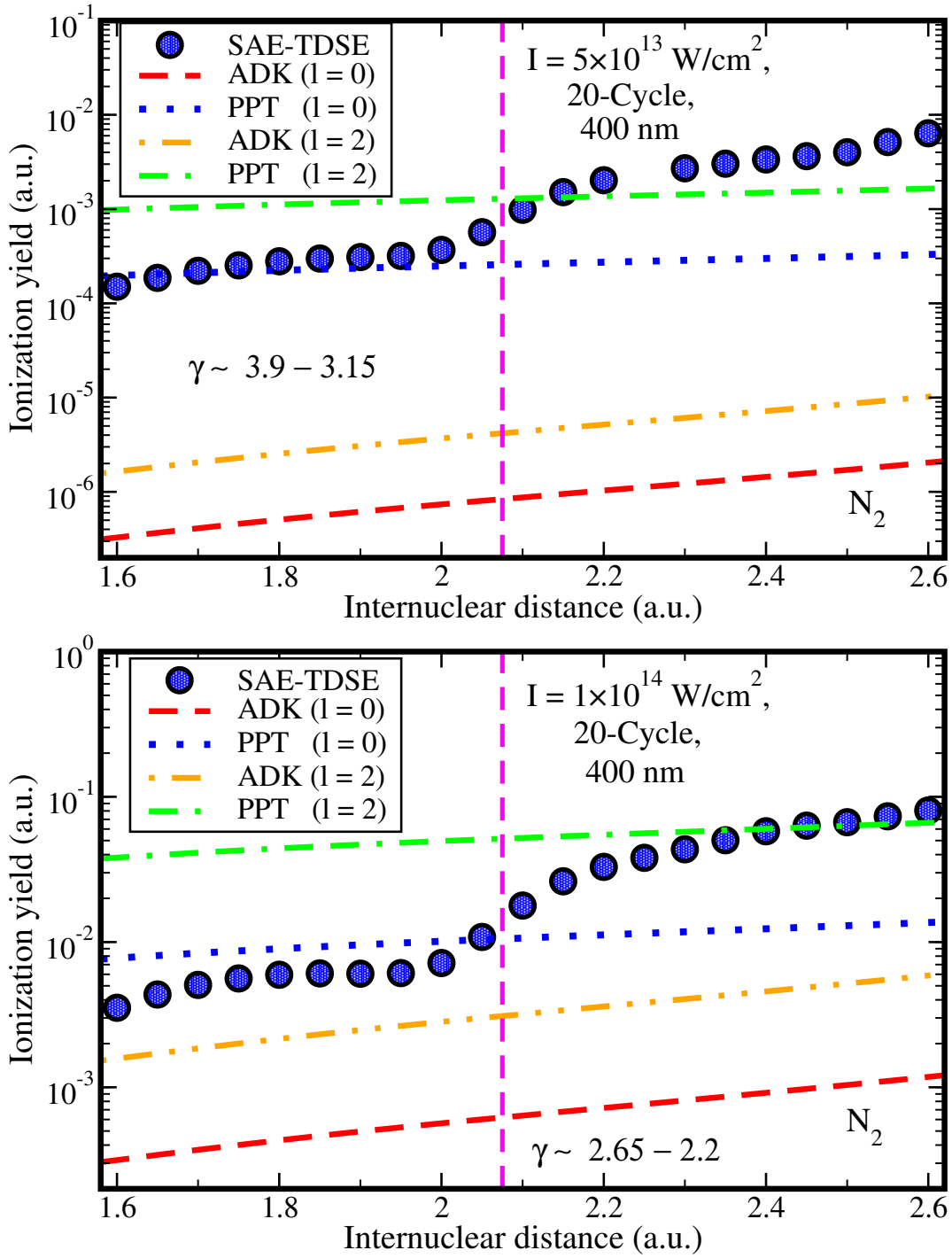

Figure 6.4: As Fig. 6.2, but for $\lambda = 400\,\text{nm}$.

molecule σ_g is mainly set up from p lobes of opposite phase pointing along the internuclear axis leading to changing in the ionization probability, see Fig. 6.1. Actually, for small internuclear distances, the p lobes do overlap to a large extent, then the electronic structure of the HOMO shrinks and the charge density becomes antisymmetric around each nucleus [185]. The antisymmetric superposition of p lobes pushes the charge density to larger distances. However, for large internuclear distances, the p lobes do not overlap to a large extent and the charge density is symmetrically arranged around each nucleus. Because of this instability in the distribution of the charge around the nucleus constitute at different values of R (antisymmetric and symmetric distributions), in addition to varying the ionization potential [146], the dependence of the ionization yield on R could be expected.

Similar trends are found if a shorter laser wavelength, 400 nm, is applied. Figure 6.4 is thus comparable to Fig. 6.2, but for wavelength 400 nm. In fact, within this short wavelength the MPI is more dominant than the TI. Consequently, the PPT model becomes more appropriate than the ADK model, as can be seen from Fig. 6.4.

To discuss the wide applicability of the ADK and PPT models, the ionization probabilities of O_2 within those models and the TDSE as a function of internuclear distance are illustrated in Fig. 6.5. Two laser peak intensities, 5×10^{13} and 1×10^{14} W/cm^2, with each wavelength, 800 nm (top panels) and 400 nm (bottom panels), are used. The values $m = 1$ and $l = \{1, 2\}$ are used in the ADK and PPT models. For smaller internuclear distances than the equilibrium value, it can be observed that the ionization yield of O_2 strongly depends on the internuclear distance than N_2. This means that O_2 molecule can be ionized at smaller internuclear distances more easily than at the equilibrium one. This confirms an earlier prediction of [77, 121], in which the vibrational motion influences the ionization rate of H_2 and O_2 more strongly than that of N_2, exactly as found in the experiments on suppressed ionization. It is clear that the ionization probability obtained from the PPT model with $l = 1$ agree with those from the SAE-TDSE in almost all cases. However, the ADK model shows better agreement with the SAE-TDSE ionization probability, with $l = 2$, at low intensity (5×10^{13} W/cm^2) in the case of 800 nm, and at high intensity (1×10^{14} W/cm^2) in the case of shorter wavelength (400 nm). The yields obtained with the ADK model using $l = 1$ partially agree with the SAE-TDSE calculations at 1×10^{14} W/cm^2 for 800 nm, since γ is approaching one. In other words, except the PPT model (with $l = 1$), neither of the ADK (with $l = \{1, 2\}$) and the PPT (with $l = 2$) models is able to show a satisfactory fit with the SAE-TDSE calculations.

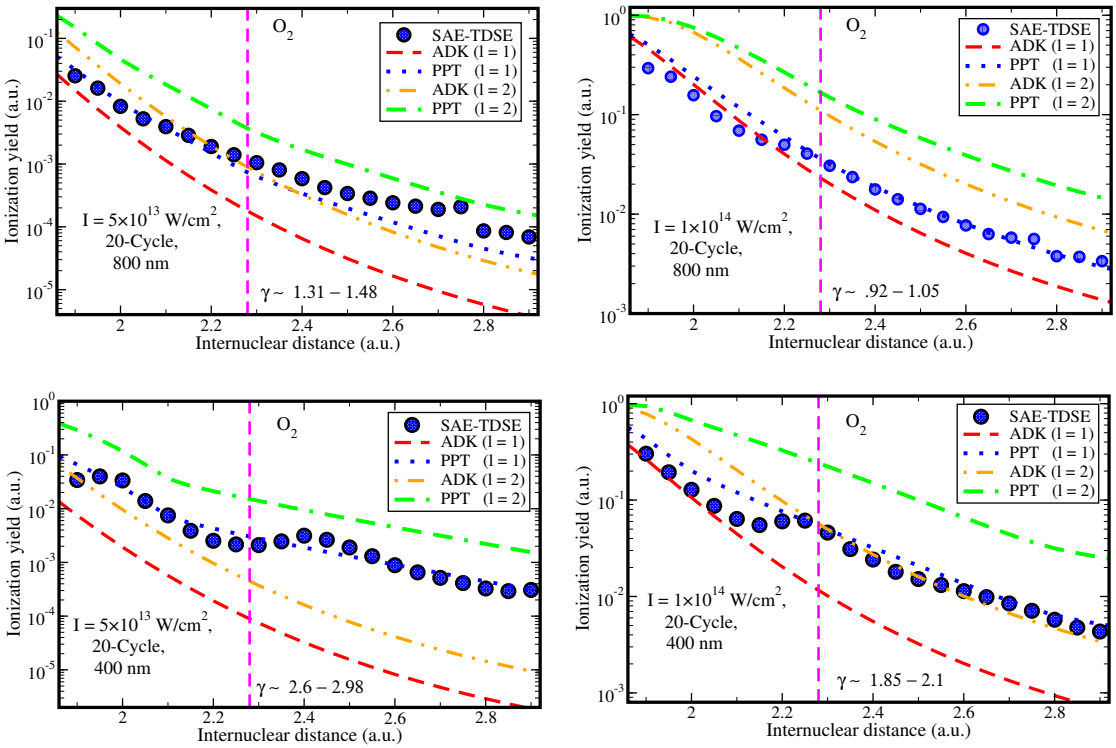

Figure 6.5: As Fig. 6.2, but for O_2 and the vertical dashed line indicates the equilibrium distance of O_2 ($2.28\,a_0$).

6.3 Population distribution of the ionic vibrational states

As already discussed in chapter 4, to get a more complete picture of the processes taking place if a molecule is exposed to laser fields, the nuclear motion has to be included. The Franck-Condon approximation is often used when considering the nuclear motion. However, a non-Franck-Condon distribution in the vibrational population of H_2^+ after ionization of H_2 was theoretically predicted and experimentally found, as was discussed in chapter 4. In this section, the corresponding ionic vibrational distributions for larger molecules than H_2, i.e. N_2 and O_2, are discussed.

For N_2 molecule, it is assumed that the neutral nitrogen molecule is initially prepared in its electronic and vibrational ground state ($X^1\Sigma_g$, $\nu = 0$). Becker *et al.* [186] analyzed the ionization of the (inner-) valence electrons of the nitrogen molecule in an intense laser pulse. They have studied the population of the vibrational states of the formed $X^2\Sigma_g^+$, $A^2\Pi_u^+$, and $B^2\Sigma_u^+$ states of N_2^+ by using the strong field S-matrix theory, which is based on Volkov states. They showed that the laser-induced population distribution in the

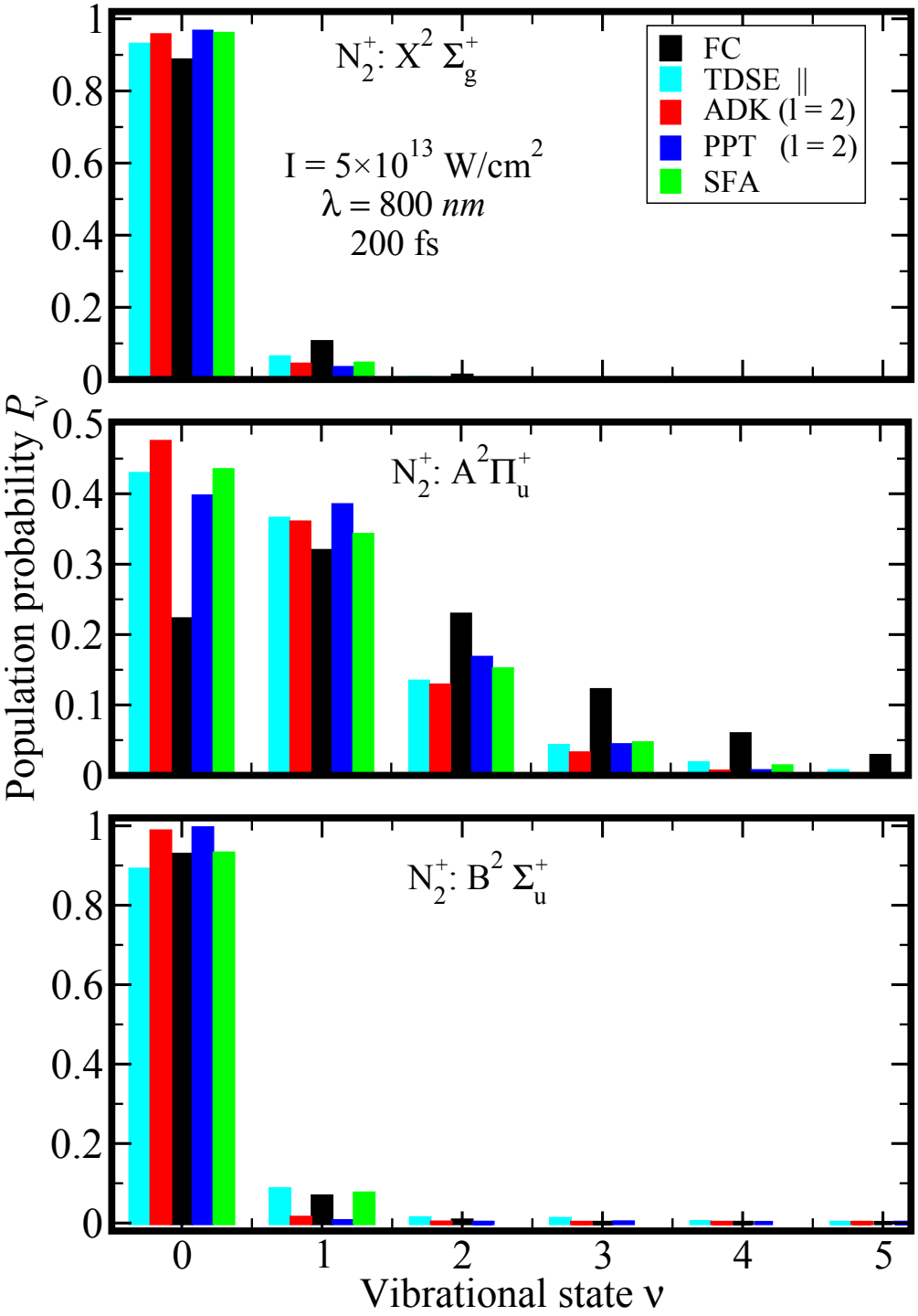

Figure 6.6: Comparison of the SAE-TDSE results (cyan columns), ADK (red columns) and PPT (blue columns) theories for the population distribution in the ground $X^2\Sigma_g^+$ (top panel), the $A^2\Pi_u^+$ (middle panel), and the $B^2\Sigma_u^+$ (bottom panel) states of the nitrogen molecular ion, in a linearly polarized laser pulse, in addition to the respective Franck-Condon distributions (black columns). The SFA results taken from Ref. [186] (green columns) are also shown. The laser pulse parameters for all graphs are the same as those given in the top panel.

electronic states of N_2^+ is shifted towards lower vibrational levels compared to the usually expected Franck-Condon distribution. This shift is due to the strong dependence of the ionization rates on the ionization potential, which was earlier predicted by Saenz [146]. The results of Becker *et al.* [186] are compared, here, with those obtained within the SAE-TDSE, ADK, and PPT (with $l = 2$) models. The same electronic and vibrational states as well as the laser parameters of the TDSE calculations are considered.

Figure 6.6 shows the population distributions over vibrational levels of the ground $X^2\Sigma_g^+$ (top panel), $A^2\Pi_u^+$ (middle panel), and $B^2\Sigma_u^+$ (bottom panel) states of N_2^+, starting from the ground electronic state of N_2 ($X^1\Sigma_g$), $\nu = 0$. A linearly polarized Ti:sapphire laser pulse with $\lambda = 800\,\text{nm}$, 76-cycles (200 fs) and the peak intensity $5{\times}10^{13}$ W/cm^2 are used. The laser-induced population of vibrational state ν is obtained by squared of Eq. (4.2), where the ionization yields are obtained by the SAE-TDSE, ADK, and PPT models. These population distributions are compared with the Franck-Condon distribution, as well as the SFA results extracted from Fig. 1 of Ref. [186]. In the present ADK and PPT calculations the ionization potential is defined by the energy difference between the electronic ground-state potential curve of the neutral molecule $X^1\Sigma_g$ and the different particular electronic state potential curves of the molecular ion. The comparison shows that the lowest vibrational levels are more populated by the laser interaction than in the case of the Franck-Condon distributions. The shift in the population probability towards lower vibrational levels is strongest for the $A^2\Pi_u^+$ state, whereas it is smaller for both the $X^2\Sigma_g^+$ state and $B^2\Sigma_u^+$ state . This finding agrees well with what has been found by Becker *et al.* [186].

In the case of O_2 molecule, the populations of the vibrational states of O_2^+ after ionized O_2 in an intense laser field according to TDSE, ADK, and PPT calculations are depicted Fig. 6.7. The shown vibrational distributions of O_2^+ are corresponding to the laser parameters used for calculating the ion yield in Fig. 6.5, the vibrational distributions of O_2^+ are shown in Fig. 6.7. For comparison, the FC vibrational distributions are also shown. It is clear that the predicted vibrational distributions significantly deviate from the FC distribution. The low vibrational states are populated more than the higher states due to the influence of vibrational motion. This result confirms the importance of considering $I_p(R)$, as was discussed in [77].

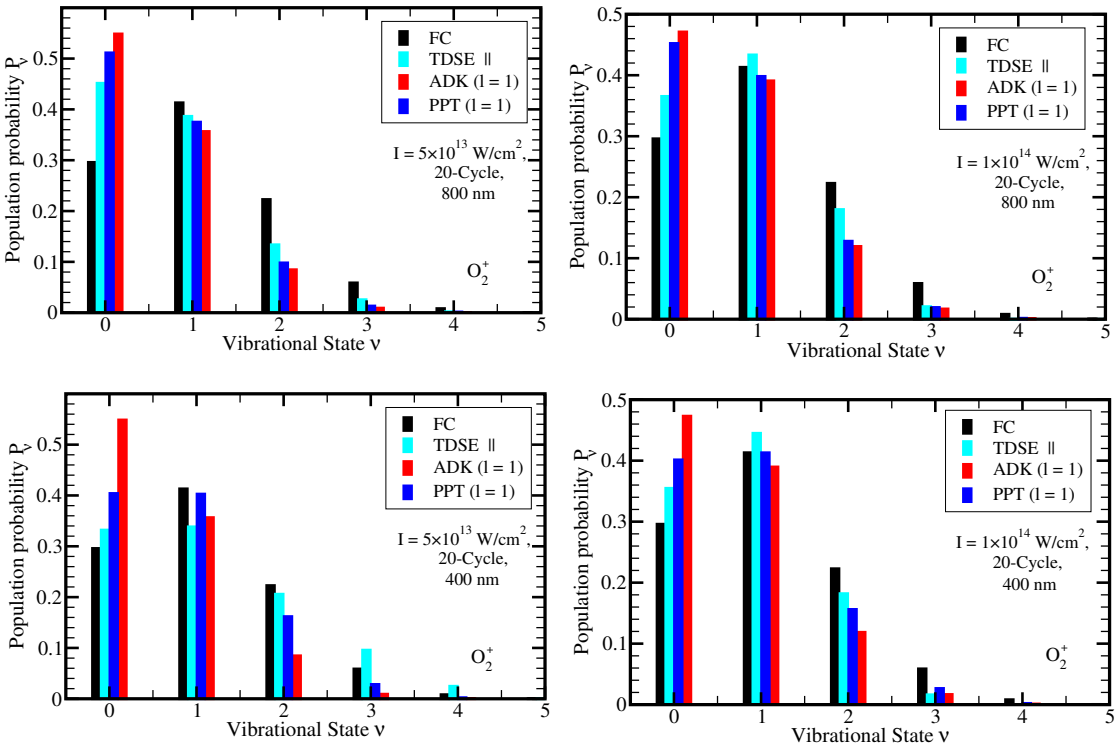

Figure 6.7: Vibrational distribution of O_2^+ after ionization in an intense laser field according to the ADK (red bars), the PPT (blue bars) models and the results of the SAE-TDSE (cyan bars). The Franck-Condon distributions are indicated with black bars. The laser wavelength in the top panels is 800 nm, while in the bottom is 400 nm. In all panels the pulse duration is 20-cycle, while the peak intensities are 5×10^{13} (left panels) and 1×10^{14} W/cm^2 (right panels).

6.4 Dependence on the intensity of the laser field

It is also interesting to consider the intensity dependence of the ionization probabilities of the HOMO of larger molecules. In chapter 5, the variation of the ionization yield with the intensity in H_2 has been studied and found that the MO-PPT can accurately predict the ionization yield at low intensity ($< 1\times10^{14}$ W/cm^2), in contrast to the MO-ADK model. In this section, the MO-ADK and MO-PPT models are applied to larger molecules than H_2, particularly N_2 and O_2. Besides, the ADK and PPT models, with appropriate values of l and m, are adopted.

Figure 6.8 displays the ionization yield of N_2 as a function of the laser peak intensity. A laser pulse with 800 nm wavelength, and pulse duration 12 cycles (32 fs) is considered. The yields are obtained by three methods based on the SAE approximation, one numer-

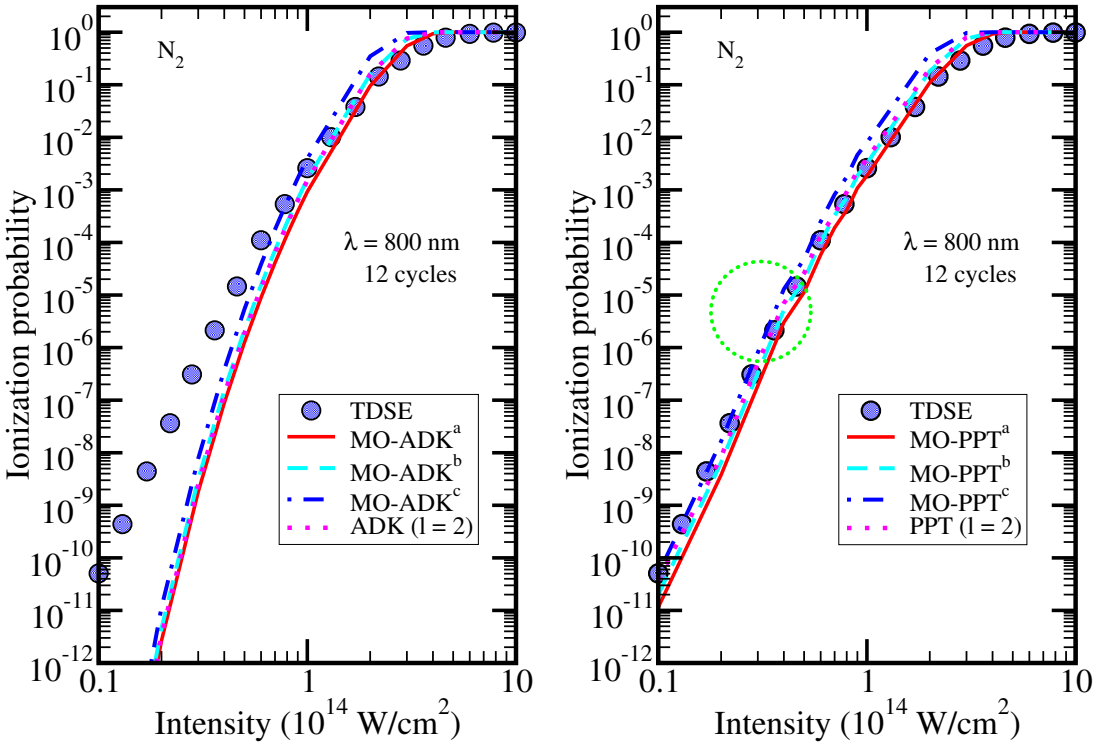

Figure 6.8: Ionization probability as a function of laser peak intensity for N_2. Ionization yields are obtained from MO-ADK and MO-PPT with the asymptotic parameters C_{lm} [28] (red line), [187] (cyan, dashed line), and [188] (blue, dashed-dot line), with the superscripts a, b, and c, respectively. These results are compared with those obtained numerically in [43] (blue, circles) by solving TDSE. The atomic ADK and PPT results with $l = 2$ (magenta, dotted line) are also shown. The green circle indicates occurring a channel closing.

ical and two analytical. The numerical results are obtained by solving the TDSE within the SAE approximation based on density-functional theory (DFT-SAE-TDSE) and the data were provided by Manohar Awasthi [43]. The analytical results are obtained by the extended ADK and PPT models (with $l = 2$ and $m = 0$), as well as the MO-ADK and MO-PPT models with three different sets of C_{lm} values [28, 187, 188] for N_2 shown in appendix E. All yields are compared in Fig. 6.8. The superscripts a, b, and c assigned to MO-ADK and MO-PPT in the figure indicate that the C_{lm} values are taken from Refs. [28], [187], and [188], respectively[4]. For comparison, the ionization potential (15.93 eV) for N_2 is used for all the models as in the TDSE calculations, although it is larger than the experimental value.

[4] Notably, the C_{lm} values given in Refs. [26, 108] are also used. It is found that the results are in agreement with those of MO-ADK^c [188], so their results are not shown in Fig. 6.8.

From Fig. 6.8, it can be clearly observed that MO-ADK and ADK yields (left panel) underestimate the numerically determined TDSE yields across a wide intensity range, specifically at peak intensities less than 2×10^{14} W/cm^2. In contrast, the MO-PPT and PPT yields (right panel) are in a good agreement (at least on a logarithmic scale) with those obtained by solving the TDSE. However, the slight deviation between the TDSE results and those obtained from both MO-PPT and PPT models is not significant. Thus, in overall there is no model which agrees with the TDSE calculations for wide intensity range. For instance, a good agreement between the MO-PPT^a and TDSE results are obtained at high intensity, but there is also a small shift between the two results at low intensity, even on a logarithmic scale. The opposite situation can be observed for the MO-PPT^b, MO-PPT^c, and PPT predictions (see the figure). Furthermore, MO-PPT and PPT roughly reproduce the channel closing observed in the TDSE yields, as displayed by the small structure in the curves (the region surrounded by a green circle). In the TDSE, PPT and MO-PPT curves channel closing is not surprising, since the number of photons needed for ionization depends on the ionization potential as well as the ponderomotive energy. The ponderomotive energy increases for increasing intensity (Eq. 2.8). Consequently, changing the number of photons leads to a channel closing displayed in Fig. 6.8.

In general, both MO-ADK and ADK models failed again to reproduce the TDSE calculations even qualitatively, since the slopes provided by the former models are incorrect. However, both MO-PPT and PPT models are able to predict the ionization probability for some diatomic molecules in agreement with the TDSE results not only qualitatively but also quantitatively.

This finding is further confirmed by considering the ionization of O_2 (HOMO is $1\pi_g$). Figure 6.9 is comparable to Fig. 6.8, the only difference is that the system under investigation is O_2. It shows the ionization probability for O_2 as a function of laser peak intensity. The ionization potential for O_2 is the one from the time-independent structure model that forms the basis for the TDSE (12.49 eV). The numerical TDSE data[5] (blue circles) are compared with the probabilities obtained within the MO-ADK, MO-PPT, extended ADK, and PPT models. The ionization probabilities for the MO-ADK and MO-PPT models are calculated with three different sets of C_{lm} values taken from [28, 108, 187]. The superscripts a, b, and d assigned to MO-ADK and MO-PPT in the figure indicate that the molecular ionization probabilities obtained using the C_{lm} coefficients given by Tong *et al.* [28] (red lines), Abu-samha and Madsen [187] (cyan dashed lines), as well as Madsen and co-workers [108] (blue dashed-dot lines), respectively. Furthermore, the

[5]These data are taken from the PhD thesis of Manohar Awasthi [43].

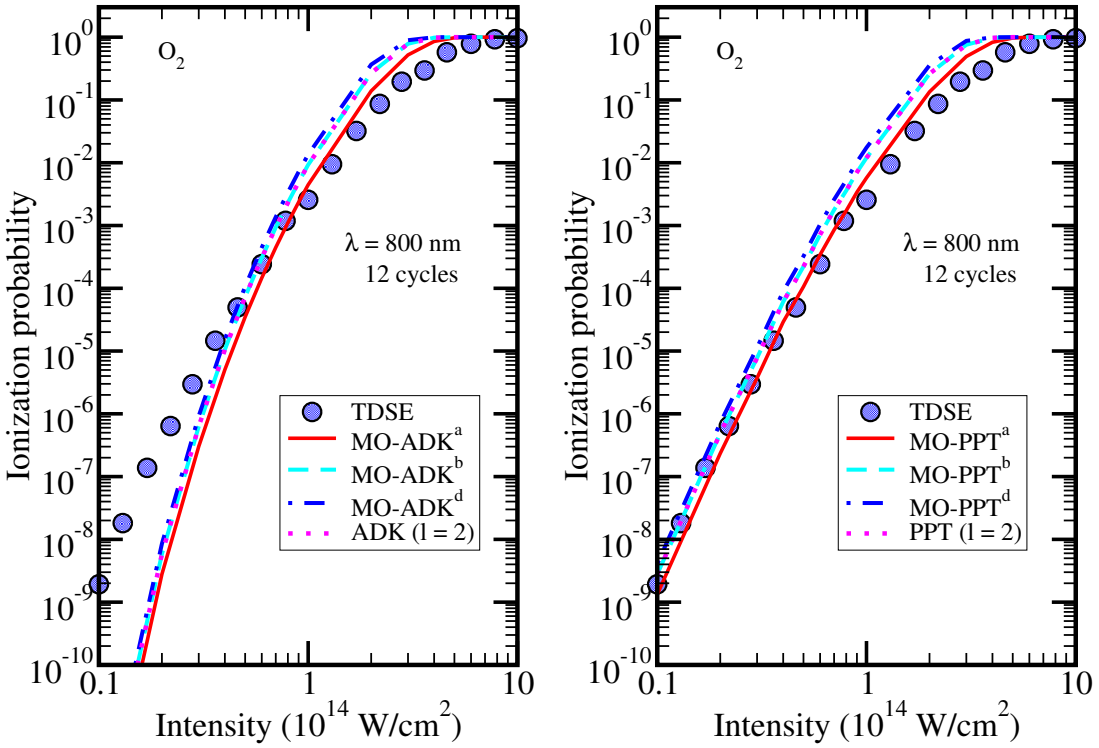

Figure 6.9: As Fig. 6.8, but in the case of O_2 molecule. The superscript d, which follows the MO-ADK and MO-PPT, refers to C_{lm} values taken from [108].

ion probabilities calculated by the extended atomic models (ADK and PPT, with $m = 1$ and $l = 2$) are also plotted (magenta dotted lines).

There is also a clear deviation between both the MO-ADK and ADK yields and the the TDSE yields. Even slopes provided by them are also incorrect. On the other hand, the curves obtained within MO-PPT and PPT approaches give a correct slope for the ionization yields, which are, roughly, close to those predicted by the SAE-TDSE. This result confirms that MO-PPT model and even the simple (extended atomic) PPT model (with proper values for l and m) can correctly predict the ionization behavior for molecular-laser interaction with a reasonable accuracy.

It is noteworthy that the asymptotic parameters C_{lm} used in the molecular ionization models are obtained by an asymptotic fitting of the wavefunctions at large distances. This parameters depend on the accuracy of the wavefunctions obtained according to the method used. Accordingly, differences in the results can be expected by using different sets of C_{lm}. Actually, there are very small shifts between the results, as seen in the MO-ADK results, not only for O_2 but also for N_2. This agreement comes from using the

same ionization potential, which affects strongly on the ionization rate, with the three different sets C_{lm} coefficients. Consequently, they should provide results most consistent with each other.

6.5 Alignment dependence of the ionization rates

As shown in chapter 5, the ionization rate of the molecules in an intense laser field depends on the alignment relative to the laser's polarization direction due to the anisotropy of the electronic charge density. For many years this alignment dependence was basically not discussed until the molecular strong-field approximation (MO-SFA) [15, 26, 108], and the molecular tunneling-ionization theory (MO-ADK) [28, 171] have been introduced. Here, the MO-ADK and MO-PPT models are used to clarify the dependence of the ionization rates of multi-electrons molecules on their alignment with respect to the direction of the laser field.

Pavičić *et al.* [168] conducted experiments on N_2, O_2, and CO_2 molecules with 40 fs and 800 nm in linear polarized laser pulses for different orientations relative to the molecular axis. They reported that the relatively strong angular dependence of the ionization can be interpreted in terms of molecular orbital theory, which means that the measured alignment dependence of the ionization reflects the structure of the HOMO. Some of theoretical studies [121, 180, 187] showed also that the angle-resolved ionization of N_2 and O_2 reproduces the symmetry of the HOMO. This finding has been reasonably well explained by using a simplified strong-field model like MO-ADK theory. On the other hand, study of alignment-dependent total ionization probability of CO_2 with ion measurement shows significant variance from the prediction of the MO-ADK theory and leads to intensive investigations [121, 189, 190]. In the following, the MO-PPT model as well as MO-ADK model are used to simulate the alignment dependence the ionization in laser-electric field for N_2 and O_2.

Figure 6.10 shows the comparison of the angle dependence of the ionization probability of N_2 (top panels) and O_2 (bottom panels) obtained by MO-ADK and MO-PPT models with that obtained by solving the TDSE [121] as well as the experimental data [187]. The ionization potential used in the analytical models (MO-ADK and MO-ADK) differs slightly from that of the numerical computations (e.g. it is 15.58 eV vs. 15.92 eV in N_2 and 12.07 eV vs. 12.50 eV in O_2). The laser intensity used for N_2 is 1.5×10^{14} W/cm^2, while for O_2 is 1.3×10^{14} W/cm^2. The angle-dependent ionization yields for N_2 and O_2 according to MO-ADK and MO-PPT models are obtained by using Eqs. (2.51), (2.50)

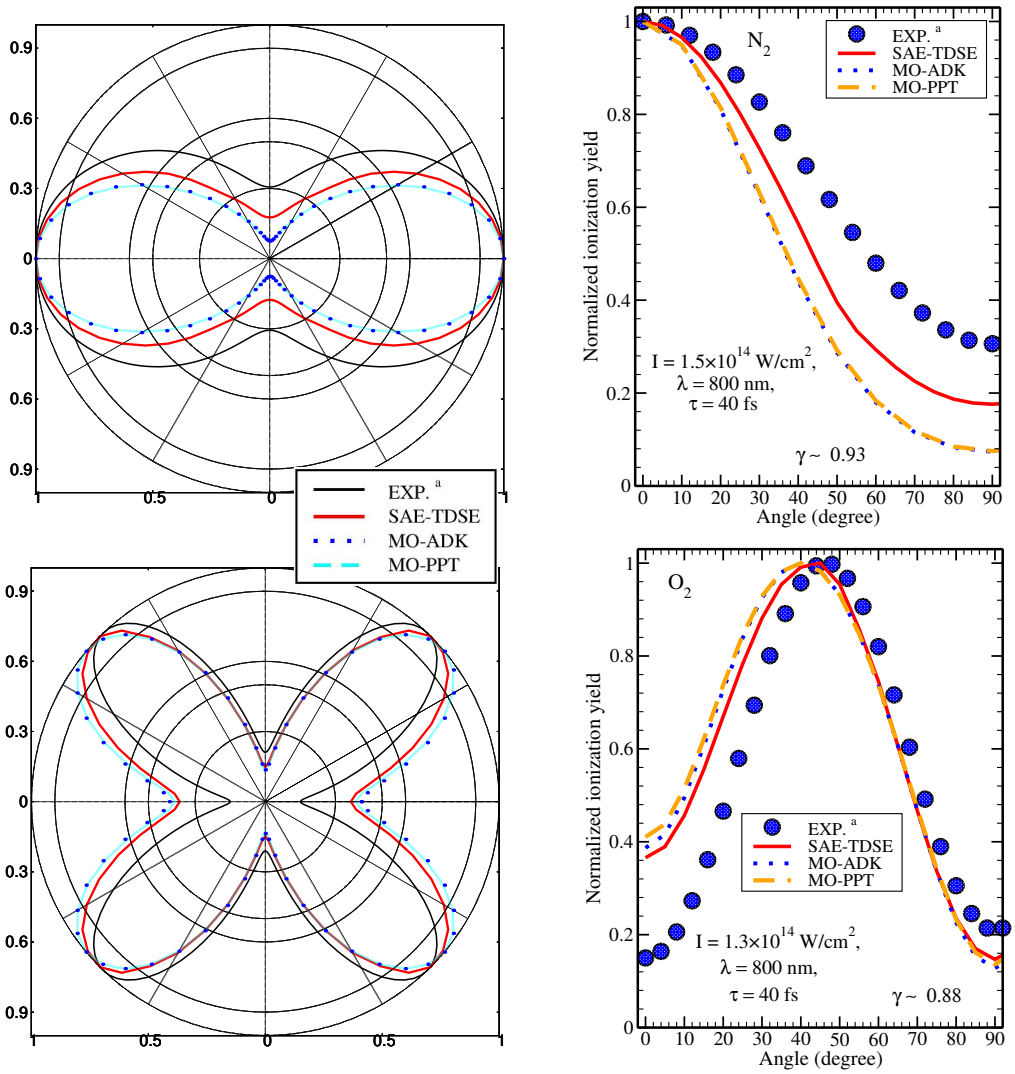

Figure 6.10: Left panels: Normalized ionization probabilities as a function of the angle between the molecular axis and the laser field direction: experimental data [168] (black) and numerical results (red lines) for the HOMO of N_2 (top) and O_2 molecules (bottom), and those obtained within both MO-ADK (blue dashed line) and MO-PPT (green dashed line) models, which are based on the values of C_{lm} [187]. Right panels: Alignment-dependent ionization yields of the HOMO orbitals for N_2 and O_2 molecules are shown. Laser peak intensities are 1.5×10^{14} W/cm^2 in N_2 and 1.3×10^{14} W/cm^2 in O_2.

and (2.52). The ionization yields are calculated based on the C_{lm} coefficients given in Ref. [187] and do not account for focal-volume effects (fluctuations of laser intensity). The pure HOMO contributions, $3\sigma_g$ for N_2 and π_g for O_2, are considered in the calculations, where the ionization from the HOMO-X orbits is neglected, where Xth molecular

orbital energetically below the HOMO (with X = 1, 2, 3, ...). Noteworthy, Telnov and Chu [175] (using TD-DFT) and Petretti *et al.* [121] (using SAE-TDSE) have studied the influence of the inner molecular orbitals on the total probability and showed that the contributions of the inner orbitals are slightly relevant for N_2, while the HOMO is clearly dominant in the case of O_2 molecule. This depends on detailed electronic structure, symmetry, and orientation angle of the molecule in addition to laser field intensity.

As can be seen in Fig. 6.10, for N_2 the ionization yield is largest for a parallel alignment and it monotonically decreases with the alignment angle up to 90°. Regarding O_2, both MO-ADK and MO-PPT predict the maximum ionization yield at 40°, which is slightly below the experimental value (45°) [168] and the theoretical one (44°) using TDSE [121]. In general the agreement is reasonable, especially for $\theta > 40°$, as can be seen from the left panels of the figure. The small shift of the maximum towards the horizontal axis can be explained by the influence of vibrational motion, since O_2 should preferentially ionized at smaller internuclear distances than at the equilibrium one (see Fig. 6.5). The larger asymmetry between parallel and perpendicular orientation found in SAE-TDSE for O_2 is a consequence of the fact that both electrons in the degenerate π_g orbitals (π_g^x, π_g^y) contribute equally in parallel orientation, but effectively only the π_g^x electron contributes in x direction. It is clear from this figure that the agreement between the results obtained from MO-ADK, MO-PPT, and TDSE with the experimental data is generally acceptable. This agreement between MO-ADK and MO-PPT models is expected, because at high intensity, MO-PPT and MO-ADK model tend to have the same formula of ionization rate, as was discussed before.

6.6 Summary

In this chapter, the ADK, PPT, MO-ADK, and MO-PPT models have been applied on large molecules such as N_2 and O_2. The variation of the ionization yield for 800 nm and 400 nm laser wavelengths as a function of the internuclear distance is presented by using three different methods, i.e. the numerical solution of the single-active electron approximation based time-dependent Schrödinger equation (SAE-TDSE), the ADK model, and the PPT model. It is noted that for smaller internuclear distances than the equilibrium value, the ionization yield of O_2 strongly depends on the internuclear distance unlike N_2. This means that O_2 molecule can be ionized at small internuclear distances more easily than at the equilibrium ones. The influence of a proper choice for the values of the l and m quantum numbers for the HOMO of the molecules for the ADK and PPT models

have also been investigated. The laser-induced population distribution of the vibrational states of the formed $X^2\Sigma_g^+$, $A^2\Pi_u^+$ and $B^2\Sigma_u^+$ states in N_2^+, and the population of the vibrational ground states of O_2^+ ($X^2\Pi_g^+$) ion are presented. The lowest vibrational levels of N_2^+ are more populated by the laser interaction than in the case of the Franck-Condon distributions. The shifting of the population probability towards lower vibrational levels is strong for the $A^2\Pi_u^+$ state, whereas it is small for both the $X^2\Sigma_g^+$, and $B^2\Sigma_u^+$ states. On the other hand, the deviation from the Franck-Condon-like distribution is clearly observed in the O_2 molecule. These observations agree with the earlier Saenz's predictions [146] about the influence of the vibrational motion on the ionization rate of O_2 is more strongly than that of N_2.

Furthermore, the dependence of the ionization yields of N_2 and O_2 on the laser peak intensity was studied within the ADK, PPT, MO-ADK, and MO-PPT models. The results were also compared with those obtained from the TDSE calculations. The comparison reveals that the ADK and MO-ADK models are most applicable at higher intensity, i.e. in the tunneling ionization regime, while they are less reliable at lower intensities, i.e. in the multi-photon regime, unlike the PPT and MO-PPT models. Whereas the former models failed to agree with the TDSE calculations across the entire laser intensity range, the ionization probabilities obtained from both the PPT and MO-PPT models fit quite well with those obtained from the TDSE in the whole intensity range. Noteworthy, it is not sense to conjugate the validity of the PPT and MO-PPT models, even the adiabatic Keldysh parameter is much greater than one, with the dominant the tunneling process in a strong laser-field-induced phenomenon, and thus the multi-photon process does not have a significant role. Because the examination of these models shows that they also contain the fundamental signature of the multi-photon process.

Additionally, the alignment dependence of the ionization yields is also investigated within MO-ADK and MO-PPT models, which compared the results with the TDSE and experimental data. The results showed that the angle-resolved ionization of N_2 and O_2 produces the symmetry of the highest occupied molecular orbital (HOMO). Further, a reasonable agreement between both MO-ADK and MO-PPT predictions with the TDSE calculations was found.

7 Summary and Conclusions

In this thesis, the ionization of the simple molecule H_2 and larger molecules like N_2 and O_2 exposed to an intense laser field is theoretically investigated using different theoretical approaches. These approaches include the numerical solution of the time-dependent Schrödinger equation (TDSE), the Ammosov-Delone-Krainov (ADK) model, the Perelomov-Popov-Terent'ev (PPT) model, the frequency corrected ADK (fc-ADK) model, the molecular ADK (MO-ADK) model, and the molecular PPT (MO-PPT) model. The dependence of the ionization yields on the laser parameters, e.g., pulse length, wavelength, and peak intensity, as well as on the alignment of molecules relative to the laser field direction has been considered. Two different laser-wavelengths (800 nm and 400 nm) with different peak intensities and various pulse lengths are used. The quasi-static ionization process constitutes the major part of this study. The transition between the quasi-static regime, where ionization does not depend on the oscillation frequency of the laser electric field, and the high-frequency regime depends on the time scale of ionization dynamics compared with the temporal variation of the laser field. Semi-quantitative measure for the ratio of the two time scales is called Keldysh parameter. In general, it is found that the ADK and MO-ADK models tend to reproduce the TDSE results only in the tunneling region. In contrast, the fc-ADK, PPT and MO-PPT models, which contain a frequency correction, are significantly more consistent with the TDSE over a wider range of laser intensities.

In order to consider the influence of vibrational motion on the strong-field ionization within the Born-Oppenheimer approximation, the internuclear distance-dependent molecular ionization rate is considered. It was found that both the ADK and MO-ADK models fail in most cases to predict the ionization yield quantitatively, although the internuclear distance dependence is qualitatively well reproduced. Nevertheless, it has been also demonstrated that using any of the above tunneling approaches is suitable for observing the nuclear wavepacket dynamics launched in the molecular ion by a laser field. The vibrational-state distributions of H_2^+ for different laser parameters are presented and shown that the low vibrational states are more populated than the higher ones. Our results confirm the strong dependence of the ionization yield on the internuclear

distance as was previously predicted and also experimentally observed. Subsequently, the wavepacket created in the molecular ion exposed to a laser field is not correctly described by the **F**ranck-**C**ondon factors that are so far used for the interpretation of the experimental data. It was also shown that the deviation from the Frank-Condon distribution is more pronounced for lower intensities, i.e. intensities below 10^{14} W/cm^2.

Furthermore, the evolution of the vibrational nuclear wavepacket on the potential curve ($1s\sigma_g$) of H_2^+ was discussed. The effect of bond softening on the dynamics of the wavepacket has been considered. It was found that the bond softening affects the ionization threshold as well as the revival time of the vibrational wavepacket. The latter decreases with increasing laser peak intensity. The reason is due to the distortion of the energy surface caused by the laser-field, leading to a reduced threshold energy compared to the field-free one. Thus, the distortion of the energy surface leads to a change of the dissociation energy and subsequently to different phases between the components of the wavepacket. It was found that in the field-free case the revival time of the vibrational wavepacket depends on the model describing the vibrational-state distribution. For example it is 283 fs, if the Franck-Condon approximation is used, and 275 fs if the R-dependent models are used in the field-free case, i.e. ignoring the bond-softening.

Some experimental and theoretical studies showed that the alignment-dependent ionization probabilities of H_2 depend on the laser intensity, and the anisotropy deviates from the prediction of the molecular tunneling ionization model (MO-ADK), which is independent on both the laser intensity and the wavelength. The origin of this deviation in the MO-ADK model was studied in this thesis within linear and circular polarized laser fields. It was found that the anisotropy for an H_2 molecule in a strong field generally decreases for increasing laser intensity and the pattern of decrease depends on the duration of the laser pulse. This finding agrees with the experimental observations. Including the focal-volume effect of the laser pulse leads to a significant improvement in the MO-ADK predictions, especially in a circular polarized field. Moreover, the absolute value of the anisotropy depends on the polarization of a laser field, i.e. linear or circular polarized. Interestingly, the MO-ADK predictions are generally in a reasonable agreement with the experimental data, in contrast to previous claims in literature, especially if the focal volume of the laser field is considered. Noteworthy, the earlier constant value of the anisotropy predicted by MO-ADK model was the value of ratio between the ionization *rates* not *yields*, since the saturation effect was not considered. In addition to the tunneling ionization probability in the presence of a static field is not the same as in a circularly polarized field, although the absolute value of the electric field intensity in the circular polarized field is time-independent. The reason for this difference is that

the probability of tunneling depends on the magnetic quantum number of a tunneling electron, since in a circularly polarized field, the projection of the electron moment is conserved in the direction of the laser wave propagation rather than in the direction of the electric field that varies with time. Furthermore, based on accurate *ab initio* ionization rates calculations for H_2 in the fixed-nuclei approximation, an adjustable parameter for the MO-ADK tunneling model into the barrier-suppression regime is presented. A further improvement in a MO-ADK prediction is found, especially at high intensities.

After using the various versions of analytical tunneling models for H_2, those versions were applied – besides solving the TDSE within the single-active-electron approximation (SAE-TDSE) – to larger the molecules N_2 and O_2. The dependence of the ionization of N_2 and O_2 on both the internuclear distance and the peak intensity was investigated and compared with the accurate TDSE calculations. The ionization yields of N_2 molecule depend weakly on the internuclear distance unlike the one of the O_2 molecule. The intensity-dependent-ionization yield for N_2 and O_2 predicted by the ADK and MO-ADK models exhibits a very poor agreement with SAE-TDSE predictions, as for the H_2 molecule. There are not only quantitative deviations but also the slopes of the curves are incorrect. This failure is not surprising according to the values of the Keldysh parameters and the classical over-the-barrier ionization threshold limits. Therefore, the applicability of the simple tunneling models like ADK and MO-ADK should be limited to a very small range of intensities. However, PPT and MO-PPT models cured the failure which was found in both ADK and MO-ADK models, respectively. Thus, the former models are able to predict qualitatively and often even quantitatively the approximate SAE-TDSE results. Noteworthy, the PPT and MO-PPT models also contain the fundamental signature of the multi-photon process like channel closing, but necessarily fail to reproduce the resonant enhanced multi-photon ionization.

The population distributions of the vibrational states of the formed $X^2\Sigma_g^+$, $A^2\Pi_u^+$, and $B^2\Sigma_u^+$ states of N_2^+, in addition to the population of the vibrational ground states of O_2^+ ($X^2\Pi_g^+$) are also presented. The lowest vibrational levels of N_2^+ are more strongly populated by the laser interaction than predicted by the Franck-Condon distributions. The shift of the population probability toward lower vibrational levels is strong for the $A^2\Pi_u^+$ state, whereas it is small for both the $X^2\Sigma_g^+$, and $B^2\Sigma_u^+$ states. On the other hand, the deviation from a Franck-Condon-like distribution is clearly observed in the O_2 molecule as it was the case for H_2 molecule. By choosing the proper values of the quantum numbers l and m that are related to the highest occupied molecular orbital, the applications of atomic ADK and PPT models to the N_2 and O_2 molecules have been investigated. Using proper values of l and m in the atomic ADK and PPT models gives

a reasonable agreement with the MO-ADK and MO-PPT results, respectively, as well as with the yields calculated numerically by solving the TDSE. Finally, the dependence of the ionization yield on the alignment of N_2 and O_2 with respect to the laser field axis was investigated within the MO-ADK and MO-PPT models. The results show that the angle-resolved ionization of N_2 and O_2 reproduces mostly the shape of the highest occupied molecular orbital (HOMO). Furthermore, a good agreement between the MO-ADK and MO-PPT predictions with the TDSE calculations was found.

In conclusion, the fc-ADK, PPT, and MO-PPT models can successfully reproduce the TDSE calculations for ionization of diatomic molecules within a wider range of laser peak intensities. The deviation from the Franck-Condon approximation have to be considered, since the electronic-binding energy and, of course, the ionization rate depend on the internuclear distance. Moreover, the focal volume of the laser pulse affects the ionization yields, so that it should be taken into account, especially for high intensities. Furthermore, the revival time of the wavepacket is sensitive to the peak intensity of the laser pulse, since it decreases for increasing peak intensity. Finally, in the presence of a circular polarized field, the mean average of the ionization rates have to be considered if the propagation of the circular polarized field is considered to be perpendicular to the molecular axis.

This work opens the way for many studies for future consideration. For example, the vibrational states distributions of the initial ground states of the molecular ion can be used to image the dynamics of the nuclear vibrational wavepacket in H_2^+ by choosing appropriate probe pulse and time delay (the delay between pump and probe pulses). Furthermore, the relativistic effects and the rotational motion are completely ignored in this work, which have to be considered in the future work and subsequently the rotational wavepackets can also be generated and investigated. For future analysis more models and molecules could be added to the comparison and more experimental data as application examples could be simulated. In addition to the validity of those tunneling models may extended to the large molecules (beyond diatomic molecules).

Appendices

A Atomic units (a.u.)

In atomic physics literature it is common to express dimensions in atomic units (a.u.). Atomic units is a unit system which aims to simplify the equations describing atomic processes on their respective time, length or energy scale. Furthermore, they give a sense of how the characteristics that are considered related to atomic scales. In addition, they allow to define whether the process is slow or fast, a length of a small or large compared to the nuclear dimensions. The atomic units originate from the typical dimensions of the hydrogen atom. They are defined by setting the electron mass m_e, the elementary charge e as well as $\hbar$ (the Planck's constant/2π) and the Coulomb force constant $1/(4\pi\epsilon_0)$, to unity[1].

Atomic units have many advantages, not least that they bring the electronic Schrödenger equation to its intrinsically simplest form, expressed in pure numbers only, so that it can be solved once for all, independent of remeasured physical quantities. The atomic units are also sensibly proportioned and "sized" such that the key atomic properties tend to have values of order unity; for example, the hydrogenic 1s orbital radius turns out to be exactly 1 a.u. of length. By working out the combination of e, m_e, and $\hbar$ whose practical units match those of a desired physical property (such as energy $m_e\, e^4/\hbar^2$, length $\hbar^2/m_e\, e^2$, and so forth), one obtains the corresponding "atomic unit" of that property, which is usually designated simply as "a.u." rather than assigned a special symbol and name for each property.

Values of atomic units for different physical quantities can be obtained starting from the values of $\hbar$, m_e, e and $4\pi\epsilon_0$ (a_0) in SI. Table 4.1 provide some basic dimensions in atomic units together with the corresponding quantity in the SI system and gives associated expressions.

[1] In the applications, the definition of atomic units is referred by the phrase "$\hbar = m_e = e = 4\pi\epsilon_0 = 1\,\mathrm{a.}u.$".

Table A.1: Conversion factors from atomic to SI units

Quantity (Symbol)	Atomic units	SI value
Mass (m_e)	m_e	$9.10939 \,.\, 10^{-31}$ Kg
Charge (Q)	e	$1.60219 \,.\, 10^{-19}$ C
Ang. mom. ($\hbar$)	$h/2\,\pi$	$1.05457 \,.\, 10^{-34}$ J/(s rad)
Permittivity (ϵ_0)	$k = 4\pi\epsilon_0$	$1.11365 \,.\, 10^{-10}$
Length (a_0)	$k\,\hbar^2/m_e\,e^2$	$5.29177 \,.\, 10^{-11}$ m
Velocity (V)	$e^2\ k\,\hbar$	$2.18769 \,.\, 10^{6}$ m s^{-1}
Energy (E_h)	$m_e\,e^4/k^2\,\hbar^2$	$4.35974 \,.\, 10^{-18}$ J
Time (τ)	$k^2\,\hbar^3/m_e\,e^4$	$2.41888 \,.\, 10^{-17}$ s
Frequency (ν_0)	$1/\tau$	$4.13414 \,.\, 10^{16}$ Hz
Power (P_0)	E_h/τ	$1.80238 \,.\, 10^{-1}$ W
Intensity (I_0)	P_0/a_0^2	$6.43641 \,.\, 10^{15}$ W cm^{-2}
El. field strength (F)	$e/k\,a_0^2$	$5.142206 \,.\, 10^{11}$ V m^{-1}
El. potential (U_0)	$e/k\,a_0$	27.11 V
El. dip. mom. (d)	$k\,\hbar^2/m_e\,e$	$8.47836 \,.\, 10^{-30}$ C m (= 2.54 Debye)
Mag. dip. mom.	$e\,\hbar/2m_e$	$9.27402 \,.\, 10^{-24}$ J/T
Momentum (P)	$m_e e^2/k\,\hbar$	$1.9929 \,.\, 10^{-26}$ Kg m/s

B The focal volume effect

One of the main challenges high-intensity experimentalists face when comparing experimental results to theoretical models and predictions is due to the geometry of the laser focus. However, for a given non-uniform of a laser pulse such as Gaussian spatial profile, the central and the outer portions of any beam correspond to very different intensities. The effect is known as the focal volume spatial intensity averaging in which often presents such as above challenge in comparing experimental results to theoretical prediction. Whereas, most of theoretical models and publications present their results for a given *single* intensity. Physically, it is not possible obtained a single intensities with some maximal value in the center of the focal plan because the laser intensity varies in the laser focus. There is no effective way to control the laser-atom interaction only to occur at the center of the laser focus with the peak intensity, mainly because the size of the laser focus is too small, which is on the order of a micron in cross section. However, near the focus there is a gradient in the intensity and off-center interactions, which happen with lower intensities than the peak intensity, cannot be avoided. Therefore, intense-field studies which require a laser to be focused to reach their necessary peak intensities commonly suffer from the focal volume effect. Focal volume effect means that a poorly-defined intensity in an experiment, since ions may be collected from a large region comparable to the size of the focus. This can be particularly disturbing in determining the mechanisms underlying ionization.

The laser focus presents a considerable complication for studying high-intensity phenomena. In recent years, with the advent of shorter and shorter pulse, focusing has become much easier than before. The relation between the waist radius, ω_0, and the beam radius, ω, for Gaussian is given by [23]

$$\omega_0 = \frac{\lambda f}{\pi \omega} \tag{B.1}$$

where, λ and f are the wavelength and the focal length. The waist radius, i. e. the radius of the focus, is defined as the radius at which the laser intensity has dropped by a factor of e^2 with respect to the intensity at the center of the focus. Along the axis

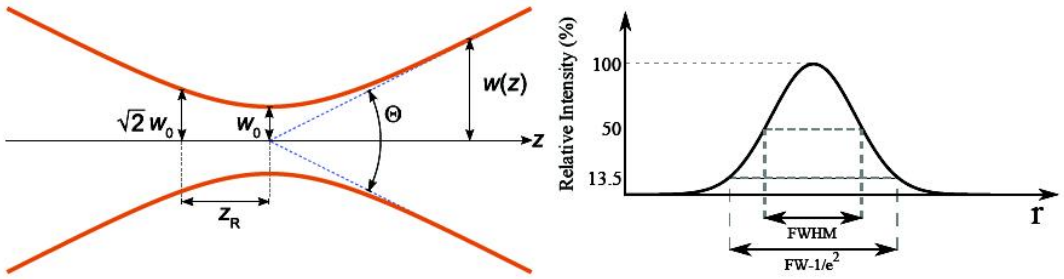

(a) Propagation of a Gaussian beam (b) Beam width definitions

Figure B.1: (a) Illustration the propagation of a Gaussian beam, in which Z_R is Rayleight range, ω_0 is the beam waist, the z direction is the direction of propagation and $\omega(z)$ is the beam width as a function of the axial distance z, and Θ is the total angular spread.
(b) shows a Gaussian profile with two common definitions of beam diameter. This figure is reprinted from Ref. [191].

of the laser beam, the length of the focus is indicated by the Rayleight range, Z_R. It is defined as longitudinal distance over which the minimum waist size ω_0 increases by a factor of $\sqrt{2}$ (see Fig. B.1(a)). It is given by

$$Z_R = \frac{\pi\,\omega_0^2}{\lambda} \tag{B.2}$$

While, the beam waist at an arbitrary z is found by

$$\omega(z) = \omega_0\sqrt{1 + z^2/Z_R^2} = \omega_0\sqrt{1 + \left(\frac{z\,\lambda}{\pi\,\omega_0^2}\right)^2}. \tag{B.3}$$

Equation (B.3) is a 2^{nd}-order polynomial; plotting this equation leads to the upper-half of the focused ray from Fig. B.1(a). Furthermore, the diameter of a beam can be determined by the Full-Width at Half Maximum (FWHM), which is defined as the full width of the beam at half of the maximum intensity. Another standard is with respect to the $1/e^2$ point, which is defined as 13.5 % of the maximum intensity (see Fig. B.1(b)).

As the beam power is increased to generate intensities high enough to saturate the ion yield, the yield increases as $P \propto I^{3/2}$ regardless the ionization process for a Gaussian beam focus [52]. This relation occurs due to the growing size of the interaction volume where the fields are strong enough to ionize the target. Quantitative inclusion of the FVE depends on the laser focus. In the case of a perfect focus of a Gaussian beam, the geometry of which is shown in Fig. B.1, the focal volume $V(I_0, I)$ where the intensity is

above some value I ($< I_0$) is given by [23]

$$V(I_0, I) \,=\, \pi\, \omega_0^2\, Z_R \left(\frac{4}{3}\beta \,+\, \frac{2}{9}\,\beta^3 \,-\, \frac{4}{3}\mathtt{arctan}(\beta) \right), \tag{B.4}$$

with

$$\beta \,=\, \sqrt{\frac{I_0 \,-\, I}{I}}\,. \tag{B.5}$$

The variation of the laser intensity along the time-envelope of the laser pulse needs to be taken into account to calculate the ionization probability. On the other hand, if the model solves the TDSE by numerical integration (for a laser pulse with given peak intensity and short pulse duration), the probabilities P will follow directly from the calculation. However, these probabilities cannot be compared directly to experimental data. Whereas, the peak laser intensity is a function of the position in the focus, the experimental data is extremely complex. In other words, the values P are only true for a certain location in the laser focus, i.e. $P = P(I)$. To obtain the expected signals, $P^{\mathrm{FVE}}(I_0)$, for a certain experiment, one must integrate over the volume of the focus, i. e.

$$P^{\mathrm{FVE}}(I_0) \,=\, \int_0^{I_0} P(I) \left[-\frac{\partial V(I_0, I)}{\partial I} \right] dI\,. \tag{B.6}$$

Where $P(I)$ is the probability density of obtaining the physical quantity with intensity I. According to Eq. (B.4), it can be derived that:

$$-\frac{\partial V(I_0, I)}{\partial I} \,\propto\, \frac{I_0}{3\, I^2} \sqrt{\frac{I_0 \,-\, I}{I}} \left(\frac{2\, I}{I_0} \,+\, 1 \right). \tag{B.7}$$

Hence, Eq. B.6 can be reworded as

$$P^{\mathrm{FVE}}(I_0) \,\propto\, \int_0^{I_0} P(I) \left[\frac{I_0}{3\, I^2} \sqrt{\frac{I_0 \,-\, I}{I}} \left(\frac{2\, I}{I_0} \,+\, 1 \right) \right] dI\,. \tag{B.8}$$

The meaning of Eq. B.8 is that an experimentally detected signal with a peak intensity I_0 contains contributions from off-center events, the weight of which at each lower intensity I is proportional to the volume of the shell with intensity I and to the probability of obtaining the physical event with intensity I.

C Solving TDSE with spectral method

An alternative approach for solving the TDSE describing molecular hydrogen exposed to short intense laser pulses will be given in this appendix. This approach based on a spectral method in which the time-dependent electronic wavefunction is expanded in terms of a superposition of field-free eigenstates that result from CI calculation and thus include correlation[1].

First of all, the basic steps for the solution of the field-free two-electron Schrödinger equation will be shown in Secs. C.1 and C.2. Followed by the details of time-propagation in the basis of field-free states that are shown in Section C.3. The calculations are based on a method developed by Prof. A. Saenz and co-workers [109, 120][2].

C.1 One-electron Schrödinger equation (OESE)

The one-electron Schrödinger equation (OESE) for a diatomic molecule is solved in prolate-spheroidal coordinates[3] within the Born-Oppenheimer approximation. This is implemented by putting the diatomic molecule in a finite volume or a box. A schematic diagram describing the system is shown in Figure C.1. The nuclei A and B are separated by the fixed internuclear distance R. The electron is at distances r_A and r_B from nuclei A and B, respectively. The coordinate transformation to prolate spheroidal coordinates ($\xi \in [1,\infty); \eta \in [-1,1]; \phi \in [0,2\pi]$) is done in the following manner,

$$\xi = \frac{r_A + r_B}{R} \quad \text{and} \quad \eta = \frac{r_A - r_B}{R}\,. \tag{C.1}$$

ϕ is the angle around the internuclear axis. It is assumed that the one-electron Hamiltonian $\hat{\mathrm{h}}$ possesses rotational symmetry with respect to the internuclear axis. Therefore, it can be written as

$$\hat{\mathrm{h}} = -\frac{1}{2}\nabla^2 + V(\xi,\eta)\,. \tag{C.2}$$

[1] This approach is also known as the spectral method.
[2] The content of this appendix follows the description given in [43, 192]
[3] For more details about prolate-spheroidal coordinates system see Sec. 2.2 in Ref. [192].

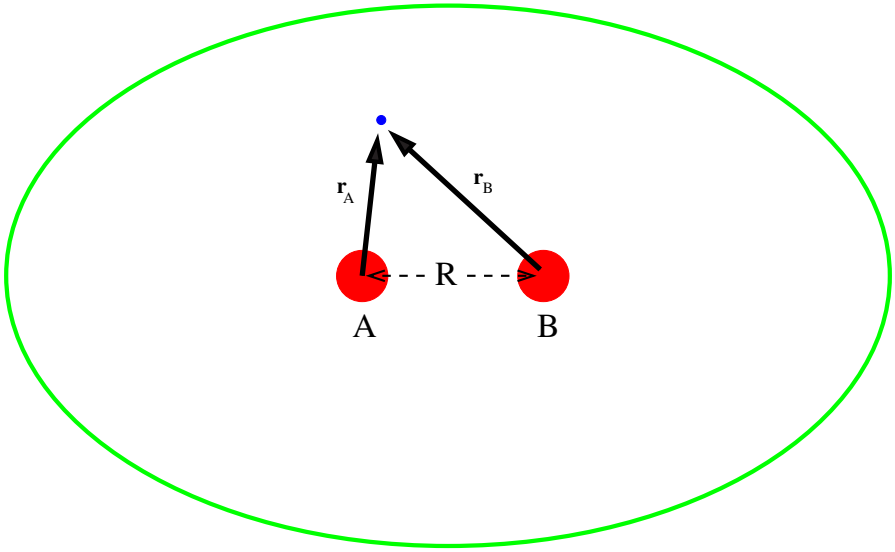

Figure C.1: A schematic representation of effective one-electron system. The green boundary represents the enclosing box.

The function $V(\xi,\eta)$ depending on the interaction between an effective electron and ionic cores is not specified at this point. Solving the OESE ($\hat{\mathrm{h}}\psi = \epsilon\psi$) yields the orbitals ψ. Due to the rotational symmetry, the orbitals ψ can be specified by the quantum numbers $\lambda = 0, 1, \ldots$ and $m = \pm\lambda$. In the case of homonuclear diatomic molecular systems, like H_2^+ , the function $V(\xi,\eta)$ satisfies the condition $V(\xi,-\eta) = V(\xi,\eta)$ and the Hamiltonian $\hat{\mathrm{h}}$ also possesses inversion symmetry with respect to the midpoint between the nuclei,

$$\xi \to \xi, \quad \eta \to -\eta, \quad \phi \to \phi + \pi\,. \tag{C.3}$$

The eigenvalue $\mathcal{P}$ of the inversion operator is equal to 1 for *g*erade and -1 for *u*ngerade states. Thus, $\{\lambda, m, [\mathcal{P}]\}$ (square bracket for optional quantum numbers) represent the set of quantum numbers for diatomic molecules. Whereas the energy does not depend on m, $|\gamma| \equiv \{\lambda, [\mathcal{P}]\}$ is introduced. For example, in the case of H_2^+ orbitals with symmetry σ_g and π_u correspond to $|\gamma| = \{0, 1\}$ and $\{1, -1\}$, respectively.

Using the rotational symmetry of the OESE,

$$\hat{\mathrm{h}}\,\psi_\nu^\gamma = \epsilon_\nu^{|\gamma|}\,\psi_\nu^\gamma, \tag{C.4}$$

the orbitals ψ_ν^γ can be written as

$$\psi_\nu^\gamma(\xi,\eta,\phi) = \frac{1}{\sqrt{2\pi}}\,\psi_\nu^{|\gamma|}(\xi,\eta)\,e^{\mathrm{i}m\phi}, \tag{C.5}$$

where $e^{\mathrm{i}m\phi}$ are the corresponding angular solutions. If the potential $V(\xi,\eta)$ has the form

$$V(\xi,\eta) = -\frac{2}{R^2(\xi^2-\eta^2)}\left\{Z_\xi(\xi)+Z_\eta(\eta)\right\} \tag{C.6}$$

with functions $Z_\xi(\xi)$ and $Z_\eta(\eta)$ depending on a single variable, the OESE is separable.

The OESE is solved in a confined volume or an elliptical 'box'. The box is spanned by ξ and η coordinates and knot-sequences are chosen in these two directions. The flexibility in choosing a knot sequence leads to an accurate description of wavefunction and energy. At each of these knot points the wavefunction is described by a B-spline of certain order. By using B-splines one gets a continuous description of the space within the box such that any wavefunction can be correctly described. The order and number of B-splines[4] [193] determine the quality of the basis set. It has to be chosen carefully and should be checked for convergence. Another important quantity is the box size. It should be sufficiently large and also checked for convergence. For further details of the solution of OESE see Ref. [120].

C.2 Two-electron basis set and configuration-interaction approach

As a basis set for solving the two-electron Schrödinger equation

$$\hat{\mathrm{H}}(1,2)\,\Psi(1,2) = \Big(\hat{\mathrm{h}}(1)+\hat{\mathrm{h}}(2)+\frac{1}{r_{12}}+V_{AB}(R)\Big)\Psi(1,2) = E\,\Psi(1,2), \tag{C.7}$$

the configuration interaction (CI) approach is used. The potential $V_{AB}(R)$ is either the Coulomb interaction Z_AZ_B/R or describes the interaction between two cores. Let Γ specify the full set of quantum numbers, $\Gamma \equiv \{\Lambda, M, S, [\mathcal{P}, \mathcal{P}^\Sigma]\}$, where $\Lambda = 0, 1, 2, \dots$ is the absolute value of the component of the total angular momentum along the internuclear axis $(\Sigma, \Pi, \Delta, \dots)$, $M = \pm\Lambda$, and the total spin $S = 0, 1$. The optional quantum numbers $\mathcal{P}$ and $\mathcal{P}^\Sigma$ specify the parity with respect to inversion symmetry (*gerade* or *ungerade*, cf. Eq. (C.3)) and, for Σ states only, with respect to a reflection at a plane

[4] *B*-splines are the main tools of the approach used in obtained the numerical results for TDSE in the present thesis.

through the nuclei,

$$\xi_i \to \xi_i, \qquad \eta_i \to \eta_i, \qquad \phi_i \to -\phi_i. \tag{C.8}$$

This transformation is equivalent to a complex conjugation of the wave function, if the normalization of the latter is chosen in such a way, that only its angular part is complex.

Normalized and fully symmetry-adapted configurations Υ_i^Γ are used in the CI calculations. The configurations are build with the aid of products of two orbitals

$$|\nu\gamma\ \bar{\nu}\bar{\gamma}\rangle \equiv \psi_\nu^\gamma(\xi_1,\eta_1,\phi_1)\,\psi_{\bar{\nu}}^{\bar{\gamma}}(\xi_2,\eta_2,\phi_2) \tag{C.9}$$

with $\bar{\gamma} \equiv \{\bar{\lambda}, \bar{m}, [\bar{\wp}]\}$. For a given configuration $\Upsilon_i^\Gamma \equiv [\nu\gamma\,\bar{\nu}\bar{\gamma}]$ the orbitals $\nu\gamma$ and $\bar{\nu}\bar{\gamma}$ satisfy the conditions $m + \bar{m} = M$ and $\wp\bar{\wp} = \mathcal{P}$. For non-$\Sigma$ states ($\Lambda \neq 0$) particle-exchange symmetry is considered using

$$[\nu\gamma\,\bar{\nu}\bar{\gamma}]_{\Lambda\neq 0} = \frac{|\nu\gamma\ \bar{\nu}\bar{\gamma}\rangle + (-1)^S|\bar{\nu}\bar{\gamma}\ \nu\gamma\rangle}{\sqrt{2(1+\delta_{\nu\bar{\nu}}\delta_{\gamma\bar{\gamma}})}} \quad . \tag{C.10}$$

For Σ states ($\Lambda = 0$) inclusion of the additional reflection symmetry leads to (note the misprint in [120])

$$[\nu\gamma\,\bar{\nu}\bar{\gamma}]_{\Lambda=0} = \frac{\big(|\nu\gamma\ \bar{\nu}\bar{\gamma}\rangle + (-1)^S|\bar{\nu}\bar{\gamma}\ \nu\gamma\rangle\big) + \mathcal{P}^\Sigma\big(|\nu\gamma\ \bar{\nu}\bar{\gamma}\rangle + (-1)^S|\bar{\nu}\bar{\gamma}\ \nu\gamma\rangle\big)^*}{\sqrt{4(1+\delta_{\nu\bar{\nu}}\delta_{|\gamma||\bar{\gamma}|})(1+\delta_{0m}\delta_{0\bar{m}})}} \tag{C.11}$$

where it was used that two different orbitals with the same ν and $|\gamma|$ can be obtained from each other by complex conjugation. Using the relation

$$\begin{aligned} |\nu\gamma\ \bar{\nu}\bar{\gamma}\rangle^* &\equiv |\nu\{\lambda, m, [\wp]\}\ \bar{\nu}\{\bar{\lambda}, \bar{m}, [\bar{\wp}]\}\rangle^* \\ &= |\nu\{\lambda, -m, [\wp]\}\ \bar{\nu}\{\bar{\lambda}, -\bar{m}, [\bar{\wp}]\}\rangle \equiv |\nu\gamma^*\ \bar{\nu}\bar{\gamma}^*\rangle \end{aligned} \tag{C.12}$$

configuration, Eq. (C.11) can finally be represented as a linear combination of products of two orbitals. Clearly, the choice of $\nu\gamma$ and $\bar{\nu}\bar{\gamma}$ has always to be done in such a way that a double occurrence of the same configuration is prevented. The two-electron problem

$$\hat{\mathrm{H}}(1,2)\,\Psi_\mu^\Gamma(1,2) = E_\mu^\Gamma\,\Psi_\mu^\Gamma(1,2) \tag{C.13}$$

is solved by an expansion of the wavefunctions as linear combinations of N_Γ configurations,

$$\Psi_\mu^\Gamma(1,2) = \sum_{i=1}^{N_\Gamma} C_{\mu i}^\Gamma \Upsilon_i^\Gamma(1,2). \tag{C.14}$$

Due to the orthonormality of the set $\{\Upsilon_i^\Gamma\}$ the ordinary matrix eigenvalue problem

$$\underline{\mathbf{H}}^\Gamma \mathbf{C}^\Gamma = E^\Gamma \mathbf{C}^\Gamma \quad \text{with} \quad \underline{\mathbf{H}}_{ij}^\Gamma = \int_{V_1}\int_{V_2} \mathrm{d}v_1\, \mathrm{d}v_2 \Upsilon_i^{\Gamma *}(1,2)\hat{\mathrm{H}}(1,2)\Upsilon_j^\Gamma(1,2) \tag{C.15}$$

is obtained. The coefficients $\{C_{\mu i}^\Gamma\}$ and energies E_μ^Γ are calculated using LAPACK subroutine DSPEVX. The CI matrix elements $\underline{\mathbf{H}}_{ij}^\Gamma$ comprise one- and two-electron integrals. The evaluation of the one-electron integrals is trivial, because the orbitals are solutions of the one-electron Hamiltonian. For further technical details see Reference [120].

The results should be checked for convergence by including additional configurations from higher or lower angular momentum states. After successfully calculating the energies and wavefunctions for the two-electron molecule, the symmetry allowed electronic transition dipole moments are also calculated.

If a time-dependent solution of H_2^+ in a laser field is needed, the symmetry allowed electronic transition dipole moments are calculated and a time-propagation is performed. The time-propagation scheme for H_2^+ and H_2 is the same and will be discussed in the next section.

C.3 Time propagation method

In this appendix, a general approach for solving the TDSE describing molecules exposed to a laser field is clarified. The method can be applied to systems where the time-dependent interaction takes place over a finite time. The time-dependent Schrödinger equation (TDSE) is solved by expanding the time-dependent wavefunction in terms of field-free (time-independent) states. The total in-field Hamiltonian of a system is given by

$$\hat{\mathrm{H}}(t) \;=\; \hat{\mathrm{H}}_0 \;+\; \hat{\mathrm{D}}(t)\,, \tag{C.16}$$

where $\hat{\mathrm{H}}_0$ is the field-free electronic Born-Oppenheimer Hamiltonian of the molecule and $\hat{\mathrm{D}}(t)$ is the operator describing the laser-molecule interaction, expressed in the velocity gauge or in the length gauge. The non-relativistic approximation is used for both operators, and the interaction with the laser field is described within the dipole approximation. In velocity gauge $\hat{\mathrm{D}}(t) = \mathbf{A}(t)\cdot\mathbf{p}/c$, and in length gauge $\hat{\mathrm{D}}(t) = -\mathbf{F}(t)\cdot\mathbf{r}$. $\mathbf{A}$ is the vector potential of the laser field, $\mathbf{p}$ is the total momentum operator of the electrons, c is the velocity of light in vacuum, $\mathbf{F}(t)$ is the electric field vector and $\mathbf{r}(\equiv \mathbf{r}_1, \mathbf{r}_2)$ is the

position vector of the electrons. The resulting TDSE

$$\mathrm{i}\,\frac{\partial}{\partial t}\Psi(\mathbf{r},t) = \hat{\mathrm{H}}\Psi(\mathbf{r},t)\,, \tag{C.17}$$

is then solved by expanding the time-dependent molecular wavefunction Ψ according to

$$\Psi(\mathbf{r},t) = \sum_{nL} b_{nL}(t)\,\phi_{nL}(\mathbf{r})\,. \tag{C.18}$$

in terms of the time-independent wavefunctions $\phi_{nL}(\mathbf{r})$. The latter are solutions of the field-free molecular Schrödinger equation

$$\hat{\mathrm{H}}_0\,\phi_{nL}(\mathbf{r}) = E_{nL}\,\phi_{nL}(\mathbf{r})\,. \tag{C.19}$$

The two-electron wavefunctions $\phi_{nL}(\mathbf{r})$ are orthonormal and symmetric with respect to the reflection symmetry. The compound index L represents the total angular momentum $(\Sigma, \Pi, \Delta, \dots)$ and the symmetry *g*erade or *u*ngerade, and in the case of Σ symmetry $P^{\Sigma} = \pm 1$. The n is just an index of a state with the particular symmetry L. The solution of the time-independent Schrödinger equation is in this approach obtained by solving Eq. (C.19) within a finite volume or a box. The solution within a finite volume leads to discretized states. Thus, the index n remains discrete even for states in the electronic continuum. The solution of Eq. (C.19) for H_2 can be obtained by doing a CI using H_2^+ orbitals or using density-functional theory (DFT) within single-active-electron (SAE) approximation. The solution of the TDSE needs the discretized, symmetry adapted electronic solution of the time-independent Schrödinger equation.

Substitution of Eq. (C.18) into the TDSE Eq. (C.17), multiplication of the result by ϕ^*_{mK}, and integration over the electronic coordinates yields

$$\mathrm{i}\,\frac{\partial}{\partial t}b_{mK}(t) \;=\; E_{mK}b_{mK}(t) \;+\; \sum_{nL} D_{mK,nL}(t)\,b_{nL}(t)\,, \tag{C.20}$$

with $D_{mK,nL}(t) = \langle \phi_{mK}\,|\hat{\mathrm{D}}(t)|\,\phi_{nL}\rangle$. $D_{mK,nL}(t)$ contains the laser-pulse parameters[5]. It should be confirmed that with this approach the complete time dependence is incorporated in the coefficients b_{nL}. The coefficients b_{nL} are complex and can be split up into real and imaginary parts for further simplification,

$$b_{nL} \;=\; b^{\mathrm{r}}_{nL} \;+\; \mathrm{i}\,b^{\mathrm{im}}_{nL}\,. \tag{C.21}$$

[5] A laser pulse can be characterized by its intensity, central frequency and spatial time profile.

Separating into real and imaginary parts gives

$$-\frac{\partial}{\partial t} b^{\mathrm{im}}_{mK}(t) \;=\; E_{mK} b^{\mathrm{r}}_{mK}(t) \;+\; \sum_{nL} D_{mK,nL}(t)\, b^{\mathrm{r}}_{nL}(t)\,, \tag{C.22}$$

$$\frac{\partial}{\partial t} b^{\mathrm{r}}_{mK}(t) \;=\; E_{mK} b^{\mathrm{im}}_{mK}(t) \;+\; \sum_{nL} D_{mK,nL}(t)\, b^{\mathrm{im}}_{nL}(t)\,. \tag{C.23}$$

These Equations are in real variables. They can be solved numerically using a solver for the coupled first-order differential equations. A commercial NAG routine, *D*02CJF, based on variable-order, variable-step Adams solver was chosen for its efficiency and time saving abilities to solve the problem.

D Eigenvalues and eigenfunctions of the vibrational-states

This appendix shows how obtained the eigenvalues and the eigenfunctions of the vibrational states of molecules.

In order to obtain the full rovibronic energy of the diatomic molecule, the eigenvalue equation

$$\left[-\frac{1}{2\mu}\frac{d^2}{dR^2} + \frac{J(J+1)}{2\mu R^2} + V(R)\right]\chi_{\nu,J}(R) = E_{\nu,J}\,\chi_{\nu,J}(R) \tag{D.1}$$

should be solved, where μ is the reduced mass of the molecule, J is the rotational quantum number, and $\chi_{\nu,J}(R)/R$ is the resulting radial nuclear wavefunction.

Instead of solving the three-dimensional Schrodinger equation describing the nuclear motion of a diatomic molecule, only the simplified rotationless quasi-one-dimensional equation

$$\left[-\frac{1}{2\mu}\frac{d^2}{dR^2} + V(R)\right]\chi_{\nu}(R) = E_{\nu}\,\chi_{\nu}(R) \tag{D.2}$$

is solved in the adiabatic BO potential curves for obtaining the complete molecular wavefunction. Equation (D.1) is solved by expanding the nuclear wavefunctions in terms of B-splines basis functions for the radial part times spherical harmonics describing the angular part [77]. In this way the Schrödinger equation is transformed into a matrix eigenvalue problem. A B-spline basis (202 B-splines of order eight, expanded on a linear knot sequence spanning $R = 0 - 12\,\mathrm{a_0}$) has been shown to give converged results for H_2 and H_2^+. In some cases it was, however, necessary to vary or lower the upper bound in order to identify the vibrational bound states in the predissociative tunneling continuum created due to bond softening in the field. In all cases, a linear knot sequence was chosen for the B-splines.

E Structure parameters C_{lm} for N_2 and O_2

In this appendix, the fitted C_{lm} structure coefficients and the experimental vertical ionization energies for N_2 and O_2 molecules, used for the MO-ADK and MO-PPT models in chapter 6, are tabulated in Table E.1.

Table E.1: The molecular and atomic properties necessary for the evaluation of the MO-ADK and MO-PPT models. The equilibrium distance (R_0), the experimental adiabatic ionization potential (I_p) and the asymptotic C_{lm} structure coefficients for N_2 and O_2 are given.

Molecule	R_{eq} (a.u.)	I_p^{exp} (eV)	C_{0m}	C_{2m}	C_{4m}	C_{6m}	Reference
N_2	2.075	15.58[a]	2.020	0.780	0.040	0.000	[28]
			2.470	1.080	0.070	0.000	[187]
			3.575	1.626	0.150	0.057	[188]
			3.350	1.620	0.120	0.000	[26]
			3.460	1.640	0.120	0.000	[108]
O_2	2.283	12.07[b]	0.000	0.620	0.030	0.000	[28]
			0.000	0.880	0.050	0.000	[187]
			0.000	1.040	0.070	0.000	[108]

[a] According to Ref. [194]
[b] According to Ref. [195]

List of Abbreviations

ATI	Above-Threshold Ionization
BSI	Barrier-Suppressed-Ionization
CI	Configuration Interaction (method)
CI-TDSE	Configuration Interaction based method for solution of Time-Dependent Schrödinger Equation
CP	Circular Polarized
DFT	Density Functional Theory
fc-ADK	frequency corrected Ammosov-Delone-Krainov (approximation)
FVE	Focal-Volume Effect
FWHM	Full Width at Half Maximum
HOHG	High Order Harmonic Generation
IWP	Initial Wavepacket
LG	Length gauge
LOPT	Lowest-order perturbation theory
LP	Linear polarized
MO-ADK	Molecular orbital Ammosov-Delone-Krainov
MO-PPT	Molecular Orbital Popov-Peremolov-Terent'ev
MPI	the Multi-Photon Ionization
NSDI	the Non-Sequential Double Ionization
OTBI	Over-The-Barrier Ionization
PPT	Popov-Peremolov-Terent'ev (approximation)
REMPI	Resonant Enhanced Multi-Photon Ionization
SAE	Single-Active Electron (approximation)
SAE-TDSE	Solving the Time-Dependent Schrödinger Equation within Single-Active Electron approximation
SFA	Strong Field Approximation
TDSE	Time-Dependent Schrödinger Equation
TDDFT	Time-Dependent Density Functional Theory
TI	Tunneling Ionization
VG	Velocity Gauge
VSD	Vibrational-State Distribution

Acknowledgments

First and foremost I would like to express my deepest gratitude to my supervisor, Prof. Dr. Alejandro Saenz, for his patient supervision, guidance, constructive criticism, valuable and continuous discussion during the progress of this work. He has always been helpful and encouraging, despite being increasingly busy the last few years. He spent hours and hours in correcting my thesis. Working under his supervision is also a great learning, (beside physics) experience, organizational and communication skills. Additionally, I wish to express my grateful appreciation of his contributions and his support in various private matters during my stay in Germany. He is a very kind person. I will stay always indebted to him because of all he has done to support me.

I would like to thank my group members for interesting work together. Special thanks to Johann Förster, E. Jobunga, Dr. Y. Vanne, Dr. M. Awasthi, Dr. A. Lühr, Dr. S. Grishkevich, and Dr. S. Petretti for their kind helps. Much thanks for Mrs. M. Götsch, the secretary of the physics institute for her valuable assistance. I also warmly thank all those nice people at Humboldt University who helped me in one way or another.

I have received considerable help, support, encouragement and otherwise from a number of people, all deserving my gratitude, especially Dr. Kh. Abu El-Ella, Dr. Y. Mustafa, Ass. Prof. Sh. Harb and Dr. A. Toghan. I would also like to extend my warmest thanks to all my friends and colleagues at South Valley University those who helped me direct or indirect during this work.

Last but not the least, I would like to express my deep thanks and appreciation to my family whose has always been supporting and encouraging. My especial gratitude and thanks to my dear wife for her all optimism, continuous encouragements and her patience. Kindly thanks to my lovely daughters, Rawan, Maryam and Salma, the sources of my happiness.

Finally I would like to thank the Egyptian Mission Department of the Egyptian higher education minster for awarding the financial support for my PhD and facilitations. I would like to express my deep thanks to the working group at the Egyptian Culture Office, Berlin, Germany, for their valuable support and assistance.

Bibliography

[1] Thomas Brabec and Ferenc Krausz, "Intense few-cycle laser fields: Frontiers of nonlinear optics", *Rev. Mod. Phys.*, vol. 72, pp. 545, 2000.

[2] P. B. Corkum and Ferenc Krausz, "Attosecond science", *Nature Phys.*, vol. 3, pp. 381, 2007.

[3] L. V. Keldysh, "Ionization in the field of a strong electromagnetic wave", *Sov. Phys. JETP*, vol. 20, pp. 1307, 1965.

[4] P. B. Corkum, "Plasma perspective on strong field multiphoton ionization", *Phys. Rev. Lett.*, vol. 71, pp. 1994, 1993.

[5] P. B. Corkum, N. H. Burnett, and F. Brunel, "Above-threshold ionization in the long-wavelength limit", *Phys. Rev. Lett.*, vol. 62, pp. 1259, 1989.

[6] Ferenc Krausz and Misha Ivanov, "Attosecond physics", *Rev. Mod. Phys.*, vol. 81, pp. 163, 2009.

[7] A. Giusti-Suzor, X. He, O. Atabek, and F. H. Mies, "Above-threshold dissociation of H_2^+ in intense laser fields", *Phys. Rev. Lett.*, vol. 64, pp. 515, 1990.

[8] ZHANG Dong-Dong, NI Qiang, LUO Si-Zuo, ZHANG Jing, LIU Hang, XU Hai-Feng, JIN Ming-Xing, and DING Da-Jun, "Ultrafast photodissociation dynamics of the F state of sulfur dioxide by femtosecond time-resolved pump-probe method", *Chin. Phys. Lett.*, vol. 28, pp. 033301, 2011.

[9] Wu Yan, Ye Hui-Liang, Zhang Jing-Tao, and Guo Dong-Sheng, "Multiple-plateau structure and scaling relation in photoelectron spectra of high-order above-threshold ionization", *Chin. Phys. B*, vol. 21, pp. 053201, 2012.

[10] D. Normand and M. Schmidt, "Multiple ionization of atomic and molecular iodine in strong laser fields", *Phys. Rev. A*, vol. 53, 1996.

[11] Li Yan, Yang Shi-Ping, Jia Xin-Yan, and Chen Jing, "Nonsequential double ionization of the aligned hydrogen molecule in strong field", *Chin. Phys. B*, vol. 19, pp. 043303, 2010.

[12] Hao Xiao-Lei, Li Wei-Dong, Liu Jie, and Chen Jing, "The effect of electron initial longitudinal velocity on non-sequential double ionization process in elliptically polarized laser field", *Chin. Phys. B*, vol. 21, pp. 083304, 2012.

[13] Wang Yu-Quan, Chen De-Ying, Xia Yuan-Qin, Fan Rong-Wei, and Lu Fa-Ming, "Nonsequential double ionization of the aligned hydrogen molecule in strong field", *Chin. Phys. B*, vol. 19, pp. 023203, 2010.

[14] I. V. Litvinyuk, Kevin F. Lee, P. W. Dooley, D. M. Rayner, D. M. Villeneuve, and P. B. Corkum, "Alignment-dependent strong field ionization of molecules", *Phys. Rev. Lett.*, vol. 90, pp. 233003, 2003.

[15] J. Muth-Böhm, A. Becker, and F. H. M. Faisal, "Suppressed molecular ionization for a class of diatomics in intense femtosecond laser fields", *Phys. Rev. Lett.*, vol. 85, pp. 2280, 2000.

[16] P. H. Bucksbaum, A. Zavriyev, H. G. Muller, and D. W. Schumacher, "Softening of the H_2^+ molecular bond in intense laser fields", *Phys. Rev. Lett.*, vol. 64, pp. 1883, 1990.

[17] L. J. Frasinski, J. H. Posthumus, J. Plumridge, K. Codling, P. F. Taday, and A. J. Langley, "Manipulation of bond hardening in H_2^+ by chirping of intense femtosecond laser pulses", *Phys. Rev. Lett.*, vol. 83, pp. 3625, 1999.

[18] A. Zavriyev, P. H. Bucksbaum, H. G. Müller, and D. W. Schumacher, "Ionization and dissociation of H_2 in intense laser fields at 1.064μm, 532nm and 355nm", *Phys. Rev. A*, vol. 42, pp. 5500, 1990.

[19] K. Hoshina, A. Hishikawa, K. Kato, T. Sako, K. Yamanouchi, E. J. Takahashi, Y. Nabekawa, and K. Midorikawa, "Dissociative ATI of H_2 and D_2 in intense soft x-ray laser fields", *J. Phys. B*, vol. 39, pp. 813, 2006.

[20] Tamar Seideman, M. Yu. Ivanov, and P. B. Corkum, "Role of electron localization in intense-field molecular ionization", *Phys. Rev. Lett.*, vol. 75, pp. 2819, 1995.

[21] T. Zuo and A. D. Bandrauk, "Charge-resonance-enhanced ionization of diatomic molecular ions by intense lasers", *Phys. Rev. A*, vol. 52, pp. R2511, 1995.

[22] S. Barmaki and H. Bachau, "Coulomb explosion of H_2^+ wave packet in ultrashort xuv laser fields with short laser pulses: The L^2 approach", *J. Phys. B*, vol. 40, pp. 463, 2007.

[23] J. H. Posthumus, "The dynamics of small molecules in intense laser fields", *Rep. Prog. Phys.*, vol. 67, pp. 623, 2004.

[24] F. H. M. Faisal, "Multiple absorption of laser photons by atoms", *J. Phys. B*, vol. 6, pp. L89, 1973.

[25] Howard R. Reiss, "Effect of an intense electromagnetic field on a weakly bound system", *Phys. Rev. A*, vol. 22, pp. 1786, 1980.

[26] Thomas Kim Kjeldsen and Lars Bojer Madsen, "Strong-field ionization of N_2: length and velocity gauge strong-field approximation and tunnelling theory", *J. Phys. B*, vol. 37, pp. 2033, 2004.

[27] M. V. Ammosov, N. B. Delone, and V. P. Krainov, "Tunnel ionization of complex atoms and of atomic ions in an alternating electromagnetic field", *Sov. Phys. JETP*, vol. 64, pp. 1191, 1986.

[28] X. M. Tong, Z. X. Zhao, and C. D. Lin, "Theory of molecular tunneling ionization", *Phys. Rev. A*, vol. 66, pp. 033402, 2002.

[29] X. M. Tong and C.D. Lin, "Empirical formula for static field ionization rates of atoms and molecules by lasers in the barrier-suppression regime", *J. Phys. B*, vol. 38, pp. 2593, 2005.

[30] A. M. Perelomov, V. S. Popov, and M. V. Terent'ev, "Ionization of atoms in an alternating electric field", *Sov. Phys. JETP*, vol. 23, pp. 924, 1966.

[31] A. M. Perelomov and V. S. Popov, "Ionization of atoms in an alternating electric field. ii", *Sov. Phys. JETP*, vol. 24(1), pp. 207, 1967.

[32] A. M. Perelomov and V. S. Popov, "Ionization of atoms in an alternating electric field. iii", *Sov. Phys. JETP*, vol. 25(2), pp. 336, 1967.

[33] Fu Yan-Zhuo, Zhao Song-Feng, and Zhou Xiao-Xin, "Multiphoton and tunneling ionization of atoms in an intense laser field", *Chin. Phys. B*, vol. 21, pp. 113101, 2012.

[34] ZhiYang Lin, XinYan Jia, ChuanLiang Wang, ZiLong Hu, HuiPeng Kang, Wei Quan, XuanYang Lai, XiaoJun Liu, Jing Chen, Bin Zeng, Wei Chu, JinPing Yao,

Ya Cheng, and ZhiZhan Xu, "Ionization suppression of diatomic molecules in an intense midinfrared laser field", *Phys. Rev. Lett.*, vol. 108, pp. 223001, 2012.

[35] Jian Wu, Heping Zeng, and Chunlei Guo, "Comparison study of atomic and molecular single ionization in the multiphoton ionization regime", *Phys. Rev. Lett.*, vol. 96, pp. 243002, 2006.

[36] A. Staudte, S. Patchkovskii, D. Pavičić, H. Akagi, O. Smirnova, D. Zeidler, M. Meckel, D. M. Villeneuve, R. Dörner, M. Yu. Ivanov, and P. B. Corkum, "Angular tunneling ionization probability of fixed-in-space H_2 molecules in intense laser pulses", *Phys. Rev. Lett.*, vol. 102, pp. 033004, 2009.

[37] Maia Magrakvelidze, Feng He, Sankar De, Irina Bocharova, Dipanwita Ray, Uwe Thumm, and I. V. Litvinyuk, "Angular dependence of the strong-field ionization measured in randomly oriented hydrogen molecules", *Phys. Rev. A*, vol. 79, pp. 033408, 2009.

[38] P. von den Hoff, I. Znakovskaya, S. Zherebtsov, M. Kling, and R. de Vivie-Riedle, "Effects of multi orbital contributions in the angular-dependent ionization of molecules in intense few-cycle laser pulses", *Appl. Phys. B*, vol. 98, pp. 659, 2010.

[39] Xi Chu, "Time-dependent density-functional-theory calculation of strong-field ionization rates of H_2", *Phys. Rev. A*, vol. 82, pp. 023407, 2010.

[40] Ying-Jun Jin, Xiao-Min Tong, and Nobuyuki Toshima, "Alignment-dependent ionization of hydrogen molecules in intense laser fields", *Phys. Rev. A*, vol. 83, pp. 063409, 2011.

[41] Bin Zhang, Jianmin Yuan, and Zengxiu Zhao, "Alignment-dependent ionization of H_2^+: From multiphoton ionization to tunneling ionization", *Phys. Rev. A*, vol. 85, pp. 033421, 2012.

[42] H. Akagi, T. Otobe, A. Staudte, A. Shiner, F. Turner, R. Dorner, D. M. Villeneuve, and P. B. Corkum, "Laser tunnel ionization from multiple orbitals in HCl", *Science*, vol. 325, pp. 1364, 2009.

[43] Manohar Awasthi, *Molecules in strong laser fields: In depth study of H_2 molecule*, PhD thesis, Humboldt-Universität zu Berlin, Germany, 2009.

[44] Merrick J. DeWitt and Robert J. Levis, "Calculating the keldysh adiabaticity parameter for atomic and polyatomic molecules", *J. Chem. Phys.*, vol. 108, pp. 7739, 1998.

[45] F. A. Ilkov, J. E. Decker, and S. L. Chin, "Ionization of atoms in the tunnelling regime with experimental evidence using Hg atoms", *J. Phys. B*, vol. 25, pp. 4005, 1992.

[46] P. Lambropoulos, "Multiphoton ionization of one-electron atoms with circularly polarized light", *Phys. Rev. Lett.*, vol. 29, pp. 453, 1972.

[47] P. Lambropoulos, "Topics on multiphoton processes in atoms", *Adv. At. Mol. Phys.*, vol. 12, pp. 87, 1976.

[48] J. R. Oppenheimer, "Three notes on the quantum theory of aperiodic effects", *Phys. Rev.*, vol. 31, pp. 66, 1928.

[49] L. D. Landau and E. M. Lifshitz, *Quantum Mechanics*, Pergamon Press, Oxford, 1965.

[50] Alejandro Saenz, "Behavior of molecular hydrogen exposed to strong dc, ac, or low-frequency laser fields: II. Comparison of ab initio and Ammosov-Delone-Krainov (ADK) rates", *Phys. Rev. A*, vol. 66, pp. 063408, 2002.

[51] Armin Scrinzi, Michael Geissler, and Thomas Brabec, "Ionization above the Coulomb barrier", *Phys. Rev. Lett.*, vol. 83, pp. 706, 1999.

[52] Cervenon M. R. and Isenor N. R, "Electron-molecule interactions. IV. Scattering by polyatomic molecules", *Opt. Commun.*, vol. 13, pp. 175, 1975.

[53] S. L. Chin, N. R. Isenor, and M. Young, "Multiphoton ionization of Hg and Xe", *Phys. Rev.*, vol. 188, pp. 7, 1969.

[54] S. L. Chin, J. E. Decker, T. D. G. Walsh, Y. Liang, and G. Xu, "Tunnel ionization of molecules by an intense CO_2", *Laser Phys.*, vol. 3, pp. 298, 1993.

[55] Christer Z. Bisgaard and Lars Bojer Madsen, "Tunneling ionization of atoms", *Am. J. Phys.*, vol. 72, pp. 249, 2004.

[56] S. F. J. Larochelle, A. Talebpour, and S. L. Chin, "Coulomb effect in multiphoton ionization of rare-gas atoms", *J. Phys. B*, vol. 31, pp. 1215, 1998.

[57] Michinori Tanaka, Masanao Murakami, Tomoyuki Yatsuhashi, and Nobuaki Nakashima, "Atomiclike ionization and fragmentation of a series of CH3–X (X: H, F, Cl, Br, I, and CN) by an intense femtosecond laser", *J. Chem. Phys.*, vol. 127, pp. 104314, 2007.

[58] Johann Förster, Yulian V. Vanne, and Alejandro Saenz, "Ionization behavior of molecular hydrogen in intense laser fields: Influence of molecular vibration and alignment", *Phys. Rev. A*, vol. 90, pp. 053424, 2014.

[59] W. Demtröder, *Atoms, Molecules and Photons*, Springer, Berlin, Germany, 2006.

[60] J. H. Posthumus, *Molecules and Clusters in Intense Laser fields*, Cambridge University Press, Cambridge, UK, 2001.

[61] M. Ferray, A. L'Huillier, X. F. Li, L. A. Lompre, G. Mainfray, and C. Manus, "Multiple-harmonic conversion of 1064 nm radiation in rare gases", *J. Phys. B*, vol. 21, pp. L31, 1988.

[62] X. F. Li, A. L'Huillier, M. Ferray, L. A. Lompré, and G. Mainfray, "Multiple-harmonic generation in rare gases at high laser intensity", *Phys. Rev. A*, vol. 39, pp. 5751, 1989.

[63] Jeffrey L. Krause, Kenneth J. Schafer, and Kenneth C. Kulander, "High-order harmonic generation from atoms and ions in the high intensity regime", *Phys. Rev. Lett.*, vol. 68, pp. 3535, 1992.

[64] A. L'Huillier, K. J. Schafer, and K. C. Kulander, "Theoretical aspects of intense field harmonic generation", *J. Phys. B*, vol. 24, pp. 3315, 1991.

[65] P. Agostini, F. Fabre, G. Mainfray, G. Petite, and N. K. Rahman, "Free-free transitions following six-photon ionization of xenon atoms", *Phys. Rev. Lett.*, vol. 42, pp. 1127, 1979.

[66] P. Kruit, J. Kimman, and M. J. Van der Wiel, "Absorption of additional photons in the multiphoton ionisation continuum of xenon at 1064, 532 and 440 nm", *J. Phys. B*, vol. 14, pp. L597, 1981.

[67] P. Kruit, J. Kimman, H. G. Muller, and M. J. van der Wiel, "Electron spectra from multiphoton ionization of xenon at 1064, 532, and 355 nm", *Phys. Rev. A*, vol. 28, pp. 248, 1983.

[68] R. R. Freeman, P. H. Bucksbaum, H. Milchberg, S. Darack, D. Schumacher, and M. E. Geusic, "Above-threshold ionization with subpicosecond laser pulses", *Phys. Rev. Lett.*, vol. 59, pp. 1092, 1987.

[69] B. W. Shore and P. L. Knight, "Enhancement of high opticla harmonics by excess-photon ionisation", *J. Phys. B*, vol. 20, pp. 413, 1987.

[70] M. Pont and M. Gavrila, "Stabilization of atomic hydrogen in superintense, high-frequency laser fields of circular polarization", *Phys. Rev. Lett.*, vol. 65, pp. 2362, 1990.

[71] Kenneth C. Kulander, Kenneth J. Schafer, and Jeffrey L. Krause, "Dynamic stabilization of hydrogen in an intense, high-frequency, pulsed laser field", *Phys. Rev. Lett.*, vol. 66, pp. 2601, 1991.

[72] M. P. de Boer, J. H. Hoogenraad, R. B. Vrijen, L. D. Noordam, and H. G. Muller, "Indications of high-intensity adiabatic stabilization in neon", *Phys. Rev. Lett.*, vol. 71, pp. 3263, 1993.

[73] J. H. Eberly and K. C. Kulander, "Atomic Stabilization by Super-Intense Lasers", *Science*, vol. 262, pp. 1229, 1993.

[74] H. Haken and H. C. Wolf, *Molecular Physics and Elements of Quantum Chemistry*, Springer-Verlag, Berlin, 1995.

[75] K. Codling and L. J. Frasinski, "Dissociative ionization of small molecules in intense laser fields", *J. Phys. B*, vol. 26, pp. 783, 1993.

[76] M. Plummer and J. F. McCann, "Orientation dependence of field ionization of the hydrogen molecular ion", *J. Phys. B*, vol. 30, pp. L401, 1997.

[77] A. Saenz, "On the influence of vibrational motion on strong-field ionization rates in molecules", *J. Phys. B*, vol. 33, pp. 4365, 2000.

[78] Henrik Stapelfeldt and Tamar Seideman, "Colloquium: Aligning molecules with strong laser pulses", *Rev. Mod. Phys.*, vol. 75, pp. 543, 2003.

[79] L. J. Frasinski, K. Codling, P. Hatherly, J. Barr, I. N. Ross, and W. T. Toner, "Femtosecond dynamics of multielectron dissociative ionization by use of a picosecond laser", *Phys. Rev. Lett.*, vol. 58, pp. 2424, 1987.

[80] M. Schmidt, D. Normand, and C. Cornaggia, "Laser-induced trapping of chlorine molecules with pico- and femtosecond pulses", *Phys. Rev. A*, vol. 50, pp. 5037, 1994.

[81] M. R. Thompson, M. K. Thomas, P. F. Taday, J. H. Posthumus, A. J. Langley, L. J. Frasinski, and K. Codling, "One and two-colour studies of the dissociative ionization and Coulomb explosion of H_2 with intense Ti:sapphire laser pulses", *J. Phys. B*, vol. 30, pp. 5755, 1997.

[82] Ch. Ellert and P. B. Corkum, "Disentangling molecular alignment and enhanced ionization in intense laser fields", *Phys. Rev. A*, vol. 59, pp. R3170, 1999.

[83] J. H. Posthumus, J. Plumridge, M. K. Thomas, K. Codling, L. J. Frasinski, A. J. Langley, and P. F. Taday, "Dynamic and geometric laser-induced alignment of molecules in intense laser fields", *J. Phys. B*, vol. 31, pp. L553, 1998.

[84] Michael Spanner, *Field-Free Alignment and Strong Field Control of Molecular Rotors. Dissertation,*, University of Waterloo, Waterloo (Ontario Canada), 2004.

[85] Tamar Seideman, "Revival structure of aligned rotational wave packets", *Phys. Rev. Lett.*, vol. 83, pp. 4971, 1999.

[86] M. Schmidt, S. Dobosz, P. Meynadier, P. D'Oliviera, D. Normand, E. Charron, and A. Suzor-Weiner, "Fragment-emission patterns from the Coulomb explosion of diatomic molecules in intense laser fields", *Phys. Rev. A*, vol. 60, pp. 4706, 1999.

[87] John P. Nibarger, Saipriya V. Menon, and George N. Gibson, "Comprehensive analysis of strong-field ionization and dissociation of diatomic nitrogen", *Phys. Rev. A*, vol. 63, pp. 053406, 2001.

[88] C. Cornaggia, J. Lavancier, D. Normand, J. Morellec, and H. X. Liu, "Intensity dependence of the multielectron dissociative ionization of N_2 at 305 and 610 nm", *Phys. Rev. A*, vol. 42, pp. 5464, 1990.

[89] C. Cornaggia, J. Lavancier, D. Normand, J. Morellec, P. Agostini, J. P. Chambaret, and A. Antonetti, "Multielectron dissociative ionization of diatomic molecules in an intense femtosecond laser field", *Phys. Rev. A*, vol. 44, pp. 4499, 1991.

[90] K. Boyer, T. S. Luk, J. C. Solem, and C. K. Rhodes, "Kinetic energy distributions of ionic fragments produced by subpicosecond multiphoton ionization of N_2", *Phys. Rev. A*, vol. 39, pp. 1186, 1989.

[91] K. Codling, L. J. Frasinski, and P. A. Hatherly, "On the field ionisation of diatomic molecules by intense laser fields", *J. Phys. B*, vol. 22, pp. L321, 1989.

[92] D. T. Strickland, Y. Beaudoin, P. Dietrich, and P. B. Corkum, "Optical studies of inertially confined molecular iodine ions", *Phys. Rev. Lett.*, vol. 68, pp. 2755, 1992.

[93] Domagoj Pavičić, *Coulomb Explosion and Intense-Field Photodissociation of Ion-Beam H_2^+, and D_2^+*, PhD thesis, der Ludwig–Maximilians–Universität M̈unchen, Germany, 2004.

[94] Alejandro Saenz, "Behavior of molecular hydrogen exposed to strong dc, ac, or low-frequency laser fields: I. Bond softening and enhanced ionization", *Phys. Rev. A*, vol. 66, pp. 063407, 2002.

[95] John R. Hiskes, "Dissociation of molecular ions by electric and magnetic fields", *Phys. Rev.*, vol. 122, pp. 1207, 1961.

[96] A. Saenz, "Enhanced ionization of molecular hydrogen in very strong fields", *Phys. Rev. A*, vol. 61, pp. 051402, 2000.

[97] A. Giusti-Suzor and F. H. Mies, "Vibrational trapping and suppression of dissociation in intense laser fields", *Phys. Rev. Lett.*, vol. 68, pp. 3869, 1992.

[98] A. Zavriyev, P. H. Bucksbaum, J. Squier, and F. Saline, "Light-induced vibrational structure in H_2^+ and D_2^+ in intense laser fields", *Phys. Rev. Lett.*, vol. 70, pp. 1077, 1993.

[99] K. Sändig, H. Figger, and T. W. Hänsch, "Dissociation dynamics of H_2^+ in intense fields – investigation of photofragments from single vibrational levels", *Phys. Rev. Lett.*, vol. 85, pp. 4876, 2000.

[100] A. Talebpour, C.-Y. Chien, and S. L. Chin, "The effects of dissociative recombination in multiphoton ionization of O_2", *J. Phys. B*, vol. 29, pp. L677, 1996.

[101] A. Talebpour, S. Larochelle, and S. L. Chin, "Suppressed tunnelling ionization of the D_2 molecule in an intense Ti:sapphire laser pulse", *J. Phys. B*, vol. 31, pp. L49, 1998.

[102] C. Guo, M. Li, J. P. Nibarger, and G. N. Gibson, "Single and double ionization of diatomic molecules in strong laser fields", *Phys. Rev. A*, vol. 58, pp. R4271, 1998.

[103] Merrick J. DeWitt, E. Wells, and R. R. Jones, "Ratiometric comparison of intense field ionization of atoms and diatomic molecules", *Phys. Rev. Lett.*, vol. 87, pp. 153001, 2001.

[104] E. Wells, Merrick J. DeWitt, and R. R. Jones, "Comparison of intense-field ionization of diatomic molecules and rare-gas atoms", *Phys. Rev. A*, vol. 66, pp. 013409, 2002.

[105] S. M. Hankin, D. M. Villeneuve, P. B. Corkum, and D. M. Rayner, "Nonlinear ionization of organic molecules in high intensity laser fields", *Phys. Rev. Lett.*, vol. 84, pp. 5082, 2000.

[106] S. M. Hankin, D. M. Villeneuve, P. B. Corkum, and D. M. Rayner, "Intense-field laser ionization rates in atoms and molecules", *Phys. Rev. A*, vol. 64, pp. 013405, 2001.

[107] X. M. Tong, Z. X. Zhao, and C. D. Lin, "Molecular tunnelling ionization and rescattering induced double ionization of H_2 and D_2 molecules", *J. Mod. Opt.*, vol. 52, pp. 185, 2005.

[108] Thomas Kim Kjeldsen and Lars Bojer Madsen, "Strong-field ionization of diatomic molecules and companion atoms: Strong-field approximation and tunneling theory including nuclear motion", *Phys. Rev. A*, vol. 71, pp. 023411, 2005.

[109] Manohar Awasthi, Yulian V. Vanne, Alejandro Saenz, Alberto Castro, and Piero Decleva, "Single-active-electron approximation for describing molecules in ultrashort laser pulses and its application to molecular hydrogen", *Phys. Rev. A*, vol. 77, pp. 063403, 2008.

[110] Song-Feng Zhao, Cheng Jin, Anh-Thu Le, T. F. Jiang, and C. D. Lin, "Determination of structure parameters in strong-field tunneling ionization theory of molecules", *Phys. Rev. A*, vol. 81, pp. 033423, 2010.

[111] Takahiro Miyazaki, Makoto Katori, and Norio Konno, "Wigner formula of rotation matrices and quantum walks", *Phys. Rev. A*, vol. 76, pp. 012332, 2007.

[112] E. P. Benis, J. F. Xia, X. M. Tong, M. Faheem, M. Zamkov, B. Shan, P. Richard, and Z. Chung, "Ionization suppression of Cl_2 molecules in intense laser fields", *Phys. Rev. A*, vol. 70, pp. 025401, 2004.

[113] Thomas Brabec, *Strong Field Laser Physics*, Springer Science + Business Media, New York, USA, 2009.

[114] ", http://en.wikipedia.org/wiki/High_Harmonic_Generation.

[115] K. J. Schafer, Baorui Yang, L. F. DiMauro, and K. C. Kulander, "Above threshold ionization beyond the high harmonic cutoff", *Phys. Rev. Lett.*, vol. 70, pp. 1599, 1993.

[116] M. Lewenstein, Ph. Balcou, M. Yu. Ivanov, Anne L'Huillier, and P. B. Corkum, "Theory of high-harmonic generation by low-frequency laser fields", *Phys. Rev. A*, vol. 49, pp. 2117, 1994.

[117] E. Cormier and P. Lambropoulos, "Optimal gauge and gauge invariance in non-perturbative time-dependent calculation of above-threshold ionization", *J. Phys. B*, vol. 29, pp. 1667, 1996.

[118] P. Lambropoulos, P. Maragakis, and Jian Zhang, "Two-electron atoms in strong fields", *Phys. Rep.*, vol. 305, pp. 203, 1998.

[119] Manohar Awasthi, Yulian V. Vanne, and Alejandro Saenz, "Non-perturbative solution of the time-dependent Schrödinger equation describing H_2 in intense short laser pulses", *J. Phys. B*, vol. 38, pp. 3973, 2005.

[120] Yulian V. Vanne and Alejandro Saenz, "Numerical treatment of diatomic two-electron molecules using a B-spline based CI method", *J. Phys. B*, vol. 37, pp. 4101, 2004.

[121] Simon Petretti, Yulian V. Vanne, Alejandro Saenz, Alberto Castro, and Piero Decleva, "Alignment-dependent ionization of N_2, O_2, and CO_2 in intense laser fields", *Phys. Rev. Lett.*, vol. 104, pp. 223001, 2010.

[122] Simon Petretti, *Molecules in strong laser fields: A theoretical study*, PhD thesis, Humboldt-Universität zu Berlin, Germany, 2013.

[123] Limor S. Spector, Shungo Miyabe, Alvaro Magana, Simon Petretti, Piero Decleva, Todd Martinez, Alejandro Saenz, Markus Guehr, and Philip H. Bucksbaum, "Multiple orbital contributions to molecular high-harmonic generation in an asymmetric top", *arXiv:1308.3733v1*, pp. 1–19, 2013.

[124] K. C. Kulander, "Time-dependent theory of multiphoton ionization of xenon", *Phys. Rev. A*, vol. 38, pp. 778, 1988.

[125] P. Hohenberg and W. Kohn, "Inhomogeneous Electron Gas", *Phys. Rev.*, vol. 136, pp. B 864, 1964.

[126] W. Kohn and L. J. Sham, "Self-consistent equations including exchange and correlation effects", *Phys. Rev.*, vol. 140, 1965.

[127] R. G. Parr and W. Yang, *Density-Functional Theory of Atoms and Molecules*, Oxford Science, 1989.

[128] Erich Runge and E. K. U. Gross, "Density-functional theory for time-dependent systems", *Phys. Rev. Lett.*, vol. 52, pp. 997, 1984.

[129] E. K. U. Gross and Walter Kohn, "Local density-functional theory of frequency-dependent linear response", *Phys. Rev. Lett.*, vol. 55, pp. 2850, 1985.

[130] M. A. L. Marques, C. A. Ullrich, F. Nogueira, A. Rubio, K. Burke, and E. K. U. Gross (eds.), *Time-Dependent Density Functional Theory*, Springer-Verlag, 2006.

[131] M. Petersilka, U. J. Gossmann, and E. K. U. Gross, "Excitation energies from time-dependent density-functional theory", *Phys. Rev. Lett.*, vol. 76, pp. 1212, 1996.

[132] Giovanni Onida, Lucia Reining, and Angel Rubio, "Electronic excitations: density-functional versus many-body green's-function approaches", *Rev. Mod. Phys.*, vol. 74, pp. 601, 2002.

[133] Brian K. McFarland, Joseph P. Farrell, Philip H. Bucksbaum, and Markus Gühr, "High harmonic generation from multiple orbitals in N_2", *Science*, vol. 322, pp. 1232, 2008.

[134] M. F. Kling, Ch. Siedschlag, A. J. Verhoef, J. I. Khan, M. Schultze, Th. Uphues, Y. Ni, M. Uiberacker, M. Drescher, F. Krausz, and M. J. J. Vrakking, "Control of electron localization in molecular dissociation", *Science*, vol. 312, pp. 246, 2006.

[135] S. Baker, J. S. Robinson, C. A. Haworth, H. Teng, R. A. Smith, C. C. Chirilă, M. Lein, J. W. G. Tisch, and J. P. Marangos, "Probing proton dynamics in molecules on an attosecond time scale", *Science*, vol. 312, pp. 424, 2006.

[136] A. Staudte, D. Pavičić, S. Chelkowski, D. Zeidler, M. Meckel, H. Niikura, M. Schöffler, S. Schössler, B. Ulrich, P. P. Rajeev, Th. Weber, T. Jahnke, D. M. Villeneuve, A. D. Bandrauk, C. L. Cocke, P. B. Corkum, and R. Dörner, "Attosecond strobing of two-surface population dynamics in dissociating H_2^+", *Phys. Rev. Lett.*, vol. 98, pp. 073003, 2007.

[137] B. Manschwetus, T. Nubbemeyer, K. Gorling, G. Steinmeyer, U. Eichmann, H. Rottke, and W. Sandner, "Strong laser field fragmentation of H_2: Coulomb explosion without double ionization", *Phys. Rev. Lett.*, vol. 102, pp. 113002, 2009.

[138] H. L. Fragnito, J. Y. Bigot, P. C. Becker, and C. V. Shank, "Evolution of the vibronic absorption spectrum in a molecule following impulsive excitation with a 6 fs optical pulse", *Chem. Phys. Lett.*, vol. 160, pp. 101, 1989.

[139] Ahmed H. Zewail, "Femtochemistry", *J. Phys. C*, vol. 97, pp. 12427, 1993.

[140] A. S. Alnaser, T. Osipov, E. P. Benis, A. Wech, C. L. Cocke, X. M. Tong, and C. D. Lin, "Rescattering double ionization of D_2 and H_2 by intense laser pulses", *Phys. Rev. Lett.*, vol. 91, pp. 163002, 2003.

[141] A. S. Alnaser, B. Ulrich, X. M. Tong, I. V. Litvinyuk, C. M. Maharjan, P. Ranitovic, T. Osipov, R. Ali, S. Ghimire, Z. Chang, C. D. Lin, and C. L. Cocke, "Simultaneous real-time tracking of wave packets evolving on two different potential curves in H_2^+ and D_2^+", *Phys. Rev. A*, vol. 72, pp. 030702, 2005.

[142] Th. Ergler, A. Rudenko, B. Feuerstein, K. Zrost, C. D. Schröter, R. Moshammer, and J. Ullrich, "Time-resolved imaging and manipulation of H_2 fragmentation in intense laser fields", *Phys. Rev. Lett.*, vol. 95, pp. 093001, 2005.

[143] Th. Ergler, B. Feuerstein, A. Rudenko, K. Zrost, C. D. Schröter, R. Moshammer, and J. Ullrich, "Quantum-phase resolved mapping of ground-state vibrational D_2 wave packets via selective depletion in intense laser pulses", *Phys. Rev. Lett.*, vol. 97, pp. 103004, 2006.

[144] Kenji Ohmori, "Wave-packet and coherent control dynamics", *Annu. Rev. Phys. Chem.*, vol. 60, pp. 487, 2009.

[145] Tannor David J, *Introduction to Quantum Mechanics: A Time-Dependent Perspective*, University Science Books, Sausalito, California, 2007.

[146] A. Saenz, "Molecular hydrogen exposed to a suddenly turned-on strong electric field or low-frequency laser", *J. Phys. B*, vol. 33, pp. 3519, 2000.

[147] X. Urbain, B. Fabre, E. M. Staicu-Casagrande, N. de Ruette, V. M. Andrianarijaona, J. Jureta, J. H. Posthumus, A. Saenz, E. Baldit, and C. Cornaggia, "Intense-laser-field ionization of molecular hydrogen in the tunneling regime and its effect on the vibrational excitation of H_2^+", *Phys. Rev. Lett.*, vol. 92, pp. 163004, 2004.

[148] W. A. Bryan, J. McKenna, E. M. L. English, J. Wood, C. R. Calvert, R. Torres, D. S. Murphy, I. C. E. Turcu, J. L. Collier, J. F. McCann, I. D. Williams, and W. R. Newell, "Isolated vibrational wavepackets in D_2^+: Defining superposition conditions and wavepacket distinguishability", *Phys. Rev. A*, vol. 76, pp. 053402, 2007.

[149] C. R. Calvert, W. A. Bryan, W. R. Newell, and I. D. Williams, "Time-resolved studies of ultrafast wavepacket dynamics in hydrogen molecules", *Phys. Rev.*, vol. 491, pp. 1, 2010.

[150] Yulian V. Vanne and Alejandro Saenz, "Ionization of molecular hydrogen and deuterium by frequency-doubled Ti:sapphire laser pulses", *Phys. Rev. A*, vol. 80, pp. 053422, 2009.

[151] Y. V. Vanne and A. Saenz, "Ionization of H_2 in intense ultrashort laser pulses: parallel versus perpendicular orientation", *J. Mod. Opt.*, vol. 55, pp. 2665, 2008.

[152] B. Fabre, J. H. Posthumus, L. Malfaire, E. M. Staicu-Casagrande, J. Jureta, C. Cornaggia, E. Baldit, and X. Urbain, "First results on tunneling ionization of H_2 with a new portable experiment", *Laser Phys.*, vol. 14, pp. 468, 2004.

[153] B. Fabre, J. H. Posthumus, V. Adrianarijaona, J. Jureta, and X. Urbain, "The vibrational excitation of frame1 after multiphoton ionization of H_2", *Laser Phys.*, vol. 13, pp. 964, 2003.

[154] Manohar Awasthi and Alejandro Saenz, "Internuclear-distance dependence of ionization of H_2 in strong laser fields", *J. Phys. B*, vol. 39, pp. S 389, 2006.

[155] T. K. Kjeldsen and L. B. Madsen, "Vibrational excitation of diatomic molecular ions in strong field ionization of diatomic molecules", *Phys. Rev. Lett.*, vol. 95, pp. 073004, 2005.

[156] Uwe Thumm, Thomas Niederhausen, and Bernold Feuerstein, "Time-series analysis of vibrational nuclear wave-packet dynamics in $D_2{}^+$", *Phys. Rev. A*, vol. 77, pp. 063401, 2008.

[157] A. Giusti-Suzor, F. H. Mies, L. F. DiMauro, E. Charron, and B. Yang, "Dynamics of H_2^+ in intense laser fields", *J. Phys. B*, vol. 28, pp. 309, 1995.

[158] P. Dietrich, M. Yu. Ivanov, F. A. Ilkov, and P. B. Corkum, "Two-electron dissociative ionization of H_2 and D_2 in infrared laser fields", *Phys. Rev. Lett.*, vol. 77, pp. 4150, 1996.

[159] J. P. Brichta, W. K. Liu, A. A. Zaidi, A. Trottier, and J. H. Sanderson, "Comparison of ADK ionization rates as a diagnostic for selective vibrational level population measurement", *J. Phys. B*, vol. 39, pp. 3769, 2006.

[160] W. A. Bryan, C. R. Calvert, R. B. King, G. R. A. J. Nemeth, J. B. Greenwood, I. D. Williams, and W. R. Newell, "Quasi-classical model of non-destructive wavepacket manipulation by intense ultrashort nonresonant laser pulses", *New J. Phys.*, vol. 12, pp. 073019, 2010.

[161] Soo-Y. Lee, "Energy shift correction for the reflection approximation", *J. Chem. Phys.*, vol. 82, pp. 4588, 1985.

[162] T. E. Sharp, "Potential-energy curves for molecular hydrogen and its ions", *Atomic Data*, vol. 2, pp. 119, 1971.

[163] A. Rudenko, Th. Ergler, B. Feuerstein, K. Zrost, C. D. Schröter, R. Moshammer, and J. Ullrich, "Real-time observation of vibrational revival in the fastest molecular system", *Chem. Phys.*, vol. 329, pp. 193, 2006.

[164] I. S. Averbukh and Perelman., "Fractional revivals: Universality in the long-term evolution of quantum wave packets beyond the correspondence principle dynamics", *Phys. Lett. A*, vol. 39, pp. 449, 1989.

[165] Marc J. J. Vrakking, D. M. Villeneuve, and Albert Stolow, "Observation of fractional revivals of a molecular wave packet", *Phys. Rev. A*, vol. 54, 1996.

[166] C. P. J. Martiny, M. Abu-samha, and L. B. Madsen, "Counterintuitive angular shifts in the photoelectron momentum distribution for atoms in strong few-cycle circularly polarized laser pulses", *J. Phys. B*, vol. 42, pp. 161001, 2009.

[167] P. Eckle, M. Smolarski, P. Schlup, J. Biegert, A. Staudte, M. Schöffler, H. G. Muller, R. Dörner, and U. Keller, "Attosecond angular streaking", *Nature Phys.*, vol. 4, pp. 565, 2008.

[168] Domagoj Pavičić, Kevin F. Lee, D. M. Rayner, P. B. Corkum, and D. M. Villeneuve, "Direct measurement of the angular dependence of ionization for N_2, O_2, and CO_2 in intense laser fields", *Phys. Rev. Lett.*, vol. 98, pp. 243001, 2007.

[169] A. S. Alnaser, S. Voss, X. M. Tong, C. M. Maharajan, P. Ranitovic, B. Ullrich, T. Osipov, B. Shan, Z. Chang, and C. L. Cocke, "Effects of molecular structure on ion disintegration patterns in ionization of O_2 and N_2 by short laser pulses", *Phys. Rev. Lett.*, vol. 93, pp. 113003, 2004.

[170] Sang-Kil Son and Shih-I Chu, "Multielectron effects on the orientation dependence and photoelectron angular distribution of multiphoton ionization of CO_2 in strong laser fields", *Phys. Rev. A*, vol. 80, pp. 011403, 2009.

[171] Z. X. Zhao, X. M. Tong, and C. D. Lin, "Alignment-dependent ionization probability of molecules in a double-pulse laser field", *Phys. Rev. A*, vol. 67, pp. 043404, 2003.

[172] Ingo Barth and Olga Smirnova, "Nonadiabatic tunneling in circularly polarized laser fields: Physical picture and calculations", *Phys. Rev. A*, vol. 84, pp. 063415, 2011.

[173] E. B. Tulenko and B. A. Zon, "On the tunneling ionization of atoms in the presence of a circularly polarized laser field", *Laser Phys.*, vol. 13, pp. 450, 2003.

[174] Xi Chu and Shih-I Chu, "Role of the electronic structure and multielectron response in ionization mechanisms of diatomic molecules in intense short-pulse lasers: An all-electron ab initio study", *Phys. Rev. A*, vol. 70, pp. 061402(R), 2004.

[175] Dmitry A. Telnov and Shih-I Chu, "Effects of electron structure and multielectron dynamical response on strong-field multiphoton ionization of diatomic molecules with arbitrary orientation: An all-electron time-dependent density-functional-theory approach", *Phys. Rev. A*, vol. 79, pp. 041401, 2009.

[176] Xu Wang, *Theory of Strong-Field Atomic Ionization for Elliptical or Circular Polarization*, PhD thesis, University of Rochester Rochester, New York, United States, 2013.

[177] Ying-Jun Jin, Xiao-Min Tong, and Nobuyuki Toshima, "Enhanced ionization of hydrogen molecular ions in an intense laser field via a multiphoton resonance", *Phys. Rev. A*, vol. 81, pp. 013408, 2010.

[178] Yulian V. Vanne and Alejandro Saenz, "Alignment-dependent ionization of molecular hydrogen in intense laser fields", *Phys. Rev. A*, vol. 82, pp. 011403, 2010.

[179] Daniel Dundas and Jan M. Rost, "Molecular effects in the ionization of N_2, O_2, and F_2 by intense laser fields", *Phys. Rev. A*, vol. 71, pp. 013421, 2005.

[180] M. Spanner and S. Patchkovskii, "One-electron ionization of multielectron systems in strong nonresonant laser fields", *Phys. Rev. A*, vol. 80, pp. 063411, 2009.

[181] Vladimir I. Usachenko, Pavel E. Pyak, and Vyacheslav V. Kim, "Comparative study of strong-field ionization in laser-irradiated F_2 and other diatomic molecules: Density-functional-theory-based molecular strong-field approximation", *Phys. Rev. A*, vol. 79, pp. 023415, 2009.

[182] Bing Shan, Xiao-Min Tong annd Zengxiu Zhao, Zenghu Chang, and C. D. Lin, "High-order harmonic cutoff extension of the O_2 molecule due to ionization suppression", *Phys. Rev. A*, vol. 66, pp. 061401(R), 2002.

[183] A. Talebpour, J. Yang, and S. L. Chin, "Semi-empirical model for the rate of tunnel ionization of N_2 and O_2 molecule in an intense Ti:sapphire laser pulse", *Opt. Commun.*, vol. 163, pp. 29, 1999.

[184] M. Lein, N. Hay, R. Velotta, J. P. Marangos, and P. L. Knight, "Interfence effects in high-order harmonic generation with molecules", *Phys. Rev. A*, vol. 66, pp. 023805, 2002.

[185] M. Gühr, B. K. McFarland, J. P. Farrell, and P. H. Bucksbaum, "High harmonic generation for N_2 and CO_2 beyond the two-point model", *J. Phys. B*, vol. 40, pp. 3745, 2007.

[186] A. Becker, A. D. Bandrauk, and S. L. Chin, "S-matrix analysis of non-resonant multiphoton ionisation of inner-valence electrons of the nitrogen molecule", *Chem. Phys. Lett.*, vol. 343, pp. 345, 2001.

[187] M. Abu-samha and L. B. Madsen, "Single-active-electron potentials for molecules in intense laser fields", *Phys. Rev. A*, vol. 81, pp. 033416, 2010.

[188] Xi Chu and Melissa McIntyre, "Comparison of the strong-field ionization of N_2 and F_2: A time-dependent density-functional-theory study", *Phys. Rev. A*, vol. 83, pp. 013409, 2011.

[189] M. Abu-samha and L. B. Madsen, "Theory of strong-field ionization of aligned CO_2", *Phys. Rev. A*, vol. 80, pp. 023401, 2009.

[190] Ryan Murray, Michael Spanner, Serguei Patchkovskii, and Misha Yu. Ivanov, "Tunnel ionization of molecules and orbital imaging", *Phys. Rev. Lett.*, vol. 106, pp. 173001, 2011.

[191] Wes Corbin Erbsen, "Non-dissociative single-electron ionization of diatomic molecules", Master's thesis, Kansas State University, Manhattan, Kansas, United States, 2013.

[192] Yulian V. Vanne, *Ionization of Molecular Hydrogen in Ultrashort Intense Laser Pulses*, PhD thesis, Humboldt-Universität zu Berlin, Germany, 2010.

[193] Carl de Boor, *A Practical Guide to Splines*, Springer, New York, 1978.

[194] A. Lofthus and P. H. Krupenie, "The spectrum of molecular nitrogen", *J. Phys. Chem. Ref. Data*, vol. 6, pp. 113, 1977.

[195] P. Baltzer, B. Wannberg, L. Karlsson, M. Carlsson Göthe, and M. Larsson, "High-resolution inner-valence uv photoelectron spectra of the O_2 molecule and configuration-interaction calculations of $^2\Pi_u$ states between 20 and 26 eV", *Phys. Rev. A*, vol. 45, pp. 4374, 1992.

[196] S. D. Ganichev, E. Ziemann, Th. Gleim, W. Prettl, I. N. Yassievich, V. I. Perel, I. Wilke, and E. E. Haller, "Carrier tunneling in high-frequency electric fields", *Phys. Rev. Lett.*, vol. 80, pp. 2409, 1998.

List of Figures

List of Tables

Selbständigkeitserklärung

ich erkläre, das ich die vorliegende Arbeit selbständig und nur unter Verwendung der angegebenen Literatur und Hilfsmittel ngefertigt habe.

Berlin, den 4 Dezember 2014 Abdou Mekky Mousa Hussien